# Turbulent combustion modeling for Large Eddy Simulation of non-adiabatic stratified flames

Renaud Mercier

**École Centrale Paris**

# THÈSE

présentée par

**Renaud Mercier**

pour l'obtention du

GRADE de DOCTEUR

Formation doctorale : Énergétique

Laboratoire d'accueil : Laboratoire d'Énergétique Moléculaire et Macroscopique, Combustion (EM2C) du CNRS et de l'ECP

# Turbulent combustion modeling for Large Eddy Simulation of non-adiabatic stratified flames

Soutenue le 4 septembre 2015

| | | | | |
|---|---|---|---|---|
| **Jury :** | Prof. | Simone | Hochgreb | Présidente |
| | Prof. | Andreas M. | Kempf | Rapporteur |
| | Prof. | Luc | Vervisch | Rapporteur |
| | Dr. | Denis | Veynante | Examinateur |
| | Dr. | Laurent | Gicquel | Examinateur |
| | Prof. | Olivier | Gicquel | Co-encadrant |
| | Prof. | Benoît | Fiorina | Directeur de thèse |

École Centrale des Arts et Manufactures
Grand Établissement sous tutelle
du Ministère de l'Éducation Nationale
Grande Voie des Vignes
92295 Châtenay-Malabry Cedex
Tél : 33 (1) 41 13 10 00
Télex : 634 991 F EC PARIS

**Laboratoire d'Énergétique Moléculaire et Macroscopique, Combustion (E.M2.C.)**
UPR 288, CNRS et École Centrale Paris
Tél : 33 (1) 41 13 10 31
Fax : 33 (1) 47 02 80 35

2015ECAP0042

*Il était un petit lutin,*
*toujours gai et plein d'entrain.*
*Il allait par les chemins,*
*son baluchon à la main,*
*trois bouts de bois pour se chauffer,*
*une bonne pomme à croquer,*
*et à lui la liberté.*

# Remerciements

C'est un long et riche périple qui s'achève. Un autre démarre. Sur le chemin, beaucoup de personnes ont tiré la charrette avec moi. C'est ici que je souhaite les remercier et tenter de leur dire combien je leur suis reconnaissant.

Je tiens avant tout à remercier les membres du jury d'avoir accepté d'évaluer mon travail. Je remercie madame la professeur Simone Hochgreb pour avoir accepté de présider le jury de la soutenance. Merci aussi pour toutes ces caractérisations détaillées de flammes turbulentes super complexes, avec des pertes thermiques, de la stratification et tout et tout.

Je remercie aussi le professeur Andreas Kempf pour avoir accepté d'être rapporteur de ma thèse. J'ai beaucoup de bons souvenirs étalés sur toute la thèse : la visite d'une ancienne usine métallurgique transformée en un vaisseau spatial de Star Wars, la finalisation des slides du TNF11 au Beer Garden et plein d'autres... J'ai aussi une pensée pour Fabian avec qui j'ai beaucoup échangé, souvent dans l'urgence !

Je remercie le professeur Luc Vervisch d'avoir, lui aussi, accepté de passer une partie de son été à lire les pages de ce manuscrit - certainement trop long - pour entendre parler de pertes thermiques et de tilde-chapeau-bar. Merci aussi pour son rapport et ses questions lors de ma soutenance. Des questions et des convictions sur lesquelles on pourrait passer (passera encore ?) des heures.

Je remercie Laurent Gicquel, d'avoir accepté d'examiner mon travail et d'avoir apporté le lien aux applications concrètes au sein du jury. Les combustionnistes sont des gens cool qui ont su faire le lien entre les développements fondamentaux et les applications industrielles.

J'ai énormément appris aux côtés de mes encadrants. Je remercie Denis Veynante pour son ouverture et son accueil. Denis, qui n'était pas dans mon encadrement, a été d'une disponibilité infinie pour discuter des idées de nouvelles modélisations, de filtrage, de plissement et d'accidents d'avions ! Je mesure la chance que j'ai eu de recevoir cet accueil.

Je remercie aussi Nasser Darabiha pour sa gentillesse, sa disponibilité et surtout pour toutes ses flammes 1D sans lesquelles rien de tout ce travail n'aurait été possible ! Je suis très heureux de pouvoir continuer à échanger avec lui dans mon travail.

Merci à Olivier Gicquel pour ses grandes leçons : le fortran, le hdf5 (en 5 minutes) mais aussi combien il était bénéfique de travailler ensemble et non chacun de son côté. Merci aussi de m'avoir fait confiance pour les projets étudiants sur la propulsion hybride. J'en profite aussi pour remercier Erika et Alain sans qui le banc moteur fusée hybride de l'ECP n'aurait pas pu voir le jour.

Et puis, *last but not least*, je tiens à remercier Benoît Fiorina, mon directeur de thèse, pour ces trois (quatre, voire cinq...) années passées à travailler ensemble. Benoît a été mon guide dans la thèse mais aussi partout où il m'a emmené : dans les forêts du Texas, dans les rues d'Austin, à Luckenback avec Tom et Jean, à Pise, en Allemagne dans le vaisseau de Star Wars, à San Francisco pour manger des burgers avec Vincent...

Tout ce travail n'aurait pas non plus été possible sans un super solveur LES, tellement bien codé : un certain YALES2 (la page Facebook ouvrira prochainement pour les fans :-) ). Je tiens donc à remercier Vincent Moureau et Ghislain Lartigue pour leur disponibilité, pour les nombreuses discussions autour des développements dans YALES2. Mais pas seulement. Je les remercie aussi pour leur soutien, leurs encouragements, leurs félicitations tout au long de ma thèse, ils m'ont donné du courage en perfusion.

J'ai une pensée pour mes collègues de bureau, Florence, Maria et Thibault. Impossible ici de décrire ce que nous avons partagé, il y a trop de choses... Bon courage à Maria et Florence qui vont bientôt terminer. Big up à mon frère maléfique, mon poteau, passé du coté obscure des expérimentateurs avec des moustaches. On a bien déchiré. Je remercie aussi ceux qui m'ont si bien accueilli à mon arrivée : Jean Caudal, Jean Lamouroux et Pierre Auzillon. Je dois beaucoup à Pierre qui m'a expliqué, sans retenue, les petits secrets du modèle F-TACLES, j'espère avoir été digne du bébé. C'est à mon tour de le passer à Adrien à qui je souhaite le meilleur pour sa thèse. Je remercie aussi la dreamteam EM2C, Bénédetta Franzelli et al., Tom, Mémé, Ronan, Adam, Matthieu ( snif :-( ) . Vous me manquez déjà. J'espère continuer à manger plein de fromage avec vous encore longtemps.

Enfin, je remercie Alice et toute ma famille pour leurs encouragements et leur soutien sans faille. Le travail et les choses bien faites pour la liberté, ce sont mon frère, mes parents et monsieur Louis - puis plus tard, Gilles - qui me les ont appris.

# Résumé

La conception des chambres de combustion industrielles (chambres de combustion aéronautiques, fours industriels, etc.) requiert une prédiction fine des phénomènes physiques dominants. En particulier, l'interaction flamme-turbulence aux échelles résolues et non-résolues, l'impact de la composition et du mélange des réactifs, l'impact des pertes thermiques et de la diffusion différentielle doivent être capturés fidèlement. C'est dans ce contexte que le modèle de combustion turbulente F-TACLES (Filtered TAbulated Chemistry for Large Eddy Simulation) a été développé afin de coupler une méthode de chimie tabulée (FPI) avec le formalisme de la simulation aux grandes échelles (LES).

Dans cette thèse, le modèle F-TACLES, initialement développé pour des écoulements adiabatiques, est étendu à la prise en compte des pertes thermiques. Un formalisme adapté à l'utilisation de bases de chimie tabulée calculées avec la diffusion différentielle est aussi proposé. Ces développements sont validés sur deux configurations : le brûleur TSF et le brûleur SWB.

La modélisation de l'interaction flamme-turbulence est ensuite étudiée. Une étude de sensibilité du modèle de plissement de sous-maille de Charlette et al. (2002) à ses paramètres et sous-modèles est réalisée sur le brûleur SWB. En particulier, une méthode d'estimation dynamique des paramètres est aussi évaluée et montre d'excellents résultats. Une généralisation du formalisme de la LES pour les écoulements réactifs est ensuite proposée afin de prendre en compte explicitement les deux filtres mis en jeu dans les simulations : le filtre associé à l'écoulement et le filtre associé à la flamme. Deux stratégies de fermetures sont proposées en se basant sur des modèles existants (F-TACLES et TFLES). Le modèle obtenu, appelé modèle F2-TACLES, est ensuite validé et comparé avec F-TACLES sur la configuration semi-industrielle PRECCINSTA.

Pour terminer, la capacité du modèle F-TACLES à capturer l'impact des pertes thermiques et de la composition des gaz frais sur la topologie de flammes est évaluée. Cette étude est réalisée sur une série de flammes $CH_4$-$H_2$-Air turbulentes en giration et prenant des formes différentes en fonction du niveau de pertes thermiques et de la composition des réactifs.

**Mots clés** : Simulation aux grandes échelles; Combustion turbulente; Chimie tabulée; Pertes thermiques; diffusion différentielle; plissement de sous-maille; Modèle F-TACLES; Modèle F2-TACLES.

# Abstract

The design of industrial combustion chambers (aeronautical engines, industrial furnaces, etc.) require a fine prediction of the different governing phenomena. Flame-turbulence interaction at resolved and unresolved scales, impact of reactants composition and mixing process, impact of heat losses and differential diffusion have to be correctly captured in such configurations. For that purpose, the turbulent combustion model F-TACLES (Filtered Tabulated Chemistry for Large Eddy Simulation) has been developed to couple tabulated chemistry with large eddy simulation (LES) formalism.

In this thesis, the F-TACLES model, initially developed for unity Lewis number and adiabatic flows, is extended to account for heat losses. A formalism allowing the use of chemical databases (1-D premixed flames) computed with differential diffusion is also proposed. The extended model is validated on two different configurations: the TSF burner and the SWB burner.

Modeling of flame-turbulence interaction is then studied. For unresolved flame-turbulence interactions, a sensitivity analysis of the Charlette et al. (2002) sub-grid scale wrinkling model to its own parameters and sub-models is performed on the SWB burner. A dynamic estimation of the model parameter is also assessed and showed very promising results. For resolved flame-turbulence interactions, a generalized formalism of the LES of reactive flows is proposed in order to account explicitly for both flame and flow filters. Two closure strategies are proposed based on the F-TACLES and TFLES models. The F2-TACLES model is then validated and compared to the original formulation of the F-TACLES model. This study is performed on the lean premixed semi-industrial PRECCINSTA burner.

The ability of the extended F-TACLES model to capture the impact of both heat losses and fresh gas composition on the flame topology is assessed. This study is conducted on a $CH_4$-$H_2$-Air turbulent and swirling flame series. These flames exhibit very different shapes depending on the level of heat losses and fuel composition.

**Keywords** : Large Eddy Simulation; Turbulent combustion; Tabulated chemistry; Heat losses; Differential diffusion; Sub-grid scale wrinkling; F-TACLES model; F2-TACLES model.

# Contents

# List of publications

## Peer-reviewed journals

- R. Mercier, V. Moureau, D. Veynante, B. Fiorina, *LES of turbulent combustion: On the consistency between flame and flow filter scales*, Proceedings of the Combustion Institute 35, Issue 2, 2015, Pages 1359-1366, ISSN 1540-7489.
- R. Mercier, T. Schmitt, D. Veynante, B. Fiorina, *The influence of combustion SGS submodels on the resolved flame propagation. Application to the LES of the Cambridge stratified flames*, Proceedings of the Combustion Institute 35, Issue 2, 2015, Pages 1259-1267, ISSN 1540-7489.
- R. Mercier, P. Auzillon, V. Moureau, N. Darabiha, O. Gicquel, D. Veynante, B. Fiorina. *LES modeling of the impact of heat losses and differential diffusion on a turbulent stratified flame*, Flow, Turbulence and Combustion, Volume 93, Issue 2, 2014, Pages 349-381, ISSN 1386-6184.
- B. Fiorina, R. Mercier, G. Kuenne, A. Ketelheun, A. Advic, J. Janicka, D. Geyer, A. Dreizler, E. Alenius, C. Duwig, P. Trisjono, K. Kleinheinz, S. Kang, H. Pitsch, F. Proch, F. Marincola, A. Kempf. *Challenging modeling strategies for LES of non-adiabatic turbulent stratified combustion*, Submitted to Combustion and Flame.
- T. F. Guiberti, R. Mercier, B. Fiorina, L. Zimmer, D. Durox, T. Schuller. *Flame shape bifurcations in a confined swirled burner: analysis of the combined effects of strain rate and heat losses*, Submitted.
- R. Mercier, T. F. Guiberti, A. Chatelier, D. Durox, T. Schuller, O. Gicquel, N. Darabiha, B. Fiorina. *Experimental and numerical study of premixed swirled combustion: influence of thermal boundary conditions on the flame stabilization*, Submitted.

## Peer-reviewed conference publications

- R. Mercier, P. Auzillon, V. Moureau, N. Darabiha, O. Gicquel, D. Veynante, B. Fiorina. *Modeling flame stabilization by heat losses using filtered tabulated chemistry for LES*, International Symposium on Turbulence and Shear Flow Phenomena 8. August 28-30th, 2013.

- R. Mercier, F. Proch, A. M. Kempf, B. Fiorina. *Numerical and modeling strategies for the simulation of the Cambridge stratified flame series*, International Symposium on Turbulence and Shear Flow Phenomena 8. August 28-30th, 2013.
- M. Demoly, J. Fissette, O. Vielpeau, A. Treilhes, N. Rizzo, J. Rèbre, J. Mulpas, V. Jacaranda Lakiss Marques, E. Jean-Bart, R. Mercier, B. Fiorina, O. Gicquel. *Design of the feed system of a Hybrid Rocket Engine.* 5th European Conference for Aeronautics and Space Sciences. July 1-5th, 2013.
- R. Mercier, T. F. Guiberti, L. Zimmer, D. Durox, O. Gicquel, N. Darabiha, T. Schuller, B. Fiorina. *Experimental and numerical studies of hydrogen enrichment impact on a non-adiabatic confined swirled flame*, Proceedings of the European Combustion Meeting, Budapest, Hungary, March 30–April 2, 2015.

# Introduction

*Cette thèse a été réalisée dans le cadre du projet ANR VALOGAZ (VALOrisation des GAZ à faible pouvoir calorifique dans les fours industriels). Ce projet s'inscrit dans le programme EESI (Efficacité Energétique et réduction des émissions de CO2 dans les Systèmes Industriels) de l'Agence Nationale de la Recherche (ANR). Il rassemble ArcelorMittal Maizières Research, IFP Energies Nouvelles et le laboratoire EM2C.*

## Challenges for the design of industrial combustion chambers

Current environmental issues motivate industries to increase the energetic efficiency and decrease the pollutant emissions of their processes. The Kyoto protocol, adopted in 1997 and applied from 2005, aimed at decreasing or limiting the greenhouse gas emissions (mainly $CO_2$) in 83 countries including Europe. In this context, a decrease of $CO_2$ emissions by 11.4 % has been observed in France between 1990 and 2012. European Commission fixed recently the new challenging objective to decrease by 80% - 95% the greenhouse gas (GHG) emissions before 2050. The main GHG such as $H_2O$ and $CO_2$ are mainly issued from the conversion of fossil fuels (coal, oil and natural gas) into thermal energy through the combustion process. In 2012, this energy conversion process achieved 92.5% of the total primary energy supply in Europe and 91.7% in the world (International Energy Agency, 2015). Although finite and running out ressource, fossil fuel remains the main world energy supplier through combustion-based technologies that need to be improved to reduce fuel consumption and polluants emissions. To achieve this objective, efforts are therefore needed in all the combustion-related activities such as transport, energy production, construction industry and industrial processes. In this context, the design of the combustion chamber is a key point to meet the previous consumption and pollution objectives. An optimized design should improve the combustion efficiency to ensure that the injected fuel is effectively burnt within the chamber and for the whole operating range. It should also increase the lifetime of the materials composing the chamber by decreasing as much as possible the temperature near the walls. The safety features are also closely linked to

the design of the injection process as well as the oxidizer-fuel mixing. Finally, the different pollutants are all created within the combustion chamber through complex chemical processes that should be predicted during the design phase which appear to be crucial for all the combustion related applications. A focus is made here on two different application domains.

The first relevant example is the aeronautical industry. Global objectives for the decrease in polluant emission has been concretized in Europe by the Advisory Concil for Aeronautics Research in Europe (ACARE, 2015). ACARE, founded in 2001, raised quantified objectives for commercial planes in terms of quality and affordability, noise and emissions, safety and airport efficiency. These objectives for the year 2020 are related to the reference of the year 2000. In particular, the challenge area "noise and emissions" proposes to decrease the $CO_2$ emissions by 50%, $NO_x$ emissions by 80% and external noise of the airplanes by 50%. To meet these objectives, especially for the reduction of $CO_2$ emissions, a drastic reduction of the fuel consumption for a given payload is required. The first challenge is here to decrease the overall mass of the airplane improving the structural design as well as the materials of the structure. The other challenge lies in the design of the engine for noise emissions and its combustion chamber for the different pollutant emissions such as $NO_x$. The reduction of pollutant emissions can be achieved through a fine control of the fuel-air mixing as well as the level of temperature in the combustion chamber. For that purpose, the design process have to include predictive tools able to capture the unsteady mixing process between fuel and reactants, the temperature field within the combustion chamber and especially near the walls and at the outlet (in order to guaranty the lifetime of each structural component). The design optimisation of aeronautical burners also has to preserve the operability range of the engine (ignition and extinction limits) and to prevent from combustion instabilities. To do so, design tools also have to capture the flame dynamics and its interactions with all the other physical phenomena holding in the chamber (mixing of the reactants, flow turbulence, acoustics, etc.).

The second example is the metallurgy industry. The Integrated Pollution Prevention and Control European directive (IPPC, 2015) aims to decrease the emissions of the most pollutant industrial processes including metallurgy. This directive promotes the use of the best available techniques (*i.e.* the less polluting or the most energetically efficient). Taking here the example of the steel production process (see Fig. 1), the recycling of the residual gases issued from the different steel production steps is a good candidate to improve the energetic efficiency of the steel mill. Three types of residual gases, identified Fig. 1, can be considered: *(i)* the Coke Oven Gas (COG) issued from the coal transformation is a high calorific value gas (38 $MJ.kg^{-1}$) which mainly contains $CH_4$ and $H_2$; *(ii)* the Blast Furnace Gas (BFG), produced during the formation of pig iron, is mainly composed of CO, $CO_2$ and $N_2$ and has a low calorific value

(3 MJ.kg$^{-1}$); *(iii)* the basic oxygen furnace gas (BOFG), produced during the conversion of pig iron into steel, is also composed of CO, $CO_2$ and $N_2$ with different proportions. Its calorific value (7 MJ.kg$^{-1}$) is slightly higher than BFG but still remains very low. A possible option consists in using these gases (individually or mixed) as a fuel in the Steel Preheating Furnaces (SPF) of the plant where they are produced. This option allows both to promote the residual gases without any transformation and transportation but also to decreases the amount of natural gas burnt in SPF. The combustion of residual gases in SPF in order to partially replace natural gas is very challenging because the chemical composition of COG, BFG and BOFG varies depending on the coal and iron ore compositions. Ideally, each burner should be able to stabilize the flames independently from the fuel composition. The objective is therefore to design new burners with an increased operating range in terms fuel composition. In this example, the main challenges for the design tools are quite similar to the aeronautical context. An additional challenge is to capture the impact of a variation in fuel composition on the turbulent combustion features (flame stability and shape, pollutant emissions, flow temperature, etc.). Furthermore, since industrial furnaces exhibit large dimensions and very slow convective time scales, the heat exchange between the burnt gases and the chamber walls are of great importance and can not be neglected.

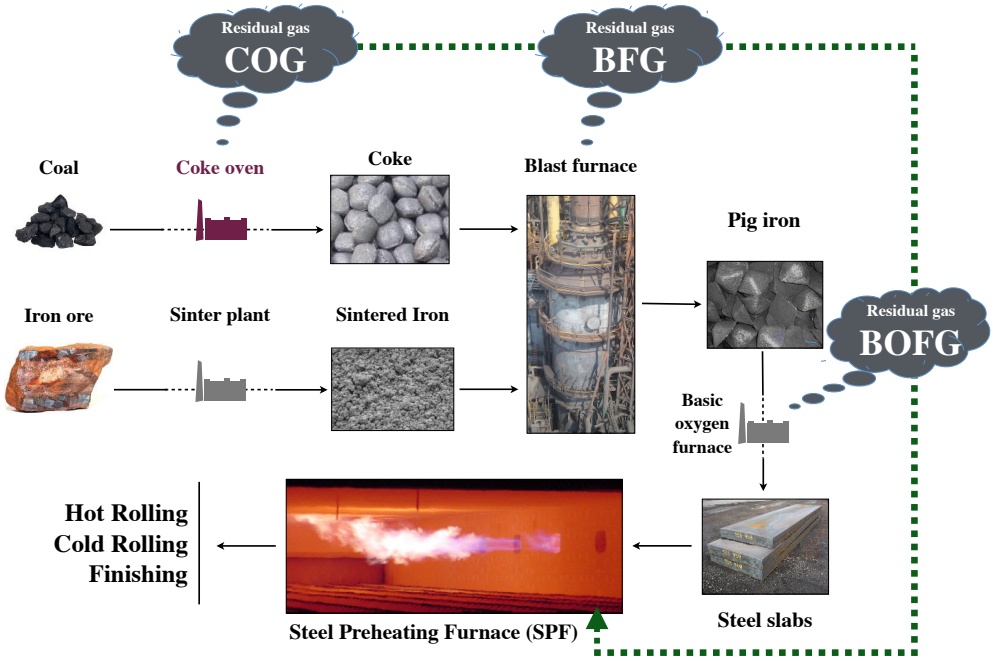


**Figure 1:** *Scheme of the steel production process including the potential recycling of residual gases*

## Predicting turbulent combustion using Large Eddy Simulation

With the recent revolution of High Performance Computing (HPC), Large Eddy Simulation (LES) is now used to design combustion chambers, for instance, in the aeronautical industry. Despite its very high computational cost compared to previous techniques (functional modeling, Reynolds-Averaged Navier-Stokes equations (RANS)), LES has the ability to resolve in time and space large turbulent eddies. As these eddies generally control the composition and energy mixing processes, LES provides a fine prediction of theses mixing phenomena which mainly govern the combustion process. These features show that LES is a very good candidate to help the design of the future industrial combustion chambers. Nevertheless, the resolution of the flame front and its interaction with the flow motion remain unaffordable, with current computational power, due to its very low time and length scales. As an illustration, a typical kerosene-air flame thickness at high pressure (encountered in aeronautical chambers, at take-off conditions) is $\delta = 0.1$ mm while an affordable grid size for such configurations would be around $\Delta_x = 1$ mm. Indeed, in practical applications, the LES filter size is larger than the flame front thickness meaning that the combustion process operates at the sub-grid scale. Therefore, the unresolved combustion process needs to modeled. This research topic is also called turbulent combustion modeling and is of major importance for the LES of combustion chambers.

The first challenge for LES turbulent combustion models is to predict the turbulent flame consumption speed which controls the flame propagation, position, stabilization process but also the local heat release. This consumption speed can be governed by different physical phenomena depending on the nature of the flame-turbulence interactions, also called turbulent combustion regime. A description of the different combustion regimes is proposed in appendix A. After a short description of each regime, an estimation of the order of magnitude of the Karlovitz number $K_a$ is performed for an aeronautical combustion chamber and a steel preheating furnace and for three given operating conditions fixed to be representative of the industrial application. These estimations, although qualitative, show that $K_a \sim 1$ for the three considered cases despite the large range of considered geometries and operating conditions. These cases are located at the edge between thin flame (or flamelet) and thin reaction zone regimes. Some authors actually locate these cases within the flamelet regime which seems to be valid for $K_a$ higher than unity (Roberts et al., 1993; Driscoll, 2008). Of course, the situation where $K_a \gg 1$ is also likely to appear in industrial configurations but will not be studied in this thesis.

Within the thin flame regime, the turbulent flame consumption speed is controlled by fresh gases composition and mixing, heat losses, and flame wrinkling due to flame-turbulence interactions. Each phenomena is of importance in

the case of industrial combustion chambers. A turbulent combustion model adapted to the LES of industrial burners should therefore be able to predict the unsteady temperature field, the pollutant formation, the flame stabilization and its dynamics. Such features are impacted by the following phenomena which have to be captured: the unsteady mixing of the reactants which may be of complex composition, the heat losses, the flame interactions with flow and acoustics. In an LES context, these phenomena operate at both the resolved (large) and unresolved (small) scales. The challenge addressed in this thesis is then to improve a modeling strategy, accounting for the impact of unresolved mixing, of complex composition of the fresh gases, of heat losses and of resolved and unresolved flame wrinkling.

This work is based on a modeling strategy developed since 2010 at EM2C laboratory and called Filtered Tabulated Chemistry for LES (F-TACLES). The F-TACLES model was developed by Fiorina et al. (2010) for adiabatic and fully-premixed flames. It was extended to partially-premixed combustion (Auzillon et al., 2012) during the thesis of Auzillon (2011). However, before the present thesis, the F-TACLES model was not adapted to industrial configurations where the phenomena, discussed previously, are important. This thesis aims to improve the F-TACLES modeling strategy for industrial configurations. For that purpose, the major contributions of this thesis are listed thereafter.

## Contributions of this thesis

- **Heat losses and differential diffusion:** This thesis extends and validates the F-TACLES model, initially developed for unity Lewis number and adiabatic flows, to account for heat losses. A formalism allowing the use of chemical databases (1-D premixed flames) computed with differential diffusion is also proposed.

- **Unresolved flame-turbulence interactions:** A sensitivity analysis of the Charlette et al. (2002a) sub-grid scale wrinkling model to its own parameters and sub-models is performed. A dynamic estimation of the model parameter is also assessed and appears to be a very promising approach.

- **Resolved flame-turbulence interactions:** A generalized formalism of the LES of reactive flows is proposed in order to account explicitly for both flame and flow filters. A new closure based on the F-TACLES model, called F2-TACLES, is derived and validated on a turbulent burner. This new version of the model improves the resolved flame dynamics.

- **Impact of heat losses and fuel composition on flame topology:**

The ability of the extended F-TACLES model to capture the impact of both heat losses and fresh gas composition on the flame topology is assessed. The extended F-TACLES model is applied to a confined and turbulent burner, called EM2C burner, representative of a sector of industrial furnace. This has been experimentally characterized by Guiberti (2015) while parallel numerical investigations where performed in this thesis.

- **Models implementation:** Both F-TACLES and F2-TACLES models have been implemented in the official release of the low-Mach LES solver YALES2, developed at CORIA laboratory (Moureau et al., 2011a). A look-up table generator, named Chemical Automatic Filtering for Engineers (CAFE), has also been developed to generate look-up tables for three different combustion models (TFLES-FPI, F-TACLES, F2-TACLES) and compatible with two different LES solvers (YALES2, AVBP).

## Organization of this manuscript

The major part of the thesis developments will be performed using the F-TACLES formalism in a low-Mach number context. This model will be extended to provide a finer description of turbulent combustion in industrial combustors. This thesis manuscript is organized in four parts:

- **Part I** identifies the technical challenges for the turbulent combustion modeling in industrial burners.

  **Chapter 1** draws a state of the art of the turbulent combustion modeling strategies for Large Eddy Simulation. The physical phenomena that should be captured by LES combustion models is first proposed. To meet these requirements, different approaches to model combustion chemistry and flame-turbulence interactions are presented. The review is restricted to the modeling of thin flame combustion regime and focuses on the models compatible with tabulated chemistry. The challenges faced by each models are identified to motivate the different studies performed in this thesis.

- **Part II** presents and validates the different modeling efforts conducted to enhance the prediction of the turbulent flame speed. These developments are performed in the framework of the F-TACLES model.

  **Chapter 2** The impact of heat losses and differential diffusion on the flame consumption speed and structure are accounted for in this chapter. A non-adiabatic database is built from burner-stabilized 1-D flames to capture the impact of a given enthalpy defect. This database is then used to correct the

turbulent flame consumption speed and thermochemical quantities. The proposed approach does not increase the overall number of coordinates in the table.

**Chapter 3** The non-adiabatic F-TACLES model is validated on two academic turbulent stratified jet flames proposed in the TNF workshop : *(i)* the Darmstadt Turbulent Stratified Flame TSF-A, *(ii)* the Cambridge Statified Swirl Burner SWB flame series. The impacts of heat losses and differential diffusion on the stabilization process, the mean velocity and the temperature fields are analyzed in this chapter.

- **Part III** focuses on the prediction of flame-turbulence interactions at the resolved and unresolved scales.

  **Chapter 4** An analysis of the impact of SGS wrinkling model on the turbulent flame structure is also conducted on the SWB flame series. The focus is made on the Charlette et al. (2002a) model. The impact of the sub-models required by the sub-grid scale wrinkling function is discussed. A more recent approach, taking advantage of the resolved wrinkling scales is also considered. This last approach, called dynamic SGS wrinkling function, shows a good agreement with experiments and limits the number of user-defined parameters.

  **Chapter 5** The coupling between the flow and flame equations at the resolved scales is discussed in this chapter. A new LES formalism for turbulent reacting flows is proposed to ensure the consistency between flame and flow filter scales. The objective is to provide a consistent mathematical framework to describe the coupling between flame and flow equations. A new LES combustion model, called F2-TACLES, is derived in this context. This formalism is validated on 1-D filtered flames and on the lean premixed turbulent combustor PRECCINSTA.

- **Part IV** The non-adiabatic F-TACLES model is applied to a confined turbulent $CH_4$-$H_2$-Air burner designed and measured at EM2C Laboratory. This burner exhibits complex physical phenomena and is representative of the combustion of residuals gases, issued from steel production process, in industrial furnaces.

  **Chapter 6** Numerical and experimental set-ups of the EM2C burner for non-reacting measurements and simulation are presented in this chapter. The choice of the operating conditions and the velocity measurements are exposed. The numerical strategy and results are presented to validate the ability of the numerical strategy to capture flow dynamics.

  **Chapter 7** Experimental measurements on the reacting case are introduced in this chapter. Two different flame shapes, called V and M, are observed depending on the fuel composition. The non-adiabatic F-TACLES model is used

to perform the LES of the two different operating conditions. For comparison purpose, the adiabatic F-TACLES model is also applied to the EM2C burner. Heat losses are found to govern the flame shape and the non-adiabatic model correctly captures the mean flame shape for both V-shape and M-shape flames.

# Part I

# Challenges for the LES of turbulent flames in industrial combustion chambers

# Chapter 1

# Large Eddy Simulation of turbulent combustion: state of the art

**Contents**

*The thin flame regime is the more likely to be found in the industrial combustion chambers considered in this thesis. The present chapter aims to answer the question: how to simulate turbulent flames evolving in the thin flame regime ? To answer this question, the main simulation techniques are introduced and the focus is made on Large Eddy Simulation where large turbulent scales are resolved while smallest ones are modeled. Therefore, modeling issues related to the unresolved turbulent structures and to the flame front are discussed. Basic requirements to model a turbulent flame in practical combustion chambers are proposed and a review of a selection of turbulent combustion models is finally performed.*

## 1.1 Motivations

Direct Numerical Simulation of turbulent flames is affordable only for very small computational domains and is therefore not appropriate to predict flame behavior in practical combustion chambers. To overcome this difficulty, a first approach consists in solving only the mean reacting flow. This can be achieved by averaging the Navier-Stokes equations to obtain a set of equations for the mean density, momentum and energy (Launder and Spalding, 1974). This simulation technique, called Reynolds-Averaged Navier-Stokes (RANS), has been very popular to simulate reactive flows during the last decades. The computational cost of RANS simulations is very low because of the two following reasons:

- The gradients of mean variables are smoother than the gradients of instantaneous variables. Consequently, the minimum grid size in the mesh is much larger than in DNS.
- RANS simulations are often used for steady computations. The computational cost is then reduced.

The main issue associated to this simulation technique is the closure of unknown terms. Indeed, models for unresolved turbulent fluctuations as well as for the chemical reactions are required. Building such models is very difficult as they have to predict the impact of all the unsteady phenomena using only resolved mean variables. Consequently, the final results are known to be very dependent on the selected modeling approaches and the prediction capacities of RANS simulation are known to be limited. Considerable efforts have been spent to derive RANS turbulent combustion models with the additional difficulty that chemical reactions are highly non-linear. Therefore, modeling the mean reaction rates is a very challenging issue, handled using various concepts reviewed in Peters (2000); Veynante and Vervisch (2002); Poinsot and Veynante (2012) and Fiorina et al. (2015b).

Unsteady RANS formulation is also used to simulate time dependent processes. This technique allows a resolution in time of very low frequency phenomena

compared to the frequencies of turbulent motions. When boundary conditions are varying in time, the URANS results may be seen as the phase-averaged response of the flow (Sagaut, 2006).

Figure 1.1 shows that Large Eddy Simulation (LES) can be seen as an intermediate alternative between DNS and RANS simulation. It consists in resolving the large scales of the flow and in modeling the small ones. A spatial filtering formalism allows to write balance equations for filtered variables. The LES filter size $\Delta$ therefore corresponds to the smallest resolved scale (*i.e.* the limit between resolved and modeled scales in Fig. 1.1). In practice, the mesh size $\Delta_x$ implicitly controls the LES filter size $\Delta$: Turbulent structures smaller than twice the mesh size are modeled while larger structures are resolved. Historically, LES has been first used for non-reactive flow (Smagorinsky, 1963) and later to reactive flows (Menon and Jou, 1991) because of its attractive features for the simulation of turbulent combustion:

- First, the largest scales are usually the more energetic which means that the majority of the flow kinetic energy is resolved in LES (Pope, 2004). The impact of the small scales modeling is then limited from an energy point of view. Large scale structures are mainly controlled by walls geometry and influence mean flame features such as turbulent flame stabilization and position. They also play an important role in thermo-acoustic instabilities. In the other hand, the small scales are less affected by the combustor geometry and are more isotropic (except very near the walls) (Biferale and Vergassola, 2001). Therefore, a more universal and reliable modeling of small turbulent scales is possible in LES.
- Another advantage compared to the RANS approach is the possibility to use the knowledge of resolved scales to model smaller ones. This concept has been first formalized for non-reactive flow by Germano et al. (1991) but has been recently extended to the turbulent combustion modeling (Charlette et al., 2002b). This point is further discussed in Chapter 4 of this thesis. Scale similarity models are also based on an approximation of unresolved quantities using the knowledge of the resolved ones (Bardina et al., 1980; Knikker et al., 2002).
- Finally, as the LES filter size $\Delta$ is basically controlled by the grid size $\Delta_x$, a mesh refinement operation is sufficient to increase the resolution of the resolved field and decrease the contribution of sub-grid scale (SGS) models. The resolution directly depends on the size of the mesh that can be afforded. LES tends to DNS when the mesh is sufficiently refined to capture all the length scales of the reactive flow.

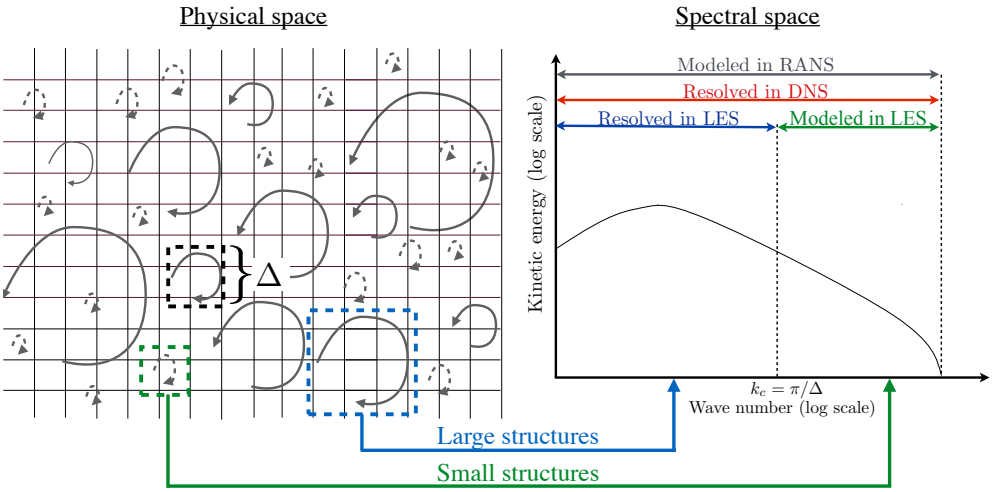


**Figure 1.1:** *Comparison of DNS, LES and RANS simulation techniques on an idealized non-reacting homogeneous and isotropic turbulent flow. $\Delta$ stands for the LES filter size. All turbulent structures are modeled in RANS (solid and dashed arrows). All turbulent structures are resolved in DNS (solid and dashed arrows). Only large turbulent structures are resolved in LES (solid line arrows) while structures smaller than the filter size $\Delta$ are modeled (dashed line arrows).*

## 1.2 Large Eddy Simulation formalism

Large Eddy Simulation is based on the resolution of spatially-filtered density, momentum, energy and chemical species balance equations. Any filtered variable $\overline{\Phi}$ is then defined as follows:

$$\overline{\Phi}(x,t) = \int \Phi(x',t) F(x-x') dx' \tag{1.1}$$

The filter kernel $F$ is commonly defined in physical space using normalized top-hat or Gaussian functions (Poinsot and Veynante, 2012). The definition of $F$ influences sub-filter scale models. When variable density flows are considered, it is also useful to define the Favre filtering operator:

$$\widetilde{\Phi} = \frac{\overline{\rho\Phi}}{\overline{\rho}} \tag{1.2}$$

Any quantity $\Phi$ is now defined as the sum of its filtered part and its sub-filter value $\phi = \overline{\phi} + \phi' = \widetilde{\phi} + \phi$". Note also that filtering operators commute with derivative operator only when the filter size is constant in space and time. When it is not the case, commutation errors exist but are generally neglected or included in the sub-grid scale models.

Low Mach number flows are governed by the following set of equations (the

derivation of these equations is detailed in Appendix B):

$$\frac{\partial \overline{\rho}}{\partial t} + \frac{\partial}{\partial x_i}(\overline{\rho}\widetilde{u_i}) = 0 \tag{1.3}$$

$$\frac{\partial}{\partial t}(\overline{\rho}\widetilde{u_j}) + \frac{\partial}{\partial x_i}(\overline{\rho}\widetilde{u_i}\widetilde{u_j}) = -\frac{\partial \overline{p_2}}{\partial x_j} + \frac{\partial \overline{\tau_{ij}}}{\partial x_i} - \frac{\partial}{\partial x_i}(\overline{\rho}(\widetilde{u_i u_j} - \widetilde{u_i}\widetilde{u_j})) + \overline{\rho}\widetilde{f_j} \tag{1.4}$$

$$\frac{\partial \overline{\rho}\widetilde{Y_k}}{\partial t} + \frac{\partial}{\partial x_i}\left(\overline{\rho}\widetilde{u_i}\widetilde{Y_k}\right) = -\frac{\partial}{\partial x_i}\left(\overline{\rho Y_k V_{k,i}}\right) - \frac{\partial}{\partial x_i}\left(\overline{\rho}(\widetilde{Y_k u_i} - \widetilde{Y_k}\widetilde{u_i})\right) + \overline{\rho}\widetilde{\dot{\omega}_{Y_k}} \tag{1.5}$$

$$\begin{aligned}\frac{\partial}{\partial t}(\overline{\rho}\widetilde{h}) + \frac{\partial}{\partial x_i}(\overline{\rho}\widetilde{u_i}\widetilde{h}) &= \frac{\partial}{\partial x_i}\left(\overline{\lambda\frac{\partial T}{\partial x_i} - \rho\sum_{k=1}^{N_{sp}}[Y_k h_k V_{k,i}]}\right) \\ &\quad -\frac{\partial}{\partial x_i}\left(\overline{\rho}(\widetilde{hu_i} - \widetilde{h}\widetilde{u_i})\right)\end{aligned} \tag{1.6}$$

$$p_0 = \overline{\rho}\widetilde{rT} \tag{1.7}$$

This system of equations exhibits several unknown terms that need to be modeled. The first unclosed term is the sub-filter stress tensor $\overline{\tau}^t_{ij} = -\overline{\rho}\left(\widetilde{u_i u_j} - \widetilde{u_i}\widetilde{u_j}\right)$ which represents the impact of the unresolved flow motions on the resolved momentum. A common modeling methodology for this term consists in expressing the tensor $\overline{\tau}^t_{ij}$ as a simple function of the resolved rate of strain tensor $S_{ij}$ as:

$$\overline{\tau_{ij}}^t = 2\overline{\rho}\nu_t^{\Delta}\left(\widetilde{S}_{ij} - \frac{1}{3}\delta_{ij}\widetilde{S}_{kk}\right) \tag{1.8}$$

where $\widetilde{S}_{ij} = \frac{1}{2}\left(\frac{\partial \widetilde{u_i}}{\partial x_j} + \frac{\partial \widetilde{u_j}}{\partial x_i}\right)$ is the rate of strain of the resolved flow field and $\nu_t^{\Delta}$ is the subgrid (or sub-filter) scale (SGS) turbulent kinematic viscosity. $\nu_t^{\Delta}$ can been seen as a viscosity which reprensents the unresolved turbulent fluxes as a purely diffusive process. In other words, the impact of all the turbulent structures smaller that $\Delta$ is modeled through $\nu_t^{\Delta}$. Turbulence models, give an expression to this sub-filter turbulent viscosity using generally algebraic expressions (Smagorinsky, 1963; Nicoud et al., 2011; Ducros et al., 1998). Dynamic[1] estimations of the algebraic model constants have also been proposed (Germano et al., 1991; Lilly, 1992). These LES turbulence models have been initially derived for non-reactive flows but are used for the simulation of reacting flows.

As for sub-filter turbulent scales, the flame front is generally thinner than the LES filter size in most of practical LES computations. A typical mesh size affordable for the LES of complex geometries is $\Delta_x \approx 1$ mm while a typical flame thickness is $\delta_l \approx 0.1$ mm (example of an aeronautical combustion chamber). The capture of the flame front propagation (speed, interaction with the flow, etc.) and its inner structure (temperature, density, chemical species, etc.) is

[1]The term "dynamic" is used here to designate the use of resolved flow motions to evaluate "on-the-fly" some unknown quantities.

then a challenge addressed by turbulent combustion models. An LES turbulent combustion model aims to provide a consistent closure of the unknown terms related to the transport of chemical species and energy:

- $\overline{\rho Y_k V_{k,i}}$ is the filtered species laminar diffusion flux.
- $\overline{\rho}(\widetilde{Y_k u_i} - \widetilde{Y_k}\widetilde{u_i})$ is the unresolved transport of the chemical species.
- $\widetilde{\dot{\omega}_k}$ is the filtered chemical reaction rate of the $k$th species.
- $\overline{\lambda \frac{\partial T}{\partial x_i} - \rho \sum_{k=1}^{N_{sp}} [Y_k h_k V_{k,i}]}$ is the filtered thermal diffusive flux.
- $\overline{\rho}(\widetilde{h u_i} - \widetilde{h}\widetilde{u_i})$ is the unresolved enthalpy flux.

In practice, modeling strategies consist either in providing a direct estimation of the above listed terms (algebraic expressions) or in providing an alternative strategy (addition of transport equations, tabulation, etc.) to access the variables of interest such as temperature, density, pollutants, etc. The different objectives and constrains for the turbulent combustion models derivation will be discussed in the following section. The discussion is restricted to the modeling of premixed (or stratified) turbulent flames evolving in the thin flame regime, commonly encountered in practical combustors.

## 1.3 Requirements for LES turbulent combustion models

It is proposed to break down the different situations that can be encountered when a turbulent flame, evolving in the thin flame (or flamelet) regime, is computed using the LES formalism. Figure 1.2 exhibits 3 different cases. For each subfigure, the non-filtered flame front (that cannot be captured on the LES grid) is defined by the black line. The filtering of the flame front at the LES filter size $\Delta$ leads to three different cases depending on the resolution of the flame wrinkling. The filtered flame front (that should be correctly captured by LES combustion models) is represented by the thick red line. $S_\Delta$ is the filtered flame consumption speed while $S_l$ denotes the local consumption speed of the non-filtered flame. The three situations, listed and described below, may coexist in a single LES computation as mesh size and turbulence levels often vary in space and time for complex geometries:

**(a)** In the first case, turbulence doesn't occur neither at the sub-filter scale nor at the resolved scale. In this context, neither the non-filtered flame front nor the LES flame front are wrinkled. The unfiltered and the filtered flame have the same surface of reaction. When fresh gases are perfectly premixed, the local flame consumption speed $S_l$ and the filtered flame consumption speed are equal $S_\Delta = S_l$.

**(b)** In the second case, the flame front is wrinkled due to the interaction with the different turbulent structures. However, the wrinkling scales are larger than the LES filter size $\Delta \approx 2\Delta_x$. In this situation, all flame wrinkling scales are resolved and no sub-filter scale wrinkling occurs. As in the first

case, the filtered flame surface is equal to the DNS flame surface and both flame fronts should propagate at the same speed $S_\Delta = S_l$ assuming that $S_l$ includes the curvature and strain effects.

**(c)** In the last case, the flame front is wrinkled at both resolved and unresolved scales. For a given volume of fluid, the filtered flame surface is lower than the non-filtered flame surface because small scale wrinkling has been lost during the filtering process. In practice, small scale wrinkling is smaller than the LES mesh size and cannot be resolved. In this case, the local filtered flame consumption speed is higher than the laminar flame consumption speed $S_\Delta > S_l$ as the flame surface at sub-filter scale is higher than the resolved flame surface.

For each scenario presented in Fig. 1.2, the modeling strategies have to correctly predict different flame features such as:

**Flame consumption speed :** The mean position of the flame front (also called mean flame brush) is very important as it indicates the location where the fuel is converted in heat release and where the temperature increases. Flame stabilization process and position are correctly predicted only if the flame consumption speed $S_\Delta$ is accurately modeled.

**Thermochemical flame structure :** Environmental standards require to be able to quantify the pollutant emissions of the industrial combustion chambers. Thus, chemical composition of burnt gases have to be predicted by the combustion models. A relevant estimation of the flow temperature is also needed to properly design the materials for the combustion chamber walls or for other sub-systems such as turbine blades located at the exit of aeronautical combustion chambers. Finally, the local heat release plays a very important role for instance in the thermo-acoustic instabilities.

**Flame-turbulence interactions :** The prediction of flame dynamics relies on the interactions between flame front and flow structures (Peters, 2000). Such phenomena also play an important role in combustion instabilities as hydrodynamic and thermo-acoustic oscillations (Poinsot and Veynante, 2012).

In practical combustion chambers, the modeling of the above listed turbulent combustion features requires to account for different physical phenomena such as:

**Mixing process :** Flame properties (length, position, temperature, ...) depend on the mixing between species (for instance between fuel and air or fresh and burnt gases). Turbulent combustion simulations are therefore

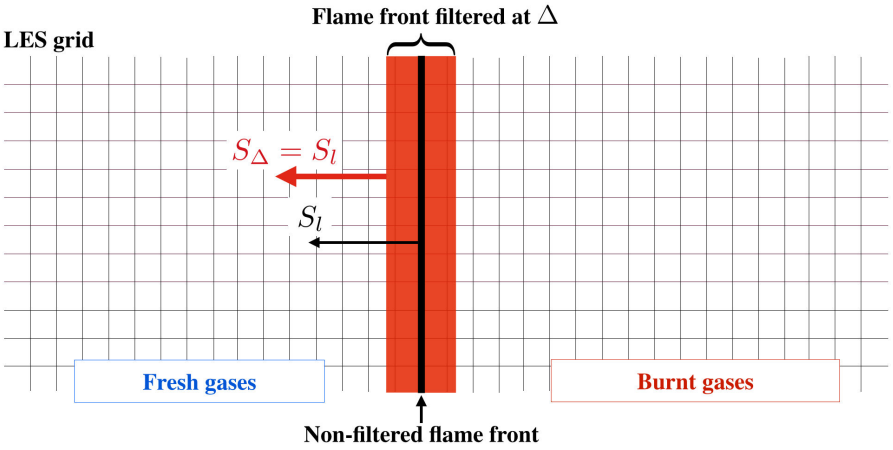


(a) Laminar flame front

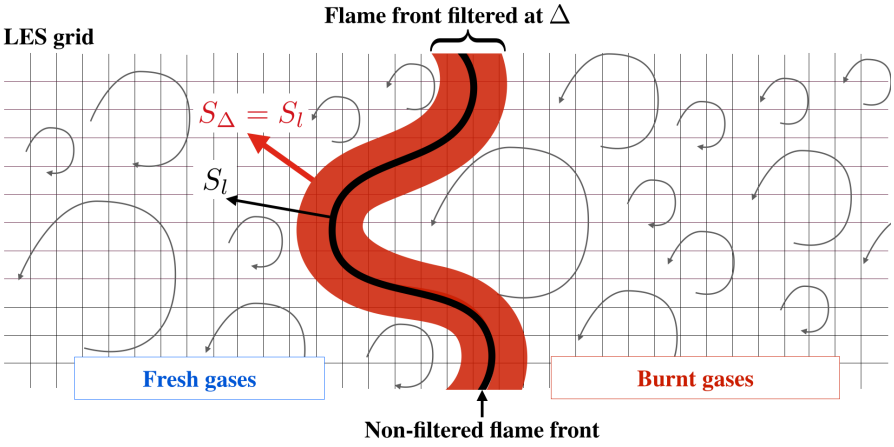


(b) Turbulent flame front - Fully-resolved wrinkling

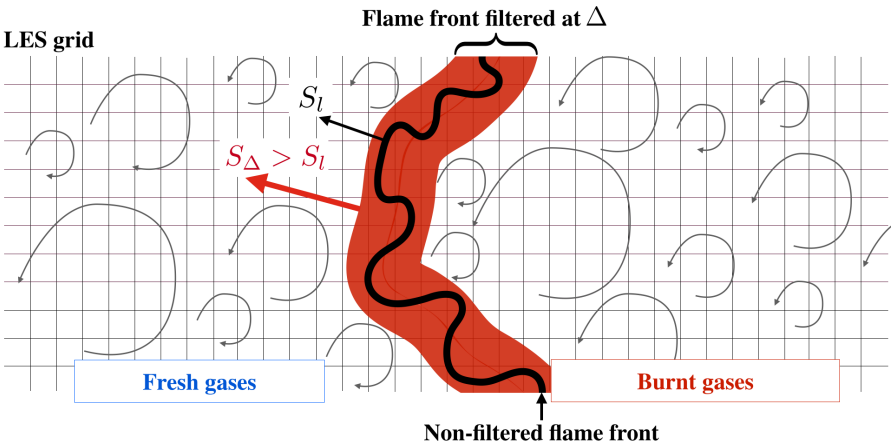


(c) Turbulent flame front - Wrinkling at sub-filter scale

**Figure 1.2:** *Schematic view of the different scenarii for the filtered flame front resolution when a thin flame front is simulated using LES. Fresh gases are supposed to be fully-premixed. Full black line: Non-filtered flame front. Broad red line: Filtered flame front (to be captured in LES).*

sensitive to the unsteady mixing process that can occur at both resolved and unresolved scales.

**Flame wrinkling :** As shown in Fig. 1.2, the interactions between turbulence and the flame front are partially resolved in LES. It is necessary to estimate the impact of unresolved wrinkling on resolved quantities and to correctly capture the two-way coupling between the flow and the flame. When all the flame wrinkling is resolved on the LES grid (cases (a) and (b)), the sub-filter scale wrinkling models should correctly handle the SGS laminar flame structure.

**Non-adiabaticity of the flow :** Heat exchange occurs between the combustor walls and the burnt gases. This phenomenon controls burnt gases temperature and composition and therefore impacts the pollutant emissions. When the flame front develops close to the burner walls, heat losses limit the chemical activity and then decrease the local consumption speed (Poinsot and Veynante, 2012). For very high levels of heat losses, flame may be locally extinguished.

**Differential diffusion :** The modeling of the diffusive transport of the chemical species impacts the prediction of the flame consumption speed and structure. For instance, the computed flame consumption speed of a stoichiometric premixed $CH_4$-Air laminar flame, computed with a detailed chemical scheme (Smith et al., 1999), may vary by 25% between a simulation where unity Lewis number assumption (simple diffusion model) is made and a simulation where a complex diffusion model is selected.

## 1.4 Chemistry modeling for LES combustion models

The structure of combustion models can generally be split into two different parts: on one side, the modeling of the chemical reaction within the flame front, and in the other hand, the coupling between the chemistry description and the LES formalism to predict flame turbulence interactions. In this section, the different possibilities to model flame chemistry in the context of LES are briefly presented.

### 1.4.1 Detailed chemistry and its reduction

The first possibility is to describe the entire set of elementary reactions identified by a detailed chemical schemes. This approach, valid for a large range of thermodynamic conditions, does not require to make assumptions on the combustion regime. Detailed chemical schemes aim to describe the chemical reaction paths as precisely as possible. Therefore, they involve numerous in-

termediate species. For instance, the chemical scheme proposed by Li et al. (2003) for $H_2/O_2$ combustion includes 11 species involved in 19 elementary reactions as shown in Fig. 1.3. When hydrocarbons are considered, the number of species and reactions are greatly increased. The GRI3.0 mechanism (Smith et al., 1999), designed for the combustion of natural gas[2] with air, counts 53 species and 325 elementary reactions. Finally, the extended version of the Dagaut et al. (1994) detailed mechanism for kerosene/air combustion, available in Luche (2003), contains 225 species and 3493 irreversible elementary reactions.

Each species in the chemical scheme requires solving an additional balance equation (Eq. B.2 in DNS and Eq. 1.5 in LES) and then increases the CPU cost. The numerical estimation of chemical reaction rates $\dot{\omega}_k$ (one for each species balance equation) requires the computation of an exponential function for each reaction considered in the chemical scheme. The computation of such functions also drastically increases the CPU cost. The direct use of detailed chemistry is therefore not possible to simulate practical configurations.

| | |
|---|---|
| ***$H_2/O_2$ Chain Reactions*** | ***Formation and Consumption of $HO_2$*** |
| 1. $H + O_2 = O + OH$ | 9. $H + O_2 + M = HO_2 + M$ [c] |
| 2. $O + H_2 = H + OH$ | $H + O_2 + M = HO_2 + M$ [d] |
| 3. $H_2 + OH = H_2O + H$ | 10. $HO_2 + H = H_2 + O_2$ |
| 4. $O + H_2O = OH + OH$ | 11. $HO_2 + H = OH + OH$ |
| | 12. $HO_2 + O = OH + O_2$ |
| | 13. $HO_2 + OH = H_2O + O_2$ |
| ***$H_2/O_2$ Dissociation/Recombination Reactions*** | ***Formation and Consumption of $H_2O_2$*** |
| 5. $H_2 + M = H + H + M$ [a] | 14. $HO_2 + HO_2 = H_2O_2 + O_2$ [e] |
| $H_2 + Ar = H + H + Ar$ | $HO_2 + HO_2 = H_2O_2 + O_2$ |
| $H_2 + He = H + H + He$ | 15. $H_2O_2 + M = OH + OH + M$ [f] |
| 6. $O + O + M = O_2 + M$ [a] | 16. $H_2O_2 + H = H_2O + OH$ |
| $O + O + Ar = O_2 + Ar$ | 17. $H_2O_2 + H = H_2 + HO_2$ |
| $O + O + He = O_2 + He$ | 18. $H_2O_2 + O = OH + HO_2$ |
| 7. $O + H + M = OH + M$ [a] | 19. $H_2O_2 + OH = H_2O + HO_2$ [e] |
| 8. $H + OH + M = H_2O + M$ [b] | $H_2O_2 + OH = H_2O + HO_2$ |

**Figure 1.3:** *Detailed $H_2/O_2$ reaction mechanism. Extracted from Li et al. (2003).*

Reduction techniques are therefore required to decrease the cost of the chemistry modeling. Skeletal mechanisms are derived from detailed chemical scheme

[2]Natural gas is a combination of hydrocarbons such as $CH_4$, $C_2H_6$, $C_3H_8$ and other species such as CO2, $N_2$ and $H_2$

with the objective of keeping a correct description of a given set of thermochemical features (species molar fractions and temperature profiles, ignition delay, laminar burning velocity, etc.) with a controlled accuracy. This reduction technique removes the species and the reactions having a small impact on the variables listed previously. For instance, Luche (2003) proposes a skeletal mechanism for kerosene with 147 species and 2427 irreversible reactions (*i.e.* a fall of 30% of chemical reactions compared to the detailed mechanism.).

A second level of drastic reduction is needed to produce chemical schemes affordable for practical computations. Global chemical scheme are built using a very small number of species and equations (typically from 1 to 4 steps). For that purpose, a set of target values and features to conserve during the reduction process is first defined (for instance, thermochemical equilibrium state, flame speed, auto-ignition time, etc.). Then a range of operating conditions is also chosen (fresh gas temperature, equivalence ratio, pressure). It is then possible to build a reduced chemical scheme which remains representative of the selected variables for the limited range of operating conditions. For example, Jones and Lindstedt (1988) proposed a 4-step mechanism for the combustion of light hydrocarbons such as methane ($CH_4$). Only 6 species are involved in this mechanism ($CH_4$, $O_2$, CO, $H_2$, $H_2O$, $CO_2$). This scheme provides a good agreement on flame speed, flame thickness and major species profiles for lean and moderately rich mixtures. A similar approach has been applied by Franzelli et al. (2010) to reduce the Luche (2003) reduced mechanism resulting in a 2-step mechanism based on 5 species.

Global chemical schemes have been used in a large series of LES of practical combustion chambers (di Mare et al., 2004; Albouze et al., 2009; Franzelli et al., 2012; Abani and Ghoniem, 2013). However, it still needs the evaluation of several reaction rates and the transport of several chemical species which is still increasing significantly the cost of reactive simulations compared to non-reacting ones. This methodology does not give access to the actual flame structure and therefore cannot capture pollutant formation, flame ignition and extinction processes. Moreover, the validity range of global schemes is also limited compared to detailed schemes.

### 1.4.2 Tabulated chemistry

A presentation of chemistry tabulation methodology is proposed in this section. Note that a more detailed review can be found in Fiorina et al. (2015b).

#### 1.4.2.1 Principle

The trajectory accessed during a given combustion process can be described as a sequence of points $\Phi = \Phi(Y_1, Y_2, ..., Y_k, ..., Y_{N_{sp}}, p, h)$ in the space $\Omega =$

$(Y_1, Y_2, ..., Y_k, ..., Y_{N_{sp}}, p, h)$ also called thermochemical space or chemical space. A trajectory $\Omega_m \in \Omega$ or a series of these trajectories in this space is called manifold.

In practice, the subspace $\Omega_m \in \Omega$ actually accessed during the combustion process is very small compare to $\Omega$. Different works proposed to decrease the number of coordinates describing the trajectory $\Omega_m$ (Maas and Pope, 1992b,a; Gicquel et al., 1999, 2000). Such strategies generally consist in:

1. Assuming the chemical subspace $\Omega_m$ accessed by a given flame prior to its effective computation.
2. Choosing a reduced set of coordinates to properly describe the identified manifold.
3. Tabulating the value of all the thermochemical variables $\Phi$ along the chemical trajectory as a function of the chosen set of coordinates.
4. Accessing the thermochemical variables with the knowledge of the coordinates variables solved during the complex computation.

The first challenge therefore consists in identifying *a priori* the manifold $\Omega_m$. This manifold can be generated using elementary combustion configurations that can be easily computed using detailed chemistry. The simplified configuration is assumed to be representative of the turbulent flame and then depends on the operating conditions of the complex burner. The most common configurations are:

- 0-D perfectly-stirred reactors (Fichet et al., 2010) or partially-stirred reactors (Enjalbert et al., 2012).
- 1-D premixed laminar flames (Gicquel et al., 2000; van Oijen and de Goey, 2000; Fiorina et al., 2003)
- 1-D non-premixed flames (Peters, 1984, 2000; Pierce and Moin, 2004)

For well defined flame regimes, a unique flame archetype is sufficient to describe the complex flame with a high fidelity. However, when the combustors exhibit very complex flame structures, several simple manifolds are needed to describe the chemistry. Some examples and applications of multi-regime approaches are given in the following. Fiorina et al. (2005a) have shown that premixed flames may be used to generate the manifold accessed by partially-premixed and diffusion flames when the equivalence ratio lies within the flammability limits. Domingo et al. (2008) also discussed the similarities between the subspaces accessed by auto-ignition and premixed flames. Knudsen and Pitsch (2012) have proposed a combination of 1-D premixed and non-premixed flames and have shown that this methodology is applicable to a wide variety of reacting flows. A more generic approach to resolve chemical trajectories for premixed, partially-premixed and pure diffusion regimes is proposed by Nguyen et al. (2010). The proposed multidimensional flamelet formalism consists in solving conservation equations directly expressed in the chemical space and prevents from the choice

of a flame archetype. A similar approach, called Reaction–Diffusion Manifolds (REDIM), is proposed by Bykov and Maas (2007, 2009) to identify iteratively the chemical subspace accessed by a given flame and for a given set of coordinates. All the previous reduction methods have been applied to gaseous combustion. However, a recent study showed that a combination of gaseous premixed, partially-premixed and non-premixed flames archetypes can also be used to model spray flames structure (Franzelli et al., 2013).

Figure 1.4 shows a summary of the different strategies used to describe the chemistry in the context of LES and RANS. Whereas detailed schemes are not affordable, they are used as a reference to build reduced chemical schemes or to generate the manifolds $\Omega_m$ accessed by simple flame archetypes. The identified chemical subspaces $\Omega_m$ are then tabulated along a reduced set of coordinates transported in the complex computation.

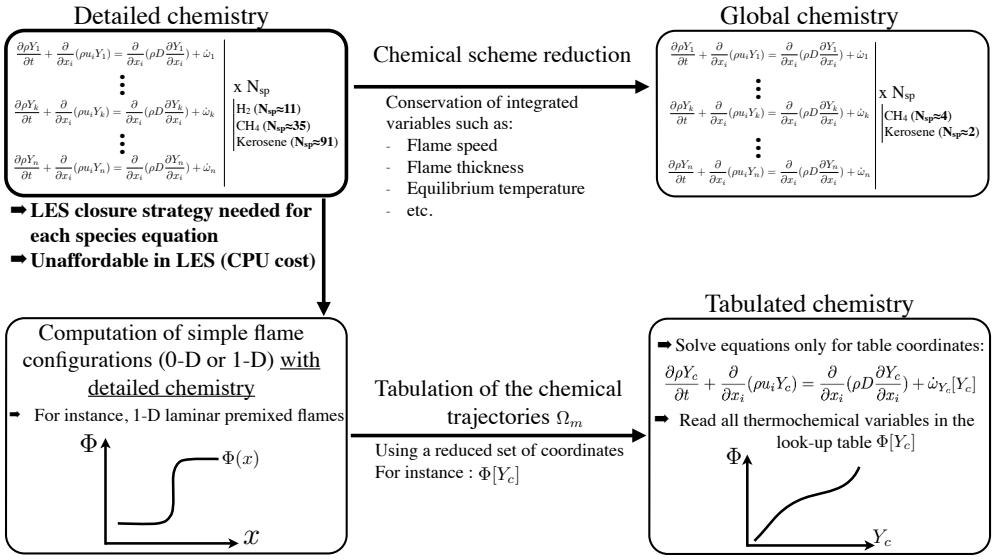


**Figure 1.4:** *Summary of the different strategies for the description of the chemistry in LES.*

### 1.4.2.2 Flame prolongation of ILDM - FPI

In this thesis, the focus is made on premixed and stratified combustion. The Flame Prolongation of ILDM (FPI) method is selected to describe the chemistry of these types of turbulent flames at a reasonable CPU cost. This tabulated chemistry method proposed by Gicquel et al. (2000), consists in generating the manifold $\Omega_m$ from a set of 1-D laminar premixed flames computed using detailed chemistry. Such 1-D flames are also called flamelets and have been first used for turbulent combustion modeling in a RANS context by Bradley et al. (1988). In such flamelets, the evolution of slow thermochemical variables can

be tracked by a very few parameters. Based on this idea, FPI has been first developed for adiabatic flows but has been extended to the more general situation of non-adiabatic flames by Fiorina et al. (2003). A very similar methodology, called Flamelet Generated Manifolds (FGM), has been developed independently by van Oijen and de Goey (2000) and also extended to non-adiabatic situations.

In this section, FPI method is described in the context of adiabatic flows. Its extension accounting for heat losses will be presented in details in Chapter 2. Two coordinates are introduced to describe the chemical trajectories in the subspace $\Omega_m$: mixture fraction and progress variable.

**Mixture fraction**

The first coordinate is the mixture fraction $Y_z$ which evolves monotonically with the fresh gas equivalence ratio $\phi$. This scalar is not impacted by the reaction process and characterizes fresh gases composition. A common definition of this scalar is built from elemental mass fractions as proposed by Bilger (1976); Williams (1985a); Barlow and Frank (1998):

$$Y_z = Y_e \tag{1.9}$$

where $Y_e$ is the mass fraction of a chemical element $e$ (for instance carbon element C) present is fresh gases. A normalized mixture fraction $z$ is introduced as:

$$z = \frac{Y_z(\phi) - Y_z(\phi_{\min})}{Y_z(\phi_{\max}) - Y_z(\phi_{\min})} \tag{1.10}$$

where $\phi_{\min}$ and $\phi_{\max}$ denote the minimum and maximum equivalence ratios encountered in the configuration to simulate. When a unity Lewis number is assumed $Le = D_{th}/D_k = 1$ for all species, the value of z does not depend on the chosen element e and the transport of $z$ is governed by the following transport equation:

$$\frac{\partial \rho z}{\partial t} + \frac{\partial}{\partial x_i}\left(\rho u_i z\right) = \frac{\partial}{\partial x_i}\left(\rho D_z \frac{\partial z}{\partial x_i}\right) \tag{1.11}$$

where the diffusivity of the mixture fraction $D_z$ is equal to the thermal diffusivity $D_z = D_{th} = \frac{\lambda}{\rho C_p}$.

When species differential diffusion is considered, the mixture fraction z is not unique anymore and not sufficient to completely capture the composition variations of the mixture. In this context, one transport equation per element have to be solved for a full description of the composition. Using some simplifications, some recent modeling approaches account for differential diffusion effects

with a limited number (1 or 2) of equations (Regele et al., 2013; Nambully et al., 2014a).

### Progress variable

The second coordinate is the progress variable $Y_c$ which evolves monotonically between fresh and burnt gases. $Y_c$ describes the progress of the reaction and is often defined from a linear combination of species mass fractions $Y_k$:

$$Y_c = \sum_{k=1}^{N_{sp}} n_k Y_k \tag{1.12}$$

where $n_k$ is a weighting coefficient associated to the $k$th species. $n_k$ are chosen to ensure a unique correspondence between the progress variable and thermochemical quantities as species mass fractions and temperature. For lean methane-air combustion, the non-normalized progress variable $Y_c$ can be defined from the $CO_2$ mass fraction as $Y_c = Y_{CO_2}$ while $Y_c = Y_{CO_2} + Y_{CO} + Y_{H_2O}$ or $Y_c = Y_{CO_2} + Y_{CO}$ are found to be more appropriate for rich combustion (Fiorina et al., 2003). For complex fresh gas compositions, the choice of these coefficients is not straightforward and can be performed systematically by resolving a minimization problem as detailed in Ihme et al. (2012). A normalized version of progress variable, denoted $c$, is often used to derive turbulent combustion models as it is completely independent of the local mixture fraction:

$$c = \frac{Y_c - Y_c^f(z)}{Y_c^{eq}(z) - Y_c^f(z)} \tag{1.13}$$

where subscripts $f$ and $eq$ denote gas state in fresh and burnt gases, respectively. The main advantage when $Y_c$ is defined from a linear combination of species mass fraction is that the corresponding balance equation can be easily derived from species glance equation (Eq. B.22) and supposing a unity Lewis number:

$$\frac{\partial \rho Y_c}{\partial t} + \frac{\partial}{\partial x_i}\left(\rho u_i Y_c\right) = \frac{\partial}{\partial x_i}\left(\rho D_{Y_c} \frac{\partial Y_c}{\partial x_i}\right) + \rho \dot{\omega}_{Y_c} \tag{1.14}$$

where $\dot{\omega}_{Y_c}$ is the progress variable reaction rate defined as $\dot{\omega}_{Y_c} = \sum_{k=1}^{N_{sp}} [n_k \dot{\omega}_k]$. The diffusivity of the progress variable is $D_{Y_c} = D_{th}$.

In an adiabatic context and supposing a unity Lewis number, the progress variable $Y_c$ and the mixture fraction $z$ give access to the tabulated thermochemical quantities $\Phi[Y_c, z]$. Detailed chemistry information are accessed by solving two additional equations (instead of $N_{sp}$ equations when all the species are transported):

$$\frac{\partial \overline{\rho}}{\partial t} + \frac{\partial}{\partial x_i}(\overline{\rho}\widetilde{u_i}) = 0 \tag{1.15}$$

$$\frac{\partial}{\partial t}(\overline{\rho}\widetilde{u_j}) + \frac{\partial}{\partial x_i}(\overline{\rho}\widetilde{u_i}\widetilde{u_j}) = -\frac{\partial \overline{p_2}}{\partial x_j} + \frac{\partial \overline{\tau_{ij}}}{\partial x_i} - \frac{\partial}{\partial x_i}(\overline{\rho}(\widetilde{u_i u_j} - \widetilde{u_i}\widetilde{u_j})) + \overline{\rho}\widetilde{f_j} \tag{1.16}$$

$$\begin{aligned}\frac{\partial \overline{\rho}\widetilde{Y_c}}{\partial t} + \frac{\partial}{\partial x_i}\left(\overline{\rho}\widetilde{u_i}\widetilde{Y_c}\right) &= \frac{\partial}{\partial x_i}\left(\overline{\rho D_{th}\frac{\partial Y_c}{\partial x_i}}\right) \\ &\quad - \frac{\partial}{\partial x_i}\left(\overline{\rho}(\widetilde{Y_c u_i} - \widetilde{Y_c}\widetilde{u_i})\right) + \overline{\rho}\widetilde{\dot{\omega}_{Y_c}}\end{aligned} \tag{1.17}$$

$$\frac{\partial \overline{\rho}\widetilde{z}}{\partial t} + \frac{\partial}{\partial x_i}(\overline{\rho}\widetilde{u_i}\widetilde{z}) = \frac{\partial}{\partial x_i}\left(\overline{\rho D_{th}\frac{\partial z}{\partial x_i}}\right) - \frac{\partial}{\partial x_i}(\overline{\rho}(\widetilde{z u_i} - \widetilde{z}\widetilde{u_i})) \tag{1.18}$$

$$p_0 = \overline{\rho}\widetilde{rT} \tag{1.19}$$

This system of equations is only valid for low-Mach number flows (see Appendix B for more details) and assuming unity Lewis number. Species differential diffusion within the turbulent flame is therefore neglected. This thesis proposes, in Chapter 2, extensions of chemistry tabulation to account for differential diffusion and non-adiabaticity effects.

## 1.5 Coupling tabulated chemistry with LES formalism

Three different approaches are generally considered to couple chemistry models and LES formalism. The first approach, called Turbulent Mixing Approach (Menon and Kerstein, 2011; Echekki et al., 2011) consists in describing flame-turbulence interactions by focusing on mixing phenomena. In an LES context, the description of progress variable $c$ or mixture fraction $z$ mixing rate is used to describe unresolved sub-grid scale quantities. The second approach consists in describing the turbulent flame front using a statistical approach (Gao and O'Brien, 1993; Cook and Riley, 1994). Each sub-grid scale variable is then estimated in terms of probability. The last approach describes the turbulent flame front as a propagating surface. For this last case, a large range of mathematical formalisms are possible to describe the surface propagation and its associated flame structure (Kerstein, 1988b; Boger et al., 1998; Colin et al., 2000; Duwig, 2007; Fiorina et al., 2010). Vervisch and Veynante (2000); Veynante and Vervisch (2002) have shown that the three approaches were linked. Exhaustive reviews are available in Veynante and Vervisch (2002); Pitsch (2006); Haworth (2010); Poinsot and Veynante (2012) and Fiorina et al. (2015b). In this section, the focus is made on the turbulence combustion models compatible with tabulated chemistry in an LES context.

### 1.5.1 Statistical approach

This approach is based on a statistical description of sub-grid scale fluctuations of the LES variables through probability density functions (PDF). Any filtered variable $\overline{\Phi}$ is then linked to its unfiltered form $\Phi$ by the following expression:

$$\overline{\Phi} = \int_{\Omega} \Phi\left(Y_1, Y_2, ..., Y_k, ..., Y_{N_{sp}}, p, h\right) \overline{P}\left(Y_1, Y_2, ..., Y_k, ..., Y_{N_{sp}}, p, h\right) d\Omega \quad (1.20)$$

where $\overline{P}$ is called joint filtered probability function (FDF) in the context of LES. As stated in Sec. 1.4, $\Phi\left(Y_1, Y_2, ..., Y_k, ..., Y_{N_{sp}}, p, h\right)$ is given by the chemistry modeling strategy. The unresolved flame turbulence interactions are described through the modeling of $\overline{P}\left(Y_1, Y_2, ..., Y_k, ..., Y_{N_{sp}}, p, h\right)$. $\overline{P}$ or $\widetilde{P} = \frac{\rho\overline{P}}{\overline{\rho}}$ can be computed through the resolution of a complex transport equation (Gao and O'Brien, 1993; Haworth, 2010) (that also needs to be closed) but may also be presumed as discussed in the following.

#### 1.5.1.1 Monotonically Integrated Large Eddy Simulation — MILES

In the framework of the statistical approach, Monotonically Integrated Large Eddy Simulation (MILES) formalism (Duwig et al., 2011; Fureby, 2007; Duwig and Fuchs, 2008; Grinstein and Kailasanath, 1995; Goldin, 2005) proposes to presume the joint filtered probability function $\widetilde{P}$ as a Dirac function $\delta$. This methodology has been applied on isobaric flames, using reduced chemistry leading to:

$$\widetilde{\Phi} = \int_{\Omega} \Phi\left(Y_1, ..., Y_{N_{sp}}, T\right) \delta\left(Y_1 - \widetilde{Y_1}, ..., Y_{N_{sp}} - \widetilde{Y_{N_{sp}}}, T - \widetilde{T}\right) d\Omega \quad (1.21)$$

In particular, the filtered reaction rate is estimated directly from the LES resolved variables using the reduced chemical scheme as:

$$\widetilde{\dot{\omega}_k} = \dot{\omega}_k\left(\widetilde{Y_1}, ..., \widetilde{Y_{N_{sp}}}, \widetilde{T}\right) \quad (1.22)$$

This approach is also called "no model" approach in the sense that the sub-grid contributions to the reaction rate are neglected. As stated in Duwig et al. (2011), the other unresolved fluxes of species and energy are generally closed using classical gradient assumptions and Fick's law for the diffusive flux:

$$\widetilde{Y_k u_i} - \widetilde{Y_k}\widetilde{u_i} = -\frac{\nu_t}{Sc^t}\frac{\partial \widetilde{Y_k}}{\partial x_i} \tag{1.23}$$

$$\widetilde{h u_i} - \widetilde{h}\widetilde{u_i} = -\frac{\nu_t}{Pr^t}\frac{\partial \widetilde{h}}{\partial x_i} \tag{1.24}$$

$$\overline{\rho V_{k,i} Y_k} = -\overline{\rho} D_k \frac{\partial \widetilde{Y_k}}{\partial x_i} \tag{1.25}$$

where $Pr^t$ and $Sc^t$ are turbulent Prandtl and Schmidt numbers, respectively. Note that these closures are not specific to the MILES approach.

This methodology has the property to correctly degenerate towards DNS and is expected to be valid for sufficiently refined flame resolutions. This approach is also valid when local turbulent mixing is very intense. The size of the reaction zone therefore increases and this zone is distributed in relatively large volumes. In such situations, the smallest turbulent scales remain unresolved while the flame thickness may be sufficiently resolved to obtain a good estimation of $\widetilde{\dot{\omega}_k}$. In practice, this situation is limited to very high turbulence levels and to flames lying in the thin or distributed reaction zone regimes. Duwig et al. (2011) proposed to introduce a resolution criteria based on a grid Damköhler number $\mathrm{Da}_\Delta$:

$$Da_\Delta = \frac{\tau_\Delta}{\tau_c} = \frac{\Delta}{\delta_l} / \frac{u_\Delta}{S_l} \tag{1.26}$$

For $Da_\Delta \ll 1$, MILES approach is valid since the sub-grid scale reaction is well stirred and homogeneous and only depends on the resolved temperature and species fields. Regarding the requirements established in 1.3, the MILES closure strategy allows to capture the inner flame structure using very fine grids (compared to the flame thickness) which may not be affordable for the LES of thin turbulent flames evolving in complex configurations. When the flame front resolution is not sufficient (which may be the case for the applications on industrial combustion chambers), the numerical scheme may impact the flame propagation by adding numerical diffusion. For that purpose, MILES approaches are often associated to flux limiters and to dedicated stabilization strategies (Duwig et al., 2011). The advantage of this approach is that the impact of heat losses and differential diffusion can be directly accounted for if a sufficiently detailed chemical scheme is used. However, a well resolved flame front is difficult to achieve in practice and numerical issues remain important.

#### 1.5.1.2 Combining Presumed Conditional Moments and FPI — PCM-FPI model

A more refined description of the sub-grid scale fluctuations consists in presuming the shape of the joint filtered probability function $\widetilde{P}$. For instance, the

Presumed Conditional Moments (PCM) approach has been combined with the FPI chemistry tabulation method by Vervisch et al. (2004) and Fiorina et al. (2005b) in a RANS context. This model has been extended to LES formalism and used in Galpin et al. (2008); Moureau et al. (2011b).

Using tabulated chemistry with isobaric and adiabatic assumptions allows to recast Eq. 1.20 as:

$$\widetilde{\Phi} = \int_{z=0}^{1} \int_{c=0}^{1} \Phi_{\Omega_m}(c,z)\, \widetilde{P}(c,z)\, \mathrm{d}c\, \mathrm{d}z \tag{1.27}$$

where the variable $\Phi_{\Omega_m}(c,z)$ is read in a FPI look-up table. Assuming that both progress variable $c$ and mixture fraction $z$ are statistically independent, the joint filtered probability function $\widetilde{P}$ expresses as $\widetilde{P}(c,z) = \overline{P}_c(c)\,\widetilde{P}_z(z)$. The shapes of $\overline{P}_c$ and $\widetilde{P}_z$ are generally modeled by $\beta$-functions denoted $P_\beta$ and parametrized by $\overline{c}$, $\widetilde{c''^2}$ for the progress variable and $\widetilde{z}$, $\widetilde{z''^2}$ for the mixture fraction. Thermochemical quantities then read:

$$\widetilde{\Phi} = \int_{z=0}^{1} \int_{c=0}^{1} \Phi_{\Omega_m}(c,z)\, P_\beta\left(c, \overline{c}, \widetilde{c''^2}\right) P_\beta\left(z, \widetilde{z}, \widetilde{z''^2}\right) \mathrm{d}c\, \mathrm{d}z \tag{1.28}$$

$\overline{c}$ and $\widetilde{c''^2}$ are estimated from $\widetilde{Y_c}$, $\widetilde{Y_c''^2}$ obtained from LES transport equations (Fiorina et al., 2005b). $\widetilde{\Phi}$ is then pre-computed and stored as a function of Favre averaged quantities $\overline{c}$, $\widetilde{c''^2}$, $\widetilde{z}$ and $\widetilde{z''^2}$ :

$$\widetilde{\Phi} = \widetilde{\Phi}[\overline{c}, \widetilde{c''^2}, \widetilde{z}, \widetilde{z''^2}] \tag{1.29}$$

Unmixedness factors $S_\Phi = \widetilde{\Phi''^2}/(\widetilde{\Phi}(1-\widetilde{\Phi}))$ varying between 0 and 1 are introduced to ease the tabulation process:

$$\widetilde{\Phi} = \widetilde{\Phi}[\overline{c}, S_c, \widetilde{z}, S_z] \tag{1.30}$$

This modeling approach presents two main issues. First, the closure of LES transport equations for the table coordinates (*i.e.* $\overline{c}$, $\widetilde{c''^2}$, $\widetilde{z}$ and $\widetilde{z''^2}$) is not straightforward. Second, several studies have shown than even if the $\beta$-function is appropriate to model RANS fluctuations, it is not fully adapted to the modeling of sub-grid scale interactions in an LES context (Fiorina et al., 2010; Olbricht et al., 2012). In particular, Fiorina et al. (2010) have shown that PCM-FPI does not correctly degenerate to laminar flames or when the flame wrinkling is fully resolved. As it is based on tabulated chemistry, PCM-FPI model also gives access to the inner thermochemical flame structure. However, it is worth noting that the description of the flame structure is built from a collection of 1-D laminar premixed flames and is therefore relevant only for turbulent flames evolving in laminar on thin flame regimes.

### 1.5.2 Geometrical approach

This class of modeling strategies describes the turbulent flame front as a propagating surface. Some of the approaches most commonly found in the literature are presented here.

#### 1.5.2.1 G-equation

A level-set methodology is used to track the flame front propagation. A given flame iso-surface $c = c_0$ is tracked by the iso-surface $G = G_0$ of a smooth scalar field $G$. $G$ is defined such as the iso-surface $G = G_0$ propagates at the speed of the $c = c_0$ surface, denoted $S_l^{c=c_0}$, relatively to the flow field characterized by its velocity $\mathbf{u}$. In DNS, $G$ is solution of the following equation (Williams, 1985b; Kerstein, 1988b) :

$$\frac{\partial G}{\partial t} + u_i \frac{\partial G}{\partial x_i} = S_l^{c=c_0} \sqrt{\frac{\partial G}{\partial x_i}\frac{\partial G}{\partial x_i}} \tag{1.31}$$

From a numerical point of view, the scalar G is smooth and does not reproduce the non-linearities of the combustion process. The flame is tracked by the iso-surface $G = G_0$ which only gives the position of a $c$ iso-surface but does not describe the inner flame structure. The LES filtering of Eq. 1.31 leads to unclosed terms that are difficult to model. In practice, the inner filtered flame layer position is given by Eq. 1.31 recast in a LES context:

$$\frac{\partial G}{\partial t} + \widetilde{u_i} \frac{\partial G}{\partial x_i} = S_T \sqrt{\frac{\partial G}{\partial x_i}\frac{\partial G}{\partial x_i}} \tag{1.32}$$

where the flow velocity $\widetilde{u_i}$ is the LES filtered velocity. SGS turbulence-flame interactions are not captured by the $G$ field. A model for $S_T$, the sub-grid scale turbulent burning velocity, which includes the increase in flame speed due to unresolved flame turbulence interactions is then required. Its estimation from known quantities is very difficult and depends on local thermodynamical conditions, equivalence ratio, strain rate but also on local sub-grid scale turbulent structures which are not resolved in LES.

The knowledge of the instantaneous position of the flame front is not sufficient to ensure the closure of the LES equation system. In particular, the density field needs to be reconstructed to ensure a proper coupling between flame and flow at the resolved scale. G-equation formalism does not natively allow this reconstruction and needs to be coupled with additional strategies to reconstruct the inner flame structure (Piana et al., 1997). A common approach consists in coupling G and progress variable $c$ equation to predict both the turbulent flame speed and the inner flamme structure given by $c$ when tabulated chemistry is used (Moureau et al., 2009; Knudsen et al., 2010, 2013). Following this idea, Roux and Pitsch (2010) and Trisjono et al. (2014) introduced a correction

of the turbulent flame speed and the chemical structure accounting for heat losses. Note also that handling the resolution of Eq. 1.32 requires dedicated numerical strategies, also called level-set methods.

#### 1.5.2.2 Flame Surface Density formalism — FSD

The previous analysis of $G$-equation shows the difficulty to capture the turbulent flame structure. An alternative is to close the filtered progress variable balance equation since $c$ tracks the flame structure. In the context of premixed turbulent combustion, Boger et al. (1998) recast the progress variable equation (Eq. 1.18) as:

$$\frac{\partial \rho c}{\partial t} + \frac{\partial}{\partial x_i}\left(\rho u_i c\right) = \rho S_d \sqrt{\frac{\partial c}{\partial x_i}\frac{\partial c}{\partial x_i}} \tag{1.33}$$

This equation is very similar to the $G$-equation and $S_d$ represents the displacement speed of an iso-c level relative to the flow. As pointed out by Boger et al. (1998), the progress variable $c$ gradient across the flame front cannot be directly resolved on an LES grid as it is generally too thin compared to the mesh size $\Delta_x > \delta_c$. The progress variable equation $c$ (Eq. 1.33) is therefore filtered at a size $\Delta$ larger that the mesh size $\Delta_x$ leading to:

$$\frac{\partial \overline{\rho}\widetilde{c}}{\partial t} + \frac{\partial}{\partial x_i}\left(\overline{\rho}\widetilde{u_i}\widetilde{c}\right) = -\frac{\partial}{\partial x_i}\left(\overline{\rho}(\widetilde{u_i c} - \widetilde{u_i}\widetilde{c})\right) + \overline{\rho S_d \sqrt{\frac{\partial c}{\partial x_i}\frac{\partial c}{\partial x_i}}} \tag{1.34}$$

Additional terms appear in the RHS of Eq. 1.34 for the more general case where equivalence ratio stratification is considered (Domingo et al., 2002; Bray et al., 2005; Duwig and Fureby, 2007). Boger and Veynante (2000) closed the unresolved turbulent flux $\overline{\rho}(\widetilde{u_i c} - \widetilde{u_i}\widetilde{c})$ using a diffusive term constructed to degenerate towards the proper flame speed in laminar cases. Boger et al. (1998) proposed to introduce generalized flame surface density $\Sigma$, representing the sub-grid flame surface density integrated over the iso-c surfaces, to model the filtered flame front displacement term as:

$$\overline{\rho S_d \sqrt{\frac{\partial c}{\partial x_i}\frac{\partial c}{\partial x_i}}} = \langle \rho S_d \rangle_s \, \Sigma \tag{1.35}$$

where $\langle \rho S_d \rangle_s$, the generalized sub-grid flame surface average of $\rho S_d$, is related to the laminar flame propagation speed. This formalism has been widely used to derive turbulent combustion models during the last decades. Boger et al. (1998); Ma et al. (2013) provide analytical expressions for $\Sigma$ depending on the resolved progress variable $\widetilde{c}$. Other studies propose to solve a transport equation for $\Sigma$ (Duclos et al., 1993; Mantel and Borghi, 1994; Vervisch et al., 1995; Choi and Huh, 1998; Hawkes and Cant, 2000; Ma et al., 2014). Another very important quantity related to the flame surface density is the sub-grid

scale wrinkling $\Xi$:

$$\Sigma = \overline{\sqrt{\frac{\partial c}{\partial x_i}\frac{\partial c}{\partial x_i}}} = \Xi\sqrt{\frac{\partial \overline{c}}{\partial x_i}\frac{\partial \overline{c}}{\partial x_i}} \tag{1.36}$$

$\Xi$ is defined as the ratio between the sub-grid flame surface and its projection in the direction of propagation. It may also be viewed as the ratio between the sub-grid scale turbulent flame speed $S_T$ and the laminar flame speed $S_l$:

$$\Xi = \frac{S_T}{S_l} \tag{1.37}$$

The modeling of the unresolved flame-turbulence interactions trough $\Xi$ is often separated from the modeling of the laminar quantities such as $\langle \rho S_d \rangle_s$ (Duwig, 2007). Different approaches have been proposed to model $\Xi$. Analytical models were first derived by Colin et al. (2000); Charlette et al. (2002a); Hawkes et al. (2012); Fureby (2005) while recent studies proposed to use the known resolved wrinkling scales to model the unknown ones (Charlette et al., 2002b; Knudsen and Pitsch, 2008; Wang et al., 2012, 2011; Schmitt et al., 2013a,b). Exhaustive comparisons of flame surface density models (Ma et al., 2013) and transport equations (Ma et al., 2014) have been recently proposed. The authors assessed the different approaches on different configurations such as a plane symmetric combustor (ORACLES burner) and a dihedral bluff-body in a channel (Volvo Rig) and a classification of the different formulations has been drawn.

From a general point of view, building models from a flame surface density approach allows to control the flame propagation speed by adopting an explicit modeling of unresolved flame turbulence interactions through $\Sigma$ or $\Xi$.

#### 1.5.2.3 Thickened flame model for LES — TFLES

An alternative to ensure a proper resolution of the flame front consists in artificially thickening the flame front to reach a sufficient flame thickness to be well resolved on the LES mesh. Butler and O'Rourke (1977) and later O'Rourke and Bracco (1979) proposed a simple modification of the species balance equation to resolve a flame front geometrically thickened by a factor $\mathcal{F}$ but propagating at its original speed. This method basically consists in multiplying the diffusion term by $\mathcal{F}$ and dividing the reaction rate by $\mathcal{F}$. This strategy has been developed in LES context by Colin et al. (2000) who also showed that the thickening process alters the flame-turbulence interactions. For that purpose, Colin et al. (2000) derived a model for the sub-grid scale wrinkling $\Xi = S_T/S_l$ leading to

the TFLES model equation:

$$\frac{\partial \overline{\rho}\widetilde{Y_k}}{\partial t} + \frac{\partial}{\partial x_i}\left(\overline{\rho}\widetilde{Y_k}\widetilde{u_i}\right) = \frac{\partial}{\partial x_i}\left(\Xi\mathcal{F}\overline{\rho}D\frac{\partial \widetilde{Y_k}}{\partial x_i}\right) + \frac{\Xi\rho\dot{\omega}_{Y_k}}{\mathcal{F}} \tag{1.38}$$

Solving Eq 1.38 for each species allows to propagate a flame front of thickness $F\delta_l$ at the sub-grid scale turbulent burning velocity $S_T = \Xi S_l$. In practice, this model is often used with a thickening factor $\mathcal{F}$ varying in space and only applied within the flame front (Légier et al., 2000). This approach has been first coupled with global chemistry and widely validated on complex geometries (Selle et al., 2004; Sommerer et al., 2004; Broeckhoven et al., 2007; Schmitt et al., 2007; Boileau et al., 2008; Staffelbach et al., 2009; De and Acharya, 2009; Franzelli et al., 2012). Efficient and robust, this modeling approach captures the impact of heat losses in the limit of the global scheme capabilities. More recently, the TFLES model has been extended to tabulated chemistry by introducing a transport equation similar to Eq. 1.38 for the filtered progress variable $Y_c$ in a premixed context (Auzillon et al., 2011; Kuenne et al., 2011):

$$\frac{\partial \overline{\rho}\widetilde{Y_c}}{\partial t} + \frac{\partial}{\partial x_i}\left(\overline{\rho}\widetilde{Y_c}\widetilde{u_i}\right) = \frac{\partial}{\partial x_i}\left(\Xi\mathcal{F}\overline{\rho}D\left[\widetilde{Y_c}\right]\frac{\partial \widetilde{Y_c}}{\partial x_i}\right) + \frac{\Xi\rho\dot{\omega}_{Y_c}\left[\widetilde{Y_c}\right]}{\mathcal{F}} \tag{1.39}$$

This approach, coupling TFLES and FPI methodologies, has been successfully extended to adiabatic stratified combustion in Kuenne et al. (2012) and to non-adiabatic situations by Ketelheun et al. (2013). For that purpose, mixture fraction and enthalpy coordinates have been added to the set of transported variables. Based on the work of Fiorina et al. (2003), burner-stabilized and preheated 1-D premixed flames have been chosen to generate the non-adiabatic chemical trajectories.

#### 1.5.2.4 Filtered TAbulated Chemistry for LES — F-TACLES

The Filtered Tabulated Chemistry for LES model, also called F-TACLES, has been first proposed by Fiorina et al. (2010) for premixed and adiabatic combustion and extended to adiabatic stratified flames by Auzillon et al. (2012). F-TACLES is designed to couple chemistry tabulation (FPI) with the spatial filtering formalism of LES. This modeling strategy uses the explicit filtering of a set of 1-D laminar premixed flames to estimate the different LES unclosed terms. In particular, this model ensures the flame front propagation at the turbulent flame speed $S_\Delta = \Xi_\Delta S_l$ whether the flame wrinkling is fully resolved ($\Xi_\Delta = 1$) or not, as both situations can occur in practical simulations (Fiorina et al., 2010).

### Fully-resolved wrinkling

In a perfectly premixed context, when flame wrinkling is fully resolved, the filtered flame front is assumed similar to a 1-D filtered laminar premixed flame. The F-TACLES model therefore estimates the LES filtered quantity $\overline{\Phi}$ as:

$$\overline{\Phi} = \int_{-\infty}^{+\infty} \Phi^{\Omega_m}(x) G_\Delta(x - x') dx' \tag{1.40}$$

where $\Phi^{\Omega_m}$ is the value of the quantity $\Phi$ extracted from the FPI database where the trajectory $\Omega_m$ is mapped from a 1-D unique laminar premixed flame[3]. The FPI database generation corresponds to the step 1 of the F-TACLES look-up table generation detailed in Fig. 1.5. $G_\Delta$ denotes a 1-D Gaussian filter kernel of size $\Delta$. The 1-D filtering operator is noted $\langle \cdot \rangle$ and corresponds to the step 2.

When mixture fraction heterogeneities are present at the sub-grid scale, the chemical trajectories $\Omega_m$ are not mapped by a unique 1-D laminar premixed flame anymore. Auzillon et al. (2012) extended the F-TACLES formalism to account for unresolved (*i.e.* sub-grid scale) mixture fraction heterogeneities as follows:

$$\overline{\rho}\widetilde{\Phi} = \int_0^1 \langle \rho\Phi | z = z' \rangle \, \overline{P}(z') \mathrm{d}z' \tag{1.41}$$

where $\langle \Phi | z = z' \rangle$ corresponds to the 1-D spatial filtering of $\Phi$ extracted from a 1-D laminar flame computed with a fresh gases mixture fraction $z = z'$. $\overline{P}$, the FDF of mixture fraction $z$, accounts for the impact of sub-grid scale mixture fraction heterogeneities on the filtered quantity $\widetilde{\Phi}$. $\overline{P}$ is presumed by a $\beta$ function $P_\beta(z, \widetilde{z}, S_z)$ as in the PCM-FPI formalism presented in Sec. 1.5.1.2. The convolution of the spatially-filtered quantities $\langle \Phi | z = z' \rangle$ with $P_\beta$ corresponds to the step 4 in Fig. 1.5. The last step consists in building the F-TACLES database where filtered thermochemical variables (temperature, species mass fraction, heat release, chemical reaction rates, etc.) and LES equations closures are stored as $\Phi = \Phi[\widetilde{Y_c}, \widetilde{z}, S_z, \Delta]$.

When no wrinkling occurs at the sub-grid scale, the filtered progress variable equation is closed following this procedure as:

$$\begin{aligned} \frac{\partial \overline{\rho}\widetilde{Y_c}}{\partial t} + \frac{\partial}{\partial x_i}\left(\overline{\rho}\widetilde{u_i}\widetilde{Y_c}\right) &= \frac{\partial}{\partial x_i}\left(\alpha_{Y_c}[\widetilde{Y_c}, \widetilde{z}, S_z, \Delta]\rho_0 D_0 \frac{\partial \widetilde{Y_c}}{\partial x_i}\right) \\ &+ \Omega_{Y_c}[\widetilde{Y_c}, \widetilde{z}, S_z, \Delta] + \overline{\rho}\widetilde{\dot{\omega}}_{Y_c}[\widetilde{Y_c}, \widetilde{z}, S_z, \Delta] \end{aligned} \tag{1.42}$$

[3]Note that $\Phi^{\Omega_m}$ can be tabulated as a function of both progress variable $Y_c$ as $\Phi^{\Omega_m}(Y_c)$ or space coordinates $x$ as $\Phi^{\Omega_m}(x)$ since $Y_c$ and $x$ are, by definition, varying monotonically along each other within the flame front. In the context of the F-TACLES model, the FPI database is described as $\Phi^{\Omega_m}(x)$ to ease the 1-D spatial filtering process.

where the filtered progress variable reaction rate reads:

$$\overline{\rho}\widetilde{\dot{\omega}}_{Y_c}[\widetilde{Y}_c,\widetilde{z},S_z,\Delta]=\int_0^1\left\langle\rho\dot{\omega}_{Y_c}|z=z'\right\rangle P_\beta(z',\widetilde{z},S_z)\mathrm{d}z' \tag{1.43}$$

The correction factor $\alpha_{Y_c}$ is tabulated from 1-D filtered premixed flames as:

$$\alpha_{Y_c}[\widetilde{Y}_c,\widetilde{z},S_z,\Delta]=\frac{\overline{\rho^* D^*_{th}\frac{\partial Y_c^*}{\partial x^*}}}{\rho_0 D_0\frac{\partial\widetilde{Y_c}^*}{\partial x^*}} \tag{1.44}$$

where $\rho_0$ and $D_0$ are reference values for the density and the molecular diffusion coefficient, respectively, generally set to fresh gas values. The superscript $^*$ denotes quantities extracted from the chemical subspace $\Omega_m$ built from 1-D laminar premixed flames using the FPI methodology. The unresolved transport term $\Omega_{Y_c}$ is also estimated using the FPI database as:

$$\Omega_{Y_c}[\widetilde{Y}_c,\widetilde{z},S_z,\Delta]=\overline{\rho_0^*(z)S_l^*(z)\frac{\partial Y_c^*}{\partial x^*}}-\overline{\rho_0^*(z)S_l^*(z)}\frac{\partial\widetilde{Y_c}^*}{\partial x^*} \tag{1.45}$$

Under these assumptions the F-TACLES model ensures that the filtered flame front propagate at $\widetilde{S}_l$ when all the wrinkling is resolved. The laminar flame speed $\widetilde{S}_l$ accounts for unresolved mixture fraction heterogeneities and reads:

$$\overline{\rho}_0\widetilde{S}_l=\int_0^1\rho_0(z')S_l\left(z'\right)P_\beta(z',\widetilde{z},S_z)\,dz' \tag{1.46}$$

where $\overline{\rho}_0=\int_0^1\rho_0(z')P_\beta(z',\widetilde{z},S_z)dz'$.

### Accounting for unresolved flame wrinkling using geometrical approach

When flame wrinkling is not completely resolved on the LES grid, the impact of unresolved flame surface on the filtered flame consumption speed $S_\Delta$ is modeled through the modeling of the sub-filter scale wrinkling function $\Xi_\Delta$:

$$S_\Delta=\Xi_\Delta\widetilde{S}_l\left(\widetilde{z},S_z\right) \tag{1.47}$$

To ensure that the filtered flame propagates at $S_\Delta$, the RHS term of the filtered progress variable equation is multiplied by $\Xi_\Delta$ following the same strategy used in the TFLES model (Colin et al., 2000). The following system of equations is therefore obtained for a low-Mach number and adiabatic flow:

$$\frac{\partial \overline{\rho}}{\partial t} + \frac{\partial}{\partial x_i}(\overline{\rho}\widetilde{u_i}) = 0 \tag{1.48}$$

$$\frac{\partial}{\partial t}(\overline{\rho}\widetilde{u_j}) + \frac{\partial}{\partial x_i}(\overline{\rho}\widetilde{u_i}\widetilde{u_j}) = -\frac{\partial \overline{p_2}}{\partial x_j} + \frac{\partial(\overline{\tau_{ij}} + \overline{\tau_{ij}}^t)}{\partial x_i} + \overline{\rho}\widetilde{f_j} \tag{1.49}$$

$$\begin{aligned}\frac{\partial \overline{\rho}\widetilde{Y_c}}{\partial t} + \frac{\partial}{\partial x_i}\left(\overline{\rho}\widetilde{u_i}\widetilde{Y_c}\right) &= \frac{\partial}{\partial x_i}\left(\Xi_\Delta \alpha_{Y_c}[\widetilde{Y_c}, \widetilde{z}, S_z, \Delta]\rho_0 D_0 \frac{\partial \widetilde{Y_c}}{\partial x_i}\right) \\ &+ \Xi_\Delta \Omega_{Y_c}[\widetilde{Y_c}, \widetilde{z}, S_z, \Delta] \\ &+ \Xi_\Delta \overline{\rho}\widetilde{\dot{\omega}_{Y_c}}[\widetilde{Y_c}, \widetilde{z}, S_z, \Delta]\end{aligned} \tag{1.50}$$

$$\frac{\partial \overline{\rho}\widetilde{z}}{\partial t} + \frac{\partial}{\partial x_i}\left(\overline{\rho}\widetilde{u_i}\widetilde{z}\right) = \frac{\partial}{\partial x_i}\left(\left(\overline{\rho}D_{th} + \frac{\mu_t}{S_{ct}}\right)\frac{\partial \widetilde{z}}{\partial x_i}\right) \tag{1.51}$$

$$\begin{aligned}\frac{\partial(\overline{\rho}\widetilde{z''^2})}{\partial t} + \frac{\partial}{\partial x_i}\left(\overline{\rho}\widetilde{u_i}\widetilde{z''^2}\right) &= \frac{\partial}{\partial x_i}\left(\frac{\mu_t}{S_{ct}}\frac{\partial \widetilde{z''^2}}{\partial x_i}\right) + 2\frac{\mu_t}{S_{ct}}|\nabla \widetilde{z}|^2 \\ &- 2C\frac{\mu_t}{S_{ct}\overline{\rho}\Delta_x^2}\widetilde{z''^2}\end{aligned} \tag{1.52}$$

$$p_0 = \overline{\rho}\widetilde{rT}[\widetilde{Y_c}, \widetilde{z}, S_z, \Delta] \tag{1.53}$$

where $\overline{\tau_{ij}}^t$ is modeled using a turbulence model chosen independently. The unresolved turbulent fluxes of mixture fraction $\widetilde{z}$ and its variance $\widetilde{z''^2}$ are closed using classical gradient assumptions (Poinsot and Veynante, 2012). $C$ is a model constant taken equal to 1. $\Xi_\Delta$ is a sub-model that can be chosen independently among the available strategies proposed in the literature (Colin et al., 2000; Charlette et al., 2002a,b; Schmitt et al., 2013b). The choice and the impact of this sub-model are discussed in details in the chapter 4 of this thesis.

An exhaustive description of the derivation and justification of each terms presented here can be found in Auzillon et al. (2012). The F-TACLES model has been used to study academic, semi-industrial and industrial configurations as briefly summarized in the following. Auzillon et al. (2011) have compared this filtering formalism with the thickening formalism on 2-D pulsed flames. This study proposes a relation between the thickening factor $F$ and the filter size $\Delta$ and shows that the filtering approach allows a better description of the flame dynamics on a given mesh grid. The F-TACLES model has been applied to the LES computation of a premixed turbulent combustion chamber in Fiorina et al. (2010). Auzillon et al. (2012) used the formulation for stratified flames to perform the LES of a partially-premixed aeronautical combustion chamber. The model was first used with analytical description of the unresolved wrinkling (Colin et al., 2000; Charlette et al., 2002a). It has also been coupled with a dynamic modeling of the sub-filter scale wrinkling $\Xi_\Delta$ for the LES of the TECFLAM burner (Schmitt et al., 2013b). Finally, F-TACLES was used to

perform the LES of a single industrial burner extracted from an helicopter combustion chamber (Auzillon et al., 2013) and more recently to study the ignition sequence of an annular combustion chamber (Philip et al., 2014). Note that, until this point, the model has been used assuming adiabatic configurations and using a unity Lewis number assumption ($Le = 1$) to model the progress variable diffusion term.

**Accounting for unresolved flame wrinkling using statistical approach**

The Filtered Laminar Flame-PDF (FLF-PDF) model, proposed by Moureau et al. (2011b), consists in modeling the unresolved flame wrinkling using a statistical formalism inspired from the PCM-FPI model. The difference is that the presumed progress variable PDF is built from the 1-D filtering of laminar premixed flames:

$$\widetilde{P}(c,\widetilde{c},\Delta') = \frac{\rho(c)G_{\Delta'}(\widetilde{x}^{\Delta'}(\widetilde{c}^{\Delta'}) - x(c))}{\overline{\rho}^{\Delta'}|\nabla c|} \tag{1.54}$$

The novelty of the FLF-PDF approach is that the flame filter width $\Delta'$, chosen constant in the F-TACLES model, depends on the SGS fluctuation level as suggested by the DNS analysis conducted by Moureau et al. (2011b). It is shown that $\Delta'$ can be recast as a function of the progress variable $\widetilde{Y}_c$ and its variance $\widetilde{Y_c''^2}$:

$$\Delta' = \Delta'(\widetilde{Y}_c, \widetilde{Y_c''^2}) \tag{1.55}$$

This approach better reproduce the progress variable PDF (Moureau et al., 2011b) in turbulent flames and intrinsically accounts for unresolved flame wrinkling. The use of the sub-grid scale wrinkling factor $\Xi_\Delta$ is then replaced by the modeling of the unclosed terms of the $\widetilde{Y_c''^2}$ balance equation. However, this strategy does not allow to degenerate natively towards laminar regime when the flame wrinkling is fully resolved. For that purpose, Nambully (2013) introduced a resolution factor $\mathcal{F}$ to detect when the flame wrinkling is fully resolved. In this situation, the flame filter size is set to a constant determined by the local mesh size as in the F-TACLES model.

FLF-PDF model has been recently extended to stratified combustion by Nambully et al. (2014a,b). In this work, the authors proposed a strategy to account for the impact of differential diffusion on the filtered mixture fraction $\widetilde{z}$ in turbulent premixed and stratified flames. A validation is performed on the Cambridge Stratifies Swirl burner.

**Step 1)** Computation of a set of 1-D laminar premixed flames with detailed chemistry

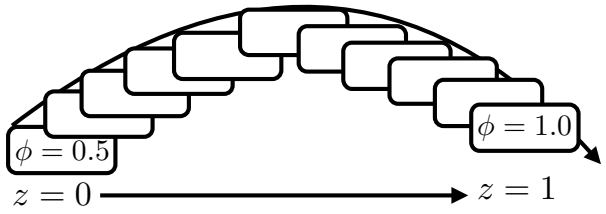


Generation of the manifold $\Omega_m$:

$$\Phi_{\text{step1}}(x,z) = \Phi^{\Omega_m}(x,z)$$

**Step 2)** Spatial filtering of each 1-D flame with a 1-D Gaussian filter

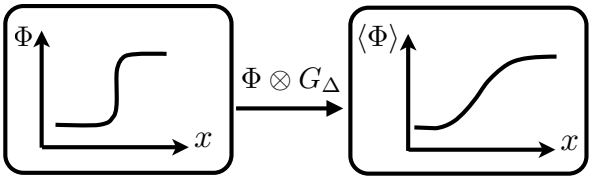


$$\overline{\Phi}_{\text{step2}}(x,z,\Delta) = \langle\Phi|z=z'\rangle = \int_{-\infty}^{+\infty} \Phi^{\Omega_m}(x,z=z')G_\Delta(x-x')dx'$$

**Step 3)** Replacing space coordinate by progress variable

$$\overline{\Phi}_{\text{step2}}(x,z,\Delta) \xrightarrow{\widetilde{Y}_c(x,z,\Delta)} \overline{\Phi}_{\text{step3}}(\widetilde{Y}_c,z,\Delta)$$

**Step 4)** Convolution of the filtered flames with a $\beta$-PDF

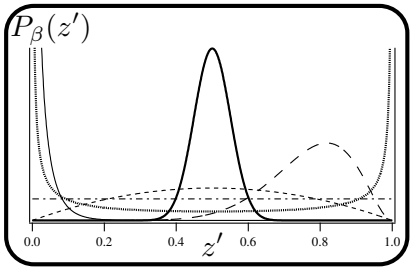


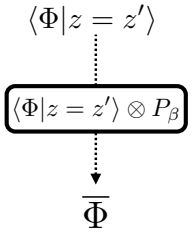


$$\overline{\Phi}_{\text{step4}}(\widetilde{Y}_c,\widetilde{z},S_z,\Delta) = \int_0^1 \langle\Phi|z=z'\rangle\, P_\beta(z',\widetilde{z},S_z)\mathrm{d}z'$$

**Step 5)** Generation of the F-TACLES look-up table with thermochemical variables & LES closure terms

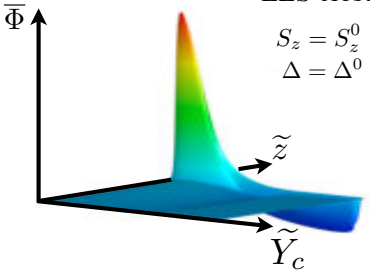


$$\overline{\Phi} = \overline{\Phi}[\widetilde{Y}_c,\widetilde{z},S_z,\Delta]$$

**Figure 1.5:** *Summary of the procedure for the construction of the F-TACLES filtered look-up table.*

## 1.6 Consistency between flame and flow filter scales

At this point, a first conclusion can be drawn on the different LES turbulent combustion modeling strategies. An important issue lies in the fact that the real flame front has a thickness that can not be resolved on the LES mesh $\delta_r < \Delta_x$. Thus, most of the combustion models aim to broaden the flame front to ensure a sufficient resolution of the inner flame structure. This strategy is explicitly introduced in the models based on a geometrical description of the flame front[4] (see Sec. 1.5.2).

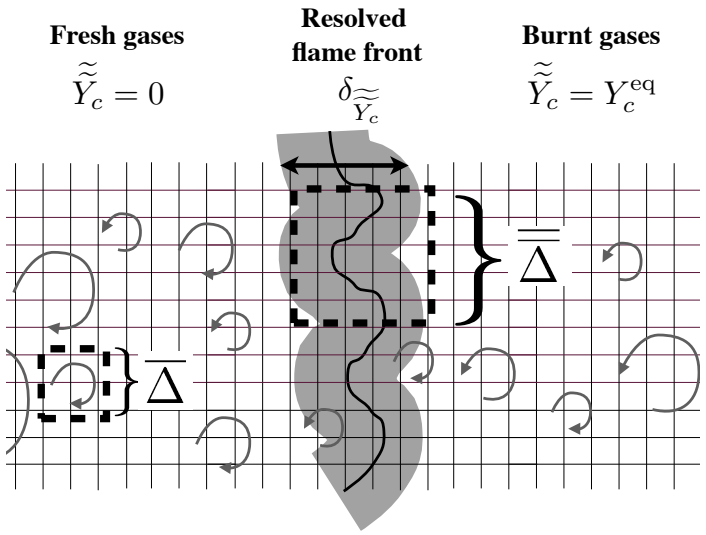


**Figure 1.6:** *Summary of the different filter scales effectively considered in the LES of turbulent flames.*

As shown in Fig. 1.6, the filter size associated to the flow field (*i.e.* to the mass and momentum equations), denoted $\overline{\Delta}$, is implicitly controlled by the mesh size $\Delta_x$, by the numerical schemes and by the turbulence model $\overline{\tau}^t$. An order of magnitude for this quantity would be $\overline{\Delta} \approx 3\Delta_x$. However, the filter size associated to the flame front (*i.e.* to the species or progress variable equations), denoted $\overline{\overline{\Delta}}$, is controlled by the combustion modeling strategy and is in practice larger than $\overline{\Delta}$. An order of magnitude for this quantity would be $\overline{\overline{\Delta}} \approx 6\Delta_x$. As it will be discussed in Chapter 5, the condition $\Delta_x < \overline{\Delta} < \overline{\overline{\Delta}}$ is necessary to ensure a proper resolution of the filtered reaction rate on a given mesh grid and therefore make the flame front propagate at the correct turbulent flame speed (Auzillon et al., 2011).

The width of the filtering operator $\overline{\cdot}$ applied to the mass and momentum equa-

[4]When a statistical description of the sub-filter scale interactions is used, the broadening of the flame front is not explicit anymore and is more difficult to control.

tions is then different from the width of the filter $\overline{\cdot}$ applied to the flame equations. This remark generates some mathematical inconsistencies in the coupling of the filtered equations as soon as the flow and flame effective filter sizes are different $\overline{\Delta} \neq \overline{\overline{\Delta}}$, which is actually the case for numerous LES combustion models. To our knowledge, this point has never been discussed in the presentation of the different turbulent models and will be studied in details in the Chapter 5 of this thesis. Consistent coupling and modeling strategies regarding the different filter sizes will be proposed.

## 1.7 Challenges for the LES modeling of industrial combustion chambers

This section summarizes the different challenges to be addressed to improve the prediction of turbulent flames in practical combustion chambers. The contributions of this thesis, restricted to the context of gaseous flows, are then reminded.

As discussed in Sec. 1.3, the design of practical configurations requires to predict the flame position, propagation speed, thermochemical structure when the wrinkling is fully resolved in the LES computation but also in the more general case where sub-filter scale wrinkling occurs. Moreover, industrial combustion chambers often exhibit heat losses that should be accounted for by the turbulent combustion models. Table 1.1 summaries the models abilities to meet the different specifications drawn in Sec. 1.3.
In the framework of the LES of turbulent premixed and stratified combustion, two modeling issues may be identified:

- The modeling strategies have to include some basic physical phenomena to model correctly the filtered flame propagation speed and the inner filtered flame structure in practical cases. For instance, most of the modeling approaches assume adiabatic combustion and/or unity Lewis number diffusion which are very strong assumptions when practical configurations are considered. Others also neglect the impact of sub-grid scale mixture fraction heterogeneities on the filtered flame propagation and structure. A challenge for the turbulent combustion modeling community is to include these ingredients to enhance prediction capabilities of the models. This issue has been recently identified and very recent studies present such model extensions. For instance, the TFLES-FPI and G-equation models have been recently extended to non-adiabatic situations by Ketelheun et al. (2013); Trisjono et al. (2014). The objective of the Part II of this manuscript is to extend and validate the F-TACLES model to account for both differential diffusion and heat losses. The extended model will be applied to a semi-industrial combustor in the Part IV.
- The flame-turbulence interactions have to be correctly predicted whether or not the flame wrinkling is fully resolved. When the flame wrinkling

is fully resolved or when the flame is purely laminar (cases (a) and (b) in Fig. 1.2), the interaction between flame and flow is fully resolved. In this case, the only challenge is to choose an adapted strategy to capture the two-way coupling between the resolved flow and the broadened flame front paying a particular attention to the consistency between flame and flow filter scales. In the more general case where the flame wrinkling is only partially resolved (Case (c) in Fig. 1.2), another issue consists in modeling the impact of the unresolved flame wrinkling by unresolved turbulent scales. Both issues are studied in the Part III of this manuscript.

| Requirements / Models | Accounts for SGS flame-turbulence interactions | Degenerates towards laminar regime | Proper coupling of flame and flow filtered equations | Accounts for SGS mixture heterogeneities | Accounts for differential diffusion | Accounts for non-adiabaticity |
|---|---|---|---|---|---|---|
| MILES (No model) | No | Only when $Da_\Delta \ll 1$ | Only when $Da_\Delta \ll 1$ | No | No | Yes |
| PCM-FPI | Statistical model ($\widetilde{c''^2}$) | No | No[1] | Yes | No | No |
| G-Equation | Modeled through $S_T$ | Yes | Needs model for the inner flame structure | Yes | - | Yes (Roux and Pitsch, 2010) |
| FSD | Modeled through $\Sigma$ | Yes | No[1] | (No)[2] | No | No |
| TFLES | Modeled through $\Xi_\Delta$ | Yes | No[1] | No | No | Yes |
| TFLES-FPI | Modeled through $\Xi_\Delta$ | Yes | No (extended in Appendix C) | (No)[2] | (No)[3] | Yes (Ketelheun et al., 2013) |
| FLF-PDF | Statistical model ($\widetilde{c''^2}$) | Yes | No[1] | Yes | Yes (only for $\widetilde{z}$) | No |
| F-TACLES | Modeled through $\Xi_\Delta$ | Yes | No (extended in Part III) | Yes | No (extended in Part II) | No (extended in Part II) |

**Table 1.1:** *State of the art of the LES combustion models for premixed and stratified combustion prior to this thesis. The different features are listed regarding the requirements drawn in Sec. 1.3. Extra comments are listed below:*
*1. In this thesis, no specific derivations are performed for these models. However, the general formalism accounting for both flame and flow filter sizes proposed in Part III also applies to these models.*
*2. For those models, accounting for sub-grid scale mixture heterogeneities should be straightforward. To that end, a statistical formalism (for instance, a $\beta$-function based on the mixture fraction) could be used directly on the thermochemical variables of interest to account for unresolved heterogeneities.*
*3. The work presented in Part II to account for differential diffusion effects in the laminar flamelet database could be easily applied to the TFLES-FPI formalism.*

# Part II

# Heat losses and differential diffusion effects on the turbulent flame propagation

# Chapter 2

# Modeling the impact of heat losses and differential diffusion on turbulent flame propagation

**Contents**

*In this chapter, the F-TACLES model, initially developed under adiabatic and unity Lewis number assumptions, is extended to account for differential diffusion and heat losses effects on the flame structure and consumption speed. This extension will be validated on different complex turbulent flames in the next chapter.*

## 2.1 Motivations

The F-TACLES model, presented in Sec. 1.5.2.4, has been devised to include detailed chemistry in LES. It captures the correct flame consumption speed when the flame wrinkling is fully or partially resolved at the LES filter scale, since both situations are frequently encountered in practical grid meshes (Fiorina et al., 2010). Auzillon et al. (2012) extended this model to adiabatic stratified combustion regimes by accounting for mixture fraction heterogeneities at the subgrid scale level. The model has been validated assuming adiabatic combustion and unity Lewis number diffusion on a swirled turbulent stratified flame experimentally investigated by Janus et al. (2004, 2005, 2007). Although these assumptions are made in numerous turbulent combustion models for Large Eddy Simulation (Fiorina et al., 2010; Auzillon et al., 2011; Duwig, 2009; Kuenne et al., 2011; Marincola et al., 2013; Proch and Kempf, 2014), it may have significant impact on the flame consumption rate.

First, accounting for differential diffusion significantly impacts the chemical flame structure. Therefore, the molecular transport model also impacts the prediction of the flame consumption speed. For instance, the simulation of a 1-D laminar methane/air premixed flame using a detailed chemical scheme[1] and assuming unity Lewis number underestimates the consumption speed by approximately 25% (Poinsot and Veynante, 2012). Recent experimental (Barlow et al., 2012; Dunn and Barlow, 2013) and numerical (Aspden et al., 2011a,b; Savre et al., 2013) studies have shown that the impact of species differential diffusion in turbulent flames depends on both flow topology and turbulent combustion regime.

Secondly, heat losses which occur in most industrial combustors also influence the chemical flame structure. Indeed, by decreasing the flame temperature, heat losses reduce chemical activities and decrease the overall flame consumption speed. When the reaction zone develops close to cooled walls, intense heat exchanges may cause local extinctions (Poinsot and Veynante, 2012).

[1] Detailed chemical schemes generally capture the proper flame consumption speed when they are associated with complex modeling of diffusion fluxes. This is why they do not reproduce the correct flame speed when they are associated with unity Lewis number assumption. However, global chemical schemes can be developed to be used together with unity Lewis number assumption (Franzelli et al., 2010). In this last case, the use of complex diffusion models may also lead to a misprediction of the flame speed. Transport model and reaction scheme cannot be considered independently.

In the context of tabulated chemistry, modeling the effect of differential diffusion and heat losses on chemical trajectories requires dedicated chemical database coordinates. The stabilization of a flame by heat losses is accurately captured using the enthalpy coordinate as shown in Fiorina et al. (2003). In an LES context, recent works have proposed to extend several models to non-adiabatic combustion. For instance, Ketelheun et al. (2013) present a non-adiabatic extension of the TFLES-FPI model while Roux and Pitsch (2010) and Trisjono et al. (2014) have extended the G-equation model using a non-adiabatic chemistry tabulation method.

Accounting for differential diffusion of all species requires the addition of several coordinates (Gicquel et al., 2000) leading to very high-dimensional databases. In a laminar context, Regele et al. (2013) proposed a technique to account for fuel differential diffusion phenomena within tabulated chemistry by adding a source term to the mixture fraction balance equation. Maragkos et al. (2013) proposed a methodology to capture differential diffusion by transporting only $N_{el} - 1$ scalars instead of $N_{sp} - 1$ (detailed chemistry) where $N_{el}$ is the number of chemical elements. Adapting these strategies to LES combustion models requires numerous physical assumptions to close the additional coordinates balance equations. Issues are the overall model performances in terms of both accuracy and CPU cost. By focusing on the impact of differential diffusion on the mixture fraction variable, Nambully et al. (2014a) add a source term to the filtered transport equation of mixture fraction. This approach showed good results for the LES of the Cambridge stratified swirling flames SWB5 and SWB9 (Nambully et al., 2014b). However, the retroaction of differential diffusion on the flow and on other chemical species was not accounted for in this work.

The objective of this chapter is to develop an LES combustion model based on tabulated chemistry which accounts for fuel stratification, heat losses and complex transport phenomena. We assume that differential diffusion and heat losses primary impact the flame dynamics through the sub-grid scale turbulent flame consumption speed. These phenomena can be modeled without increasing the dimension of thermochemical database as shown in Sections 2.2 and 2.3. The importance of these modeling improvements will be evaluated in Chapter 3 through the LES of different turbulent stratified flames stabilized on two different generic burners.

## 2.2 Modeling adiabatic stratified combustion using tabulated chemistry with differential diffusion

### 2.2.1 Differential diffusion modeling assumptions

From a general point of view, complex diffusive transport of the chemical species controls several phenomena in both laminar and turbulent flames such as:

- The flame propagation is controlled by an equilibrium between chemical reactions and species diffusion process. A proper modeling of both phenomena is then essential to predict correctly flame consumption speed and its chemical structure in both laminar and turbulent situations.
- Preferential diffusion effects may also influence the turbulent flow chemical composition. Barlow et al. (2012) and Dunn and Barlow (2013) showed that turbulent structures in fresh gases and near the flame front may isolate preferentially the chemical species of the flame diffusing towards fresh gases. In very particular cases, when flow area with high residence time exists, this phenomenon may cause significant modifications of the local equivalence ratio (and then thermochemical equilibrium) in the burnt gases. These conclusions are corroborated by the numerical studies proposed by Katta and Roquemore (2013) and Nambully et al. (2014a,b).
- Thermo-diffusive instabilities may create flame surface (wrinkling) as detailed by Poinsot and Veynante (2012). This phenomenon appears as soon as the Lewis number is under unity. These instabilities are of importance in laminar cases and vanish in turbulent flows since the flame wrinkling by turbulent motions becomes the governing phenomenon.

Accounting for 3-D differential diffusion effects in the LES of a turbulent flames is a very difficult challenge. First, as stated in Sec. 2.1, only few chemistry reduction techniques have been proposed to account for complex transport. In such approaches, the number of coordinates and transported variables substantially increases compared to the unity Lewis number cases. Second, this modeling issue becomes much more complex in an LES context as molecular species diffusion occurs partially at the sub-grid scale. The modeling of sub-grid scale differential diffusion effects is very challenging and, to the author's knowledge, has never been performed without making *a priori* assumptions on the turbulent flame structure.

In this thesis, it has been chosen to include differential diffusion effects within the framework of the FPI method where the turbulent flame structure is assumed similar to a 1-D laminar premixed flame. For that purpose, the FPI thermochemical database used to build the F-TACLES model will be now mapped using a set of 1-D laminar premixed flames computed with complex modeling of species diffusive transport. This approach allows to capture the impact of differential diffusion in the direction normal to the flame front (as it is captured

in the detailed 1-D flame computations) but neglects the species differential diffusion in other directions. From a phenomenological point of view, this assumption means that:

- The flame consumption speed and structure are assumed similar to a 1-D laminar flame computed with differential diffusion.
- Thermo-diffusive instabilities are neglected since the effect of differential diffusion on chemical trajectories in the direction tangential to the flame front is neglected.
- 3-D complex transport effects are also neglected when they result from an interaction between the flame structure and the turbulent eddies which cannot be captured by the 1-D laminar flame collection.

In the following sections, the impact of differential diffusion on the 1-D premixed flame characteristics is formalized and quantified. Then, under the assumptions mentioned here, the F-TACLES formalism for adiabatic stratified flames (Auzillon et al., 2012) initially developed under unity Lewis number assumption is generalized to account for differential diffusion in the direction normal to the flame front.

### 2.2.2 Impact of differential diffusion model on premixed flamelet structure and propagation

The F-TACLES formalism relies on the FPI tabulation method. It supposes that the inner flame structure is not altered by turbulent eddies and is similar to a 1-D laminar premixed freely-propagating flame. The chemical trajectories accessed during the LES of the turbulent flame are described by the manifold $\Omega_m$ mapped by a set of 1-D premixed flamelets computed under detailed chemistry using the following equations:

$$\dot{m} = \rho u \tag{2.1}$$

$$\dot{m}\frac{dT}{dx} = \frac{1}{C_p}\frac{d}{dx}\left(\lambda\frac{dT}{dx}\right) - \frac{1}{C_p}\sum_{k=1}^{N_{sp}}\left[\rho Y_k V_k C_{p_k}\right]\frac{dT}{dx} - \frac{1}{C_p}\sum_{k=1}^{N_{sp}}\left[\rho\dot{\omega}_k h_k\right] \tag{2.2}$$

$$\dot{m}\frac{dY_k}{dx} = -\frac{d}{dx}\left(\rho Y_k V_k\right) + \rho\dot{\omega}_k \qquad (k = 1, ..., N_{sp}) \tag{2.3}$$

$$p = \rho\frac{R}{\overline{W}}T \tag{2.4}$$

with $x$ the spatial coordinate, $\dot{m}$ the mass flow rate per unit of time and surface. $\dot{m} = \dot{M}/A$ where $\dot{M}$ is the mass flow rate and $A$ the surface of reference set to unity. $u$ is the velocity of the fluid mixture while $\rho$ is the density and $T$ the temperature. $\lambda$ denotes the thermal conductivity of the mixture. The mean constant pressure heat capacity of the mixture reads $C_p = \sum_{k=1}^{N_{sp}} Y_k C_{p_k}$ with $Y_k$ the mass fraction of the $k^{\text{th}}$ species, $N_{sp}$ the total number of species and

$C_{p_k}$ the constant pressure heat capacity of the $k^{\text{th}}$ species. $h_k$ is the specific sensible plus chemical enthalpy of the $k^{\text{th}}$ species. $p$ denotes the pressure considered constant across the flame, $R$ is the universal gas constant and $\overline{W}$ is the mean molecular weight of the mixture. The chemical reaction rates $\dot{\omega}_k$ [$s^{-1}$] are estimated from Arrhenius laws where coefficients are extracted from a given detailed chemical scheme. In addition, transport properties of the species, as the diffusion velocity $V_k$, also need to be modeled.

The corrected Hirschfelder and Curtiss approximation (Hirschfelder et al., 1969) estimates accurately the diffusion velocity $V_k$. This approximation introduces an effective diffusion coefficient $D_k$ of each chemical species in the mixture:

$$\rho Y_k V_k = \rho \left( -\frac{W_k}{\overline{W}} D_k \frac{dX_k}{dx} + Y_k V_c \right) \tag{2.5}$$

where $X_k$ is the molar fraction of the $k^{\text{th}}$ species and $W_k$ its molecular weight. $V_c$ is a velocity correction introduced to ensure mass conservation regardless of the modeling assumptions for $D_k$. Two modeling assumptions are possible to estimate the diffusion coefficient $D_k$ (Poinsot and Veynante, 2012):

- A realistic representation is to account for differential species diffusion. The effective diffusivity $D_k$ of the $k^{\text{th}}$ species is then computed from binary diffusion coefficients (Hirschfelder et al., 1969).
- A simpler and very common strategy assumes that all species diffusivities $D_k$ are equal to the mixture thermal diffusivity $D_{th} = \lambda/(\rho C_p)$. Under these conditions, the Lewis number $Le = D_{th}/D_k = 1$ and the diffusion velocities are recast as $\rho Y_k V_k = -\rho D_{th} \frac{dY_k}{dx}$.

The flamelet structure and consequently the chemistry tabulation strongly depend on the species diffusion model. For instance Fig. 2.1 shows profiles of $CO_2$ and $H_2$ mass fractions as well as temperature across a stoichiometric methane-air flame computed at constant pressure using the detailed chemical scheme proposed by Lindstedt (1997) for $CH_4$/Air which includes 29 species and 141 reactions. Figure 2.1 shows that the species mass fraction profiles are very sensitive to the molecular diffusion modeling. To analyze global flame properties, the flame thickness $\delta_c$ and the flame consumption speed $S_l^0$ are respectively introduced as $\delta_c = Y^b_{CO_2}/\max(\nabla Y_{CO_2})$ and $S_l^0 = 1/(\rho^f Y^b_{CO_2}) \int_{-\infty}^{+\infty} \rho \dot{\omega}_{CO_2} dx_n$, where $\rho^f$ and $Y^b_{CO_2}$ denote respectively the fresh gases density and the $CO_2$ mass fraction in burnt gases. $x_n$ denotes the direction normal to the flame front. Both quantities are plotted in Fig. 2.2 as a function of fresh gases equivalence ratio $\phi$. The $CO_2$ mass fraction and flame thickness appear weakly sensible to the molecular diffusion model whereas the flame consumption speed decreases by 25% when unity Lewis number is assumed compared to the complex diffusion case (taken as a reference here).

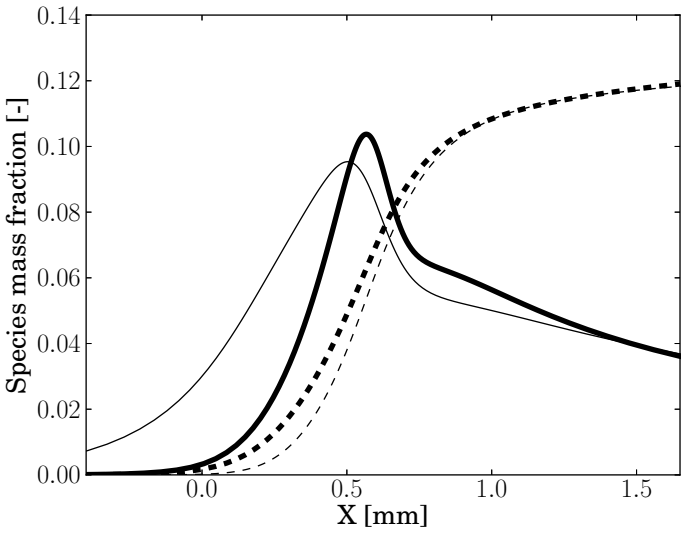


(a) Species mass fractions.
Legend: - - - $Y_{CO_2}$ (Le $\neq$ 1). **- - -** $Y_{CO_2}$ (Le = 1). —$10^2 \cdot Y_{H_2}$ (Le $\neq$ 1). — $10^2 \cdot Y_{H_2}$ (Le = 1).

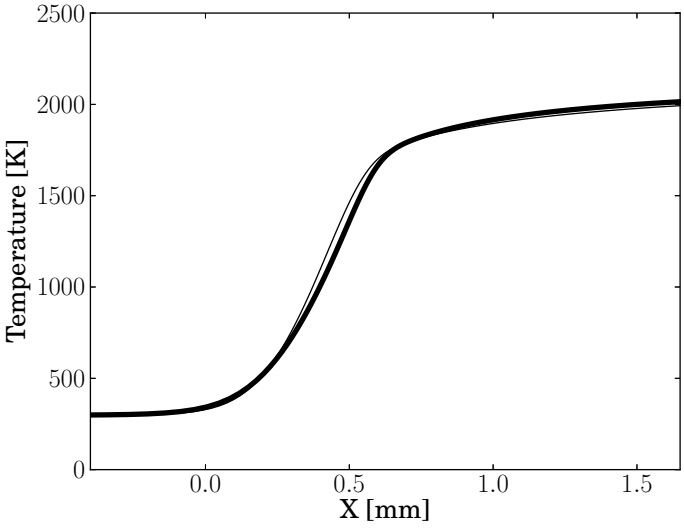


(b) Temperature. Legend: —T (Le $\neq$ 1). — T (Le = 1).

**Figure 2.1:** *Comparison of thermochemical structure of stoichiometric methane-air flames computed under both differential diffusion and unity Lewis number assumptions.*

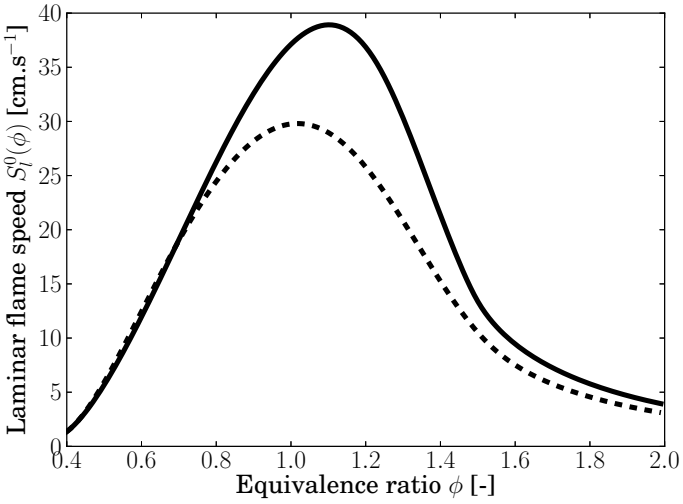


(a) Laminar flame speed $S_l^0$.

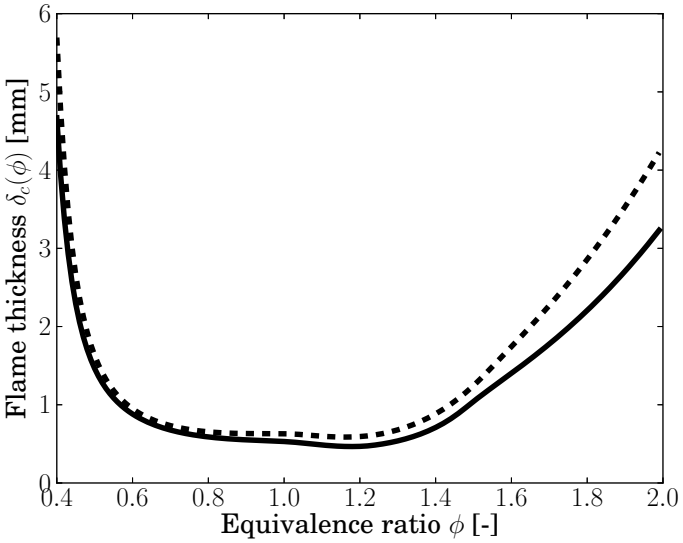


(b) Flame thickness $\delta_c$.

**Figure 2.2:** *Laminar flame speed $S_l^0$ for as a function of the equivalence ratio $\phi$ of the methane-air mixture. Legend: —Differential diffusion case. − − Unity Lewis number case.*

### 2.2.3 Chemistry tabulation issues

Within the FPI formalism, thermochemical quantities computed from adiabatic premixed flamelets are stored in a look-up table as a function of two coordinates: the non-normalized progress variable $Y_c$, which evolves monotonically between fresh and burnt gases, and the non-normalized mixture fraction $Y_z$ which evolves monotonically between oxidizer and fuel streams. $Y_z$, tracks the 1-D premixed flamelets used for chemistry tabulation and varies monotonically with the fresh gas equivalence ratio $\phi$. The non-normalized progress variable $Y_c$ together with the non-normalized mixture fraction $Y_z$ uniquely describe the thermochemical subspace accessed in the adiabatic 1-D premixed flamelets collection as:

$$\Phi = \Phi[Y_c, Y_z] \tag{2.6}$$

where $\Phi$ denotes any thermochemical quantity. $Y_z$ can be based either on carbon element mass fraction or on the non-reacting species such as $N_2$ when NOx chemistry is neglected. In both cases, $Y_z$ remains constant across the flamelet when a unity Lewis number is assumed. When differential diffusion is accounted for, both $Y_c$ and $Y_z$ vary across the flamelet elements used to tabulate the chemistry. This issue drastically increases the complexity of the tabulation process.

An alternative approach is proposed here. As the chemistry tabulation is based on a collection of 1-D premixed flamelets computed independently, the impact of differential diffusion in the direction tangential to the flame front (i.e. between each flamelet) is not accounted for. However, the species differential diffusion in the direction normal to the flame front is captured by the 1-D premixed flamelet elements and allows for instance to correctly predict the laminar flame consumption speed. Under these assumptions, the evolution of $Y_z$ across the flame front can be described, as any other quantity varying across the flame front, by the progress variable $Y_c$ and the fresh gas equivalence ratio $\phi$:

$$Y_z = Y_z\left(Y_c, \phi\right) \tag{2.7}$$

One discrete value of $Y_z^{eq} = Y_z\left(Y_c = Y_c^{eq}, \phi\right) = Y_z^{eq}\left(\phi\right)$ is then associated to a single premixed flamelet computed at fresh gas equivalence ratio $\phi(Y_z^{eq})$. Equation 2.7 can then be recast as follows:

$$Y_z = Y_z\left(Y_c, Y_z^{eq}\right) \tag{2.8}$$

Therefore, combining Eq. 2.6 and Eq. 2.8 leads to an equivalent tabulation of

the thermochemical quantities under the previously detailed assumptions:

$$\Phi = \Phi[Y_c, Y_z^{eq}] \tag{2.9}$$

To ease the tabulation process, the normalized mixture fraction $z$ is then introduced:

$$z = \frac{Y_z^{eq}(\phi) - Y_z^{eq}(\phi_{\min})}{Y_z^{eq}(\phi_{\max}) - Y_z^{eq}(\phi_{\min})} \tag{2.10}$$

The different assumptions detailed previously allow to transport $z$ as a passive scalar in the LES computation:

$$\frac{\partial \rho z}{\partial t} + \nabla \cdot (\rho u z) = \nabla \cdot (\rho D_z \nabla z) \tag{2.11}$$

where $D_z$, the diffusivity of the mixture fraction is supposed equal to the thermal diffusivity leading to $D_z = D_{th} = \lambda/(\rho C_p)$.

The non-normalized progress variable $Y_c$ and the mixture fraction $z$ finally give access to the tabulated thermochemical quantities $\Phi[Y_c, z]$. In the present work, the value of $N_2$ mass fraction is chosen to define $Y_z$.

### 2.2.4 Accounting for differential diffusion using FPI method

Different modeling alternatives are reviewed in this section to account for differential diffusion using the FPI method and without increasing the number of dimensions of the chemical look-up table. This step is necessary to prepare the use of chemical database computed with complex transport in an LES context.

#### 2.2.4.1 Approach 1: Correcting the flame consumption speed only

The most simple approach is to assume that the major consequence of unity Lewis number assumption is a misprediction of the flame consumption speed. By neglecting the impact of differential diffusion on the flame structure, it is then possible to correct directly the turbulent flame consumption speed by a factor $\zeta^{DD}$ defined as:

$$\zeta^{DD} = \frac{S_l(\text{Complex diffusion})}{S_l(\text{Le=1})} \tag{2.12}$$

where $S_l$(Le=1) and $S_l$(Complex diffusion) are estimated from 1-D premixed flames computed with unity Lewis number assumption and with complex transport modeling, respectively. In the context of tabulated chemistry, this flame speed correction factor is used to correct the progress variable propagation

speed by multiplying the RHS terms as follows:

$$\frac{\partial \overline{\rho}\widetilde{Y_c}}{\partial t}+\frac{\partial}{\partial x_i}\left(\overline{\rho}\widetilde{u_i}\widetilde{Y_c}\right)=\zeta^{DD}\left(\frac{\partial}{\partial x_i}\left(\overline{\rho D_{th}\frac{\partial Y_c}{\partial x_i}}\right)-\frac{\partial}{\partial x_i}\left(\overline{\rho}(\widetilde{Y_c u_i}-\widetilde{Y_c}\widetilde{u_i})\right)+\overline{\rho}\widetilde{\dot{\omega}}_{Y_c}\right) \tag{2.13}$$

This approach can be used with any turbulent combustion model presented in Sec. 1.5. Using the F-TACLES model, the filtered progress variable equation (Eq. 1.50) becomes:

$$\begin{aligned}\frac{\partial \overline{\rho}\widetilde{Y_c}}{\partial t}+\frac{\partial}{\partial x_i}\left(\overline{\rho}\widetilde{u_i}\widetilde{Y_c}\right) &= \frac{\partial}{\partial x_i}\left(\zeta^{DD}\Xi_\Delta\alpha_{Y_c}[\widetilde{Y_c},\widetilde{z},S_z,\Delta]\rho_0 D_0\frac{\partial \widetilde{Y_c}}{\partial x_i}\right) \quad (2.14)\\ &+ \zeta^{DD}\Xi_\Delta\Omega_{Y_c}[\widetilde{Y_c},\widetilde{z},S_z,\Delta]\\ &+ \zeta^{DD}\Xi_\Delta\overline{\rho}\widetilde{\dot{\omega}}_{Y_c}[\widetilde{Y_c},\widetilde{z},S_z,\Delta] \quad (2.15)\end{aligned}$$

where all the tabulated terms $\Phi=\Phi[\widetilde{Y_c},\widetilde{z},S_z,\Delta]$ are evaluated from 1-D laminar premixed flames computed under unity Lewis number assumption as detailed in Sec. 1.5.2.4. When the flame flame wrinkling is fully resolved ($\Xi_\Delta=1$), one may verify that this approach applied to the F-TACLES model ensures that the flame propagation speed equals $S_l$(Complex diffusion):

$$S_l=\frac{1}{\overline{\rho}^f(\widetilde{Y_c^{eq}}-\widetilde{Y_c^f})}\int_{-\infty}^{+\infty}\zeta^{DD}\overline{\rho}\widetilde{\dot{\omega}}_{Y_c}dx_n=\zeta^{DD}S_l(\text{Le=1})=S_l(\text{Complex diffusion}) \tag{2.16}$$

Despite its simplicity, this methodology does not account for the impact of differential diffusion on the inner thermochemical flame structure. In the following, other alternatives are proposed to make a deeper use of the chemistry tabulation with differential diffusion.

#### 2.2.4.2 Approach 2: Generalized progress variable equation

This approach, proposed in Mercier et al. (2014) and also adopted in Nambully et al. (2014a,b), consists in conserving a definition of the progress variable based on chemical species as $Y_c=\sum_{k=1}^{N_{sp}}n_kY_k$. In this context, the filtered progress variable equation reads:

$$\frac{\partial \overline{\rho}\widetilde{Y_c}}{\partial t} + \frac{\partial}{\partial x_i}\left(\overline{\rho}\widetilde{u_i}\widetilde{Y_c}\right) = -\frac{\partial}{\partial x_i}\left(\overline{\sum_{k=1}^{N_{sp}}[n_k \rho Y_k V_k]}\right) - \frac{\partial}{\partial x_i}\left(\overline{\rho}(\widetilde{Y_c u_i} - \widetilde{Y_c}\widetilde{u_i})\right) + \overline{\rho}\widetilde{\dot{\omega}}_{Y_c} \tag{2.17}$$

(2.18)

This equation is closed within F-TACLES formalism as:

$$\frac{\partial \overline{\rho}\widetilde{Y_c}}{\partial t} + \frac{\partial}{\partial x_i}\left(\overline{\rho}\widetilde{u_i}\widetilde{Y_c}\right) = \frac{\partial}{\partial x_i}\left(\Xi_\Delta \alpha_{Y_c}[\widetilde{Y_c}, \widetilde{z}, S_z, \Delta]\rho_0 D_0 \frac{\partial \widetilde{Y_c}}{\partial x_i}\right) \tag{2.19}$$

$$+ \Xi_\Delta \Omega_{Y_c}[\widetilde{Y_c}, \widetilde{z}, S_z, \Delta] + \Xi_\Delta \overline{\rho}\widetilde{\dot{\omega}}_{Y_c}[\widetilde{Y_c}, \widetilde{z}, S_z, \Delta]$$

(2.20)

In this formulation, the second $\Omega_{Y_c}$ and third $\widetilde{\dot{\omega}}_{Y_c}$ RHS terms are not modified. The correction factor $\alpha_{Y_c}$ is tabulated from 1-D filtered premixed flames computed with differential diffusion (in fact, with any formulation of the diffusive flux $\rho Y_k V_k$) as:

$$\alpha_{Y_c}[\widetilde{Y_c}, \widetilde{z}, S_z, \Delta] = -\frac{\overline{\sum_{k=1}^{N_{sp}}\left(n_k \rho^* Y_k^* V_k^*\right)}}{\left(\rho_0 D_0 \frac{\partial \widetilde{Y_c^*}}{\partial x^*}\right)} \tag{2.21}$$

where the superscript * denotes values extracted from the 1-D laminar flame computed with complex diffusive transport. This diffusion correction factor captures differential diffusion effects in the direction $x^*$ normal to the flame front.

## 2.3 Accounting for heat-losses effects on flame consumption speed and flow field

### 2.3.1 Generation of a non-adiabatic chemical database

van Oijen and de Goey (2000) and Fiorina et al. (2003) have extended tabulated chemistry approaches to non-adiabatic situations by introducing the sensible plus chemical enthalpy of the mixture $h = \int_{T_0}^{T} C_p dT + \sum_{k=1}^{N_{sp}} \Delta h_k^0 Y_k$ to account for heat losses. $\Delta h_k^0$ is the mass formation enthalpy of the $k^{\text{th}}$ species. The chemical look-up table is constructed from a set of one-dimensional laminar premixed flames stabilized on a porous isothermal burner (Kee et al., 1992) and computed for various equivalence ratio in the flammability range and different enthalpy levels, using detailed chemistry. Governing equations are identical to the freely-propagating flame equations (2.1) to (2.4) while boundary conditions differ. This set of equations is solved on a domain defined as $x \in [0; +\infty[$ where

$x = 0$ is the position of the burner nozzle. Inlet boundary conditions at $x = 0$ are prescribed solving (Kee et al., 1992):

$$\rho^n u^n = \dot{m} \tag{2.22}$$

$$Y_k^n = Y_k^f - \frac{\rho^n Y_k^n V_k^n}{\dot{m}} \tag{2.23}$$

$$T^n = T_0 \tag{2.24}$$

where the superscript $f$ denotes the fresh gas injected into the porous isothermal burner, the superscript $n$ denotes gas state at the burner nozzle (x=0). Mass flow rate $\dot{m}$ is a prescribed quantity as well as inlet flow composition $Y_k^f$ and temperature $T_0$. No reactions are considered within the porous burner and the enthalpy defect results from heat exchanges between the stabilized flame and isothermal burner nozzle.

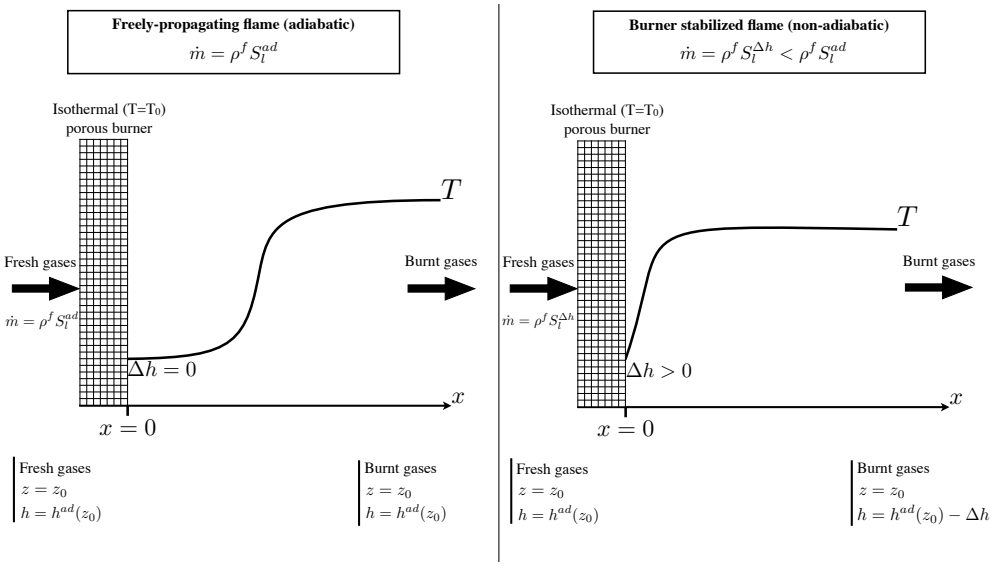


**Figure 2.3:** *Schematic of the configuration of burner-stabilized flames computations. (Left) When the fresh gases mass flow rate $\dot{m}$ corresponds to adiabatic conditions, an adiabatic freely-propagating flame is obtained. (Right) When the mass flow rate decreases, the flame stabilizes at the porous burner lips and heat losses occur at the isothermal burner nozzle.*

When the flow rate $\dot{m}$ decreases, heat losses to the burner increase and the flame enthalpy $h$ decreases until extinction. This can be shown by integrating the enthalpy balance equation, leading to:

$$h^{eq}(z, \dot{m}) = h^f(z) - \left[\frac{\lambda}{\dot{m}} \frac{\partial T}{\partial x}\right]_{x=0} \tag{2.25}$$

where $h^{eq}$ is the enthalpy of the fully burnt gases. The adiabatic limit is obtained when mass flow rate satisfies $\dot{m} = \rho^f S_l^{ad}$ [2]. This solution corresponds to 1-D freely-propagating premixed flame. In this situation, there is no heat exchange between the flame and the burner and enthalpies of fresh and burnt gases are then equal and only depend on mixture fraction $z$:

$$h^f = h^{eq}(z) = h^{ad}(z) \tag{2.26}$$

For unity Lewis number flames, the enthalpy level remains constant in the whole computational domain: $h(x) = h^{eq}$ with $x \in ]0; +\infty[$. However, when complex transport is considered, the enthalpy varies across the reaction zone. To facilitate the tabulation procedure, the strategy proposed in Sec. 2.2.3 for the mixture fraction coordinate is also applied to the enthalpy coordinate: neglecting the impact of differential diffusion in the direction tangential to the flame front, equilibrium enthalpy $h^{eq}$ is used to track the 1-D burner-stabilized flames. For practical issues, the enthalpy defect $\Delta h$ is used as table coordinate:

$$\Delta h(z, \dot{m}) = h^{ad}(z) - h^{eq}(z, \dot{m}) = h^f(z) - h^{eq}(z, \dot{m}) \tag{2.27}$$

The consumption speed $S_l\,(z, \Delta h)$ can then be computed from the consumption rate of burner-stabilized flames by integrating Eq. 2.3, written for the progress variable $Y_c$, along the direction normal to the flame front:

$$\begin{aligned} \rho^f S_l(z, \Delta h) \quad = \quad & \frac{1}{{Y_c}^{eq}(z, \Delta h) - {Y_c}^{n}(z, \Delta h)} \cdot \\ & \left( \int_0^{+\infty} \rho^{**} \dot{\omega}_{Y_c}^{**}(x', z', \Delta h) dx' + [\rho^{**} Y_k^{**} V_k^{**}]_{x=0} \right) \end{aligned} \tag{2.28}$$

The superscript $^{**}$ refers to a burner-stabilized non-adiabatic flamelet computed with detailed chemistry. In this expression, $x = 0$ corresponds to the burner nozzle while $Y_c^n$ and $Y_c^{eq}$ denote progress variable values at burner nozzle and fully burnt gases respectively. The non-adiabatic laminar flame consumption speed $S_l(z, \Delta h)$ is plotted in Fig. 2.4 as a function of the equivalence ratio $\phi$ for different enthalpy defects $\Delta h$. The bold line represents the adiabatic case. Increasing the heat losses causes a decrease of the consumption rate and consequently of the flame speed $S_l(z, \Delta h)$. The flame extinguishes when flame speed $S_l$ has decreased to a minimal value supposed here equal to 5 cm.s$^{-1}$.

[2] A flame with $\dot{m} > \rho^f S_l^{ad}$ would also be adiabatic but not stabilized.

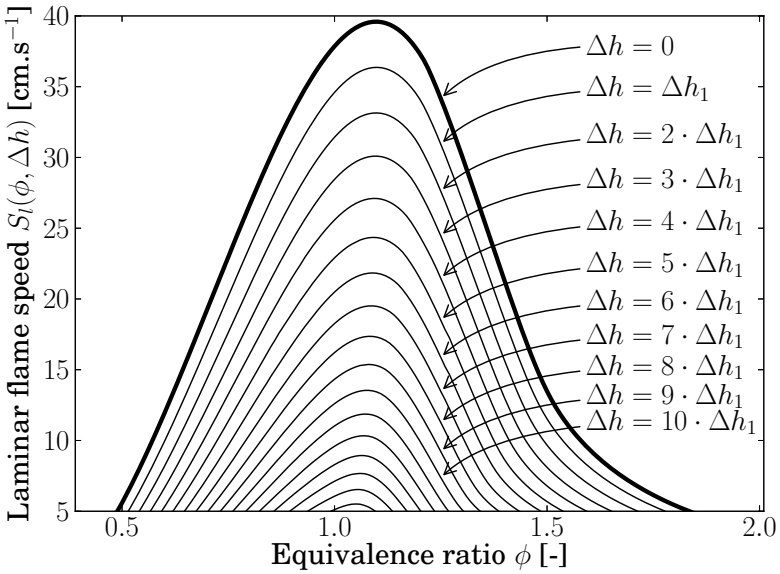


**Figure 2.4:** *Consumption speed $S_l(\phi, \Delta h)$ of non-adiabatic burner-stabilized 1-D flames as a function of equivalence ratio $\phi$ at several enthalpy defects computed with complex transport model for diffusion velocities. Reference enthalpy defect is taken here as $\Delta h_1 = 5.2 \cdot 10^4$ $J.kg^{-1}$. Fresh gas temperature $T_0$ is set to $T_0 = 298.0$ $K$.*

### 2.3.2 Non-adiabatic F-TACLES formalism

The enthalpy defect is introduced in the original F-TACLES formalism described in Sec. 1.5.2.4 as follows:

$$\overline{\rho\dot{\omega}_{Y_c}} = \Xi_\Delta \int_0^1 \int_0^{\Delta h_{max}} \left\langle \rho\dot{\omega}_{Y_c} \Big|_{\Delta h = \Delta h'}^{z=z'} \right\rangle \overline{P}(z', \Delta h')\, d\Delta h'\, dz' \tag{2.29}$$

where $\Delta h_{max} = \Delta h_{max}(z)$ is the maximal enthalpy defect. In practice $\Delta h_{max}(z)$ is estimated by cooling burnt gases at given mixture fraction $z$ to the minimal temperature encountered in the computational domain (Fiorina et al., 2003). The joint Filtered Density Function (FDF) $\overline{P}(z', \Delta h')$ accounts for mixture fraction and enthalpy defect subgrid scale variations. The conditional filtered value of the reaction rate at $z = z'$ and $\Delta h = \Delta h'$ reads:

$$\left\langle \rho\dot{\omega}_{Y_c} \Big|_{\Delta h = \Delta h'}^{z=z'} \right\rangle = \int_{-\infty}^{+\infty} \rho\dot{\omega}_{Y_c}^{**}(x_n', z', \Delta h') G_\Delta(x_n - x_n')\, dx_n' \tag{2.30}$$

$\overline{P}(z', \Delta h')$ is decomposed as $\overline{P}(z', \Delta h') = \overline{P}(z')\overline{P}(\Delta h')$ assuming that mixture fraction and enthalpy defects are independent variables.[3] In a second step, the fluctuations of enthalpy defect are assumed to be resolved at the LES scale.

[3]Note that this assumption would not be reasonable if local enthalpy $h$ were considered because the adiabatic value of $h$ directly depends on the mixture composition.

$\overline{P}(\Delta h')$ therefore reduces to a Dirac $\delta$ function. Then, the FDF is simplified as follows:

$$\overline{P}(z', \Delta h') \approx P_\beta(z', \widetilde{z}, S_z)\, \delta\left(\Delta h' - \Delta\widetilde{h}\right) \tag{2.31}$$

where $\Delta\widetilde{h}$ is the filtered enthalpy defect.

The estimation of different F-TACLES closure terms such as $\alpha_{Y_c}$, $\Omega_{Y_c}$ or the filtered reaction rate $\widetilde{\omega}_{Y_c}$ using Eq. (2.29) is actually not straightforward. Indeed, as the spatial dimension covered by a burner-stabilized flame evolves between 0 and $+\infty$, the filter operator $G_\Delta$ in Eq. 2.30 cannot be applied. Therefore, an alternative strategy based on the correction of the flame consumption speed is proposed to account for heat losses.

### 2.3.3 Filtered flame consumption speed

For planar filtered flames, integrating the filtered reaction rate modeled by Eq. (2.29) along the direction normal to the reaction layer provides the subgrid scale turbulent flame speed $S_\Delta$ (Auzillon et al., 2012):

$$\overline{\rho}_0 S_\Delta = \Xi_\Delta \underbrace{\int_0^1 \rho_0(z') S_l\left(z', \Delta\widetilde{h}\right) P_\beta(z', \widetilde{z}, S_z)\, dz'}_{\overline{\rho}_0 \widetilde{S}_l\left(\widetilde{z}, S_z, \Delta\widetilde{h}\right)} \tag{2.32}$$

where $\overline{\rho}_0 = \int_0^1 \rho_0(z') P_\beta(z', \widetilde{z}, S_z) dz'$. The heat loss correction factor $\gamma$ is then introduced:

$$\gamma[\widetilde{z}, S_z, \Delta\widetilde{h}] = \frac{\widetilde{S}_l\left(\widetilde{z}, S_z, \Delta\widetilde{h}\right)}{\widetilde{S}_l\left(\widetilde{z}, S_z, \Delta\widetilde{h} = 0\right)} \tag{2.33}$$

where $\widetilde{S}_l\left(\widetilde{z}, \widetilde{z''^2}, \Delta\widetilde{h}\right)$ is defined in Eq. (2.32). Figure 2.5 shows the evolution of $\gamma$ for different values of equivalence ratio $\phi$ and unmixedness factor $S_z$. Both unity Lewis number and complex transport situations are plotted. Even if the modeling of diffusion velocities has an impact on laminar consumption speeds (See Fig. 2.2), the heat loss correction factor is not significantly impacted by the transport assumption. The same conclusion can be achieved for the variance of mixture fraction. However, $\gamma$ is very sensitive to the equivalence ratio (or mixture fraction) meaning that, for a given level of enthalpy defect, a lean or reach flame will extinguish before a stoichiometric flame.

The correction factor $\gamma[\widetilde{z}, S_z, \Delta\widetilde{h}]$, pre-computed and stored in a look-up table, will be used to enhance the F-TACLES adiabatic formalism in the following

section.

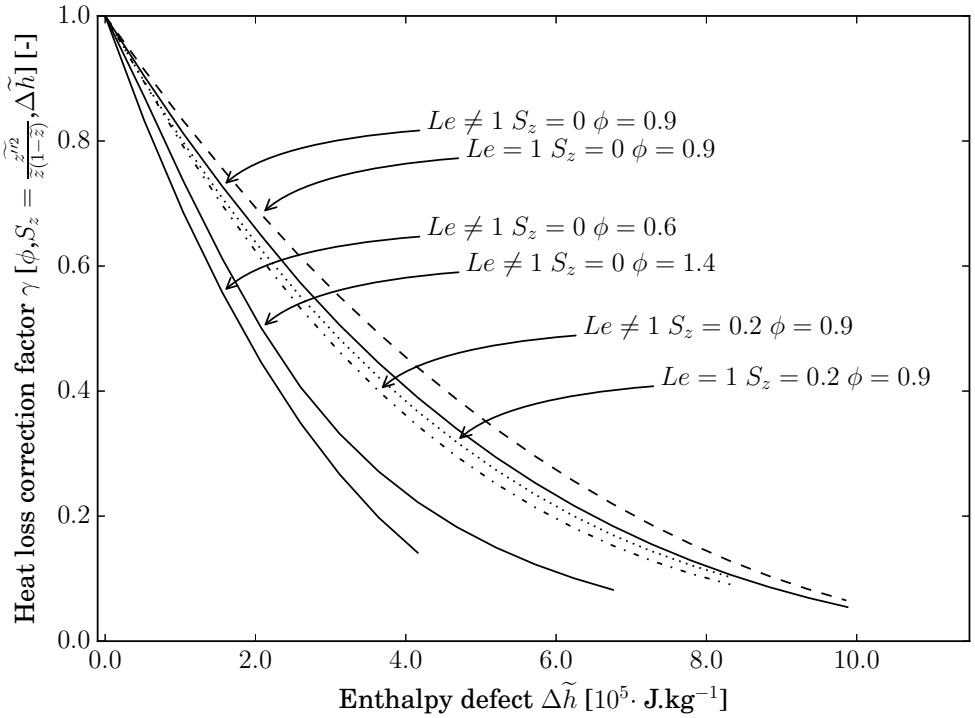


**Figure 2.5:** *Heat loss correction factor* $\gamma$ *for* $\phi \in \{0.6; 0.9; 1.4\}$ *and* $S_z = \widetilde{z''^2}/(\widetilde{z}(1-\widetilde{z})) \in \{0.0; 0.2\}$ *as a function of enthalpy defect* $\Delta h$.
*Legend :* — $Le \neq 1$ $S_z = 0$. - - - $Le = 1$ $S_z = 0$. · - · $Le \neq 1$ $S_z = 0.2$. · · · $Le = 1$ $S_z = 0.2$.

### 2.3.4 F-TACLES model for non-adiabatic stratified flames

The F-TACLES model is extended to non-adiabatic flames. The mathematical formalism includes the differential diffusion formulation introduced in Sec. 2.2.

#### 2.3.4.1 Filtered progress variable balance equation

The filtered progress variable equation (see Sec. 1.5.2.4) is now modified as follows:

$$\begin{aligned}\frac{\partial \overline{\rho}\widetilde{Y_c}}{\partial t} + \frac{\partial}{\partial x_i}(\overline{\rho}\widetilde{u_i}\widetilde{Y_c}) &= \frac{\partial}{\partial x_i}\left(\Xi_\Delta\ \gamma[\widetilde{z}, S_z, \Delta\widetilde{h}]\ \alpha^{ad}_{Y_c}[\widetilde{Y_c}, \widetilde{z}, S_z, \Delta]\, \rho_0 D_0\, \frac{\partial \widetilde{Y_c}}{\partial x_i}\right) \\ &- \Xi_\Delta\ \gamma[\widetilde{z}, S_z, \Delta\widetilde{h}]\ \Omega^{ad}_{Y_c}[\widetilde{Y_c}, \widetilde{z}, S_z, \Delta] \\ &+ \Xi_\Delta\ \gamma[\widetilde{z}, S_z, \Delta\widetilde{h}]\ \overline{\rho}\widetilde{\dot{\omega}}^{ad}_{Y_c}[\widetilde{Y_c}, \widetilde{z}, S_z, \Delta] \qquad (2.34)\end{aligned}$$

The integration of Eq. 2.34 in the direction normal to the flame front shows that this formalism ensures the propagation of a planar filtered flame propagate at the subgrid scale turbulent flame speed:

$$\begin{aligned} S_\Delta &= \Xi_\Delta \, \widetilde{S}_l \left( \widetilde{z}, S_z, \Delta\widetilde{h} \right) \\ &= \Xi_\Delta \, \gamma[\widetilde{z}, S_z, \Delta\widetilde{h}] \, \widetilde{S}_l \left( \widetilde{z}, S_z, \Delta\widetilde{h} = 0 \right) \end{aligned} \tag{2.35}$$

This formalism guarantees that the filtered flame propagates at the laminar flame speed when no turbulent flame interactions occurs at the SGS level. Indeed, when the subgrid scale flame wrinkling factor becomes unity ($\Xi_\Delta = 1$), unresolved transport fluxes and chemical reaction rates are entirely estimated from the filtered chemical look-up table, built from filtered one-dimensional laminar flamelets. Note that as for the adiabatic model formalism, the loop-up table built from adiabatic freely-propagating 1-D flames and introduced in Sec. 1.5.2.4 is used to compute $\alpha_{Y_c}^{ad}$, $\Omega_{Y_c}^{ad}$ and $\widetilde{\dot{\omega}}_{Y_c}^{ad}$. The non-adiabatic correction factor $\gamma$ is tabulated separately from burner-stabilized flames.

The proposed extension of the F-TACLES model to non-adiabatic situations is designed to predict correctly the non-adiabatic flame consumption. Several advantages regarding its practical implementation can be noted:

- This approach conserves the adiabatic closures of the F-TACLES model based on a set of filtered adiabatic freely-propagating 1-D flames. Therefore, the look-up table generator for adiabatic cases can be used directly to generate the different terms $\Phi^{ad}$ appearing in the non-adiabatic formulation.
- Despite the addition of a new tabulated term $\gamma$ in the filtered progress variable equation, the total number of table coordinates is not increased when heat losses are accounted for.

The closure of the mixture fraction table coordinates $\widetilde{z}$ and $\widetilde{z''^2}$ are achieved using the same classical strategies than in the adiabatic model formulation resulting in Eqs. (5.38) and (5.39). The estimation of the enthalpy defect $\Delta\widetilde{h}$ is detailed in the following section.

#### 2.3.4.2 Filtered enthalpy balance equation

As the adiabatic enthalpy $h^{ad}(z)$ expresses linearly as a function of the mixture fraction $z$, the relation $\widetilde{h}^{ad}(z) = h^{ad}(\widetilde{z})$ is satisfied. In the present context of Large Eddy Simulation, filtered enthalpy defect $\widetilde{\Delta h} = \Delta\widetilde{h}$ can be evaluated from transported scalars $\widetilde{z}$ and $\widetilde{h^{eq}}$:

$$\Delta\widetilde{h} = \widetilde{h}^{ad}(z) - \widetilde{h}^{eq} = h^{ad}(\widetilde{z}) - \widetilde{h}^{eq} \tag{2.36}$$

Assuming a low Mach number flow and neglecting viscous heating, volume forces and the impact of species differential diffusion in the direction tangential to the flame front, the passive scalar $h^{eq}$ is solution of the following balance equation:

$$\frac{\partial(\rho h^{eq})}{\partial t} + \nabla \cdot (\rho \mathbf{u} h^{eq}) = \nabla \cdot (\rho D_{th} \nabla h^{eq}) + \dot{Q} \tag{2.37}$$

where $\dot{Q}$ denotes volumic enthalpy production rate such as radiative heat transfer and is neglected in this thesis. Applying LES formalism to this equation and adopting a classical gradient assumption (Eq. 1.24) to close unresolved convective flux leads to a passive scalar equation for filtered enthalpy $\widetilde{h^{eq}}$:

$$\frac{\partial(\overline{\rho}\widetilde{h^{eq}})}{\partial t} + \nabla \cdot (\overline{\rho}\widetilde{\mathbf{u}}\widetilde{h^{eq}}) = \nabla \cdot \left( \left( \overline{\rho D_{th}} + \frac{\mu_t}{Pr_t} \right) \nabla \widetilde{h^{eq}} \right) \tag{2.38}$$

where $Pr_t$ is the turbulent Prandtl number taken equal to $Pr_t = 1.0$.

In practice, the boundary conditions for Eq. 2.38 depend on the temperature and composition of the flow (progress variable and mixture fraction). Boundary conditions are in practice implemented by *a priori* tabulating the enthalpy at the boundaries $\widetilde{h}_{bc}$ as $\widetilde{h}_{bc} = \widetilde{h}_{bc}\left[\widetilde{Y}_c, \widetilde{z}, T_{bc}\right]$ where $T_{bc}$ is the user-defined temperature boundary condition. This look-up table is built from the collection of 1-D burner-stabilized flames prior to the computation. $\widetilde{h}_{bc}$ is then actualized with updated values of thermochemical conditions at the boundaries at each time step of the LES.

#### 2.3.4.3 Filtered ideal gas law equation

Since the spatial filtering of 1-D burner-stabilized flames is not possible, the filtered temperature $\widetilde{T}$ cannot be directly extracted from the non-adiabatic database (since it is not a filtered database). $\widetilde{T}$ is therefore estimated from the filtered adiabatic look-up table. A linear scaling correction is then applied to recover the correct equilibrium temperature in both adiabatic and non-adiabatic situations without changing the fresh gas temperature:

$$\widetilde{T} = \widetilde{T}^{ad}_{\widetilde{Y}_c=0} + \frac{\widetilde{T}^{\Delta h}_{\widetilde{Y}_c=\widetilde{Y}_c^{eq}} - \widetilde{T}^{ad}_{\widetilde{Y}_c=0}}{\widetilde{T}^{ad}_{\widetilde{Y}_c=\widetilde{Y}_c^{eq}} - \widetilde{T}^{ad}_{\widetilde{Y}_c=0}} \left( \widetilde{T}^{ad}_{\widetilde{Y}_c} - \widetilde{T}^{ad}_{\widetilde{Y}_c=0} \right) \tag{2.39}$$

where $\widetilde{T}^{ad}_{\widetilde{Y}_c}$ is the adiabatic temperature extracted from the filtered adiabatic look-up table as $\widetilde{T}^{ad}[\widetilde{Y}_c, \widetilde{z}, S_z, \Delta]$. $\widetilde{T}^{\Delta h}_{\widetilde{Y}_c=\widetilde{Y}_c^{eq}}$ is the non-adiabatic equilibrium temperature extracted from the non-filtered non-adiabatic database:

$$\begin{aligned}\widetilde{T}^{\Delta h}_{\widetilde{Y_c}=\widetilde{Y_c}^{eq}} &= \frac{1}{\overline{\rho}^{\Delta h}_{\widetilde{Y_c}=\widetilde{Y_c}^{eq}}} \int_0^1 \rho^{**} T^{**} \left(\widetilde{Y_c}^{eq}, z', \Delta\widetilde{h}\right) P_\beta(z') dz' \\ &= \widetilde{T}^{\Delta h}_{\widetilde{Y_c}=\widetilde{Y_c}^{eq}}[\widetilde{z}, S_z, \Delta\widetilde{h}] \end{aligned} \tag{2.40}$$

where the superscript $^{**}$ refers to a burner-stabilized non-adiabatic flamelet and $\overline{\rho}^{\Delta h}_{\widetilde{Y_c}=\widetilde{Y_c}^{eq}} = \int_0^1 \rho^{**}\left(\widetilde{Y_c}^{eq}, z', \Delta\widetilde{h}\right) P_\beta(z', \widetilde{z}, S_z) dz'$. Equation 2.39 is devised to recover the adiabatic filtered temperature $\widetilde{T} = \widetilde{T}^{ad}_{\widetilde{Y_c}}$ when the flow is adiabatic (*i.e.* when $\widetilde{T}^{\Delta h}_{\widetilde{Y_c}=\widetilde{Y_c}^{eq}} = \widetilde{T}^{ad}_{\widetilde{Y_c}=\widetilde{Y_c}^{eq}}$). This ensures that non-adiabatic F-TACLES formulation degenerates exactly towards adiabatic formulation when the flow is adiabatic.

The same strategy is used to compute the filtered term $\widetilde{rT}$, used to estimate the filtered density in the ideal gas law:

$$\overline{\rho} = \frac{\overline{p_0}}{\widetilde{rT}} \tag{2.41}$$

where the thermodynamic pressure $\overline{p_0}$ is assumed constant in the computational domain in the context of a low-Mach number assumption. $r = R/\overline{W}$, where $R$ is the ideal gas constant and $\overline{W}$ the mean molecular weight.

#### 2.3.4.4 Summary of the F-TACLES model for non-adiabatic flows

Under the low-Mach number assumption, the final LES system of equations for non-adiabatic reacting flows closed with the F-TACLES strategy reads:

$$\frac{\partial \overline{\rho}}{\partial t} + \frac{\partial}{\partial x_i}(\overline{\rho}\widetilde{u_i}) = 0 \tag{2.42}$$

$$\frac{\partial}{\partial t}(\overline{\rho}\widetilde{u_j}) + \frac{\partial}{\partial x_i}(\overline{\rho}\widetilde{u_i}\widetilde{u_j}) = -\frac{\partial \overline{p_2}}{\partial x_j} + \frac{\partial \overline{\tau_{ij}} + \overline{\tau_{ij}}^t}{\partial x_i} + \overline{\rho}\widetilde{f_j} \tag{2.43}$$

$$\begin{aligned}\frac{\partial \overline{\rho}\widetilde{Y_c}}{\partial t} + \frac{\partial}{\partial x_i}\left(\overline{\rho}\widetilde{u_i}\widetilde{Y_c}\right) &= \frac{\partial}{\partial x_i}\left(\Xi_\Delta \gamma[\widetilde{z}, S_z, \Delta\widetilde{h}]\alpha_{Y_c}^{ad}[\widetilde{Y_c}, \widetilde{z}, S_z, \Delta]\rho_0 D_0 \frac{\partial \widetilde{Y_c}}{\partial x_i}\right) \\ &+ \Xi_\Delta \gamma[\widetilde{z}, S_z, \Delta\widetilde{h}]\Omega_{Y_c}^{ad}[\widetilde{Y_c}, \widetilde{z}, S_z, \Delta] \\ &+ \Xi_\Delta \gamma[\widetilde{z}, S_z, \Delta\widetilde{h}]\overline{\rho}\widetilde{\dot{\omega}}_{Y_c}^{ad}[\widetilde{Y_c}, \widetilde{z}, S_z, \Delta]\end{aligned} \tag{2.44}$$

$$\frac{\partial \overline{\rho}\widetilde{z}}{\partial t} + \frac{\partial}{\partial x_i}\left(\overline{\rho}\widetilde{u_i}\widetilde{z}\right) = \frac{\partial}{\partial x_i}\left(\left(\overline{\rho D_{th}} + \frac{\mu_t}{S_{ct}}\right)\frac{\partial \widetilde{z}}{\partial x_i}\right) \tag{2.45}$$

$$\begin{aligned}\frac{\partial(\overline{\rho}\widetilde{z''^2})}{\partial t} + \frac{\partial}{\partial x_i}\left(\overline{\rho}\widetilde{u_i}\widetilde{z''^2}\right) &= \frac{\partial}{\partial x_i}\left(\frac{\mu_t}{S_{ct}}\frac{\partial \widetilde{z''^2}}{\partial x_i}\right) + 2\frac{\mu_t}{S_{ct}}|\nabla \widetilde{z}|^2 \\ &- 2C\frac{\mu_t}{S_{ct}\overline{\rho}\Delta_x^2}\widetilde{z''^2}\end{aligned} \tag{2.46}$$

$$\frac{\partial(\overline{\rho}\widetilde{h^{eq}})}{\partial t} + \frac{\partial}{\partial x_i}(\overline{\rho}\widetilde{u_i}\widetilde{h^{eq}}) = \frac{\partial}{\partial x_i}\left(\left(\overline{\rho D_{th}} + \frac{\mu_t}{P_{rt}}\right)\frac{\partial \widetilde{h^{eq}}}{\partial x_i}\right) \tag{2.47}$$

$$p_0 = \overline{\rho}\widetilde{rT} \tag{2.48}$$

In this system of equations:

- $\overline{\tau_{ij}}^t$ and $\mu_t$ is prescribed by the LES turbulence model.
- $\Xi_\Delta$ is estimated by the sub-filter scale wrinkling model (See Chapter 4).
- $\gamma$ corrects the filtered flame consumption speed to account for heat losses and is tabulated from a set of non-adiabatic 1-D burner-stabilized premixed flames, computed with complex modeling of diffusive fluxes.
- $\alpha_{Y_c}^{ad}$ is the progress variable diffusion factor tabulated from a set of filtered adiabatic 1-D freely-propagating premixed flames, computed with complex modeling of diffusive fluxes.
- $\Omega_{Y_c}^{ad}$ is the progress variable unresolved convective fluxes due to thermal expansion and is tabulated from a set of filtered adiabatic 1-D freely-propagating premixed flames, computed with complex modeling of diffusive fluxes.
- $\widetilde{\dot{\omega}}_{Y_c}^{ad}$ is the progress variable reaction rate, tabulated from a set of filtered adiabatic 1-D freely-propagating premixed flames and computed with complex modeling of diffusive fluxes.
- $\rho_0$ and $D_0$ are reference values, constant in time and space, chosen equal

to their values in fresh gases.
- $S_{ct}$ and $P_{rt}$ are the turbulent Schmidt and Prandtl number, respectively, assumed constant in time and space.
- $C$ is a model constant, taken equal to $C = 1$.
- $\widetilde{rT}$ is computed using the strategy described in Sec. 2.3.4.3.

The proposed extension of the F-TACLES model has been implemented in the low-Mach number code YALES2 (Moureau et al., 2011a). 1-D simulations of planar laminar non-adiabatic flames have been performed. The predicted propagation speed of the non-adiabatic flame front is consistent with Eq. 2.35 which validates the methodology and the implementation procedure when the flame is not wrinkled by the turbulence motions. A summary of the look-up tables and their stored terms is proposed in Tab 2.1 for both adiabatic and non-adiabatic formulations. Note that, for the YALES2 solver, the total retrieval cost for all the tabulated terms is less than 5% of an iteration time. When linear interpolations are used to read the tables during the LES computation, a classical discretization is 100 linearly distributed points for the $\widetilde{Y}_c$ coordinate, 100 points for the $\widetilde{z}$ coordinate with a refinement within the flammability limits, 15 points for the $S_z$ coordinate with a parabolic refinement around $S_z = 0$. A unique point for the $\Delta$ coordinate is often used when the mesh size is constant in the flame region. The discretization of $\Delta\widetilde{h}$ and $T_{bc}$ depends on the operating conditions. In this thesis, 50 points were used along both coordinates.

| Formulation | Look-up table | Stored terms |
|---|---|---|
| Adiabatic | $\Phi^{ad}[\widetilde{Y}_c, \widetilde{z}, S_z, \Delta]$ | $\alpha^{ad}_{Y_c}$, $\Omega^{ad}_{Y_c}$, $\widetilde{\dot{\omega}}^{ad}_{Y_c}$, $\widetilde{T}^{ad}$, $\widetilde{rT}^{ad}$, $\widetilde{\mu}^{ad}$, $\widetilde{Y_k}^{ad}$ |
| Non-adiabatic | $\Phi^{ad}[\widetilde{Y}_c, \widetilde{z}, S_z, \Delta]$ | $\alpha^{ad}_{Y_c}$, $\Omega^{ad}_{Y_c}$, $\widetilde{\dot{\omega}}^{ad}_{Y_c}$, $\widetilde{T}^{ad}$, $\widetilde{rT}^{ad}$, $\widetilde{\mu}^{ad}$, $\widetilde{Y_k}^{ad}$, $Y_c^{\text{raw}}$ |
| | $\Phi_1^{\Delta h}[\widetilde{z}, S_z, \Delta\widetilde{h}]$ | $\gamma$, $\widetilde{T}^{\Delta h}_{\widetilde{Y_c}=\widetilde{Y_c}^{eq}}$, $\widetilde{rT}^{\Delta h}_{\widetilde{Y_c}=\widetilde{Y_c}^{eq}}$ |
| | $\Phi_2^{\Delta h}[\widetilde{Y}_c, \widetilde{z}, T_{bc}]$ | $\widetilde{h}_{bc}$ (boundary conditions) |
| | $\Phi_3^{\Delta h}[Y_c^{\text{raw}}, \widetilde{z}, \Delta\widetilde{h}]$ | post-processing variables |

**Table 2.1:** *Summary of the look-up tables and their stored terms for both adiabatic and non-adiabatic formulations of the F-TACLES model implemented in YALES2.*

In the next chapter, the F-TACLES model is used to perform the LES computation of two different turbulent stratified flames.

# Chapter 3

# Validation of the non-adiabatic F-TACLES model on turbulent stratified flames

**Contents**

*The F-TACLES model is now able to account for sub-grid scale mixture fraction heterogeneities, heat losses and uses a thermochemical database generated using complex diffusive transport modeling. In this chapter, the influence of the different modeling strategies on complex turbulent flames is investigated. Two different generic burners, designed and measured in the framework of the TNF workshop, are considered. They mainly differ by the flame stabilization process: the first burner involves a central pilot flame while the second stabilizes the turbulent flame using a central bluff-body. Both stabilization processes are influenced by heat losses.*

## 3.1 TNF workshop: an initiative to compare experimental and numerical results on complex turbulent flames

The international workshop on measurement and computation of turbulent (non)premixed flames (TNF Workshop, 2014) is an international collaboration gathering experimental and computational research teams. The main objective of this workshop, holding every two years since 1996, is to provide advanced diagnostics results on relevant academic turbulent flames in order to test, validate and improve the turbulent combustion modeling strategies.

In the context of this thesis, two different generic burners, presented during the TNF workshop, have been selected to validate the model developments:

**TSF flame series** The Turbulent Stratified Flame (TSF) burner has been designed at Technische Universität Darmstadt (TUD). This methane-air generic burner consists of three 5 mm-staged concentric tubes placed in an air co-flow. Burnt gases exit from the central tube to stabilize the flame while inlet velocity and mixture conditions of the two other tubes can be controlled independently. This burner allows to generate turbulent flames with or without equivalence ratio stratification but also with and without shear between the two injected streams leading to a set of 11 different operating conditions. Several experimental studies characterized the flow (Seffrin et al., 2010) and thermochemical (Böhm et al., 2011) features of this flame series. Different turbulent combustion models have then been used to simulate this flame in an LES framework (Roux and Pitsch, 2010; Kuenne et al., 2012; Ketelheun et al., 2013; Mercier et al., 2013a; Trisjono et al., 2014; Mercier et al., 2014; Marincola et al., 2013). It is also worth noting that the LES computation results of the different research teams have been quantitatively compared by Fiorina et al. (2015a)

**SwB flame series** The Cambridge stratified swirl burner (SwB) has been de-

signed at Cambridge University. It consists in two concentric tubes surrounding a central bluff-body. As for the TSF burner, both the equivalence ratio and the velocity of the two injected streams can be controlled independently. This burner also allows to add rotational momentum to the outer stream thanks to a swirl injector. The different combinations of the burner parameters lead to a set of 16 different operating conditions. Albeit recent, the SwB flame series have been widely investigated experimentally (Sweeney et al., 2011b; Barlow et al., 2012; Sweeney et al., 2013, 2012a,b; Zhou et al., 2013; Euler et al., 2014). As for the TSF burner, some research teams involved in the TNF workshop have conducted numerical investigations on this burner (Nambully et al., 2014a,b; Katta and Roquemore, 2013; Mercier et al., 2013b, 2015b; Proch and Kempf, 2014).

In the following sections, the LES of the TSF and SwB burners are presented taking a particular care to the analysis of the contributions of both heat losses and differential diffusion sub-models.

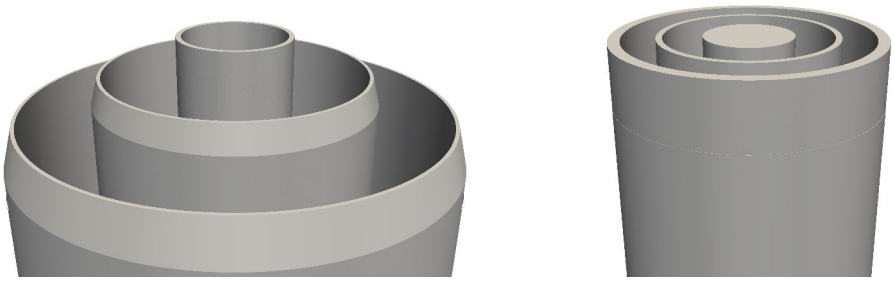

(a) TSF Burner (b) SwB Burner

**Figure 3.1:** *Schematic view of the TSF and SwB burners. Common length scales are used to ease the comparison of burner sizes.*

## 3.2 LES of the Darmstadt Turbulent Stratified Flame TSF-A

The non-adiabatic F-TACLES model is now used to simulate the Turbulent Stratified Flame A (TSF-A). This section first describes the TSF experimental configuration and provides details on the boundary conditions and computational domain of the numerical simulation. LES results are then discussed regarding experimental measurements.

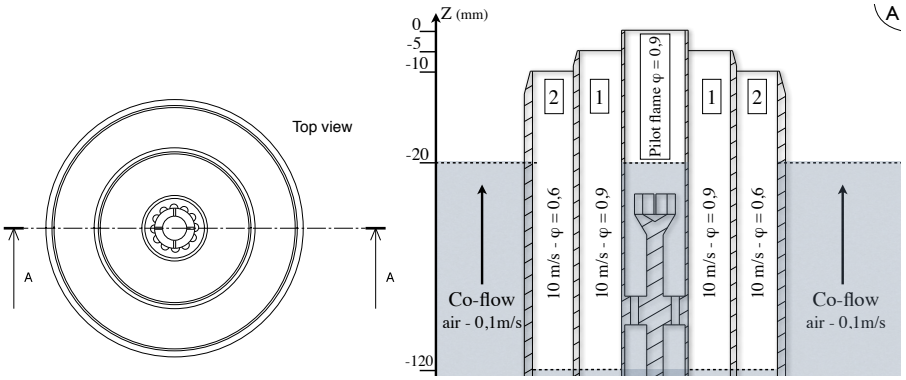


**Figure 3.2:** *Longitudinal cut of the TSF Burner. The indicated inlet conditions correspond to the case TSF-A. The white area indicates the computational domain.*

### 3.2.1 Experimental configuration

The unconfined TSF $CH_4$-air generic burner (Böhm et al., 2011; Seffrin et al., 2010) consists of three 5 mm-staged concentric tubes placed in a 0.1 m.s$^{-1}$ air co-flow. A schematic of the burner is shown in Fig. 3.2 and a detailed description of the tubes dimensions is provided in Tab. 3.1.

One TSF case is investigated in this thesis. In order to ease the results interpretation, it has been chosen to first focus on a flame without shear between both tubes. Inlet velocity and mixture conditions are indicated in Tab. 3.2 for the considered case TSF-A. Burnt gases exit from the central tube to stabilize the flame. Pilot, first and second tubes are denoted by subscripts $p$, *1* and *2* respectively. Equivalence ratio $\phi$ and Reynolds numbers $Re$ are indicated for both non-reacting case TSF-A-i1 with pilot flame burning only and reacting case TSF-A-r. Bulk velocities $v = \dot{m}/(\rho^f \cdot A^{exit})$ computed from fresh gas density $\rho^f$ and exit area of each tube $A^{exit}$ are also indicated.

| | Pilot tube | Tube 1 | Tube 2 |
|---|---|---|---|
| Inner diameter | 14.8 mm | 37 mm | 60 mm |
| Hydraulic diameter | 14.8 mm | 20 mm | 20 mm |
| Tube exit position | Z = 0 mm | Z = -5 mm | Z = -10 mm |
| Tube thickness | 0.75 mm | 1.5 mm | 2 mm |
| Chamfer angle | 0° | 15° | 15° |
| Tube lip thickness | 0.75 mm | 0.5 mm | 0.5 mm |

**Table 3.1:** *Geometrical characteristics of the TSF generic burner.*

| Case | $\phi_p$ | $v_p$ (m.s$^{-1}$) | $\phi_1$ | $v_1$ (m.s$^{-1}$) | $Re_1$ | $\phi_2$ | $v_2$ (m.s$^{-1}$) | $Re_2$ |
|---|---|---|---|---|---|---|---|---|
| TSF-A-i1 | 0.9 | 1 | 0 | 10 | 13 800 | 0 | 10 | 13 300 |
| TSF-A-r | 0.9 | 1 | 0.9 | 10 | 13 800 | 0.6 | 10 | 13 300 |

**Table 3.2:** *TSF-A operating conditions for both reacting and pilot burning only cases.*

### 3.2.2 Numerical set-up

#### 3.2.2.1 LES solver and filtered database generation

The low Mach numbers encountered in the TSF-A flame ($M \approx 0.03$) allows using the low-Mach number code YALES2 (Moureau et al., 2011a) to perform the computation. A tetrahedral mesh of 5.4 million nodes has been designed. The mean cell size in the flame region is about 1.1 mm, corresponding to 4 times the laminar flame reaction thickness[1] $\delta_r$ and 1.5 times the thermal thickness[2] $\delta_l$ . A F-TACLES look-up table is generated from a collection of methane-air laminar flames. The F-TACLES filter width is set to $\Delta = 5.8$ mm. It corresponds to a ratio $\Delta/\delta_r \approx 15$ and is representative of realistic industrial burners LES where this ratio typically varies between 5 and 20 (Boileau et al., 2008). Figure 3.3 shows the resulting computational domain and mesh size repartition in a longitudinal plane.

A centered fourth-order finite volume scheme is used for spatial discretization. Time integration of convective terms is performed explicitly using the TRK4 fourth-order scheme characterized by Kraushaar (2011). Closure of Reynolds stresses is performed both using the WALE model (Nicoud and Ducros, 1999) and the Smagorinsky (1963) approach with a dynamic estimation of the model coefficient (Germano et al., 1991; Lilly, 1992).

As the objective of the TSF-A computations is to challenge first the new developments of F-TACLES (heat losses and differential diffusion), a single model is retained for the sub-filter scale winkling $\Xi_\Delta$. The influence of the different submodels for $\Xi_\Delta$ on the mean flame brush will be extensively discussed in chapter 4. In this chapter, $\Xi_\Delta^{Y_c}$ is estimated using the model proposed by Charlette et al. (2002a) with improvements proposed by Wang et al. (2011):

$$\Xi_\Delta^{Y_c} = \left(1 + \min\left[\frac{\Delta}{\delta_l^0} - 1, \Gamma_\Delta\left(\frac{\Delta}{\delta_l^0}, \frac{u'_\Delta}{S_l^0}, Re_\Delta\right)\frac{u'_\Delta}{S_l^0}\right]\right)^\beta \tag{3.1}$$

[1] The flame reaction thickness $\delta_r$ is estimated from the half-height width of the progress variable reaction rate $\dot{\omega}_{Y_c}$.

[2] The thermal thickness $\delta_l$ is estimated from $\delta_l = (T^b - T^u)/\max(\mathrm{d}T/\mathrm{d}x^*)$ where $T^u$ and $T^b$ are the temperatures of unburnt and burnt gases, respectively, taken from an adiabatic 1-D premixed flame.

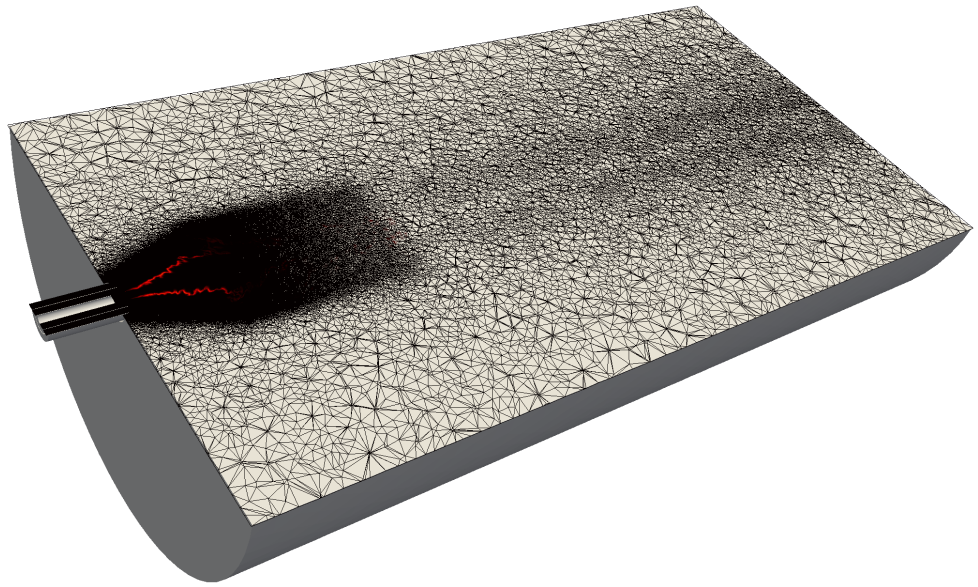

(a) Whole computational domain

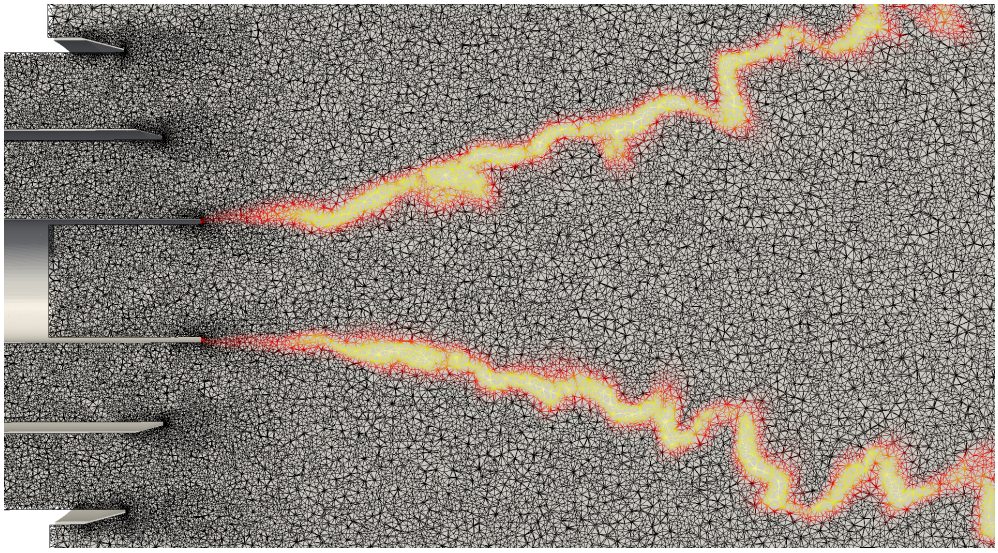

(b) Near flame region

**Figure 3.3:** *Half portion of the TSF-A computational domain. A longitudinal cut of the mesh is shown and colored by the filtered progress variable reaction rate* $\widetilde{\dot{\omega}}_{Y_c}$*. The mesh is refined within the injection tubes* ($\Delta_x \approx 0.5$ *mm) and the flame region* ($\Delta_x \approx 1.0$ *mm). In those regions, the characteristic mesh size is* $\Delta_x = 0.5$ *mm for the coarse grid.*

where the efficiency function $\Gamma_\Delta$ takes into account the net straining effect of all relevant turbulent scales smaller than $\Delta$. $Re_\Delta$ and $u'_\Delta$ are the subgrid scale Reynolds number and velocity fluctuations, respectively, while $\delta_l^0$ is the laminar flame thickness. The empirical $\beta$ parameter is set to $\beta = 0.5$ for the TSF-A flame computations. The influence of $\beta$ on the mean flame brush will be also investigated in chapter 4.

Chemical look-up tables are computed with REGATH thermochemistry package developed at the EM2C laboratory (Pons et al., 2009; Candel et al., 2011) and employing the Lindstedt (1997) detailed chemical scheme for $CH_4$-Air without accounting for the NOx chemistry leading to 29 species and 141 reactions.

As the focus is made on the impact of heat losses on the flame propagation, their effects on the species mass fractions are neglected in this chapter. This assumption will be justified *a posteriori* in Sec. 3.2.4.3. Therefore, the species mass fractions are directly extracted from the adiabatic filtered database as $\widetilde{Y}_k^{ad}[\widetilde{Y}_c, \widetilde{z}, S_z, \Delta]$ in both adiabatic and non-adiabatic computations.

#### 3.2.2.2 Modeling issues for mixture fraction FDF

A specific mixture fraction FDF modeling strategy is adopted for the TU Darmstadt stratified flame configuration where four streams are involved. Pilot ($\phi = 0.9$), stream 1 ($\phi = 0.9$), stream 2 ($\phi = 0.6$) and air ($\phi = 0$) locations are indicated in Fig. 3.2. As stream 1 and pilot correspond to the same equivalence ratio, three different mixture fraction streams are injected in the computational domain. The mixture fractions $z$ for pilot-stream 1 ($\phi = 0.9$), stream 2 ($\phi = 0.6$) and air co-flow ($\phi = 0$), are based on the richest and leanest streams:

$$
\begin{aligned}
z_p = z_1 = \frac{Y_{N_2}^f(\phi=0.9) - Y_{N_2}^f(\phi=0)}{Y_{N_2}^f(\phi=0.9) - Y_{N_2}^f(\phi=0)} &= 1 \\
z_2 = \frac{Y_{N_2}^f(\phi=0.6) - Y_{N_2}^f(\phi=0)}{Y_{N_2}^f(\phi=0.9) - Y_{N_2}^f(\phi=0)} &= 0.6780 \\
z_{cf} = \frac{Y_{N_2}^f(\phi=0) - Y_{N_2}^f(\phi=0)}{Y_{N_2}^f(\phi=0.9) - Y_{N_2}^f(\phi=0)} &= 0
\end{aligned}
$$

Considering the geometry of the burner, a direct mixing between air and stream 1-pilot never occurs. Then, the modeling strategy for the mixture fraction FDF depends whether mixing occurs between stream 1-pilot and stream 2 or between stream 2 and air. The air co-flow stream mainly dilutes the burnt gases without impacting the reaction zone. Therefore the effects of sub-grid scale mixture fraction heterogeneities on reaction zone are neglected between air co-flow and stream 2 (when $0 < \widetilde{z} < z_2$). However, they are considered between stream

1-pilot and stream 2 (when $z_2 < \widetilde{z} < 1$) using a $\beta$-function as mentioned in Sections 1.5.2.4 and 2.3. The FDF of mixture fraction $\overline{P}(z')$ is therefore estimated as follows:

- when $0 < \widetilde{z} < z_2$:
$$\overline{P}(z') \approx \delta(\widetilde{z} - z') \tag{3.2}$$
- when $z_2 < \widetilde{z} < 1$:
$$\overline{P}(z') \approx \begin{cases} 0 & \text{when } 0 < z' < z_2 \\ \frac{1}{1-z_2} \frac{(\zeta)^{a-1}(1-\zeta)^{b-1}}{\int_0^1 (\zeta^*)^{a-1}(1-\zeta^*)^{b-1} d\zeta^*} & \text{when } z_2 < z' < 1 \end{cases} \tag{3.3}$$

where

$$\zeta = \frac{z' - z_2}{1 - z_2} \tag{3.4}$$

$$a = \widetilde{\zeta}\left(\frac{\widetilde{\zeta}(1-\widetilde{\zeta})}{\widetilde{\zeta''^2}} - 1\right) \tag{3.5}$$

$$b = a\left(\frac{1}{\widetilde{\zeta}} - 1\right) \tag{3.6}$$

#### 3.2.2.3 Velocity boundary conditions

The white area shown in Fig. 3.2 indicates the computational domain. Turbulence generator, flame holder and premixed pilot flame are not simulated. Reference position ($Z = 0$ mm) in the burner symmetry axis is set at the exit plane of pilot tube. Flow field starts from $Z = -120$ mm for tubes 1 and 2 while pilot tube injection plane is located at $Z = -20$ mm. The flow is injected through the burner into an unconfined domain modeled by a 1520 mm long cylinder, starting at $Z = -20$ mm and ending at $Z = 1500$ mm with a diameter of 800 mm. The mean velocities prescribed as inlet conditions are issued from the numerical simulation of the flow within the burner performed by Kuenne et al. (2012). Homogeneous and isotropic turbulence (HIT), generated from a Passot and Pouquet (1987) spectrum, is injected in the three tubes and adjusted to match fluctuating velocities profiles measured at $Z = 1$ mm in the non-reacting case TSF-A-i1. For both adiabatic and non-adiabatic cases, injected velocity profiles are adjusted so that mean mass flow rates match experimental data detailed in Tab. 3.2.

#### 3.2.2.4 Thermal boundary conditions

The value of the pilot tube wall temperature has been estimated from balancing heat exchange between the wall and the flow passing in both tube 1 and pilot. For that purpose, a RANS 2D-axisymmetric computation of the fluid flow inside the burner coupled with conductive heat transfer within the burner wall (between pilot and slot 1) has been conducted with Fluent software (ANSYS® Fluent, 2009). Computational domain has been defined from $Z = -30$ mm (pilot flame location) to $Z = 10$ mm (downstream the pilot exit). It includes

both pilot and tube 1 flows separated by the pilot tube wall. Both fluid and solid domains are discretized with a 200 000 nodes mesh. Burnt gases are injected at the inlet of pilot tube section at the adiabatic temperature of 2132 K without turbulence. Fresh gases are injected at the inlet of tube 1 at a temperature of 298 K with a turbulence intensity of 5% which is a typical value for fully developed velocity profile. An isothermal condition of 298 K is set at the bottom boundary of the pilot tube wall ($Z = -30$ mm) for which physical and thermal properties have been chosen from classical ceramic (porcelain).

Results obtained from this simulation predict heat exchange between stream 1 and pilot stream and also mean temperature distribution in both fluid and solid parts. Figure 3.4 shows the temperature field obtained in the RANS computational domain. Due to the small thickness of the wall, its temperature is found homogeneous and equal to 750 K. This value is found to be weakly dependent on the prescribed temperature at the bottom boundary of the pilot tube wall. Thermal boundary layer is thick within the pilot tube while it seems to be very thin on fresh gas side. This is due to density and mass flow differences between both streams and has been validated experimentally by near-wall thermocouple temperature measurements in Seffrin et al. (2010). Therefore enthalpy rise in the tube 1 is neglected and not considered here.

The temperature prediction obtained with the RANS computation is still above experimental measurements. Figure 3.4 shows that temperature value at the pilot tube exit remains mostly equal to the adiabatic temperature while measurements show that axial temperature is between 1850K and 2000K. An additional heat exchange, probably radiative heat losses, holds within the pilot tube but is not captured by the present approach. In order to ensure relevant comparisons with experiments, the measured temperature profile at $Z = 15$ mm is selected as a reference profile to be fitted by simulation. For that purpose, temperature of burnt gas at the injection plate of the pilot tube is set constant to $T_p^{\text{inlet}} = 2000$ K and inner walls temperature is also set constant to $T_p^{\text{wall}} = 750$ K to match the reference experimental profile.

### 3.2.3 Simulated cases

Two simulations are first conducted to study the results sensitivity to the numerical parameters (turbulence model and mesh resolution). Five simulations are then performed to discriminate the individual and combined effects of both differential diffusion and heat losses modeling. All the results are compared to the experimental data. Table 3.3 gives details about the different simulated cases.

In the adiabatic simulations, both burner walls and pilot stream are assumed adiabatic. Heat losses are not considered meaning that $\gamma$ correction factor is

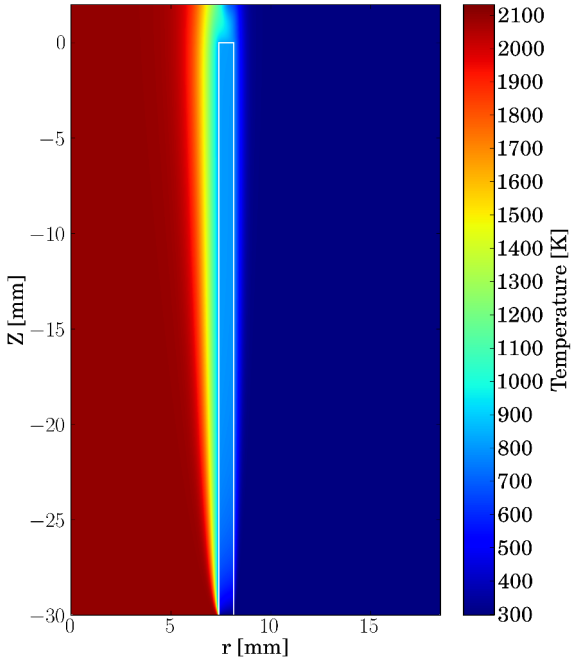


**Figure 3.4:** *Temperature field of the RANS 2D-axisymmetric computation. Heat exchange on both fluid and solid domains are resolved.*

| Simu. # | Characteristic mesh size $\Delta_x$ | Turbulence model | Pilot inner wall temp. $T_p^{wall}$ | Pilot inlet temp. $T_p^{inlet}$ | Flamelet diffusion model | 1 FTT cost [CPU hour] |
|---|---|---|---|---|---|---|
| 1 | 1.1 mm | WALE | Adiabatic | Adiabatic | Hirschfelder et al. | 17 800 |
| 1-m | 0.6 mm | WALE | Adiabatic | Adiabatic | Hirschfelder et al. | 205 000 |
| 1-t | 1.1 mm | Dyn. Sma. | Adiabatic | Adiabatic | Hirschfelder et al. | 16 100 |
| 2 | 1.1 mm | WALE | Adiabatic | Adiabatic | Le = 1 | 19 500 |
| 3 | 1.1 mm | WALE | 750 K | 2000 K | Le = 1 | 21 600 |
| 4 | 1.1 mm | WALE | 750 K | 2000 K | Hirschfelder et al. | 19 500 |
| 5 | 1.1 mm | WALE | 550 K | 2000 K | Hirschfelder et al. | 19 500 |

**Table 3.3:** *Table of simulated cases. The flow-through-time (FTT) is estimated as* $FTT = L/v = 20$ *ms with* $L = 0.2$ *m the height of the reaction zone and* $v = 10$ $m.s^{-1}$ *the bulk velocity of both tubes 1 and 2. All the listed simulations are performed on the reacting case TSF-A-r with a constant flame filter size* $\Delta = 5.8$ *mm. These computations are conducted on an IBM Blue Gene/Q machine on 1024 cores.*

set to $\gamma = 1$ and that only adiabatic table is accessed during the simulation. Simulations 1 and 2 aim to compare the influence of the diffusive transport modeling assumption during the chemical database generation. Simulation 1 uses the Hirschfelder et al. (1969) model while simulation 2 assumes a unity Lewis number for all the chemical species. Simulation 1-m allows a mesh sensitivity analysis while the objective of the simulation 1-t is to evaluate the results sensitivity to the SGS turbulence model.

Three non-adiabatic LES are performed. As mentioned in Sec. 3.2.2.4, a constant temperature $T_p^{\text{inlet}} = 2000$ K is imposed at the inlet of the pilot stream and the inner wall of this tube is assumed to be isothermal with $T_p^{\text{wall}} = 750$ K while other walls are adiabatic. Simulations 3 and 4 are similar to simulations 1 and 2, respectively, except that heat losses are accounted for. Since no experimental measurements are available to validate the estimated temperature $T_p^{\text{wall}}$, an extra simulation (Simu. 5) has been performed with $T_p^{\text{wall}} = 550K$ in order to evaluate results sensitivity to this parameter.

Flow statistics are obtained by azimuthal and time averaging instantaneous solutions following recommendations by Veynante and Knikker (2006) over a physical time corresponding to 10 flow-through-times based on the pilot stream velocity. This statistics accumulation is started after a 5 flow-through-times period to ensure that the steady state is reached.

### 3.2.4 Results analysis

#### 3.2.4.1 Sensitivity to numerical and flow modeling parameters

The objective of this section is first to identify the results sensitivity to the mesh refinement level. For that purpose, the simulation of TSF-A-r configuration is performed under adiabatic assumption on two different grids. As

detailed in Tab. 3.3, the grid spacing in the flame region are $\Delta_x = 1.1$ mm for the simulation 1 and $\Delta_x = 0.6$ mm for the simulation 1-m. Mean velocity field and temperature fields predicted by both simulations are compared with experimental data in Fig. 3.5. As little differences are observed, the coarser grid ($\Delta_x = 1.1$ mm) is well-suited to the present configuration and selected for the simulation 2 to 5 listed in Tab. 3.3.

Secondly, the simulation 1-t is performed with the same parameters than simulation 1 but using localized dynamic Smagorinsky's model (Smagorinsky, 1963; Germano et al., 1991; Lilly, 1992) instead of WALE model (Nicoud and Ducros, 1999) to close the unresolved Reynolds stresses. The results are also plotted in Fig. 3.5 and show that the mean flow and temperature fields are weakly dependent from the SGS turbulence modeling assumption.
To conclude, simulations results weakly depend on the mesh parameters and SGS turbulence model. The following results analysis will then focus on the impact of the LES turbulent combustion model.

#### 3.2.4.2 Impact of heat losses on the burner flow field

All the large eddy simulations introduced in Sec. 3.2.3 have been performed with identical inlet mass flow rates as detailed in 3.2.2.3. However density fields within the pilot tube are significantly different whether heat losses are considered or not. This is particularly visible on Fig. 3.6 where mean axial velocity $U_z$ within the burner is plotted for both adiabatic and non-adiabatic reacting cases (TSF-A-r). These results are compared to experimental profiles extracted from the non-reacting case TSF-A-i1 where only the pilot flame is burning while pure air is injected into tubes 1 and 2. LES mean profiles slightly differs at the injection plane ($Z = -20$ mm) because a lower inlet temperature is prescribed in the non-adiabatic computation. This gap increases along the burner axis because of the misprediction of thermal boundary layer in the adiabatic case. Comparison with experiments at $Z = 1$ mm, for $0$ mm $< r < 8$ mm, clearly shows that axial velocity profiles are overestimated by around 2 m.s$^{-1}$ when heat losses are neglected. This illustrates the impact of heat losses on predicted flow field through the local modification of density within thermal boundary layer. Figure 3.6 plots the RMS axial velocity within the burner and shows that turbulence at the exit of tubes 1 and 2 is well developed and also in agreement with experimental data from the case TSF-A-i1.

Mean axial and radial components of the velocity field downstream the burner for the fully reacting case TSF-A-r are shown in Figs. 3.7 and 3.8 as a function of the radial distance at six axial positions ($Z = 50$, 75, 100, 125, 150 and 200 mm). Corresponding RMS of velocity are plotted in Figs. 3.9 and 3.10. In adiabatic case, the flow field prediction fairly agrees with the experimental data except for the mean axial velocity (Fig. 3.7) at the center line of the

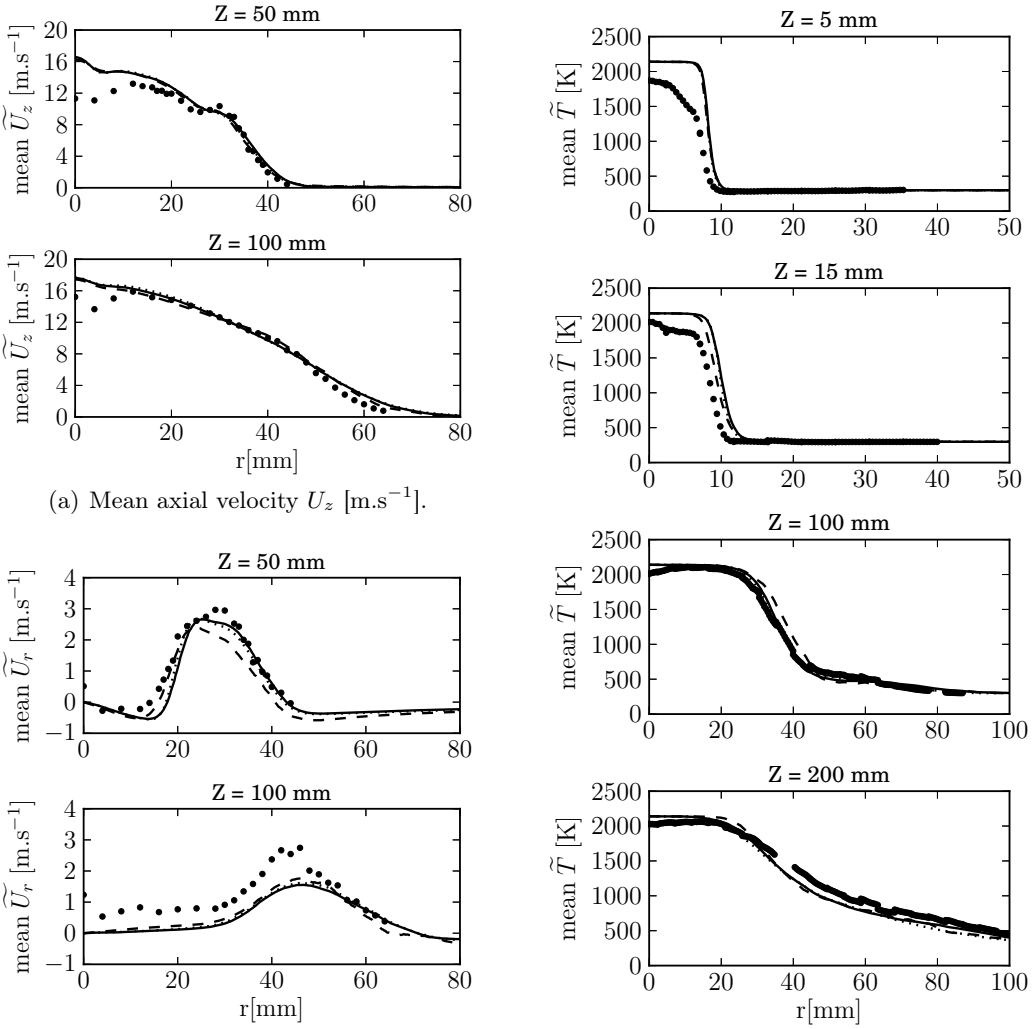


(a) Mean axial velocity $U_z$ [m.s$^{-1}$].

(b) Mean temperature T [K].

(c) Mean radial velocity $U_r$ [m.s$^{-1}$].

**Figure 3.5:** *Sensitivity to numerical and flow modeling parameters. Mean velocity and temperature fields for two different mesh grids ($\Delta_x = 1.1$ / $\Delta_x = 0.6$) and two different turbulence models (WALE / Dynamic Smagorinsky).*
*Legend: —$\Delta_x = 1.1$ mm, WALE. – – $\Delta_x = 0.6$ mm, WALE. · · · $\Delta_x = 1.1$ mm, Dynamic Smagorinsky, • • TSF-A-r measurments.*

burner. This result agrees with previous adiabatic computations conducted by Kuenne et al. (2012); Marincola et al. (2013). This gap is around 4 m.s$^{-1}$ and is attributed to both the convection downstream of the pilot tube velocity overestimation and the misprediction of thermal expansion at the flame basis discussed in Sec. 3.2.4.3. As expected, the non-adiabatic simulations recover the right mean axial velocity while fluctuations profiles are not impacted by the heat losses assumption. This is also the case of mean and RMS profiles of radial

velocity where only a radial shift corresponding to a translation downstream of the mean flame brush can be noted. This point is also discussed in Sec. 3.2.4.3.

The sensitivity to the prescribed pilot wall temperature $T_p^{\text{wall}}$ is analyzed comparing simulations 4 ($T_p^{\text{wall}} = 750K$) and 5 ($T_p^{\text{wall}} = 550K$) in Fig 3.11. Results are found weakly sensitive to this imposed boundary condition. Only small differences on mean temperature profiles nearby the burner exit can be noted while mean flame brush position is not impacted.

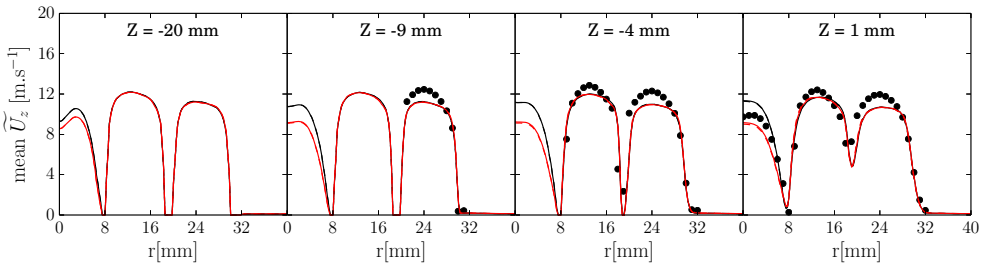


(a) Mean axial velocity $U_z$

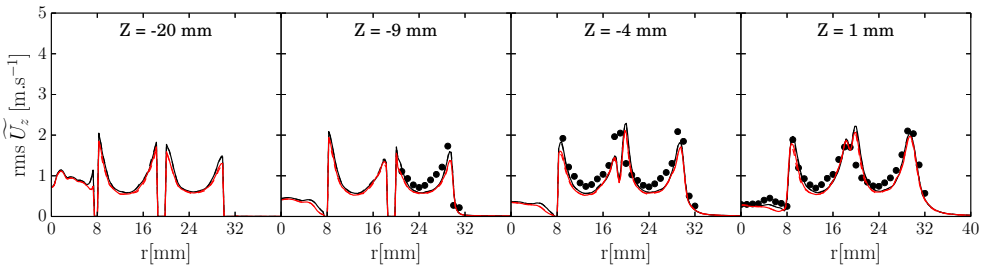


(b) RMS of axial velocity $U_z$

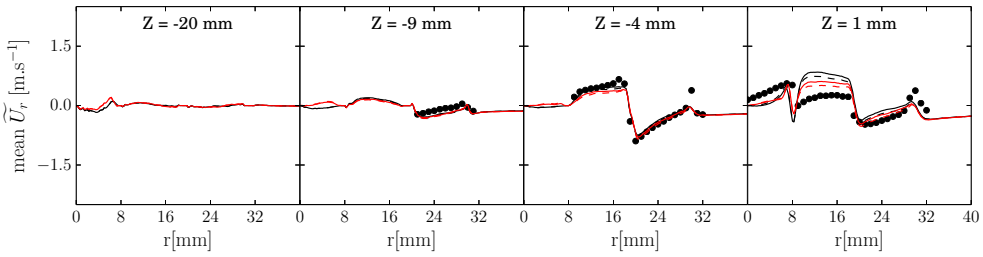


(c) Mean radial velocity $U_r$

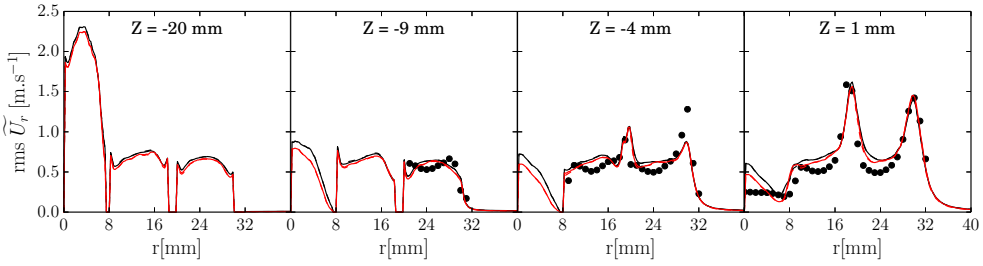


(d) RMS of radial velocity $U_r$

**Figure 3.6:** *Mean and RMS axial velocity within the burner for both adiabatic and non-adiabatic cases and both Le=1 and Hirschfelder et al. (1969) diffusion models. Legend : — Adiabatic, $Le \neq 1$. - - - Adiabatic, $Le = 1$. — Non-adiabatic, $Le \neq 1$. - - - Non-adiabatic, $Le = 1$. ● ● TSF-A-r measurments.*

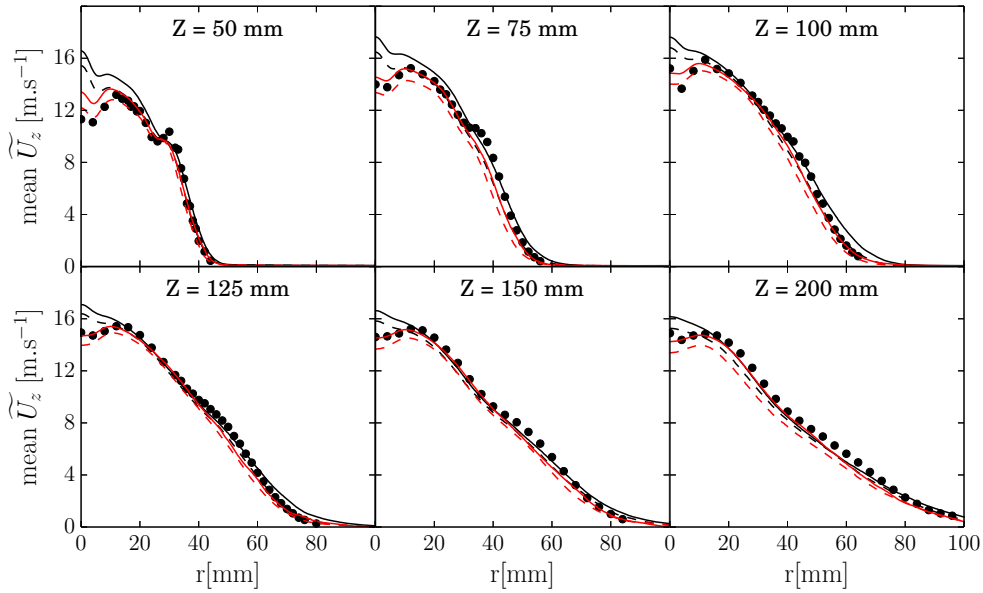


**Figure 3.7:** *Mean axial velocity at six distances Z from the pilot tube exit. Legend : — Adiabatic, Le ≠ 1. - - - Adiabatic, Le = 1. — Non-adiabatic, Le ≠ 1. - - - Non-adiabatic, Le = 1. • • TSF-A-r measurments.*

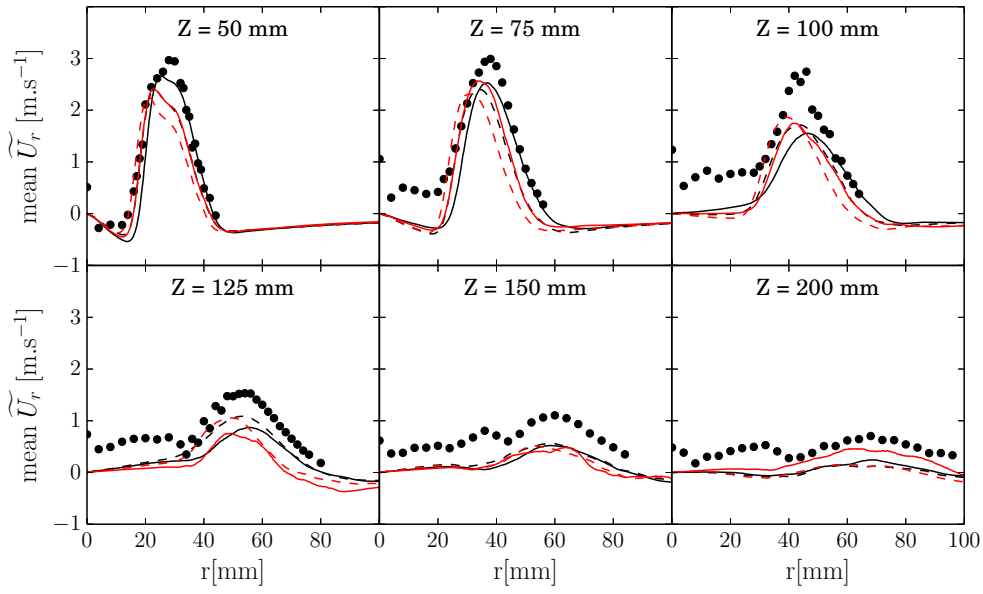


**Figure 3.8:** *Mean radial velocity at six distances Z from the pilot tube exit. Legend : — Adiabatic, Le ≠ 1. - - - Adiabatic, Le = 1. — Non-adiabatic, Le ≠ 1. - - - Non-adiabatic, Le = 1. • • TSF-A-r measurments.*

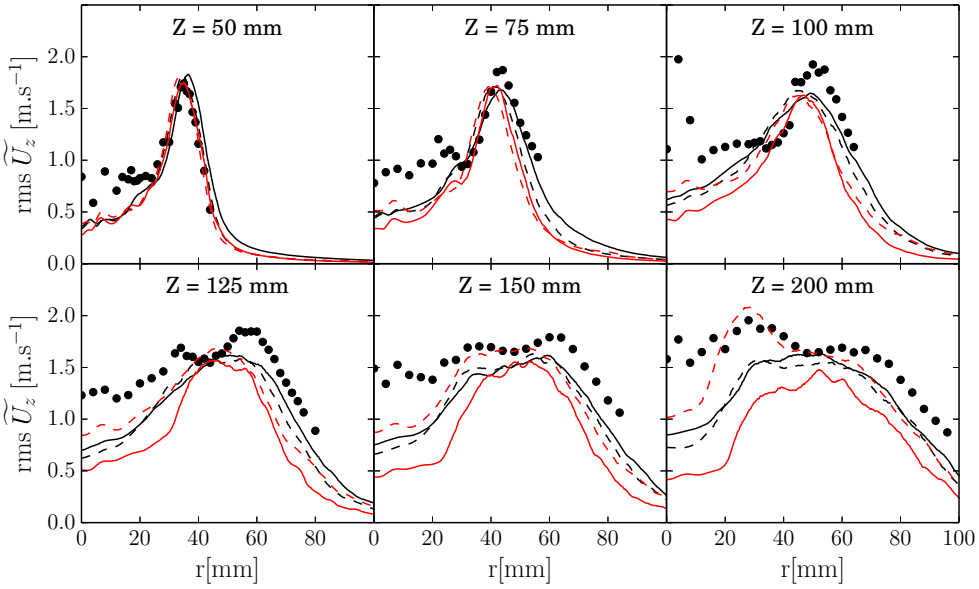


**Figure 3.9:** *RMS of axial velocity at six distances Z from the pilot tube exit. Legend : — Adiabatic, Le ≠ 1. - - - Adiabatic, Le = 1. — Non-adiabatic, Le ≠ 1. - - - Non-adiabatic, Le = 1. ● ● TSF-A-r measurments.*

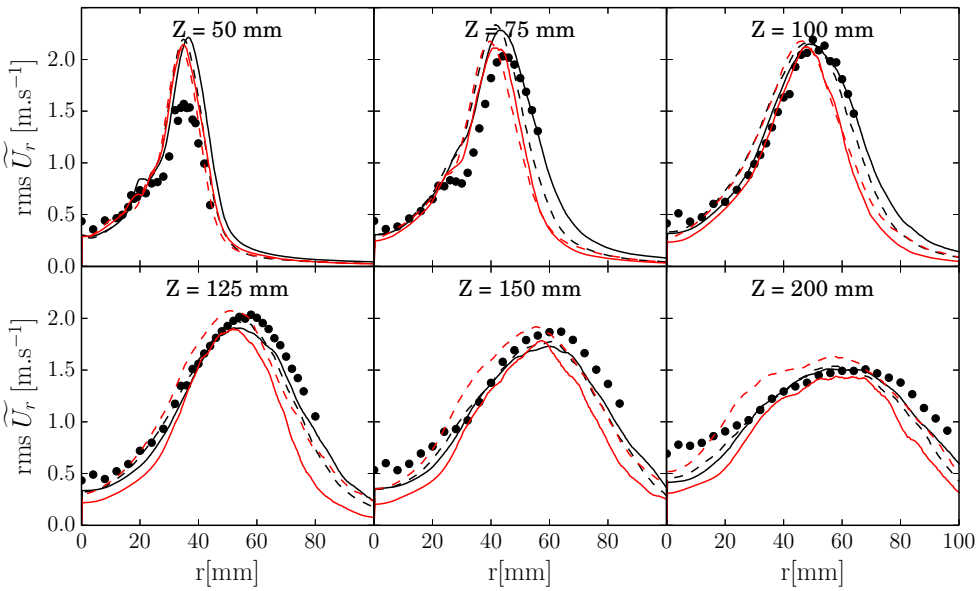


**Figure 3.10:** *RMS of radial velocity at six distances Z from the pilot tube exit. Legend : — Adiabatic, Le ≠ 1. - - - Adiabatic, Le = 1. — Non-adiabatic, Le ≠ 1. - - - Non-adiabatic, Le = 1. ● ● TSF-A-r measurments.*

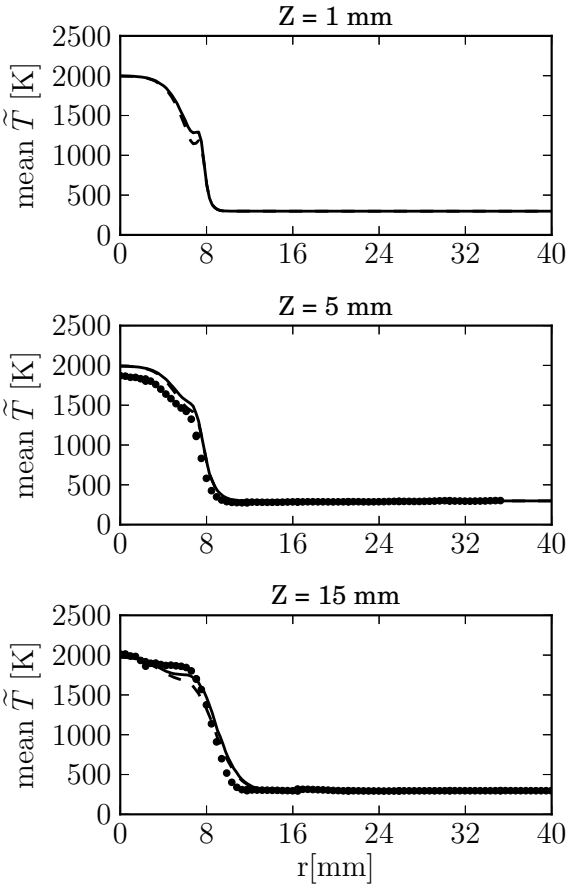


**Figure 3.11:** *Mean temperature downstream the burner exit for two different prescribed pilot wall temperatures* $T_p^{wall}$.
*Legend :* — *Non-adiabatic, Le* $\neq 1$, $T_p^{wall} = 750K$. - - - *Non-adiabatic, Le* $\neq 1$, $T_p^{wall} = 550K$. • • *TSF-A-r measurments.*

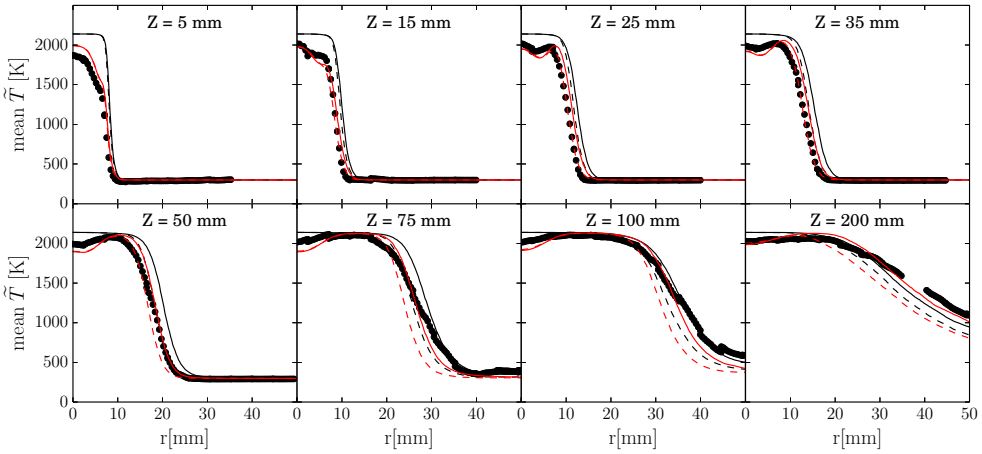


**Figure 3.12:** *Mean temperature at eight distances Z from the pilot tube exit. Legend : — Adiabatic, Le ≠ 1. - - - Adiabatic, Le = 1. — Non-adiabatic, Le ≠ 1. - - - Non-adiabatic, Le = 1. • • TSF-A-r measurments.*

### 3.2.4.3 Flame stabilization process

Mean and RMS of temperatures are now compared to experimental data in Figs. 3.12 and 3.13 at eight axial distances from the pilot exit ($Z$ = 5, 15, 25, 35, 50, 75, 100 and 200 mm). A shift of the flame front prediction compared to the measurements is observed in the adiabatic simulations. This result is consistent with adiabatic LES flame simulations previously published using Flame Surface Density (Marincola et al., 2013) and Thickened Flame (Kuenne et al., 2012) approaches, respectively. At the distances $Z = 5$ mm and $Z = 15$ mm, the numerical simulation overestimates the measured temperature of the jet by approximately 400 K to 600 K. This significant gap demonstrates that the pilot stream is cooled by the burner walls and therefore injected below the adiabatic conditions. It appears that this gap is closely linked to the effect of heat exchange within the pilot tube presented in Sec. 3.2.4.2. Inner pilot tube boundary layer is cooled by the wall resulting in a decrease of injected burnt gas enthalpy. As a consequence, non-adiabatic conditions hold at the exit of the pilot tube.

The heat loss correction factor $\gamma$ introduced in Eq. (2.33) illustrates the non-adiabaticity of the flow in this area. Figure 3.14 plots a longitudinal cut of TSF burner colored by mean value of enthalpy $\widetilde{h^{eq}}$ (right side) and correction factor $\gamma$ (left side). It shows that considering heat losses at the wall causes an important decrease of the enthalpy in the near-burner region and leads to local flame extinctions. Indeed, $\gamma = 0$ very near the burner walls and it increases continuously when going further downstream so that the flame propagation speed tends continuously to the adiabatic flame speed. Figure 3.14 also shows that

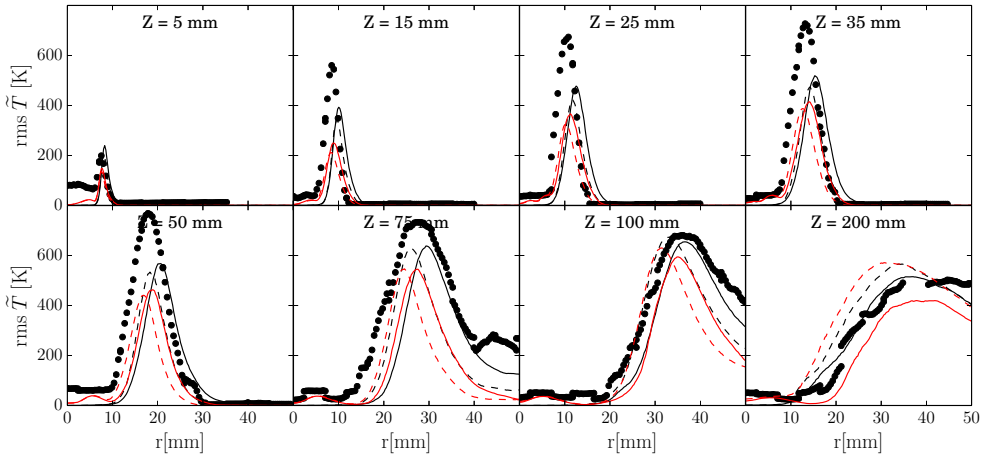


**Figure 3.13:** *RMS of temperature at eight distances Z from the pilot tube exit. Legend : — Adiabatic, Le ≠ 1. - - - Adiabatic, Le = 1. — Non-adiabatic, Le ≠ 1. - - - Non-adiabatic, Le = 1. • • TSF-A-r measurments.*

the flow is fully adiabatic far from the pilot stream. Neglecting the impact of heat losses on the species mass fractions is then reasonable everywhere except in the pilot flow near the centerline. Slight errors are therefore expected, for instance on the chemical equilibrium state, but should be located close to the pilot tube exit and vanish further downstream or far from the centerline.

Flame consumption speed at the pilot tube exit is then very low resulting in a slight translation of the mean flame front position downstream as shown in Fig. 3.15(a) where isolines of mean progress variable source term are plotted in both adiabatic and non-adiabatic cases. This phenomenon has also been observed in the experiment by direct visualization and its effect on instantaneous flame surface is shown in Fig. 3.15(b), displaying an isosurface of filtered progress variable reaction rate colored by local mixture fraction. Three different zones can be distinguished in this figure:

1. The near burner area is characterized by a very weak reaction (and then thermal expansion) zone influenced by burnt gas cooled within the pilot tube inner thermal boundary layer.
2. A turbulent premixed flame is then clearly identified between $Z = 10$ mm and $Z = 45$ mm where fresh gases issue only from tube 1.
3. In the last zone a stratified flame front is observed where equivalence ratio evolves essentially between $\phi = 0.9$ and $\phi = 0.6$, corresponding respectively to $\widetilde{z}$ =1 and $\widetilde{z}$ =0.6780 filtered mixture fractions.

Figure 3.12 shows that heat losses modeling strategy significantly improves the

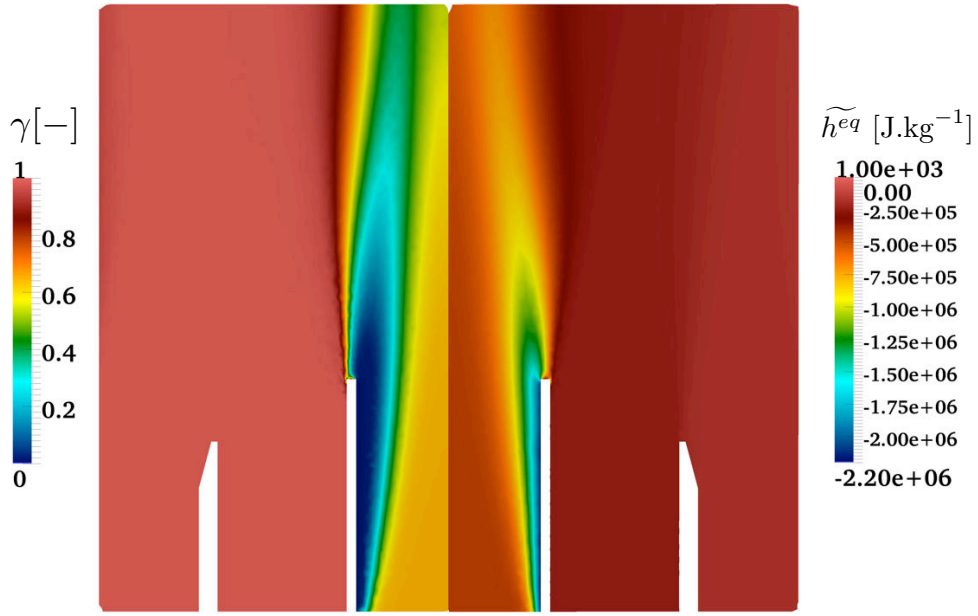


**Figure 3.14:** *2D longitudinal cut of the TSF burner colored by mean correcting factor $\gamma$ (left side) and mean filtered enthalpy $\widetilde{h}^{eq}$ (right side).*

prediction of mean temperature field. This result is in agreement with the conclusions of previous studies by Ketelheun et al. (2013); Trisjono et al. (2014). Heat losses induce a shift towards the burner axis of the RMS profiles of temperature, as shown in Fig. 3.13.

The F-TACLES model also gives an access to chemical flame structure. In this section, the chemical species are extracted from the adiabatic filtered chemtable as $\widetilde{Y_k}^{ad}$. Mean and RMS species mass fractions and mixture fraction are then compared with experimental measurements. Figures 3.16 to 3.23 show mean and RMS mass fraction of $CH_4$, $O_2$, $H_2O$ and $CO_2$ while the statistics of normalized mixture fraction are compared to experimental values in Figs. 3.24 and 3.25. The shift noted for mean temperature profiles is confirmed by the results obtained for chemical species. Both temperature and species mass fractions amplitudes of resolved RMS remain lower than measured RMS. These differences are expected as LES RMS does not include the SGS contribution. Therefore, a conclusion regarding the model ability to capture scalar fluctuations is difficult. The estimation of unresolved scalar RMS remains an issue and would require a model, for example for the SGS Filtered Density Function $P(Y_k)$ (Veynante and Knikker, 2006), which is out of the scope of the present study.

Another physical phenomenon, neglected here, may be associated to heat losses to control flame lift-off process. Heat diffusion from burnt gases to fresh gases

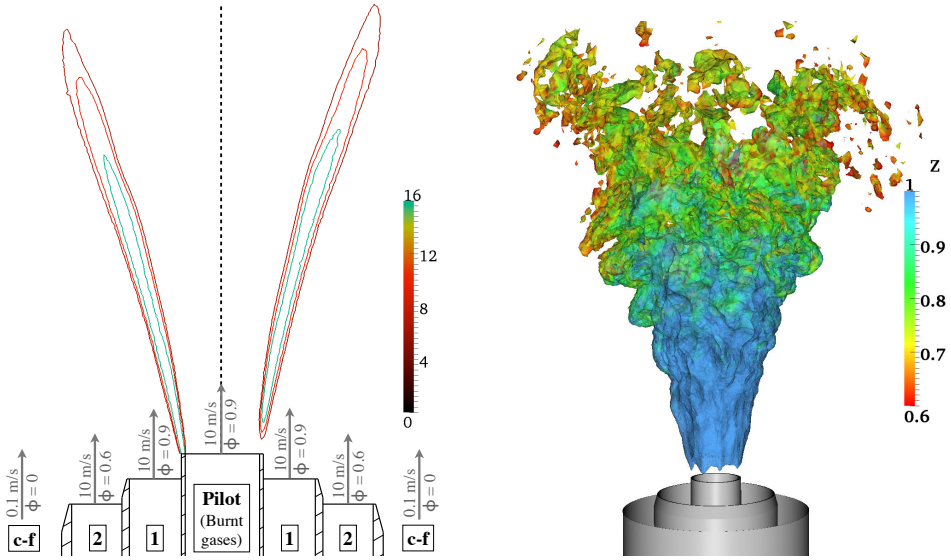


(a) Isolines of mean filtered reaction rate $\widetilde{\overline{\rho}\dot{\omega}_{Y_c}}$ [kg.s$^{-1}$.m$^{-3}$] for adiabatic (left) and non-adiabatic (right) simulations. Injected bulk velocities and equivalence ratio are detailed for each tubes and co-flow.

(b) Instantaneous iso-surface of reaction rate $\widetilde{\overline{\rho}\dot{\omega}_{Y_c}} = 10$ kg.s$^{-1}$.m$^{-3}$ colored by normalized filtered mixture fraction $\widetilde{z}$ for non-adiabatic simulation.

**Figure 3.15:** *Visualizations of mean and instantaneous reaction rate for both adiabatic and non-adiabatic simulations.*

and ignition time scales at the exit of the pilot tube might not be negligible compare to convective time scales. Therefore, transient ignition of the fresh gases may also play a role on the weak reaction zone identified at the vicinity of the pilot tube lip. Simple one-dimensional direct numerical simulations have shown that characteristic time of ignition at fresh/burnt gas interface (*i.e.* at the interface located over pilot tube lips) was associated to a lift-off height smaller than the measurements by one order of magnitude. This analysis seems to indicate that transient ignition phenomena are not governing the flame stabilization process which is more influenced by the local enthalpy defect.

#### 3.2.4.4 Effect of differential diffusion

Differential diffusion is accounted through the filtering and the tabulation of flamelets computed with complex transport models. This formalism has been derived assuming that the internal structure of the flame in the turbulent flow is similar to the structure of a monodimensional unstretched laminar flame. Therefore, this formalism reproduces the effect of differential diffusion of the chemical species in the direction normal to the flame front. As stated in Sec. 2.2.1, differential diffusion effects in other directions or in interaction with the turbulence is not considered here.

Because of low axial velocities encountered in the TSF-A configuration, the flame position is found to be very sensitive to the prediction of laminar flame speed by the combustion model. As shown in Fig. 2.2, accounting for differential diffusion can significantly modify the predicted laminar flame speed. Mean and RMS temperature profiles plotted in Fig. 3.12 and 3.13 and mean and RMS species mass fractions plotted in Fig. 3.16 to 3.23 show that accounting for complex transport normal to the flame front significantly modifies the mean flame brush angle. Radial profiles located near the burner exit ($Z = 5$ mm and $Z = 15$ mm) do not show differences because flame basis location is not modified by the differential diffusion assumption but is more governed by aerodynamics behind the pilot tube lip. However, further downstream profiles show increasing gaps when distance to the burner exit increases. It can be noted that temperature and species profiles predicted by simulations 1 and 4 between $Z = 25$ mm and $Z = 50$ mm are very close because of the counteraction of heat losses on mean flame position and differential diffusion on mean flame angle. This is not the case from $Z = 75$ mm to $Z = 200$ mm where simulation 1 (unity Lewis number assumption) shows an important misprediction of mean flame brush by underestimating laminar consumption speed and then mean flame angle.

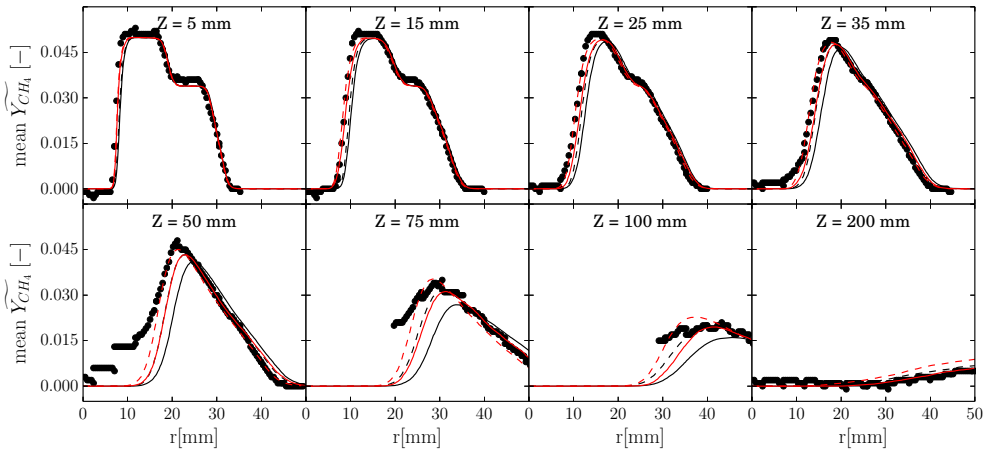


**Figure 3.16:** *Mean $CH_4$ mass fraction at eight distances Z from the pilot tube exit. Legend : — Adiabatic, $Le \neq 1$. - - - Adiabatic, $Le = 1$. — Non-adiabatic, $Le \neq 1$. - - - Non-adiabatic, $Le = 1$. • • TSF-A-r measurments.*

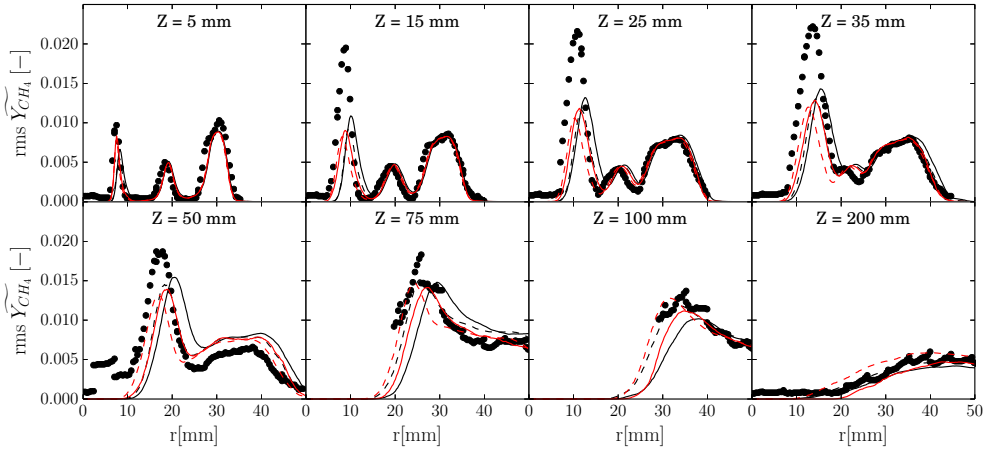


**Figure 3.17:** *RMS of $CH_4$ mass fraction at eight distances Z from the pilot tube exit. Legend : — Adiabatic, $Le \neq 1$. - - - Adiabatic, $Le = 1$. — Non-adiabatic, $Le \neq 1$. - - - Non-adiabatic, $Le = 1$. • • TSF-A-r measurments.*

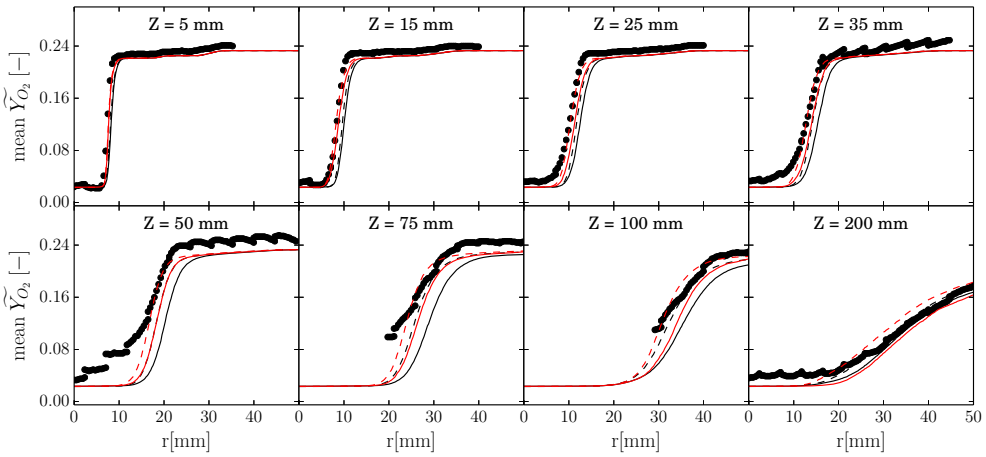


**Figure 3.18:** *Mean $O_2$ mass fraction at eight distances Z from the pilot tube exit. Legend : — Adiabatic, $Le \neq 1$. - - - Adiabatic, $Le = 1$. — Non-adiabatic, $Le \neq 1$. - - - Non-adiabatic, $Le = 1$. • • TSF-A-r measurments.*

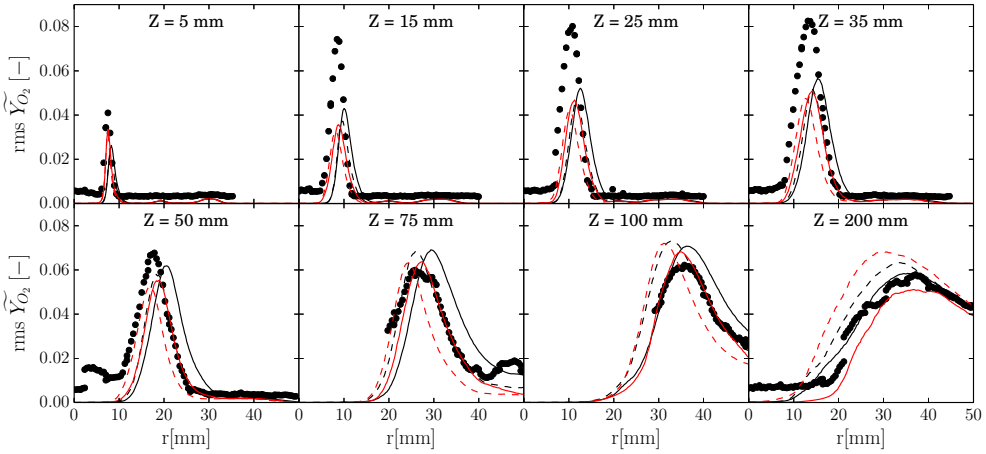


**Figure 3.19:** *RMS of $O_2$ mass fraction at eight distances Z from the pilot tube exit. Legend : — Adiabatic, $Le \neq 1$. - - - Adiabatic, $Le = 1$. — Non-adiabatic, $Le \neq 1$. - - - Non-adiabatic, $Le = 1$. • • TSF-A-r measurments.*

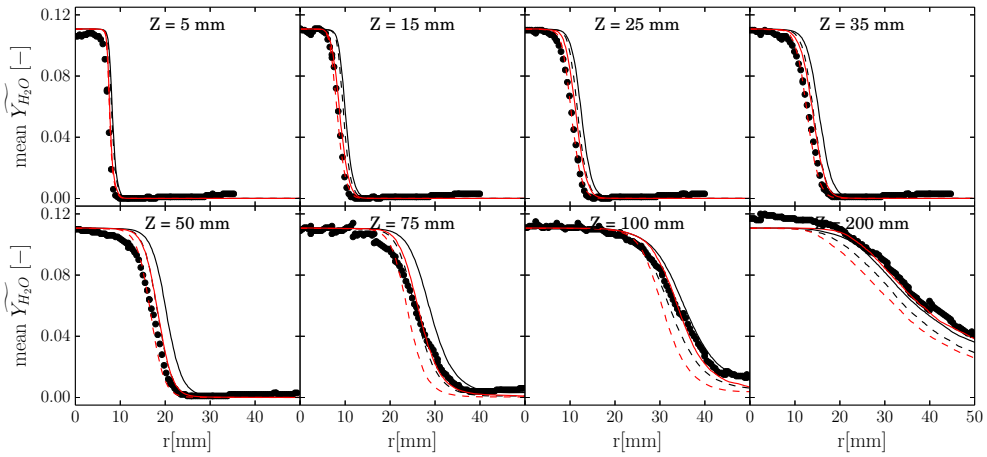


**Figure 3.20:** *Mean $H_2O$ mass fraction at eight distances Z from the pilot tube exit. Legend : — Adiabatic, Le ≠ 1. - - - Adiabatic, Le = 1. — Non-adiabatic, Le ≠ 1. - - - Non-adiabatic, Le = 1. • • TSF-A-r measurments.*

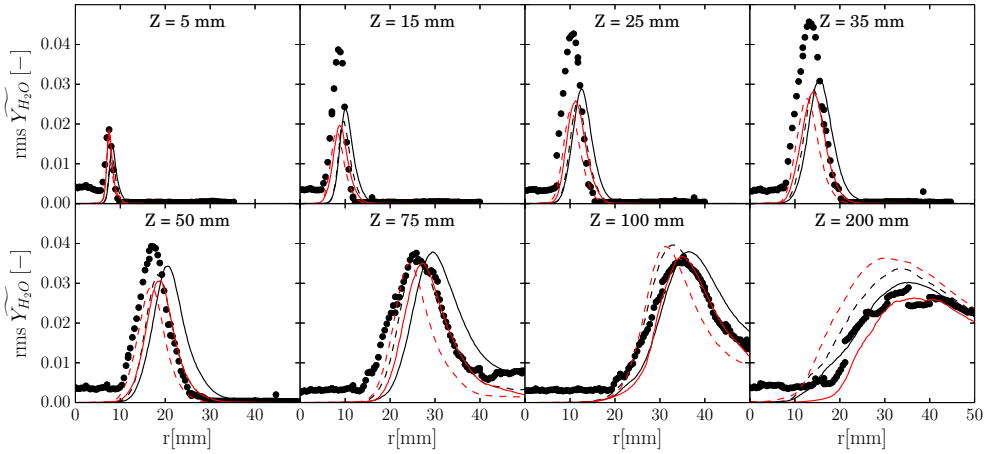


**Figure 3.21:** *RMS of $H_2O$ mass fraction at eight distances Z from the pilot tube exit. Legend : — Adiabatic, Le ≠ 1. - - - Adiabatic, Le = 1. — Non-adiabatic, Le ≠ 1. - - - Non-adiabatic, Le = 1. • • TSF-A-r measurments.*

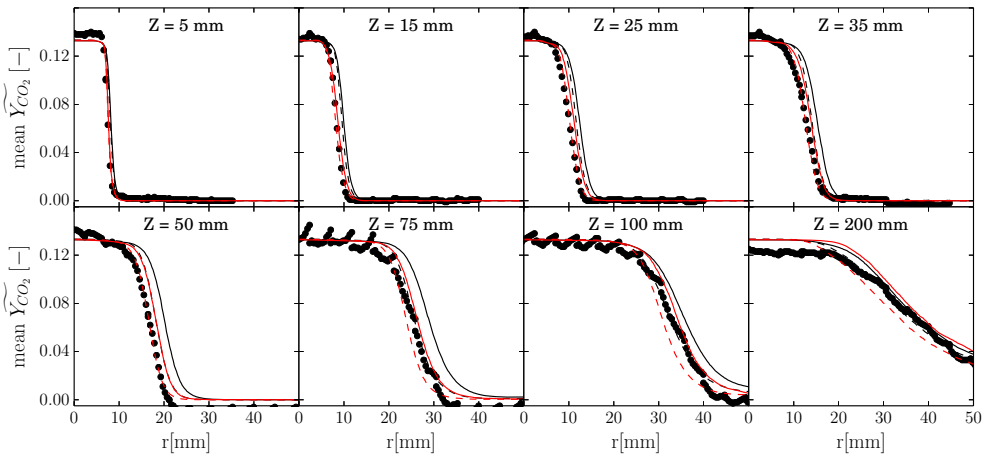


**Figure 3.22:** *Mean $CO_2$ mass fraction at eight distances Z from the pilot tube exit. Legend : — Adiabatic, $Le \neq 1$. - - - Adiabatic, $Le = 1$. — Non-adiabatic, $Le \neq 1$. - - - Non-adiabatic, $Le = 1$. ● ● TSF-A-r measurments.*

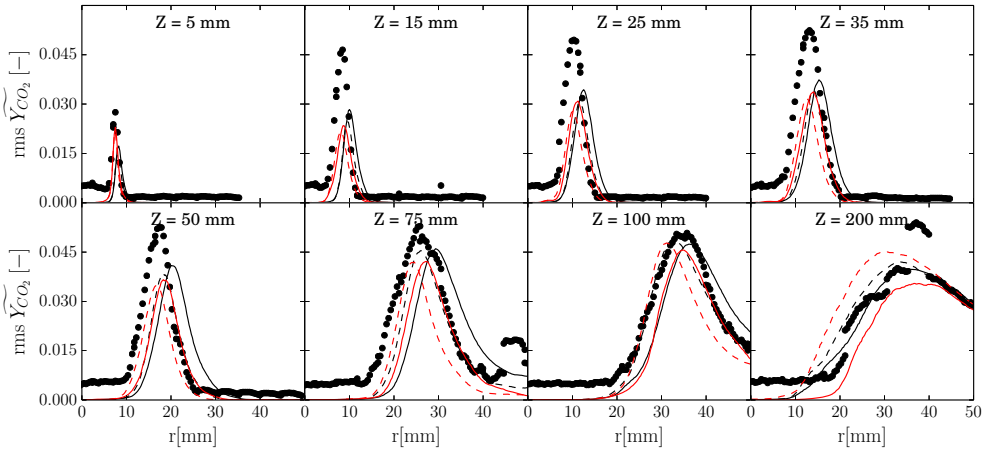


**Figure 3.23:** *RMS of $CO_2$ mass fraction at eight distances Z from the pilot tube exit. Legend : — Adiabatic, $Le \neq 1$. - - - Adiabatic, $Le = 1$. — Non-adiabatic, $Le \neq 1$. - - - Non-adiabatic, $Le = 1$. ● ● TSF-A-r measurments.*

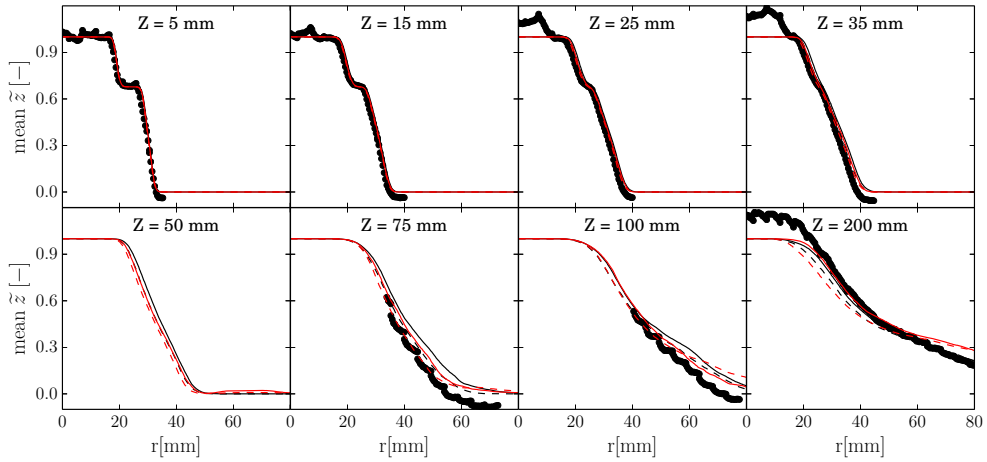


**Figure 3.24:** *Mean normalized mixture fraction at eight distances Z from the pilot tube exit.*
*Legend : — Adiabatic, Le ≠ 1. - - - Adiabatic, Le = 1. — Non-adiabatic, Le ≠ 1. - - - Non-adiabatic, Le = 1. • • TSF-A-r measurments.*

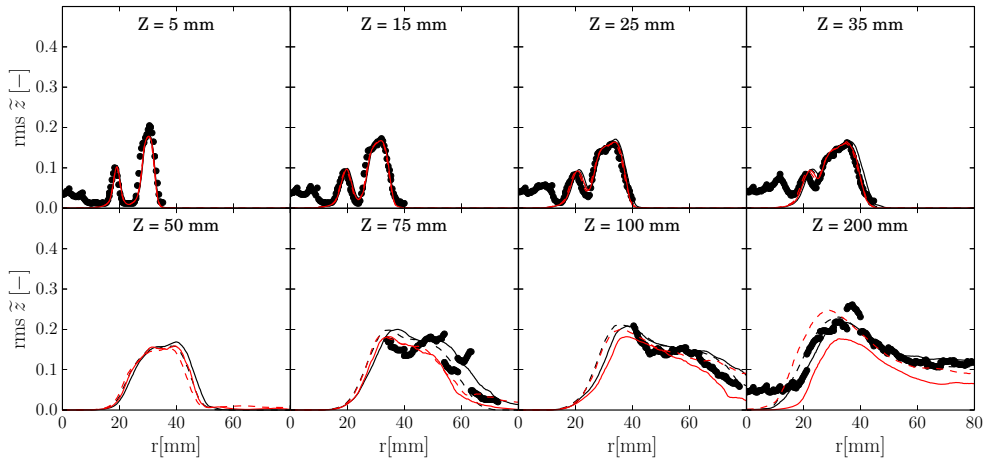


**Figure 3.25:** *RMS of normalized mixture fraction at eight distances Z from the pilot tube exit.*
*Legend : — Adiabatic, Le ≠ 1. - - - Adiabatic, Le = 1. — Non-adiabatic, Le ≠ 1. - - - Non-adiabatic, Le = 1. • • TSF-A-r measurments.*

## 3.3 LES of the Cambridge SwB non-swirling flames

This section presents the LES of two different non-swirling flames experimented at Cambridge. The first one is premixed (SwB1) while the second one is stratified (SwB5). These flames differ from the TSF-A case since they are stabilized using a central bluff-body. Moreover, a shear layer is created between both injections tubes promoting the turbulent mixing in the stratified case. Wall surface temperatures have been measured on the SwB burner for the different flame configurations. This allows to perform non-adiabatic computations with well-defined thermal boundary conditions. The experimental and numerical setups are first introduced. Then, the impact of heat losses on flame stabilization and temperature field is discussed.

### 3.3.1 Experimental configuration

The Cambridge stratified swirl burner (SwB), studied by Sweeney et al. (2011b), is composed of two concentric tubes surrounding a central bluff-body. The burner dimensions and the different injected streams are illustrated in Fig. 3.26. The inner (i) and outer (o) methane-air streams inlets are controlled independently in terms of bulk velocity $U$ and equivalence ratio $\phi$. A surrounding air co-flow of velocity $U_{cf} = 0.4$ m.s$^{-1}$ isolates the flame from ambient perturbations. The injected streams temperature is $T_0 = 298.0$ K. A wide range of operating conditions have been experimentally investigated by varying the level of fuel/air stratification and swirl. The numerical work focuses here on three non-swirling cases for which operating conditions are indicated in Tab. 3.4: the non-reacting configuration SwBc, the premixed reactive configuration SwB1 and the stratified reactive configuration SwB5. Available experimental data include velocity (Zhou et al., 2013) and thermochemical quantities (Sweeney et al., 2011b, 2013, 2012a,b) such as temperature, species and local equivalence ratio profiles.

**Table 3.4:** *Operating conditions*

| Case | $\phi_i[-]$ | $\phi_o[-]$ | $\phi_{cf}[-]$ | $\overline{U_i}[\frac{m}{s}]$ | $\overline{U_o}[\frac{m}{s}]$ | $\overline{U_{cf}}[\frac{m}{s}]$ |
|---|---|---|---|---|---|---|
| SwBc | 0 | 0 | 0 | 8.31 | 18.7 | 0.4 |
| SwB1 | 0.75 | 0.75 | 0 | 8.31 | 18.7 | 0.4 |
| SwB5 | 1.0 | 0.5 | 0 | 8.31 | 18.7 | 0.4 |

Recent measurements of the bluff-body wall temperature using phosphor thermometry have been performed by Euler et al. (2013, 2014). The comparison of these measurements for each SwB flames shows that the bluff-body wall surface cannot be assumed adiabatic. For both SwB1 and SwB5 cases, Figure 3.27 shows that the temperature varies approximatively between 650 K and 900 K which is very far from the adiabatic temperature approximately equal to 2000 K. The second important point is that the surface temperature

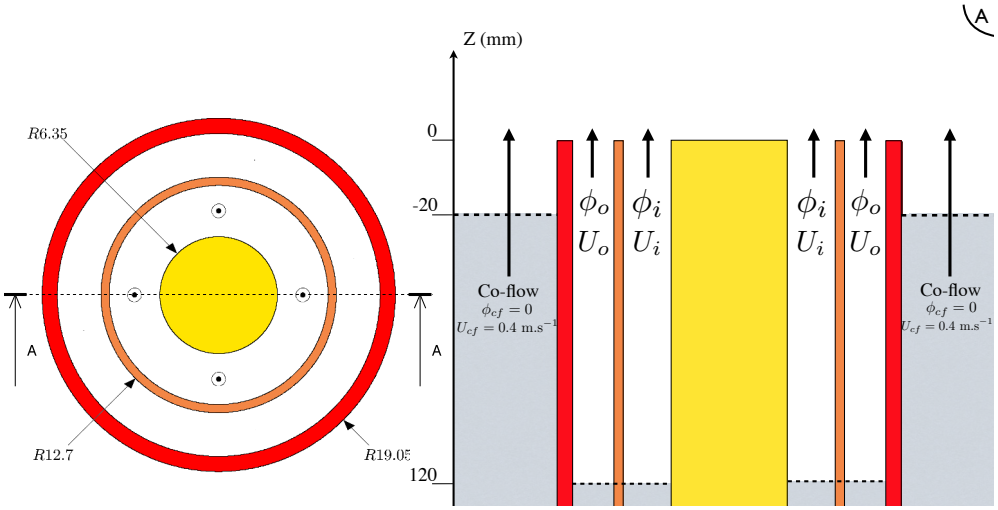


**Figure 3.26:** *Longitudinal cut of the SWB burner. The indicated inlet conditions correspond to the case TSF-A. The white area indicates the computational domain.*

level significantly depends on both the equivalence ratio and the swirl intensity. Therefore, an objective of this study is to analyze the impact of heat losses on the inner recirculation zone (IRZ) and on the flame stabilization process.

### 3.3.2 Numerical set-up

LES are performed using the YALES2 low-Mach number, unstructured finite volume flow solver (Moureau et al., 2011a). Fourth-order schemes are used for both spatial discretization and time integration. The SGS turbulence is described by the $\sigma$-model (Nicoud et al., 2011) as suggested by Proch et al. (2013). The tabulated chemistry is coupled to the LES balance equations with the non-adiabatic stratified F-TACLES model. As for the TSF-A flame, the sub-filter scale winkling $\Xi_\Delta$ is modeled as in Wang et al. (2011) with a constant $\beta$ parameter ($\beta = 0.5$). Chemistry is tabulated from a collection of 1-D laminar premixed flames computed with the Lindstedt (1997) mechanism and with the Hirschfelder et al. (1969) model for species diffusive transport terms. In the non-adiabatic LES, the species mass fractions are estimated using the same approach as for the TSF-A burner.

The SwB burner exhibits three injected streams with three different equivalence ratios: tube $i$, tube $o$ and the air co-flow. The sub-grid scale mixture fraction PDF is modeled as proposed in Sec. 3.2.2.2. Mean velocity profiles are imposed at Z = -120 mm assuming an analytical power-law profile:

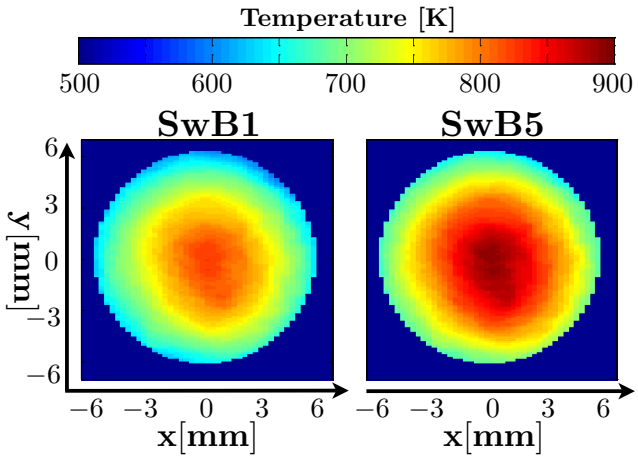


**Figure 3.27:** *Measured bluff-body surface temperatures for SwB1 and SwB5 cases. Extracted from Euler et al. (2013).*

$$w = r_2 - r_1 \tag{3.7}$$

$$d(r) = r - \frac{r_1 + r_2}{2} \tag{3.8}$$

$$U(r) = U_{\max}\left(1 - \left(\frac{2d(r)}{w}\right)^4\right) \tag{3.9}$$

where $r_1$ and $r_2$ denote respectively the radius of the inner and outer walls of the considered injection stream. $U_{\max}$ is set to 10.5 m.s$^{-1}$ and 22.4 m.s$^{-1}$ for the inner and outer tubes, respectively. These values have been chosen to conserve the mass flow rate in both tubes $i$ and $o$. Homogeneous and isotropic turbulence (Passot and Pouquet, 1987) is superimposed to the mean velocity profiles at Z = -120 mm and is adjusted to match velocity fluctuations profiles measured at Z = 2 mm (Z = 0 mm being the plane located at the burner exit). The turbulent intensity is set to 10% while the integral length scale is $L_e \approx D_h/4 \approx 3.0$ mm where $D_h$ denotes the hydraulic diameter.

### 3.3.3 Simulated cases

To validate the correct resolution of the flow, LES of the non-reacting case is performed on two tetrahedral meshes featuring 6.2 and 17.6 million nodes. The reference mesh has a mesh size in the flame region of $\Delta_x = 0.5$ mm while the refined mesh exhibits smaller cells in this region since $\Delta_x = 0.25$ mm. A comparison between both computations shows that the coarser grid is sufficient to capture SwB flow dynamics. This reference grid, shown in Fig. 3.28, features a characteristic mesh size in the flame region $\Delta_x \approx \delta_l^0$ leading to a major contri-

bution of the combustion model in the LES.

Both premixed (SwB1) and stratified (SwB5) non-swirling cases are simulated. For each operating conditions, two LES have been conducted: a first one assumes an adiabatic burner while a second one imposes the measured surface temperatures at the burner walls to account for non-adiabaticity. The characteristics of the different simulations are summarized in Tab. 3.5 and are analyzed below.

**Table 3.5:** *Simulated cases. The flow-through-time (FTT) is estimated as* $FTT = L/\overline{U_i} = 10$ *ms with* $L = 0.1$ *m the height of the reaction zone and* $\overline{U_i} = 10$ $m.s^{-1}$ *the bulk velocity of inner tube. The F-TACLES filtered look-up tables are generated with a flame filter size* $\Delta = 2.5$ *mm. These computations are conducted on an IBM Blue Gene/Q machine on 1024 cores.*

| Simu. # | Exp. Config | $N_{nodes}$ | $T_{bluff\text{-}body}$ | 1 FTT cost [CPU hour] |
|---|---|---|---|---|
| SWB-C-FI | SwBc | $17.6 \cdot 10^6$ | Adiabatic | 72500 |
| SWB-C-CO | SwBc | $6.2 \cdot 10^6$ | Adiabatic | 9200 |
| SWB-1-AD | SwB1 | $6.2 \cdot 10^6$ | Adiabatic | 16800 |
| SWB-1-NAD | SwB1 | $6.2 \cdot 10^6$ | Expe. | 16900 |
| SWB-5-AD | SwB5 | $6.2 \cdot 10^6$ | Adiabatic | 18500 |
| SWB-5-NAD | SwB5 | $6.2 \cdot 10^6$ | Expe. | 18800 |

As for the TSF-A simulations, flow statistics are obtained by azimuthal and time averaging instantaneous solutions over a physical time corresponding to 10 flow-through-times based on the pilot stream velocity.

### 3.3.4 Results analysis

#### 3.3.4.1 Mesh resolution analysis on the non-reacting case SwBc

The LES of the non-reacting case (SwBc) is performed on the two meshes described in Sec. 3.3.3. Mean and RMS of the velocity field are compared in Fig. 3.29 to Laser Doppler Anemometry (LDA) experimental data, provided by Zhou et al. (2013), at four different distances from the burner exit (Z = 2, 10, 30 and 50 mm). This figure shows a good agreement of both mean and RMS of axial velocity profiles between the LES and the measurements. This conclusion also holds for the mean radial velocity which has relatively low amplitudes (of the order of 1 $m.s^{-1}$). Note that the RMS of radial velocity are overestimated by both LES. This misprediction of around 1.5 $m.s^{-1}$, independent of mesh resolution, has also been noticed in other simulations which uses the same boundary conditions (Mercier et al., 2013b). Figure 3.29 also shows that the reference mesh is sufficient to capture mean velocity fields.

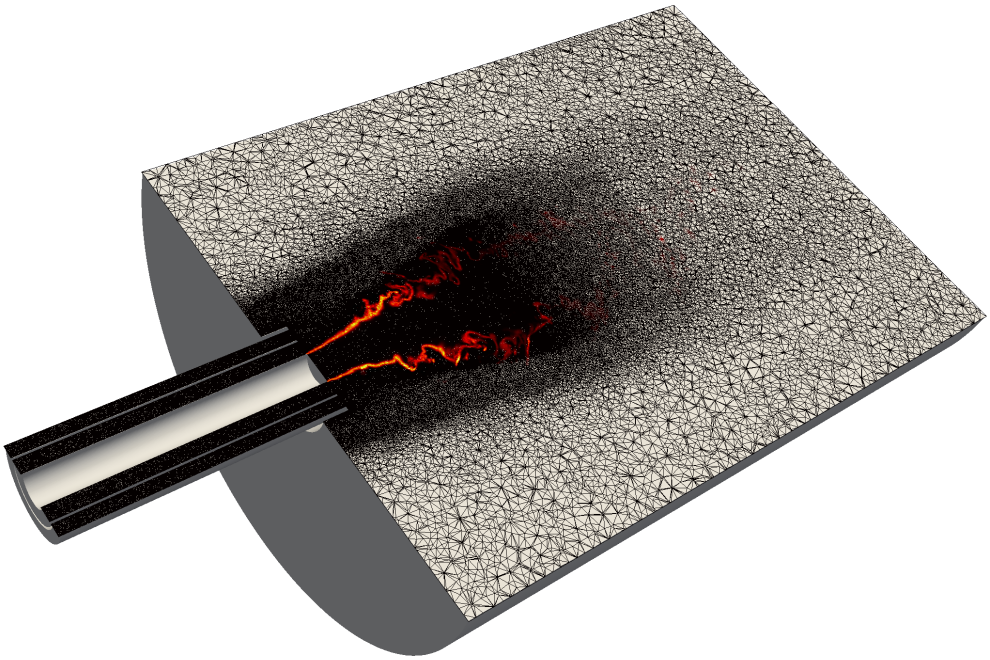

(a) Whole computational domain

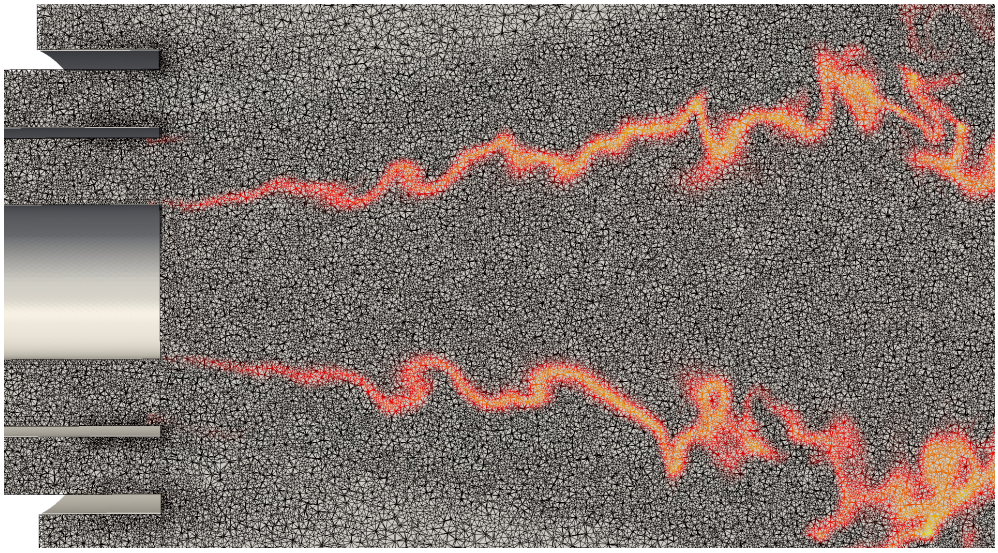

(b) Near flame region

**Figure 3.28:** *Half portion of the SwB computational domain. A longitudinal cut of the coarse mesh is shown and colored by the filtered progress variable reaction rate* $\widetilde{\omega}_{Y_c}$*. The mesh is refined within the injection tubes and the flame region. In those regions, the characteristic mesh size is* $\Delta_x \approx 0.5$ *mm for the coarse grid.*

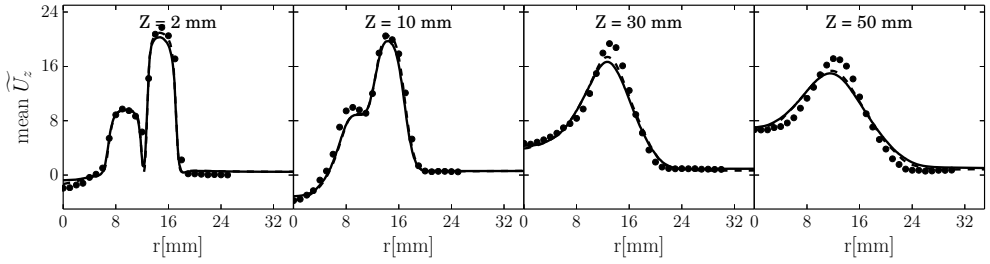


(a) Mean axial velocity $U_z$

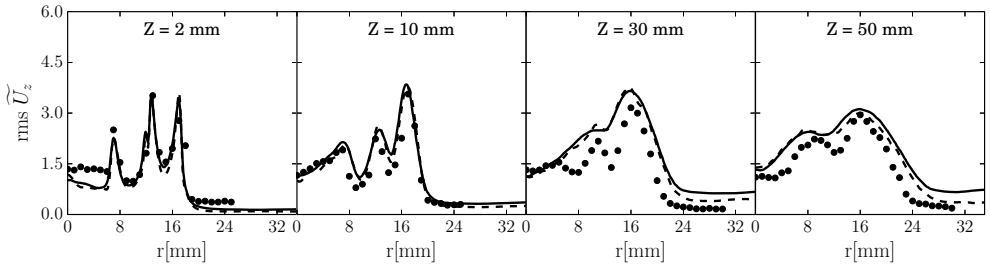


(b) RMS of axial velocity $U_z$

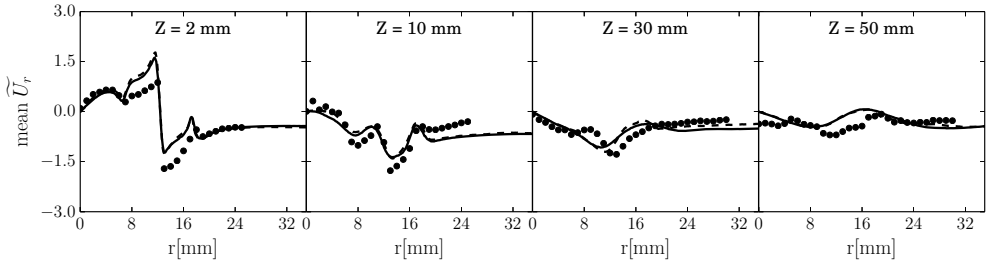


(c) Mean radial velocity $U_r$

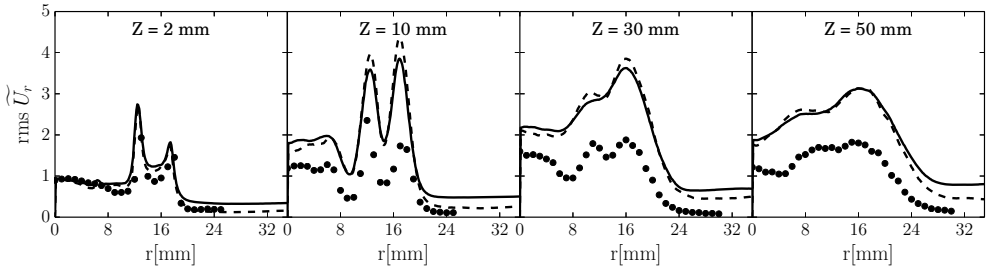


(d) RMS of radial velocity $U_r$

**Figure 3.29:** *Radial profiles of the velocity for the non-reacting case SwBc at several distances from the burner exit. — Reference mesh (SWB-C-CO). - - - Refined mesh (SWB-C-FI). • • Experiments.*

### 3.3.4.2 Impact of heat losses on the flame stabilization process

For both SwB1 and SwB5 cases, measured bluff-body temperature shown in Fig. 3.27 is imposed in the non-adiabatic LES as thermal boundary conditions. In this paragraph, all the results will be shown only for the stratified SwB5 case but also hold for the fully-premixed case. Indeed, the flame stabilization process and its sensitivity to heat losses is found to be very similar for both cases. Figure 3.30 compares two instantaneous views of the filtered progress variable reaction rate iso-surface extracted from adiabatic (SWB-5-AD) and non-adiabatic (SWB-5-NAD) simulations of the SwB5 case. The flame is anchored at the burner bluff-body for adiabatic conditions while the non-adiabatic simulation predicts a lifted flame. Indeed, heat losses affect the flow enthalpy and influence the turbulent filtered flame propagation speed through the factor $\gamma$ (Eq. (2.35)).

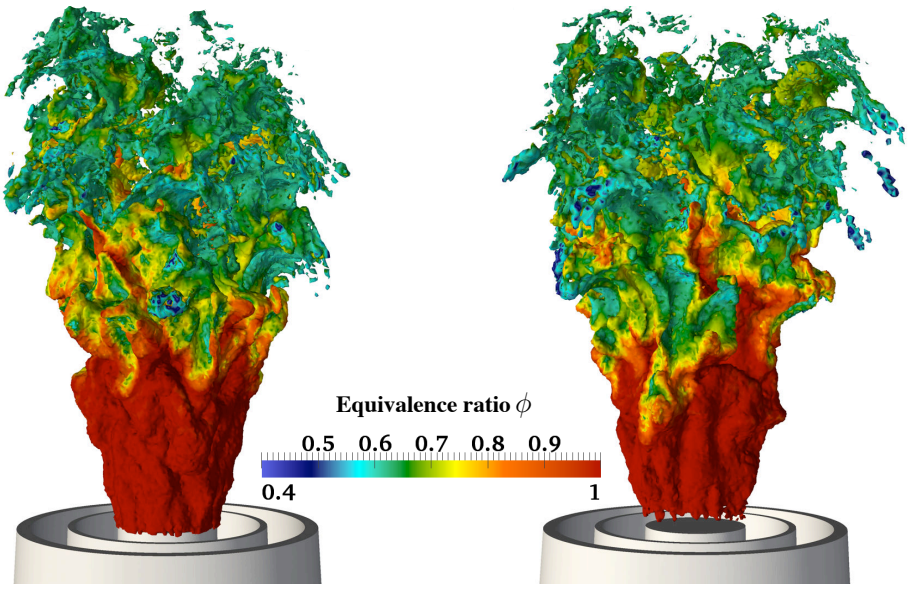


**Figure 3.30:** *Isosurface of filtered progress variable reaction rate* $\overline{\rho}\widetilde{\dot{\omega}}_{Y_c} = 0.5\overline{\rho}\widetilde{\dot{\omega}}_{Y_c}^{max}$ *colored by fresh gas equivalence ratio* $\phi$ *for the stratified (SwB5) case. Left: Adiabatic computation (SWB5-AD). Right: Non-adiabatic computation (SWB5-NAD).*

Figure 3.31 shows mean and RMS of axial and radial velocity profiles for the stratified (SwB5) case. Adiabatic and non-adiabatic simulations differ in the inner recirculation zone (IRZ) located at $r < 6$ mm near the burner exit. The non-adiabatic simulation predicts a faster rotation of the recirculation zone evidenced by a larger absolute value of the negative axial velocity as well as an increase of the radial velocity for $Z < 10$ mm. The RMS of axial and radial velocity are not significantly impacted by heat exchanges near the burner walls.

Figure 3.31 show a modification of the flow dynamics due to heat losses. This

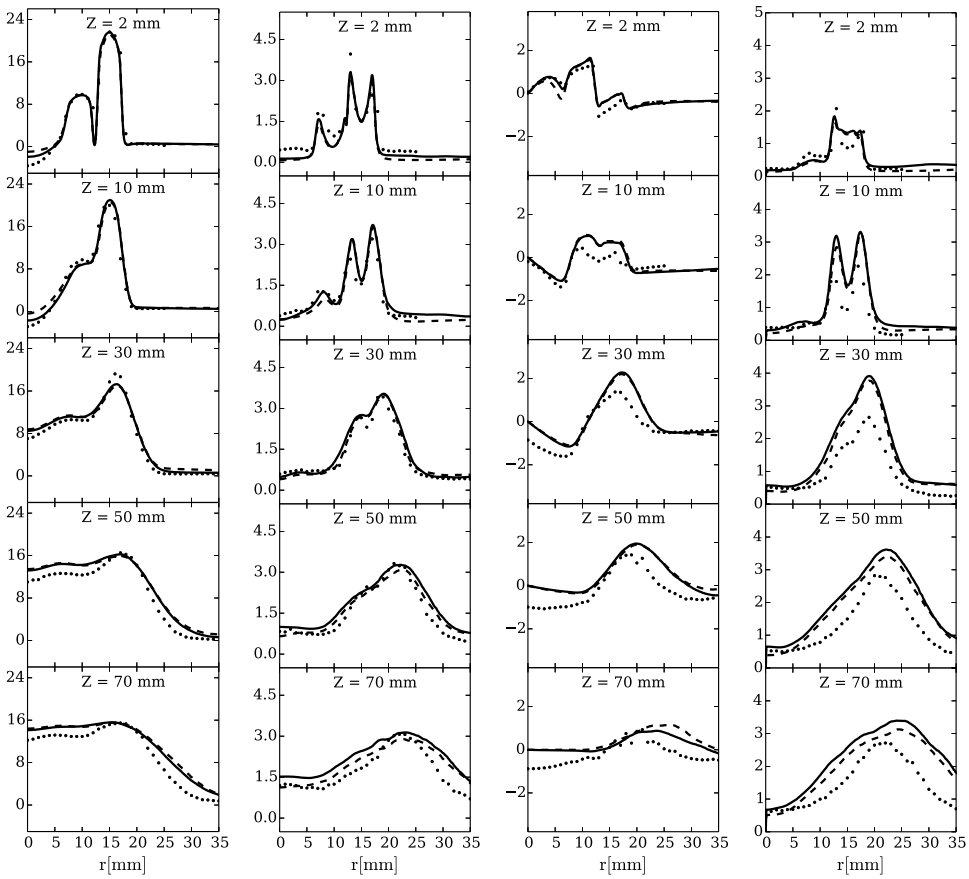


(a) Mean axial velocity $U_z$ [m.s$^{-1}$] (b) RMS of axial velocity $U_z$ [m.s$^{-1}$] (c) Mean radial velocity $U_r$ [m.s$^{-1}$] (d) RMS of radial velocity $U_r$ [m.s$^{-1}$]

**Figure 3.31:** *Radial profiles of the velocity for the stratified case (SwB5) at different distances from the burner exit. Legend : - - - Adiabatic computation (SWB5-AD). — Non-adiabatic computation (SWB5-NAD). • • Experiments.*

trend is more visible in Fig. 3.32 which compares medium cross section of mean axial velocity iso-surfaces in the IRZ for the SwB5 case. Both the position and the dynamics of the IRZ differ between SWB5-AD and SWB5-NAD as thermal expansion is reduced near the burner wall when heat losses are considered. The non-adiabatic iso-lines better predict the shape and height of the IRZ. The same conclusions are drawn for the fully-premixed case SwB1.

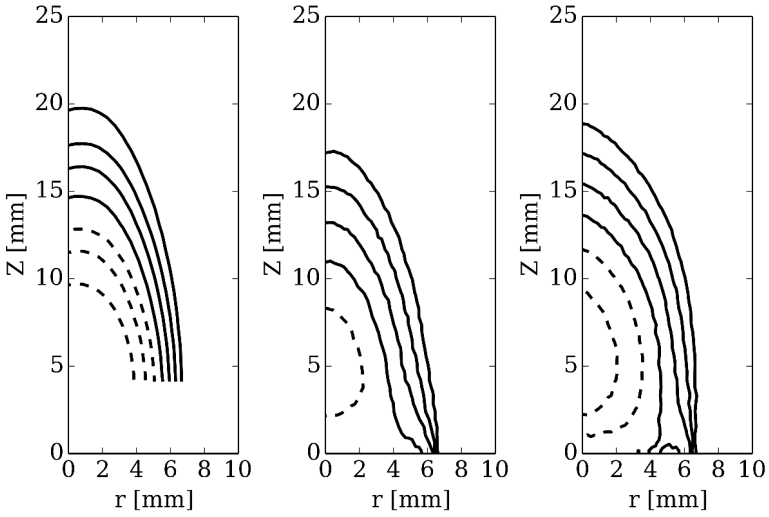


(a) Experiments (2-D PIV) (b) SWB5-AD (c) SWB5-NAD

**Figure 3.32:** *Cross section in the medium plane of the iso-surfaces of mean axial velocity $\widetilde{U_z}$ for the stratified case (SwB5). For a each figure, isolines values are, from right to left, $\widetilde{U_z} = \{3; 2; 1; 0; -1; -2; -3\}$ $m.s^{-1}$. Dashed lines: $\widetilde{U_z} < 0$ ; Solid lines: $\widetilde{U_z} \geq 0$.*

#### 3.3.4.3 Cross effect of heat losses and differential diffusion on the temperature field

Figure 3.33(a) compares mean radial profiles of temperature against experimental data for both SwB1 and SwB5 cases. As expected, the adiabatic simulation of SwB5 flame overestimates the burnt gases temperature for $r < 6$ mm by about 150 K while the non-adiabatic simulation, accounting for the IRZ cooling at the bluff-body wall surface, correctly captures it. However, this tendency is not verified in the SwB1 case, where the adiabatic LES predicts surprisingly well the IRZ temperature which is now underestimated by the non-adiabatic LES. This phenomenon is explained by comparing computed and measured equivalence ratio in Fig. 3.33(b). As discussed in Barlow et al. (2012); Katta and Roquemore (2013); Dunn and Barlow (2013), experiments revealed that atom balances (atomic mass fractions) were not conserved across the flame brush going from reactants to products. This phenomenon seems to result from preferential diffusion of $H_2$ and $H_2O$ toward the reactants followed by convective transport of these species away from the local flame brush. Equilibrium temperature is consequently affected by this elemental composition variation. This complex phenomenon is not captured by the F-TACLES model as detailed in Sec. 2.2.1. An approach to capture the impact of preferential transport on the transported mixture fraction has been proposed by Nambully

et al. (2014a) and was successfully applied in Nambully et al. (2014b). However, once the shift in mixture fraction is correctly captured, accounting for its effects on the inner thermochemical flame structure remains a very challenging issue not addressed in this thesis. An *a priori* estimation of the error induced by such assumption in both SwB1 and SwB5 is nevertheless proposed. Figure 3.34, plots the equilibrium temperature as a function of the equivalence ratio, for two different enthalpy defects $\Delta h$. $\Delta h = 0$ corresponds to the adiabatic equilibrium temperature while $\Delta h = 1.5 \cdot 10^5$ J/kg is the mean enthalpy defect extracted from the centerline of the IRZ in non-adiabatic computations. The variation of equivalence ratio $\Delta\phi$ due to differential diffusion is estimated from experimental data. $\Delta\phi$ is shown in Fig. 3.33(b) for both cases SwB1 and SwB5. The temperature variations $\delta T_{\Delta h}$ and $\delta T_{\Delta\phi}$ due to heat losses and differential diffusion, respectively, are identified for both SwB1 and SwB5. As the IRZ mixture of SwB5 is almost stoichiometric, it is observed in Fig. 3.34 that $\delta T_{\Delta h} \gg \delta T_{\Delta\phi}$, explaining why neglecting differential diffusion across iso-equivalence ratio will not lead to significant departure between measured and predicted temperature (Fig. 3.33(a) right). At the opposite, $\delta T_{\Delta h} \approx -\delta T_{\Delta\phi}$ for the lean fully-premixed SwB1 case. Then, the non-adiabatic simulation without accounting for complex transport effect cannot capture accurately the IRZ temperature. The SwB1 adiabatic simulation actually predicts fairly well the burnt gases temperature (Fig. 3.33(a) left) because of two compensating errors.

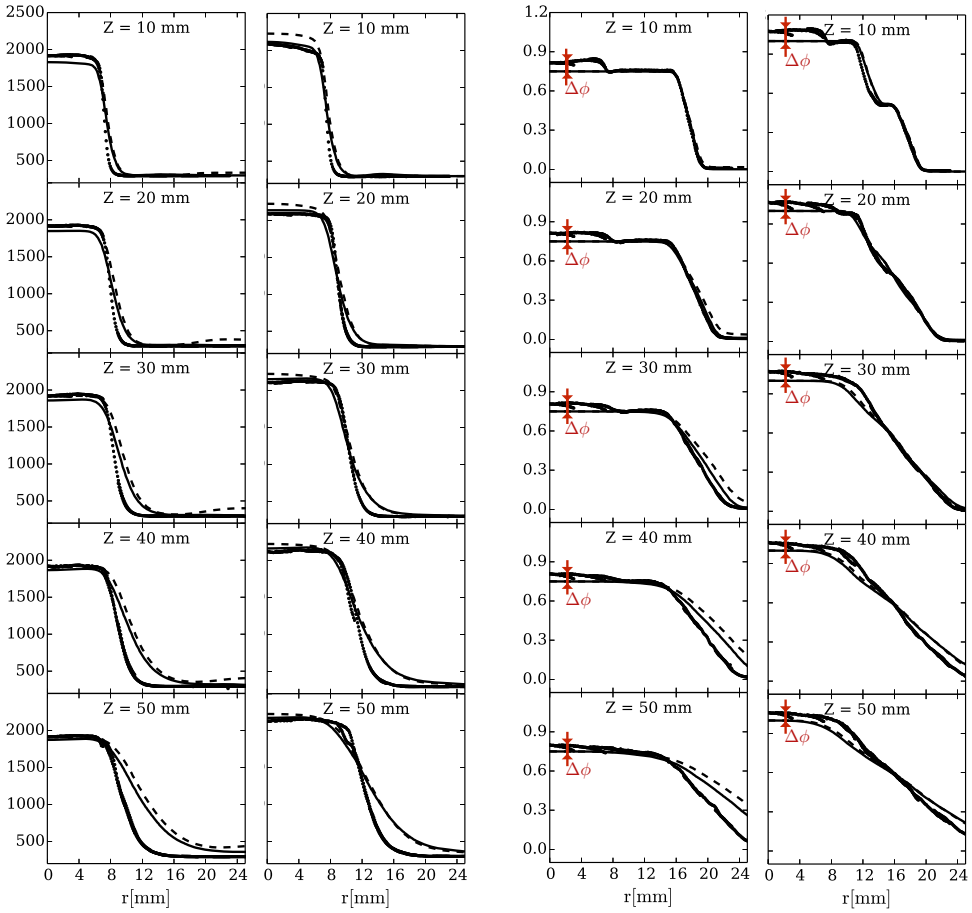


(a) Mean temperature $T$ [K] for the Premixed/SwB1 (left) and Stratified/SwB5 (right) cases

(b) Mean fresh gas equivalence ratio $\phi$ [-] for the Premixed/SwB1 (left) and Stratified/SwB5 (right) cases

**Figure 3.33:** *Mean temperature $\widetilde{T}$ and equivalence ratio $\phi$ radial profiles for both premixed and stratified flames. Legend : - - - adiabatic computations (SWB1-AD and SWB5-AD). — non-adiabatic computations (SWB1-NAD and SWB5-NAD). • • experiments.*

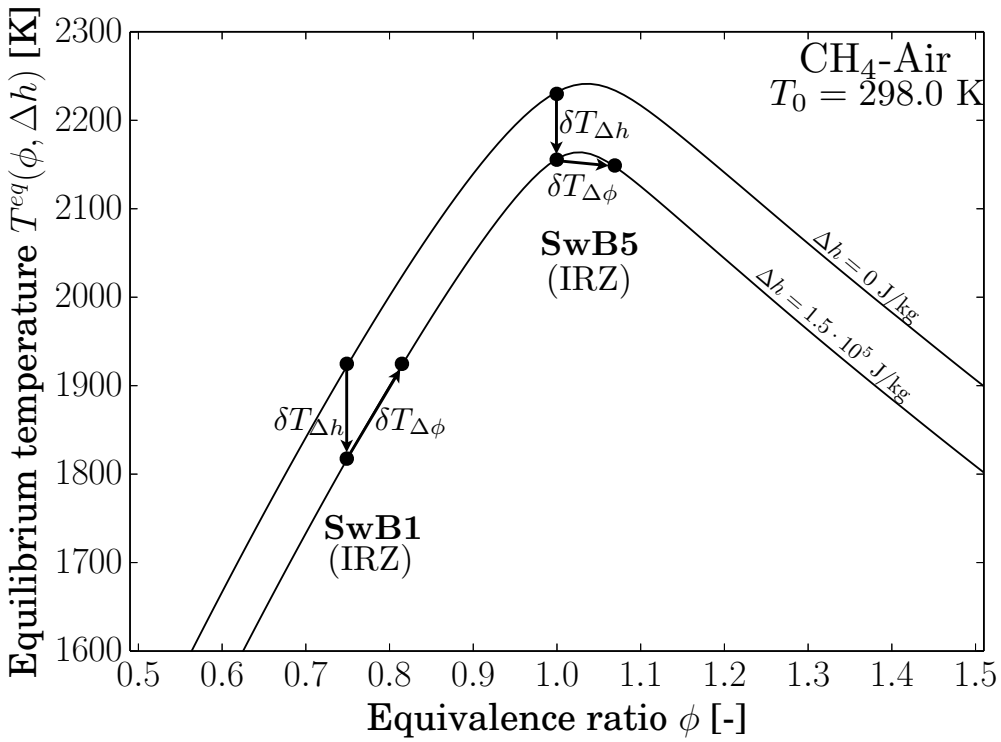


**Figure 3.34:** *Equilibrium temperature function of fresh gas equivalence ratio $\phi$ for adiabatic and non-adiabatic situations. $CH_4$-Air fresh gas temperature is taken equal to $T_0 = 298.0$ K. Legend: upper curve: adiabatic ($\Delta h = 0$); lower curve: non-adiabatic ($\Delta h = 1.5 \cdot 10^5$ J/kg).*

## 3.4 Conclusion

The objective of the present chapter was to apply the non-adiabatic F-TACLES model derived in Chapter 2 to complex turbulent flames. For that purpose, we have retained two target flames of the TNF workshop, experimentally characterized using advanced diagnostics. The numerical study of the TSF-A flame has shown the influences of non-adiabaticity and differential diffusion modeling strategy on the turbulent flame structure and stabilization process. Two main effects have been exhibited:

- Heat losses greatly decrease the turbulent flame consumption speed near the burner lips and cause a lift-off of the flame front. The flame is then translated downstream compared to adiabatic simulations causing a shift of all the 1-D radial profiles.
- The modeling of differential diffusion in the 1-D flames used to generate the F-TACLES database mainly impacts the flame consumption speed. Therefore, the mean turbulent flame brush is mainly impacted through the flame angle which opens wider when complex transport models are used.

These investigations on non-adiabatic turbulent flames allowed to gain further insight in the capabilities and limits of the non-adiabatic F-TACLES model. The impact of heat losses and differential-diffusion on the flame propagation and flow field seems to be well captured in practical LES computations. However, as stated in Sec. 2.1, 3-D complex transport phenomena, such as preferential diffusion of $H_2$ and $H_2O$ out of the flame front are not captured by the present approach.

The last element of the flame propagation modeling is the capture of the impact of the flame turbulence interactions in the LES computation. This challenging issue is investigated in the next part of this thesis manuscript.

# Part III

# Capturing the flame-turbulence interactions at unresolved and resolved scales

# Chapter 4

# Modeling the sub-filter scale flame wrinkling

**Contents**

*This part of the thesis focuses on the modeling of flame-turbulence interactions. In a LES context, these interactions can be either resolved (when wrinkling scales are larger than the LES filter size) or unresolved (when wrinkling scales are smaller than the LES filter size). The present chapter presents a comparison of different approaches to model the impact of unresolved flame wrinkling on the turbulent flame consumption speed. In particular, a sensitivity analysis on the flame wrinkling model parameters and their sub-models is conducted and the different approaches are applied to the SwB5 non-adiabatic turbulent stratified flame. As this flame shows quasi-laminar and highly turbulent reaction zones, the ability of the models to capture both regimes is analyzed.*

## 4.1 Motivations

The non-adiabatic F-TACLES model for stratified combustion, described in Sec. 1.5.2.4 and 2.3.2, closes the filtered progress variable equation as:

$$\begin{aligned}\frac{\partial\overline{\rho}\widetilde{Y_c}}{\partial t}+\frac{\partial}{\partial x_i}\left(\overline{\rho}\widetilde{u_i}\widetilde{Y_c}\right) &= \frac{\partial}{\partial x_i}\left(\Xi_\Delta^{Y_c}\gamma[\widetilde{z},S_z,\Delta\widetilde{h}]\alpha_{Y_c}^{ad}[\widetilde{Y_c},\widetilde{z},S_z,\Delta]\rho_0 D_0\frac{\partial\widetilde{Y_c}}{\partial x_i}\right)\\ &+ \Xi_\Delta^{Y_c}\gamma[\widetilde{z},S_z,\Delta\widetilde{h}]\Omega_{Y_c}^{ad}[\widetilde{Y_c},\widetilde{z},S_z,\Delta]\\ &+ \Xi_\Delta^{Y_c}\gamma[\widetilde{z},S_z,\Delta\widetilde{h}]\overline{\rho}\widetilde{\dot{\omega}}_{Y_c}^{ad}[\widetilde{Y_c},\widetilde{z},S_z,\Delta] \qquad (4.1)\end{aligned}$$

In this formulation, three different sub-models are present. First, the contribution of each RHS term $\Phi^{ad}[\widetilde{Y_c},\widetilde{z},S_z,\Delta]$ is obtained by filtering 1-D laminar premixed flames (for instance, the filtered progress variable reaction rate $\widetilde{\dot{\omega}}_{Y_c}^{ad}$). This term also includes the impact of unresolved mixture fraction heterogeneities through the convolution with a $\beta$-function proposed by Auzillon et al. (2012). Second, the tabulated term $\gamma$ accounts for the impact of heat losses on the turbulent flame propagation. This term has been introduced in the Chapter 2 of this thesis. Both $\gamma$ and $\Phi^{ad}$ are built from 1-D laminar flames. The impact of the unresolved interactions between the flame front and turbulent scales on the LES filtered unclosed terms is captured by the sub-filter scale wrinkling $\Xi_\Delta^{Y_c}$. The filtered flame front (*i.e.* the filtered progress variable front) propagates at the sub-filter scale turbulent flame speed $S_\Delta$ obtained by integrating Eq. 2.44 in the direction normal to the propagation direction:

$$\overline{\rho^f}S_\Delta = \Xi_\Delta^{Y_c}\gamma\int_0^1 \rho^f\left(z'\right)S_l{}^{ad}\left(z'\right)\overline{P}\left(z'\right)\,dz' \qquad (4.2)$$

where $S_l{}^{ad}(z)$ is the consumption speed of a freely-propagating adiabatic laminar premixed flame within fresh gases of mixture fraction $z$ and density $\rho^f$. From a modeling point of view, the separation of both laminar and turbulent contribution is actually used in all the turbulent combustion models based on

geometrical description of the flame front (see Sec. 1.5.2). A general formulation of the filtered reaction rate has been recently proposed by Veynante et al. (2013) for the level-set, the thickened flame, the flame surface density and the F-TACLES models. In those models, a the flamelet regime is assumed and the sub-grid scale turbulent flame speed $S_\Delta$ is often deposed as:

$$S_\Delta = \Xi_\Delta S_l \tag{4.3}$$

where $S_l$ is the consumption speed of a planar flame which can be a function of the local equivalence ratio $\phi$, enthalpy defect $\Delta h$, strain rate $\kappa$, etc. In the flamelet regime, assuming that the flame thickness is negligible compared with the LES filter size $\delta \ll \Delta$, the ratio between resolved and planar flame consumption speed can also be recast in terms of flame surface as:

$$\Xi_\Delta = \frac{S_\Delta}{S_l} = \frac{A_\Delta}{A_n} \tag{4.4}$$

where $A_\Delta$ is the total flame surface in the filtering volume of size $\Delta$ while $A_n$ is the projection of the total flame surface in a plane normal to the direction of the filtered flame front propagation.

Different approaches have been proposed to estimate $\Xi_\Delta$ using resolved quantities. A possibility is to assume that the flame wrinkling geometrical structures are similar over a wide range of scales. In this context, early studies by Gouldin (1987); Gouldin et al. (1989) proposed to use the fractal mathematical framework to describe the flame surface area in a given volume. If $A_\ell$ denotes the flame surface area contained in a cubic volume $\ell^3$ of side $\ell$, defining the minimum scale of wrinkling as $\delta_c$, it is possible to estimate $A_\ell$ as (Gouldin et al., 1989):

$$\frac{A_\ell}{\ell^3} = \delta_c^{2-D} \ell^{D-3} \tag{4.5}$$

where D is the fractal dimension. $2 \leq D \leq 3$ for a fractal surface. $D = 2$ corresponds to a planar surface without fractal structures while $D = 3$ correspond to a flame surface occupying all the cube. In the context of the modeling of LES sub-filter scale wrinkling, the size of the cubic volume may be associated to the LES filter size $\ell = \Delta$. This filtering volume contains the flame surface $A_\ell = A_\Delta$ and Eq. 4.5 may be recast as:

$$\frac{A_\Delta}{\Delta^2} = \left(\frac{\Delta}{\delta_c}\right)^{D-2} \tag{4.6}$$

where the area of a cubic volume face $\Delta^2$ is an estimation of the projection of the total flame surface $A_\Delta$ in a plane normal to the direction of the filtered flame front propagation leading to $\Delta^2 \approx A_n$. Therefore, an estimation of the

sub-filter scale wrinkling $\Xi_\Delta$ is given by the following expression:

$$\Xi_\Delta = \frac{S_\Delta}{S_l} = \frac{A_\Delta}{A_n} = \left(\frac{\Delta}{\delta_c}\right)^{D-2} \tag{4.7}$$

This expression is based on a simplified geometrical description of the flame front which does not capture the physical phenomena occurring during flame-turbulence interactions. Moreover, submodes are still needed for $D$ and $\delta_c$, which likely depend on the local flow and flame features. In practice, this power-law expression has been enhanced to provide a finer representation of flame-turbulence interaction phenomena. For instance, Charlette et al. (2002a,b) proposed an unresolved wrinkling modeling strategy based on the power-law formalism of Eq 4.7. The authors proposed to first quantify the impact of the different turbulent scales individually using DNS of flame-vortex interactions. Then, the impact of each individual turbulent scale has been integrated along a turbulence spectrum assumed homogeneous and isotropic at the sub-filter scale. The final formulation (Wang et al., 2011), derived to fit the results given by the integration procedure but also capture different asymptotic behavior, reads:

$$\Xi_\Delta = \left(1 + \max\left[0, \min\left[\frac{\Delta}{\delta_c} - 1, \Gamma_\Delta\left(\frac{\Delta}{\delta_c}, \frac{u'_\Delta}{S_l^0}, Re_\Delta\right)\frac{u'_\Delta}{S_l^0}\right]\right]\right)^\beta \tag{4.8}$$

where $Re_\Delta = \left(u'_\Delta \Delta\right)/\nu$ and $u'_\Delta$ are the subgrid scale Reynolds number and turbulence intensity, respectively, while $\delta_c$ is the inner wrinkling cut-off scale estimated as $\delta_c = \delta_l^0$ by Charlette et al. (2002a,b); Wang et al. (2011) and as $\delta_c = 2\delta_l^0$ in Schmitt et al. (2013a). $\beta$ is a model parameter which can be seen as a fractal-like dimension $\beta \approx D - 2$. The efficiency function $\Gamma_\Delta$ estimates the net straining effect of all turbulent scales smaller than $\Delta$.

This formulation has been assessed in *a priori* DNS analysis by Chakraborty and Klein (2008); Chakraborty and Cant (2009) and widely used in LES of complex turbulent flames during the last decade (Ketelheun et al., 2013; Auzillon et al., 2012; Kuenne et al., 2012; Garby et al., 2013; Auzillon et al., 2013; Kuenne et al., 2011; Schmitt et al., 2013b,a; Wang et al., 2011, 2012; Hernández-Pérez et al., 2011; Di Sarli et al., 2009; Mercier et al., 2015b,a, 2014).

It is worth noting that this formulation has been derived to correctly capture the limits:

- When the LES filter size becomes thinner than the wrinkling cut-off scale $\Delta < \delta_c$, the model correctly degenerates towards DNS since $\Xi_\Delta = 1$ (*i.e.* $S_\Delta = S_l$).
- For large sub-filter scale turbulence intensities ($u'_\Delta \gg S_l^0$), the sub-grid scale wrinkling factor $\Xi_\Delta$ reduces to the fractal-like power-law given by

Eq. (4.7):

$$\Xi_\Delta = \left(\frac{\Delta}{\delta_c}\right)^\beta \tag{4.9}$$

- Without SGS turbulence ($u'_\Delta \to 0$), the flame wrinkling is fully resolved (see Sec. 1.3) and the model correctly degenerates as $\Xi_\Delta \to 1$ (*i.e.* $S_\Delta = S_l$).

Model given by Eq. (4.8) has been designed under the assumption that turbulence and flame front are in equilibrium and that the turbulence spectrum is homogeneous and isotropic at the sub-filter scale. The parameter $\beta$ and the subgrid scale velocity fluctuations $u'_\Delta$ are not known *a priori* since they depend of the local flame and flow features. Additional submodels are then required for these quantities. The objective of this chapter is to study the model sensitivity to both sub-models on a complex turbulent flame which exhibits various levels of turbulence intensity as it is often the case in practical combustion chambers.

## 4.2 Sub-models for the sub-filter scale turbulent intensity $u'_\Delta$

### 4.2.1 Prandtl-Kolmogorov approach

The Prandtl-Kolmogorov approach (Prandtl, 1946; Kolmogorov, 1942) assumes that the turbulent eddy viscosity $\nu_t$ expressed linearly as a function of the length scale $\Delta_x$ and the square root of the sub-grid scale kinetic energy $k_\Delta$ as:

$$\nu_t = C_k \Delta_x k_\Delta^{1/2} \tag{4.10}$$

where $C_k$ is a constant. The sub-grid scale turbulent intensity $u'_{\Delta_x}$ is linked to the sub-grid scale kinetic energy $k_\Delta$ if the turbulence is assumed homogeneous and isotropic at the sub-grid scale:

$$k_\Delta = \frac{1}{2}\left(3u'_{\Delta_x}\right) \tag{4.11}$$

Combining Eqs. 4.10 and 4.11 gives an expression for $u'_{\Delta_x}$ in terms of the turbulent eddy viscosity $\nu_t$:

$$u'_\Delta = \left(\frac{2}{3}\right)^{1/2} \frac{\nu_t}{C_k \Delta_x} \tag{4.12}$$

As discussed in Wang et al. (2011), the turbulent intensity should be expressed at the flame filter scale $\Delta$ which differs from the cell size $\Delta_x$. For that purpose it is assumed that both $\Delta$ and $\Delta_x$ lie in the inertial range of the turbulence

spectrum supposed homogeneous and isotropic. In this range, the kinetic energy follows the scaling law $k_\Delta \propto \Delta^{2/3}$ which may also be recast as $u'_\Delta \propto \Delta^{1/3}$. Therefore, the sub-filter scale turbulent intensity $u'_\Delta$ finally reads:

$$u'_\Delta = u'_{\Delta_x} \left(\frac{\Delta}{\Delta_x}\right)^{1/3} = \left(\frac{2}{3}\right)^{1/2} \frac{\nu_t}{C_k \Delta_x} \left(\frac{\Delta}{\Delta_x}\right)^{1/3} \tag{4.13}$$

The value of the model constant $C_k$ is actually the parameter of the model which will be studied in this thesis. Two different values will be selected to conduct a sensitivity analysis. In order to choose these values in a relevant range, the estimation of the order of magnitude is first conducted. A methodology to estimate $C_k$ has been proposed by Moureau (2004). $C_k$ is expressed as a function of the Smagorinsky constant $C_s$ assuming a local equilibrium between production and dissipation of the sub-grid scale kinetic energy $k_\Delta$:

$$C_k = \pi^{1/3} \left(\frac{2}{3C_K}\right)^{1/2} C_s^{4/3} \tag{4.14}$$

where $C_K$ is the Kolmogorov constant $C_K \approx 1.4$. The Smagorinsky constant $C_s$ depends on the flow configuration. For instance, $C_s = 0.18$ for homogeneous and isotropic turbulence while $C_s = 0.10$ is an optimal value for turbulent channel flows exhibiting shear layers (Deardorff, 1970). For those cases, the corresponding values of $C_k$ are $C_k = 0.10$ and $C_k = 0.05$, respectively. However, neither HIT nor channel flows correspond exactly to practical combustions chambers. For this reason, we will conduct a sensitivity study on this model parameter.

Unfortunately, the Prandtl-Kolmogorov model does not guaranty $u'_\Delta = 0$ in laminar flows. Indeed, the thermal expansion across the flame front accelerates the flow. Most of the turbulence models will then predict $\nu_t \neq 0$ leading to $u'_\Delta \neq 0$. As a consequence, the wrinkling factor modeled by Eq. 4.8 will not degenerate to laminar flame regimes as required in Sec. 1.3.

### 4.2.2 Colin et al. (2000) approach

In order to suppress the contribution of the thermal expansion across the flame front, Colin et al. (2000) proposed to define an operator which subtracts the dilatational part of the resolved velocity field. The model, initially derived to predict the turbulence intensity at the scale $n_x\Delta_x$, has been adapted by Wang et al. (2011) to focus on the sub-filter scale turbulence intensity:

$$u'_\Delta = c_2 \Delta_x^3 \left|\nabla^2 \left(\nabla \times \widetilde{\mathbf{u}}\right)\right| \left(\frac{\Delta}{n_x \Delta_x}\right)^{1/3} \tag{4.15}$$

where $n_x = 10$ and $c_2 = 2$ are model constants. This model will also be considered in the further parametric study.

## 4.3 Estimation of the fractal-like model parameter $\beta$

### 4.3.1 Static formulation

Various values of $\beta$ have been reported in the literature depending on the flame and flow topology as well as the turbulence intensity. Charlette et al. (2002a) reported that $\beta = 0.5$ produces reasonable behavior of SFS wrinkling model over a significant range of flame and turbulence parameters. More recently, the DNS of a lean premixed turbulent flame (Moureau et al., 2011b) has been post-processed by Veynante et al. (2013) to compute the value of $\beta$ for various flame filter scales $\Delta$. The value of $\beta = 0.337$ is found to fit correctly the DNS data. Veynante et al. (2013) also note that this value is in good agreement with early studies on fractal models (Gouldin, 1987; Kerstein, 1988a). In a LES context, the value $\beta \approx 0.3$ is also often used in the literature (Wang et al., 2011; Schmitt et al., 2013b,a). Consequently, there is no unique and universal value of $\beta$ which vary in complex turbulent situations and certainly depends on the local flow and flame features.

### 4.3.2 Dynamic formulation

An alternative is to automatically adjust $\beta$ from the resolved wrinkling scales which are accessible in LES (Wang et al., 2011, 2012; Veynante et al., 2013; Schmitt et al., 2013a; Charlette et al., 2002b). Following the original idea of the Germano et al. (1991) dynamic model for unresolved momentum transport, the $\beta$ parameter is expressed by making equal the flame surface density $\Sigma$ at an effective filter scale $\widehat{\overline{\Delta}}$ estimated from two different filter sizes of the resolved scales range. For that purpose, a test-filter operator $\widehat{\cdot}$ of size $\widehat{\Delta}$ is introduced such as $\widehat{\Delta} \geq \Delta$ where $\Delta$ is the flame filter size. An effective filter operator $\widehat{\overline{\cdot}}$ is also defined as equivalent to the successive convolution of any variable $\Phi$ with the flame filter $\overline{\cdot}$ of size $\Delta$ and test filter $\widehat{\cdot}$ of size $\widehat{\Delta}$ as:

$$\widehat{\overline{\Phi}} = \widehat{\left(\overline{\Phi}\right)} \tag{4.16}$$

In practice, Gaussian filters are often used as they are easy to implement[1] for unstructured meshes and on massively parallel architectures. In this context, the effective filter size $\widehat{\overline{\Delta}}$ reads:

$$\widehat{\overline{\Delta}} = \sqrt{\widehat{\Delta}^2 + \Delta^2} \tag{4.17}$$

[1]Gaussian filters are easily implemented by using successively the numerical diffusion operator available in the CFD code (Moureau et al., 2011b).

The generalized flame surface density (Boger et al., 1998) at the scale $\widehat{\overline{\Delta}}$ reads:

$$\Sigma_{\widehat{\overline{\Delta}}} = \widehat{\overline{|\nabla c|}} = \widehat{\left(\overline{|\nabla c|}\right)} = \widehat{\Sigma_{\Delta}} \tag{4.18}$$

Using the FSD formalism presented in Sec. 1.5.2.2, it is possible to express these different terms using the sub-filter scale wrinkling function $\Xi$ leading to:

$$\Sigma_{\widehat{\overline{\Delta}}} = \Xi_{\widehat{\overline{\Delta}}} \left|\nabla \widehat{\overline{c}}\right| = \widehat{\Xi_{\Delta} |\nabla \overline{c}|} \tag{4.19}$$

Charlette et al. (2002b) pointed out that even if the relation 4.19 is theoretically valid at each node of the LES mesh, the very local application of the dynamic procedure may lead to unphysical results. This issue may also be viewed from the statistical point of view. As the dynamic procedure uses resolved scales to estimate the model parameters for unresolved processes, this estimation should be made using a sufficient number of "samples" (*i.e.* average the known quantities over a volume larger than a single mesh cell). For that purpose, a "locally averaged" formulation of Eq. 4.19 as been proposed:

$$\left\langle \Xi_{\widehat{\overline{\Delta}}} \left|\nabla \widehat{\overline{c}}\right| \right\rangle = \left\langle \widehat{\Xi_{\Delta} |\nabla \overline{c}|} \right\rangle \tag{4.20}$$

where $\langle \cdot \rangle$ averages over a given volume that may be chosen in a different manners as discussed in Schmitt et al. (2013a,b).

At this point, it is worth noting that the original Charlette et al. (2002a) model (Eq. 4.8) was first used by Wang et al. (2011); Schmitt et al. (2013b) to model $\Xi_{\Delta}$ and $\Xi_{\widehat{\overline{\Delta}}}$ in this expression. The recent DNS analysis conducted by Veynante et al. (2013) however showed that the model is saturated (Eq. 4.9) in practical configurations. This results was also noticed in LES computations such as the one performed by Schmitt et al. (2013b). Therefore, it is reasonable and more convenient to use the saturated form of the Charlette et al. (2002a) model, which actually corresponds to a fractal-like power law. Equation 4.20 then reads:

$$\left\langle \left(\frac{\widehat{\overline{\Delta}}}{\delta_c}\right)^{\beta} \left|\nabla \widehat{\overline{c}}\right| \right\rangle = \left\langle \widehat{\left(\frac{\Delta}{\delta_c}\right)^{\beta}} |\nabla \overline{c}| \right\rangle = \left\langle \left(\frac{\Delta}{\delta_c}\right)^{\beta} \widehat{|\nabla \overline{c}|} \right\rangle \tag{4.21}$$

Assuming that $\beta$ is uniform over the averaging volume defined by $\langle \cdot \rangle$ and remains constant for the model at both $\Delta$ and $\widehat{\overline{\Delta}}$ scales, the model parameter

can be computed using the following expression:

$$\beta = \frac{\ln\left(\left\langle\left|\widehat{\nabla\widetilde{c}}\right|\right\rangle / \left\langle\left|\nabla\widehat{\widetilde{c}}\right|\right\rangle\right)}{\ln\left(\widehat{\Delta}/\Delta\right)} \tag{4.22}$$

Based on an infinitely thin flame front assumption, Veynante et al. (2013) proposed to replace the unknown Reynolds-filtered progress variables $\bar{c}$ by the Favre-filtered quantities $\widetilde{c}$ as:

$$\beta \approx \frac{\ln\left(\left\langle\left|\widehat{\nabla\widetilde{c}}\right|\right\rangle / \left\langle\left|\nabla\widehat{\widetilde{c}}\right|\right\rangle\right)}{\ln\left(\widehat{\Delta}/\Delta\right)} \tag{4.23}$$

The validity of this approximation was also confirmed from DNS analysis. The normalized progress variable $\widetilde{c}$ is estimated from the resolved progress variable $\widetilde{Y_c}$ as $\widetilde{c} = \widetilde{Y_c}/\widetilde{Y_c^{\mathrm{eq}}}$ where $\widetilde{Y_c^{\mathrm{eq}}} = \frac{1}{\overline{\rho}^{eq}} \int_0^1 \rho Y_c^{\mathrm{eq}}(z') P_\beta(z', \widetilde{z}, S_z) dz'$.

## 4.4 Impact of $u'_\Delta$ and $\beta$ sub-models on the SwB5 non-adiabatic turbulent stratified flame

The influence of the sub-models for $\beta$ and $u'_\Delta$ on the simulation of the non-adiabatic turbulent stratified flame SwB5 is studied in this section. The SWB5 flame is chosen because the thermochemical equilibrium in the IRZ is not impacted by the preferential diffusion phenomena (See Sec. 3.3.4.3) and can be correctly captured by the non-adiabatic F-TACLES model. The experimental and numerical set-up have been described in the chapter 3 (See Sec. 3.3). The non-adiabatic F-TACLES model, presented in Sec. 2.3.4, is selected for the simulation. Several LES are performed only modifying the modeling strategy for the unresolved flame wrinkling $\Xi_\Delta^{Y_c}$ leading to a set of 7 different computations detailed in the following section.

### 4.4.1 Simulated cases

A parametric study is performed through 7 numerical simulations whose characteristics are summarized in Tab. 4.1. The first simulations uses the original Charlette et al. (2002a) model with a constant value of the parameter $\beta = 0.5$ as originally proposed by the authors. These LES only differ by the sub-filter scale (SFS) velocity fluctuation model. The SWB5-NAD-CH1 case uses the Prandtl-Kolmogorov approach and Eq. (4.13) to model the sub-filter scale turbulence intensity $u'_\Delta$ with a model constant $C_k = 0.1$ while the simulation SWB5-NAD-CH2 uses $C_k = 0.05$. The Colin et al. (2000) approach (See Sec. 4.2.2) is used in SWB5-NAD-CO to model $u'_\Delta$.

The second part of the simulations uses the saturated form (Eq. (4.9)) of the Charlette et al. (2002a) model to investigate the influence of the $\beta$ parameter. Two simulations, namely SWB5-NAD-B5 and SWB5-NAD-B3, have been performed with $\beta = 0.5$ and $\beta = 0.3$, respectively. In the computation SWB5-NAD-BD, the $\beta$ parameter is not kept constant anymore. The dynamic procedure employed in Schmitt et al. (2013a) is then employed to estimate $\beta$ from the resolved flame wrinkling as detailed in Sec. 4.3. Note that as the configuration is axysymmetric along the SwB burner axis, the $\beta$ parameter, computed dynamically in SWB5-NAD-BD, is supposed to evolve only in the streamwise direction. Therefore, the volume averaging $\langle \cdot \rangle$ operation in Eq. (4.23) is conditioned over radial slices of thickness $4\boldsymbol{\Delta}$.

To better estimate the influence of the unresolved sub-filter scale wrinkling, an LES computation of the SwB5 flame is performed without accounting for unresolved wrinkling (SWB5-NAD-B0 is conducted using $\Xi_\Delta = 1$).

**Table 4.1:** *Simulated cases. The flow-through-time (FTT) is estimated as* $FTT = L/\overline{U_i} = 10$ *ms with* $L = 0.1$ *m the height of the reaction zone and* $\overline{U_i} = 10$ *m.s*$^{-1}$ *the bulk velocity of inner tube. The F-TACLES filtered look-up tables are generated with a flame filter size* $\Delta = 2.5$ *mm. These computations are conducted on an IBM Blue Gene/Q machine on 1024 cores.*

| Simu. # | $\Xi_\Delta$ model | $u'_\Delta$ model | $\beta$ model | 1FTT cost [hCPU] |
|---|---|---|---|---|
| SWB5-NAD-CH1 | Eq. 4.8 | Eq. 4.13 ($C_k = 0.1$) | 0.5 | 18800 hCPU |
| SWB5-NAD-CH2 | Eq. 4.8 | Eq. 4.13 ($C_k = 0.05$) | 0.5 | 18800 hCPU |
| SWB5-NAD-CO | Eq. 4.8 | Eq. 4.15 | 0.5 | 19000 hCPU |
| SWB5-NAD-B5 | $\Xi_\Delta = (\Delta/\delta_c)^\beta$ | - | 0.5 | 18400 hCPU |
| SWB5-NAD-B3 | $\Xi_\Delta = (\Delta/\delta_c)^\beta$ | - | 0.3 | 18400 hCPU |
| SWB5-NAD-BD | $\Xi_\Delta = (\Delta/\delta_c)^\beta$ | - | Dynamic | 22300 hCPU |
| SWB5-NAD-B0 | $\Xi_\Delta = 1$ | - | - | 18000 hCPU |

## 4.4.2 Results analysis

### 4.4.2.1 Resolved flame wrinkling

Figure 4.1 shows an instantaneous iso-surface of progress variable reaction rate $\widetilde{\dot{\omega}}_{Y_c}$ colored by the normalized mixture fraction $\widetilde{z}$. The resolved flame wrinkling varies with the centerline position: the flame front is weakly affected by turbulent motions near the burner exit since the incoming flow only exhibits a low level of turbulence, generated in the injection tube. When the flame front crosses the turbulent shear layer holding between tubes $i$ and $o$, the reactive layer is more wrinkled. The level of wrinkling still increases further downstream where turbulent structures are created at the shear layer between the injected streams and the air co-flow. Assuming similarity between resolved and unresolved wrinkling scales, the same complex behavior is expected for $\Xi_\Delta$ as it

directly represents the flame wrinkling at the sub-filter scale. This distribution of the flame wrinkling is confirmed by LES computations performed by other groups on finer grids (Proch and Kempf, 2014; Nambully et al., 2014a,b). This flame exhibits then different levels of flame-turbulence interactions, from quasi-laminar to strongly wrinkled flame fronts.

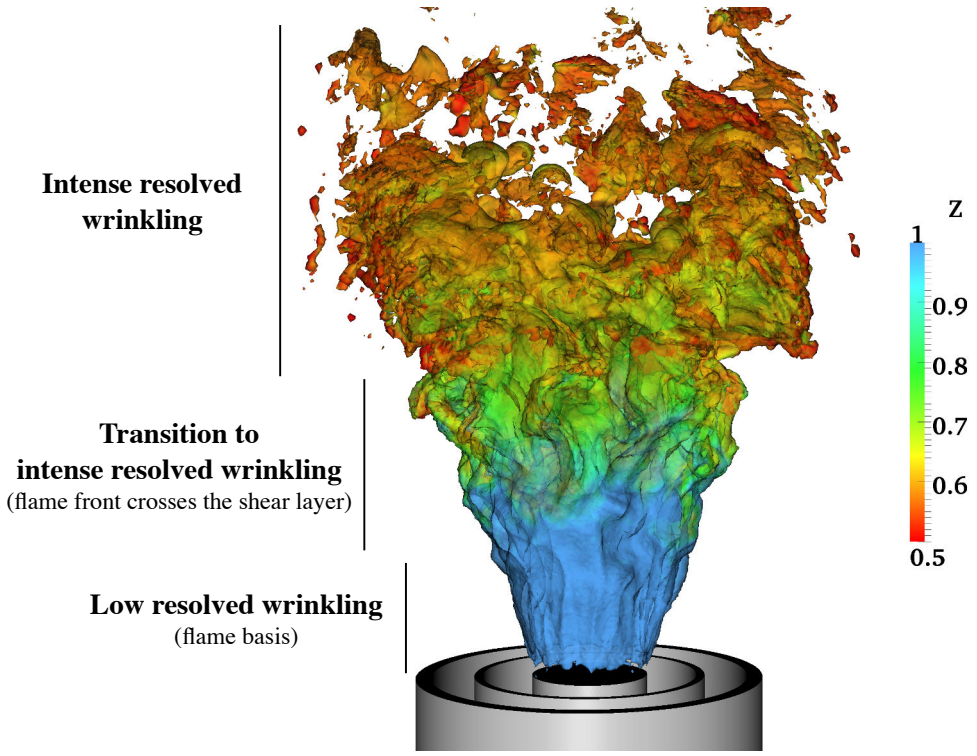


**Figure 4.1:** *Instantaneous iso-surface of the filtered progress variable reaction rate* $\widetilde{\dot{\omega}}_{Y_c}$ *colored by the resolved mixture fraction* $\widetilde{z}$ *for the non-adiabatic stratified computation of the SwB5 flame (SWB5-NAD-BD).*

#### 4.4.2.2 Sensitivity to the $u'_\Delta$ sub-model

Radial profiles of mean and RMS of temperature are compared to experimental data in Fig. 4.2. In this paragraph, the focus is made on the influence of $u'_\Delta$ sub-model (SWB5-NAD-CH1, SWB5-NAD-CH2 and SWB5-NAD-CO). SWB5-NAD-CH2 mispredicts the mean flame brush position for axial distances $Z \geq 20$ mm. However, SWB5-NAD-CH1 predicts a flame brush closer to experimental measurements, showing that the results are very sensitive to the Prandtl-Kolmogorov model constant $C_k$ in Eq. (4.13). The simulation SWB5-NAD-CO also gives a good prediction of the mean flame brush but the same sensitivity to the $u'_\Delta$ model constant is expected. The first conclusion is that the prediction of the turbulent flame position is then strongly correlated to the

$u'_\Delta$ sub-model uncertainties.

Figure 4.3 shows the resolved mixture fraction for the different LES considered here. The mean mixing profiles are not strongly impacted by $u'_\Delta$ model and more generally by the $\Xi_\Delta$ modeling strategy. The mixing process, mainly controlled by the flow field, is not sensitive to a slight modification of the mean flame brush prediction. The same conclusion holds for the RMS of mixture fraction even if a slight translation of the profiles is observed far from the burner exit.

#### 4.4.2.3 Sensitivity to the $\beta$ parameter

The influence of the $\beta$ parameter is then studied by focusing on the computations where the saturated formulation of $\Xi_\Delta$ is used (SWB5-NAD-B5, SWB5-NAD-B3, SWB5-NAD-B0 and SWB5-NAD-BD). The SWB5-NAD-B3 leads to fair agreement with experimental data downstream whereas SWB5-NAD-B5 and SWB5-NAD-B0 completely mispredict the mean flame position. The saturated formulation of $\Xi_\Delta$ is however not relevant to predict flame wrinkling observed in quasi-laminar flame regimes. This is why neither SWB5-NAD-B5 nor SWB5-NAD-B3 methods predict the flame brush position at the first axial locations, near the flame basis. Therefore, a constant $\beta$ parameter fails in predicting the different wrinkling regimes observed at both the flame basis and in the intense wrinkling zone (Fig. 4.1).

As shown by plots of SWB5-NAD-BD simulation, dynamic estimation of $\beta$ brings then enough flexibility to Eq. (4.9) for capturing both quasi-laminar and turbulent flame regimes. Figure 4.4 shows a schematic view of the procedure used to estimate dynamically the fractal-like model parameter $\beta$. In the present study, $\beta$ only varies along the burner axis and is computed using a sliding volume averaging operation shown in Fig. 4.4. This strategy provides a very good prediction of the mean properties of the flame both at the quasi-laminar flame basis[2] ($\beta = 0.15$ at Z = 10 mm) and further downstream where the flame is fully turbulent ($\beta \approx 1.0$ at Z = 40 mm). The dynamic estimation of the $\beta$ parameter only induces a 20 % increase in computational costs as shown in Tab. 4.1.

[2]The dynamic estimation of the $\beta$ parameter goes theoretically to zero in laminar cases or when the wrinkling is fully resolved as shown by Veynante et al. (2013)

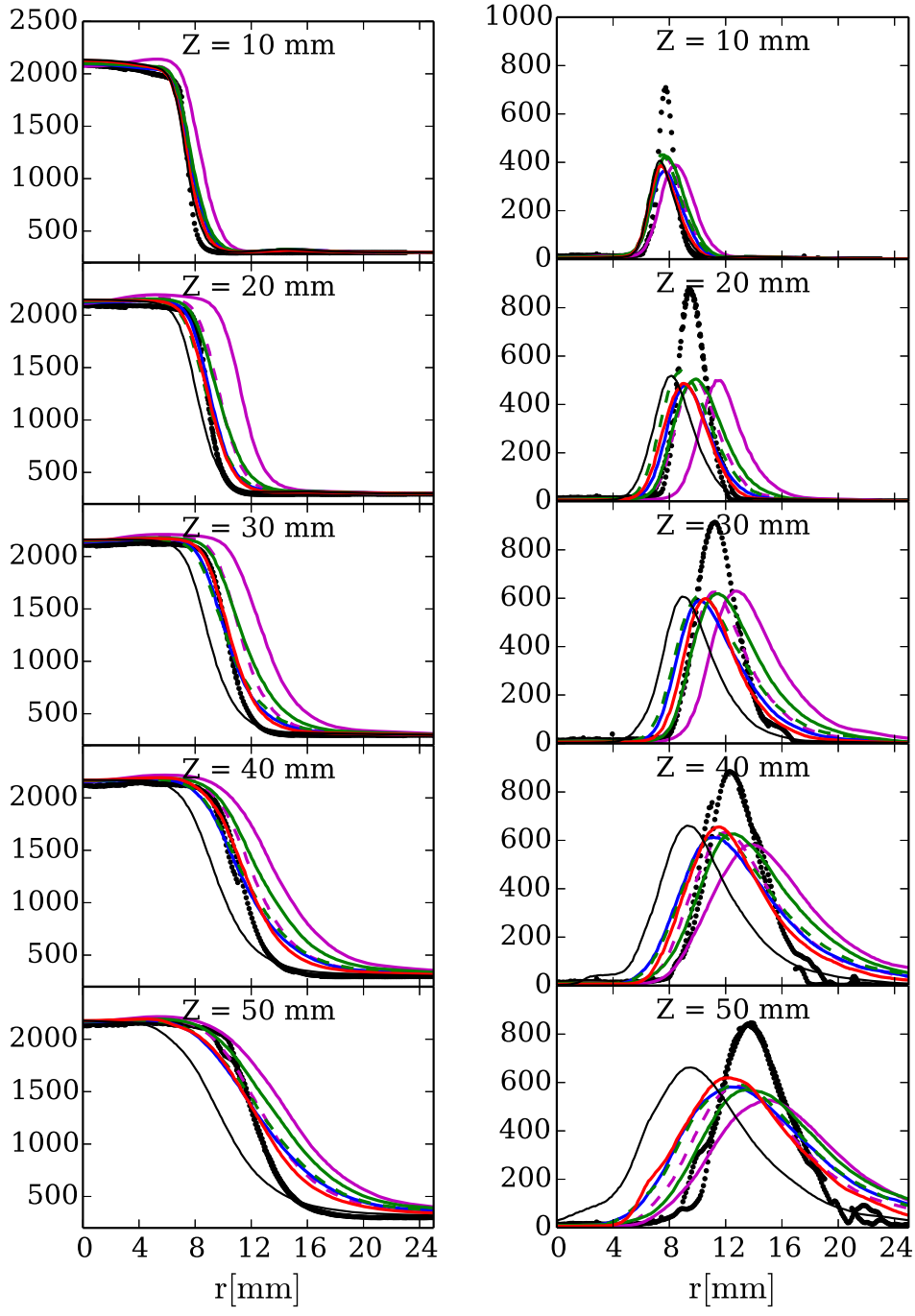


(a) Mean (b) RMS

**Figure 4.2:** *Radial profiles of mean and RMS of temperature $\widetilde{T}$ [K] for the stratified case (SwB5). Legend: - - - SWB5-NAD-CH1; — SWB5-NAD-CH2; — SWB5-NAD-CO; — SWB5-NAD-B5; - - - SWB5-NAD-B3; — SWB5-NAD-BD; — SWB5-NAD-B0; • • Experiments.*

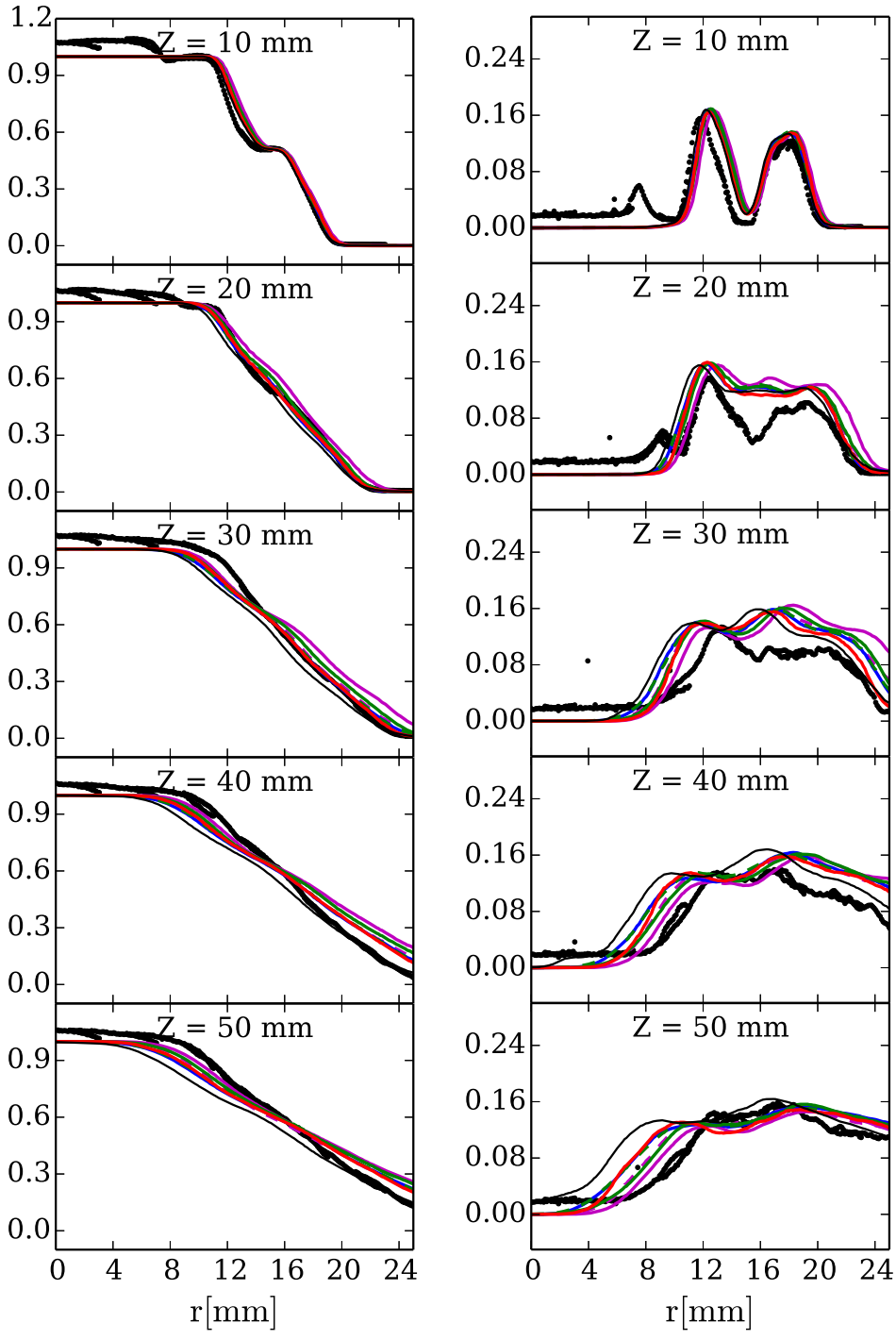


(a) Mean (b) RMS

**Figure 4.3:** *Radial profiles of mean and RMS of normalized mixture fraction $\widetilde{z}$ [-] for the stratified case (SwB5). Legend: - - - SWB5-NAD-CH1; — SWB5-NAD-CH2; — SWB5-NAD-CO; — SWB5-NAD-B5; - - - SWB5-NAD-B3; — SWB5-NAD-BD; — SWB5-NAD-B0; • • Experiments.*

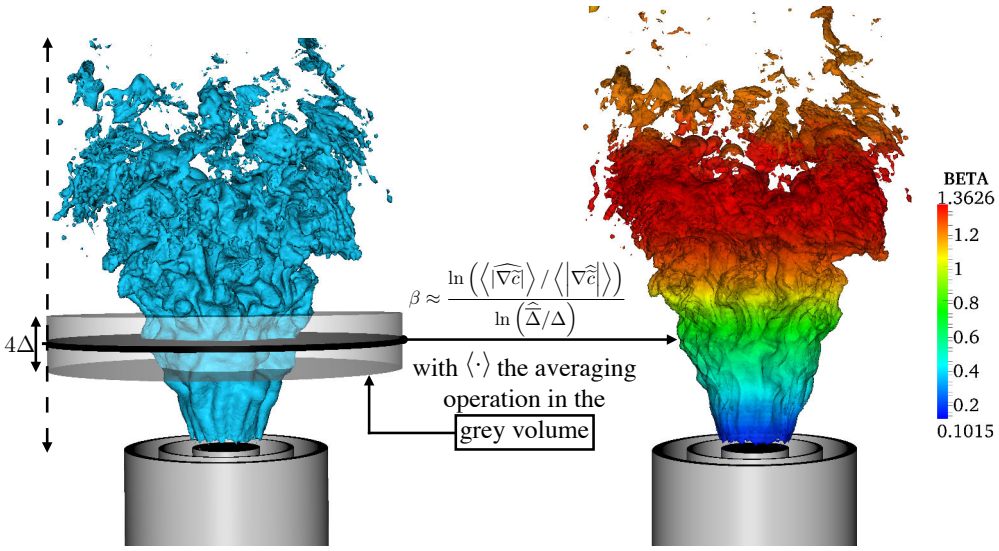


**Figure 4.4:** *Instantaneous iso-surfaces of the filtered progress variable reaction rate* $\widetilde{\dot{\omega}}_{Y_c}$*. (Left) Schematic view of the volume averaging operation needed for the dynamic estimation of the* $\beta$ *parameter. (Right) The iso-surface is colored by the* $\beta$ *parameter computed at a given instant using the dynamic procedure.*

### 4.4.3 Influence of the unresolved wrinkling model on the flow dynamics

Figures 4.5 and 4.6 show the radial profiles of axial and radial velocity statistics at several distances from the burnet exit. As for the temperature field, the prediction of unresolved wrinkling greatly impact the flow field. The main differences between each cases are observed near the centerline ($r < 15$ mm). The mean flame brush is in direct correlation with the level of mean axial and radial velocities: the axial velocity increases with the opening of the flame brush. The dynamic estimation of the $\beta$ parameter applied to the saturated form of the Charlette et al. (2002a) model captures both the flow field at the flame basis and further downstream.

The impact of the unresolved wrinkling model on the flow dynamics is also illustrated by analyzing the inner recirculation zone. Figure 4.7 compares cross section of mean axial velocity iso-surfaces at the IRZ location for the SwB5 case. The adiabatic computations performed in Chapter 3 is also added for comparison purpose. First, both the position and the dynamics of the IRZ differ between SWB5-AD-CH1 and SWB5-NAD-CH1 as thermal expansion is reduced near the burner wall when heat losses are considered. A direct correlation between the height of the IRZ (Fig. 4.7) and the mean flame brush position near the burner exit (Fig. 4.2) is observed: the highest opening angles of the mean flame brush induce to the smallest recirculation zones. It is worth noting that SWB5-NAD-BD provides a very good prediction of the mean flame brush position, the flow and the IRZ aerodynamic.

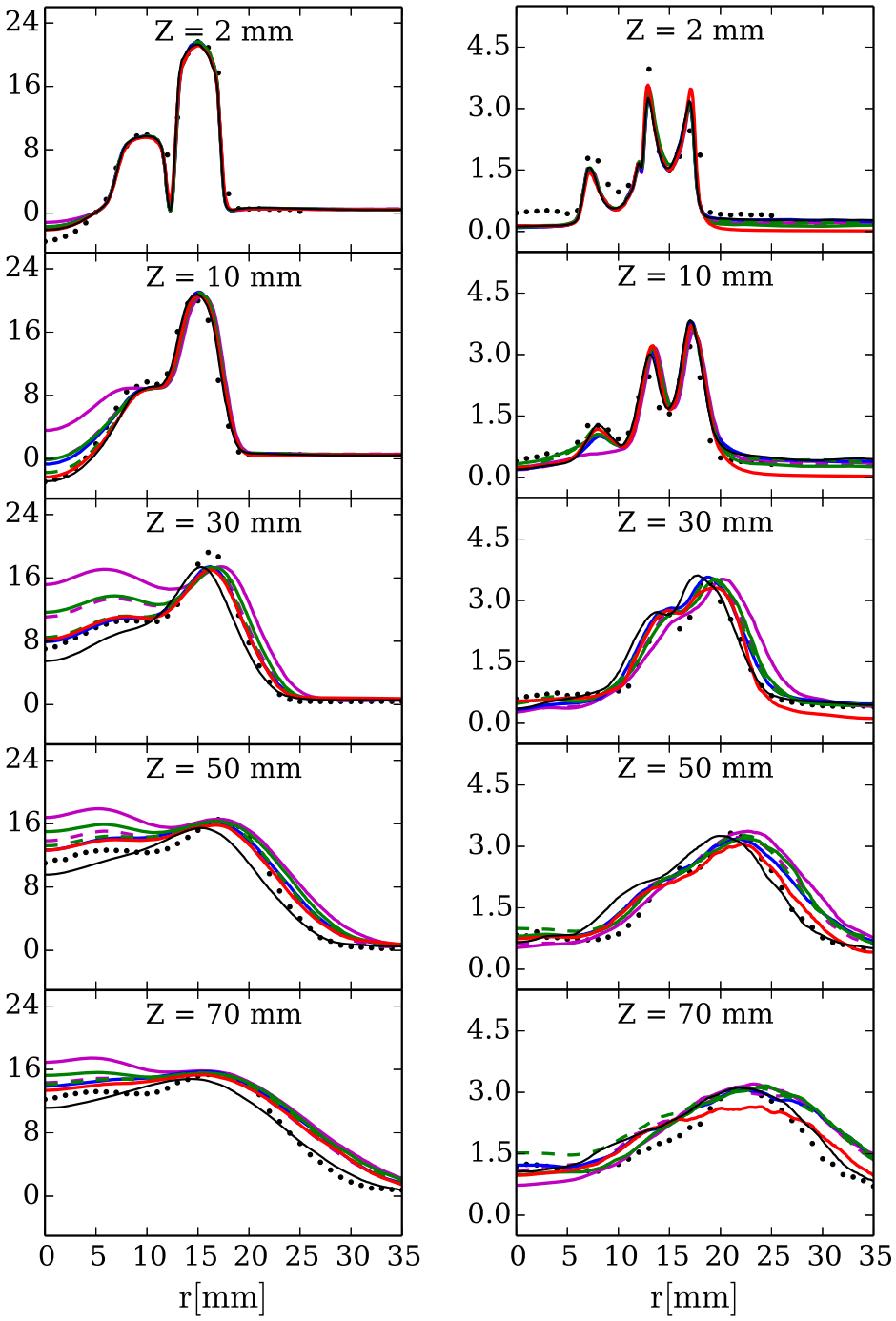


(a) Mean (b) RMS

**Figure 4.5:** *Radial profiles of mean and RMS of axial velocity $\widetilde{U}_z$ $[m.s^{-1}]$ for the stratified case (SwB5). Legend: - - - SWB5-NAD-CH1; — SWB5-NAD-CH2; — SWB5-NAD-CO; — SWB5-NAD-B5; - - - SWB5-NAD-B3; — SWB5-NAD-BD; — SWB5-NAD-B0; • • Experiments.*

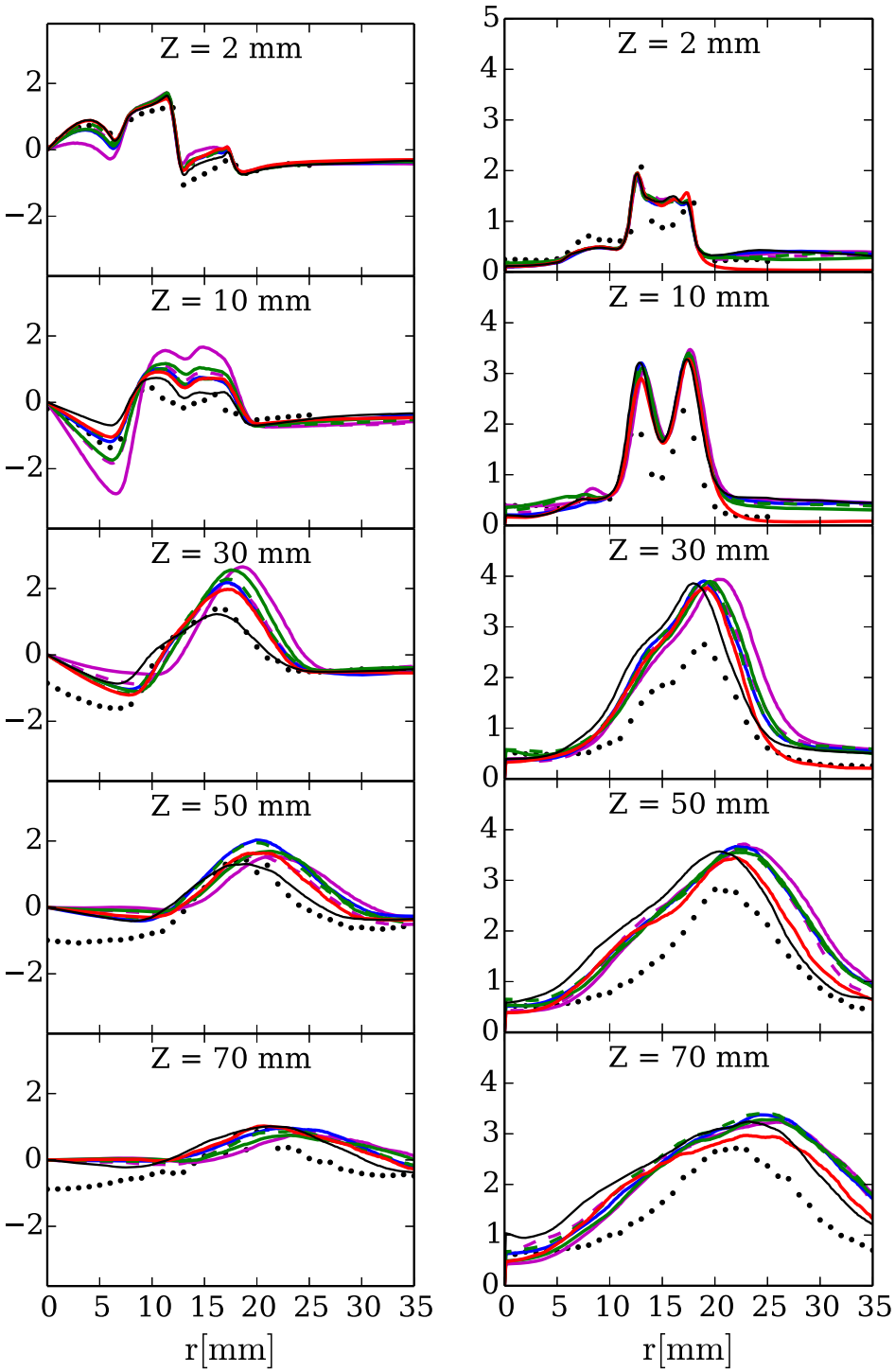


(a) Mean (b) RMS

**Figure 4.6:** *Radial profiles of mean and RMS of radial velocity $\widetilde{U}_r$ $[m.s^{-1}]$ for the stratified case (SwB5). Legend: - - - SWB5-NAD-CH1; — SWB5-NAD-CH2; — SWB5-NAD-CO; — SWB5-NAD-B5; - - - SWB5-NAD-B3; — SWB5-NAD-BD; — SWB5-NAD-B0; • • Experiments.*

(a) Exp. (2-D PIV) (b) AD-CH1 (c) NAD-CH1 (d) NAD-CH2 (e) NAD-CO (f) NAD-B5 (g) NAD-B3 (h) NAD-BD (i) NAD-B0

**Figure 4.7:** *Cross section in the medium plane of the iso-surfaces of mean axial velocity $\widetilde{U}_z$ for the stratified case (SwB5). For a each figure, isolines values are, from right to left, $\widetilde{U}_z = \{3; 2; 1; 0; -1; -2; -3\}$ $m.s^{-1}$. Dashed lines: $\widetilde{U}_z < 0$ ; Solid lines: $\widetilde{U}_z \geq 0$.*

## 4.5 Towards a parameter-free modeling approach

It has been shown that complex turbulent flames exhibits different levels of wrinkling depending of the flow fields and stabilization process. Static subgrid scale wrinkling models are very sensitive to $u'_\Delta$ sub-model uncertainties. To limit this phenomenon, we retain a fractal-like formulation ($\Xi_\Delta = (\Delta/\delta_c)^\beta$) and estimate the unique parameter $\beta$ from resolved scales through a dynamic procedure. This method, described in Sec. 4.1, capture both quasi-laminar and turbulent regimes found in the SwB5 flame. Indeed, the dynamic formulation is sufficiently flexible to capture the flame brush position over the whole computational domain. Similar conclusions will be observed with other modeling approaches based on flame surface considerations where $\Xi_\Delta$ model is involved.

From a practical point of view, the dynamic modeling approach combined to the non-adiabatic F-TACLES model present different advantages:

- This non-adiabatic turbulent combustion model is almost parameter-free. The last quantity that could be considered as a parameter of the model is the inner cut-off scale $\delta_c$. In the literature, this variable is either set to $\delta_c = \delta_l^0$ or $\delta_c = 2\delta_l^0$ and would necessitate deeper studies such as DNS analysis.
- It captures correctly laminar (no wrinkling) and turbulent (highly wrinkled) flames.
- It captures correctly adiabatic and non-adiabatic turbulent flames.
- The extra computational cost of the dynamic procedure is limited ($\approx$ +20% for the cases studied in this thesis).

# Chapter 5

# Coupling flame and flow filtered equations: a new LES formalism for turbulent combustion

**Contents**

*A recurrent issue in LES of turbulent combustion is that the flame thickness is smaller than the grid size. Broadening of the reactive layer is then mandatory to ensure a proper propagation of the filtered flame front. Once the flame front has been broadened by the LES combustion model, two main issues arise. First, as discussed in the previous chapter, the flame wrinkling lost during the broadening process has to be modeled using known LES quantities. Second, to avoid under-resolved reactive layers, the filter size associated to the flame broadening is much larger than the filter size associated to the flow. The reactive flow governing equations exhibit then two filter operators of different sizes dedicated to the flow field and the flame front, respectively. The mathematical issues between flame and flow filter sizes in LES of turbulent premixed flames are discussed in the present chapter. A general formalism consistent with the two different filter sizes is proposed. Then, new closures of the resulting LES balance equations system are derived using F-TACLES modeling approach. The new model, called F2-TACLES, is first validated by computing 1-D premixed filtered flames. LES of a lean turbulent premixed burner is finally performed to validate the feasibility of the proposed approach.*

## 5.1 Two filter scales in LES of turbulent combustion

In the general context of the LES of turbulent combustion, the reactive flow may be decomposed as two different interacting phenomena illustrated by Fig. 5.1 showing the propagation of a filtered flame front in a turbulent flow. The first one is the turbulent flow field filtered at size $\overline{\Delta}$. The turbulent structures larger than $\overline{\Delta}$ are resolved on the LES grid while smaller ones are modeled by the LES turbulence model. The main role of this model is to predict correctly the dissipation of the unresolved structures at the sub-filter scale. The turbulence model is designed to provide the turbulent viscosity representative of the dissipation of turbulent scales smaller than $\overline{\Delta}$ (which is then a parameter of the model). In practice, the flow filter size $\overline{\Delta}$ also depends on the local mesh size and the numerics of the LES solver because turbulent structures larger than $\overline{\Delta}$ has to be numerically resolved on the LES grid. The smallest resolved scales will then be captured only if they are resolved on a sufficient number of grid points directly depending on the selected numerical strategy. According to Pope (2000), the velocity field $\widetilde{\mathbf{u}}$, Favre-filtered by a Gaussian function of width $\overline{\Delta}$, is well resolved on the LES grid of size $\Delta_x$ when the resolution criteria $\overline{\Delta} > 2\Delta_x$ is satisfied. As for the smallest turbulent scales in general, the flame thickness, defined as $\delta_{Y_c} = {Y_c}^{eq}/\max(|\nabla Y_c|)$, is thinner than the mesh size $\Delta_x$. The basic LES formalism depicted in Sec. 1.2 is therefore applied to the species equations (or progress variable equation). Filtering the progress variable field at the width $\overline{\Delta}$ introduces a resolved flame front of thickness $\delta_{\widetilde{Y}_c} \approx \overline{\Delta}$. As further illustrated in Sec. 5.2.1, the chemical reaction layer (for instance, the

variable $\widetilde{\dot{\omega}}_{Y_c}$) is then under-resolved on the LES grid inducing a misprediction of the flame propagation speed. This issue is well-known and different alternatives have been proposed in the literature to ensure a proper flame propagation speed (Fiorina et al., 2015b). Most of them, based on the geometrical description of the turbulent flame front, are described in Sec. 1.5.2.

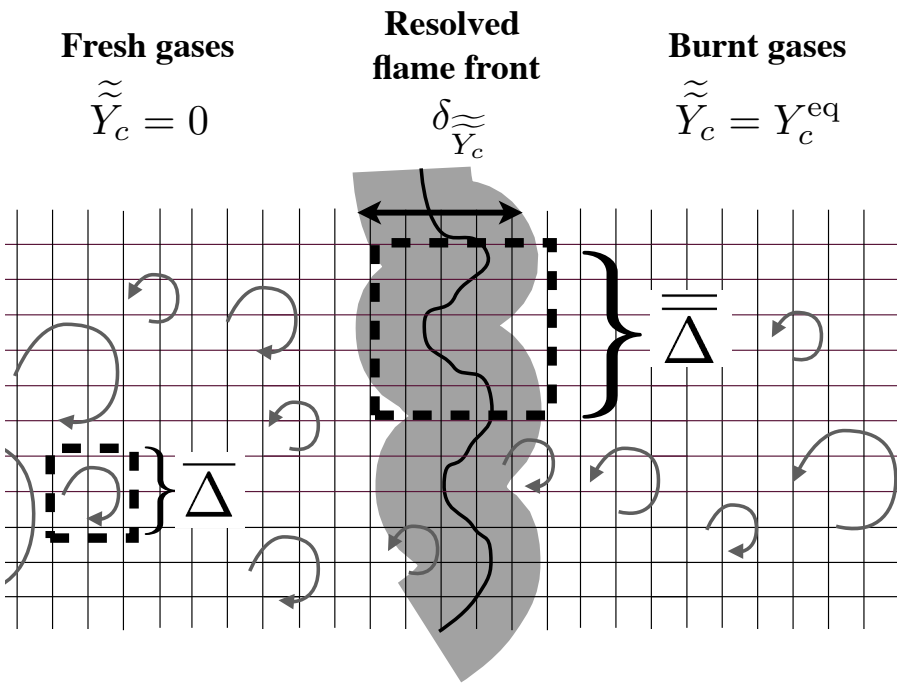


**Figure 5.1:** *Filter size issues in premixed turbulent combustion LES.*

A possible approach consists in applying a filter of size $\overline{\overline{\Delta}} > \overline{\Delta}$ to the flame front. Initially developed for infinitely thin flame front and for single-step chemistry (Boger et al., 1998; Duwig, 2007, 2009), the filtering strategy has been extended to tabulated chemistry leading to the F-TACLES model presented in this thesis. For this model, simulations of propagating filtered premixed planar flames show that the flame resolution criterion $\overline{\overline{\Delta}}/\Delta_x$ depends on the numerical scheme. For instance, the criterion $\overline{\overline{\Delta}}/\Delta_x \geq 8$ is required by the third order TTGC numerical scheme (Colin and Rudgyard, 2000) to predict the proper propagation speed of a laminar premixed filtered flame (Fiorina et al., 2010). The same criterion is obtained for the TFV4A scheme (Kraushaar, 2011) in section 5.4.1.

LES of turbulent combustion therefore involves two filter operators of size $\overline{\overline{\Delta}}$ and $\overline{\Delta}$. The influence of these two different filter operators on the mathematical formalism of both LES equations and combustion models has never been studied

and is investigated here. This chapter is organized as follows. In the first part, the two filter size are included in the LES formalism and consistency issues are discussed. In the second part, in new closure strategy is proposed in the framework of the F-TACLES model. A new model, called F2-TACLES, is then implemented and validated on both laminar and turbulent flames. A similar closure for the thickened flame model TFLES is also proposed in Appendix C.

## 5.2 Coupling flame and flow filtered equations

### 5.2.1 Problem formalism

**Table 5.1:** *Definitions of the filtering operators*

| Filter size | Reynolds | Favre |
|---|---|---|
| $\overline{\Delta}$ | $\overline{\Phi}$ | $\widetilde{\Phi} = \overline{\rho\Phi}/\overline{\rho}$ |
| $\overline{\overline{\Delta}}$ | $\overline{\overline{\Phi}}$ | $\widetilde{\widetilde{\Phi}} = \overline{\overline{\rho\Phi}}/\overline{\overline{\rho}}$ |

Filtering operators used in this chapter are indicated in Tab. 5.1. $\overline{\Phi}$ and $\widetilde{\Phi}$ denote the Reynolds and Favre filtering of a variable $\Phi$ at size $\overline{\Delta}$ while $\overline{\overline{\Phi}}$ and $\widetilde{\widetilde{\Phi}}$ are defined as the values of $\Phi$ filtered at size $\overline{\overline{\Delta}}$. Note that the filter size $\Delta$ is not used anymore because of its ambiguous definition: depending of the context, $\Delta$ is associated either to the flow filter size $\overline{\Delta}$ or to the flame filter size $\overline{\overline{\Delta}}$. In the context of non-reacting flows, continuity and momentum equations are filtered at the scale $\overline{\Delta}$ leading to the following system:

$$\begin{aligned} \frac{\partial \overline{\rho}}{\partial t} + \nabla \cdot (\overline{\rho}\widetilde{\mathbf{u}}) &= 0 \\ \frac{\partial \overline{\rho}\widetilde{\mathbf{u}}}{\partial t} + \nabla \cdot (\overline{\rho}\widetilde{\mathbf{u}}\widetilde{\mathbf{u}}) &= -\nabla \overline{p_2} + \nabla \cdot \left(\overline{\tau} + \overline{\tau}^t\right) \end{aligned}$$

where $\overline{\rho}$ and $\widetilde{\mathbf{u}}$ are the filtered density and velocity vector, respectively. $\overline{\tau}$ is the filtered viscous tensor and $\overline{\tau}^t = -\overline{\rho}\left(\widetilde{\mathbf{u}\mathbf{u}} - \widetilde{\mathbf{u}}\widetilde{\mathbf{u}}\right)$ the Reynolds stresses. In a low-Mach number context, $p_2$ denotes the hydrodynamic pressure (See Sec. B.6).

Considering reactive flows, the propagation of a flame front is governed by the chemical species balance equation:

$$\frac{\partial \rho Y_k}{\partial t} + \nabla \cdot (\rho \mathbf{u} Y_k) = -\nabla \cdot (\rho Y_k V_k) + \rho \dot{\omega}_{Y_k} \tag{5.1}$$

where $Y_k$, $\dot{\omega}_{Y_k}$ and $V_k$ are the mass fraction, the chemical reaction rate and the molecular diffusion velocity of the $k$-th species, respectively. Note that in the context of tabulated chemistry, Eq. (5.1) is replaced by the progress

variable equation. Assuming steady state in the flame coordinate system, the integration of Eq. (5.1) in the direction $x_n$ normal to the flame front gives the flame consumption speed $S_l$:

$$S_l = \frac{1}{\rho^u(Y_k^b - Y_k^u)} \int_{-\infty}^{+\infty} \rho\dot{\omega}_{Y_k} dx_n \tag{5.2}$$

where superscripts $u$ and $b$ refer to fresh and burnt gases states, respectively. Equation (5.2) shows that a reliable computation of the flame surface propagation requires a fine numerical resolution of the chemical reaction rate $\dot{\omega}_{Y_k}$ involved in the integral of the RHS. This issue is illustrated in Fig. 5.2 showing the temperature and $CO_2$ chemical reaction rate $\rho\dot{\omega}_{Y_{CO_2}}$ normalized by its maximum value and extracted from a 1-D laminar premixed $CH_4$-air flame computed using a detailed chemical scheme (Lindstedt, 1997). This numerical flame solution, resolved on a very fine grid, serves as a reference. Squares symbols, separated by a constant distance $\Delta_x = 0.5$ mm, are superimposed to each filtered variable profile. It illustrates the position of a virtual grid of size $\Delta_x \approx \delta_{Y_c}$ representative of the typical mesh grids found in LES of complex combustion chambers. The unfiltered temperature profile in Fig. 5.2(a) is first filtered at the flow filter size $\overline{\Delta}$. The chemical reaction rate in Fig. 5.2(b) is then filtered at two different sizes ($\overline{\Delta} = 3\Delta_x$ and $\overline{\overline{\Delta}} = 10\Delta_x$), chosen for illustration purpose, and normalized by the maximum filtered values. The reference chemical reaction rate profiles are shown by the solid lines whereas chemical reaction rate profiles, which would be resolved on the LES grid (assuming first order reconstruction), are shown by dashed lines. The reconstruction of the temperature filtered at size $\overline{\Delta}$ is satisfying and does not imply a filtering with a larger filter size. The same conclusion also holds for the density profile. However, the chemical reaction rate $\overline{\rho\dot{\omega}_{Y_{CO_2}}}$, filtered at the size $\overline{\Delta}$, is under-resolved on the LES grid, which would lead to numerical errors in the RHS integral estimation of Eq. (5.2). At the opposite, filtering the flame front at a size $\overline{\overline{\Delta}} > \overline{\Delta}$ correctly describes the profile of $\overline{\overline{\rho\dot{\omega}_{Y_{CO_2}}}}$. Therefore, a sufficient resolution of the flame front is ensured by filtering chemical species balance equation (5.1) at a size $\overline{\overline{\Delta}}$ larger than the flow filter size $\overline{\Delta}$ leading to the following equation system:

$$\frac{\partial\overline{\rho}}{\partial t} + \nabla\cdot(\overline{\rho}\widetilde{\mathbf{u}}) = 0 \tag{5.3}$$

$$\frac{\partial\overline{\rho}\widetilde{\mathbf{u}}}{\partial t} + \nabla\cdot(\overline{\rho}\widetilde{\mathbf{u}}\widetilde{\mathbf{u}}) = -\nabla\overline{p_2} + \nabla\cdot\left(\overline{\tau} + \overline{\tau}^t\right) \tag{5.4}$$

$$\frac{\partial\overline{\overline{\rho}}\widetilde{\widetilde{Y_k}}}{\partial t} + \nabla\cdot\left(\overline{\overline{\rho}}\widetilde{\widetilde{\mathbf{u}}}\widetilde{\widetilde{Y_k}}\right) = -\nabla\cdot\left(\overline{\overline{\rho Y_k V_k}}\right) - \nabla\cdot\left(\overline{\overline{\rho}}\widetilde{\widetilde{\mathbf{u}Y_k}} - \overline{\overline{\rho}}\widetilde{\widetilde{\mathbf{u}}}\widetilde{\widetilde{Y_k}}\right) + \overline{\overline{\rho\dot{\omega}_{Y_k}}} \tag{5.5}$$

LES of turbulent combustion therefore implies to solve the system of Eqs. (5.3), (5.4) and (5.5), involving simultaneously the two filter scales $\overline{\Delta}$ and $\overline{\overline{\Delta}}$. In this

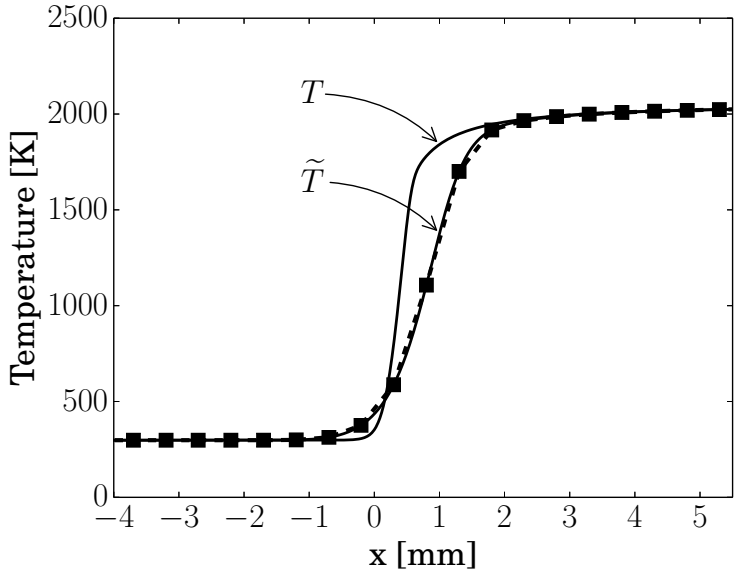


(a) Temperature

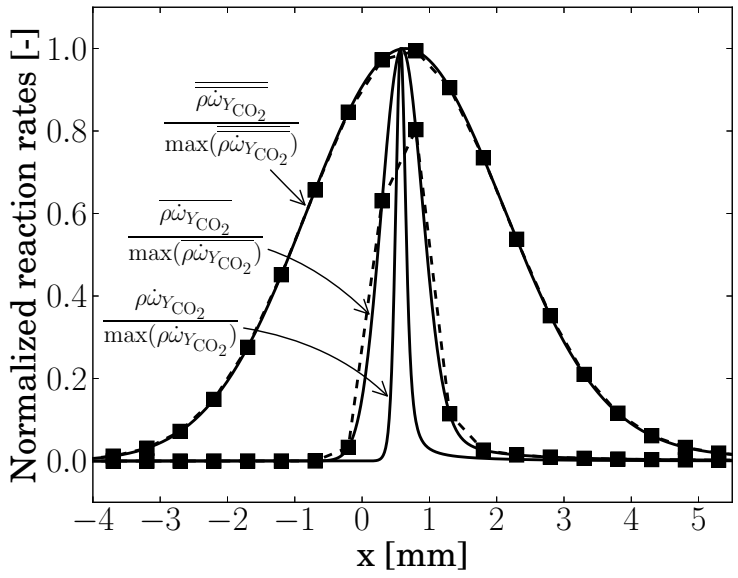


(b) $CO_2$ normalized reaction rate

**Figure 5.2:** *Comparison of unfiltered and filtered quantities. Solid lines: exact unfiltered and filtered variables. Dashed lines: reconstruction of the filtered quantities on a virtual mesh (squares) of size* $\Delta_x = 0.5$ *mm. Filter sizes are* $\overline{\Delta} = 3\Delta_x = 1.5$ mm *and* $\overline{\overline{\Delta}} = 10\Delta_x = 5$ mm.

system, the equations are not coupled through the density and velocity variable since $\widetilde{\widetilde{\mathbf{u}}} \neq \widetilde{\mathbf{u}}$ and $\overline{\overline{\rho}} \neq \overline{\rho}$. Several strategies to treat different flow and flame filter scales are presented below.

### 5.2.2 Classical approach: ad hoc coupling of flame and flow filtered equations

The first strategy is to implicitly substitute the filtered velocity fields $\widetilde{\mathbf{u}}$ and $\widetilde{\widetilde{\mathbf{u}}}$ by a unique variable $\hat{\mathbf{u}}$. In this context, LES of reacting flow is then governed by the following set of equations:

$$\frac{\partial \overline{\overline{\rho}}}{\partial t} + \nabla \cdot \left(\overline{\overline{\rho}}\hat{\mathbf{u}}\right) = 0 \tag{5.6}$$

$$\frac{\partial \overline{\overline{\rho}}\hat{\mathbf{u}}}{\partial t} + \nabla \cdot \left(\overline{\overline{\rho}}\hat{\mathbf{u}}\hat{\mathbf{u}}\right) = -\nabla \overline{p_2} + \nabla \cdot \left(\overline{\tau} + \overline{\tau}^t\right) \tag{5.7}$$

$$\frac{\partial \overline{\overline{\rho}}\widetilde{\widetilde{Y_k}}}{\partial t} + \nabla \cdot \left(\overline{\overline{\rho}}\hat{\mathbf{u}}\widetilde{\widetilde{Y_k}}\right) = -\nabla \cdot \left(\overline{\overline{\rho Y_k V_k}}\right) - \nabla \cdot \left(\overline{\overline{\rho}}\widetilde{\widetilde{\mathbf{u}Y_k}} - \overline{\overline{\rho}}\hat{\mathbf{u}}\widetilde{\widetilde{Y_k}}\right) + \overline{\overline{\rho\dot{\omega}_{Y_k}}} \tag{5.8}$$

$$p_0 = \overline{\overline{\rho}}\widetilde{\widetilde{rT}} \tag{5.9}$$

where the thermodynamic pressure $p_0$ is assumed constant in space for low-Mach number flows. $r = R/W$ where $R$ is the ideal gas constant and $W$ the mean molecular weight. The system of Eqs. (5.6)-(5.10), widely used in the literature[1], remains however ad hoc and mathematically inconsistent because it can not be derived from the Navier-Stokes equations. The density $\overline{\overline{\rho}}$, the term $\widetilde{\widetilde{rT}}$ and the chemical species $\widetilde{\widetilde{Y_k}}$, are filtered at the scale $\overline{\overline{\Delta}}$ to ensure a sufficient numerical resolution of the flame front. However, hydrodynamic pressure $\overline{p_2}$, viscous tensor $\overline{\tau}$ and Reynolds stresses $\overline{\tau}^t$ are filtered at $\overline{\Delta}$, adapted to resolved flow field variables. The variable $\hat{\mathbf{u}}$ satisfies the two following asymptotic behaviors:

1. Far from the reaction zone, the filtered velocity field $\hat{\mathbf{u}}$, solution of Equation (5.7), is not influenced by the flame. In the context of premixed combustion, as $\overline{\overline{\rho}}$ is constant in fresh and burnt gases, the filter size associated to the velocity field is $\overline{\Delta}$ and $\hat{\mathbf{u}} = \widetilde{\mathbf{u}}$. The LES equation system (5.6)-(5.10) then reduces to the exact equations (5.3) and (5.4). Using the present formalism therefore allows to efficiently resolve the flow field out of the flame front since it is only filtered at the optimal size $\overline{\Delta}$.
2. Across the reactive layer, flame thermochemical variables and density are filtered at the width $\overline{\overline{\Delta}}$. The heat expansion affects the velocity $\hat{\mathbf{u}}$. When no turbulence occurs within the flame front, the filter size associated to

[1] In the literature, even if the LES turbulent combustion models are built to broaden the flame front at a size larger than the flow filter size, flame and flow filter sizes are never explicitly distinguished. The resolved LES equation system is then written with a unique filter size $\Delta$ which is actually equivalent to the introduction of the notation $\hat{\mathbf{u}}$ proposed here.

the velocity $\hat{\mathbf{u}}$ is then $\overline{\overline{\Delta}}$ and $\hat{\mathbf{u}} = \widetilde{\widetilde{\mathbf{u}}}$. The conservation equations (5.6)-(5.10) written in the flame referential correctly degenerates towards exact filtered 1-D premixed laminar flame equations as:

$$\begin{aligned} \overline{\overline{\rho}}\widetilde{\widetilde{\mathbf{u}}} &= \text{cte} \\ \nabla\cdot\left(\overline{\overline{\rho}}\widetilde{\widetilde{\mathbf{u}}}\widetilde{\widetilde{Y_k}}\right) &= -\nabla\cdot\left(\overline{\overline{\rho Y_k V_k}}\right) - \nabla\cdot\left(\overline{\overline{\rho}}\widetilde{\widetilde{\mathbf{u}Y_k}} - \overline{\overline{\rho}}\widetilde{\widetilde{\mathbf{u}}}\widetilde{\widetilde{Y_k}}\right) + \overline{\overline{\rho\dot{\omega}_{Y_k}}} \\ p_0 &= \overline{\overline{\rho}}\widetilde{\widetilde{rT}} \end{aligned}$$

However, considering the general case of a wrinkled premixed or stratified flame, the filter size $\hat{\Delta}$ implicitly associated to $\hat{\mathbf{u}}$ is not clearly identified. Indeed, the impact of the flow patterns resolved at the scale $\overline{\Delta}$ on the flame front filtered at $\overline{\overline{\Delta}}$ may bias the description of flame/turbulence interactions (Peters, 2000; Pitsch, 2005). The velocity $\hat{\mathbf{u}}$ within the flame front is affected by two different phenomena: *(i)* the turbulent SGS fluxes, which are modeled by an implicit filter of size $\overline{\Delta}$ (Duwig, 2007, 2009; Fiorina et al., 2010; Pope, 2000); *(ii)* thermal expansion, induced by the density filtered at $\overline{\overline{\Delta}}$. This modeling issue is intrinsic to most turbulent combustion models designed to capture the filtered flame thickness. For instance, it is the case for both thickening (Colin et al., 2000) and filtering (Boger and Veynante, 2000) approaches developed to properly resolved the flame front. A dedicated approach is mandatory to ensure the consistency between SGS turbulence model and turbulent combustion model within the flame front.

#### 5.2.2.1 Description of the studied configuration

The different modeling alternatives considered in the following will be tested on the PRECCINSTA burner, a lean atmospheric turbulent burner characterized using advanced diagnostics by (Meier et al., 2007). The computational domain comprises a plenum, an industrial swirl injector integrated in a square combustion chamber equipped with optical access as shown in Fig. 5.3. Three different operating conditions have been investigated varying the global equivalence ratio of the $CH_4$-Air fresh gases ($\phi = \{0.70; 0.75; 0.83\}$). An unstable flame is experimentally observed for $\phi \leq 0.75$. The PRECCINSTA burner has been widely used in the literature as a reference to assess and validate LES turbulent models (Roux et al., 2005; Moureau et al., 2007; Galpin et al., 2008). For instance, the thickened flame model introduced in Sec. 1.5.2.3 was selected to study the unstable case first by Roux et al. (2005) who simulated the $\phi = 0.75$ case. Using the same combustion model, Franzelli et al. (2012) conducted the LES of both stable ($\phi = 0.83$) and unstable ($\phi = 0.75$) cases. They showed that the mixing process upstream the injector exit was governing the flame instability. More recently, the REDIM tabulated chemistry method was used by Wang et al. (2014) and coupled to a statistical formalism to model

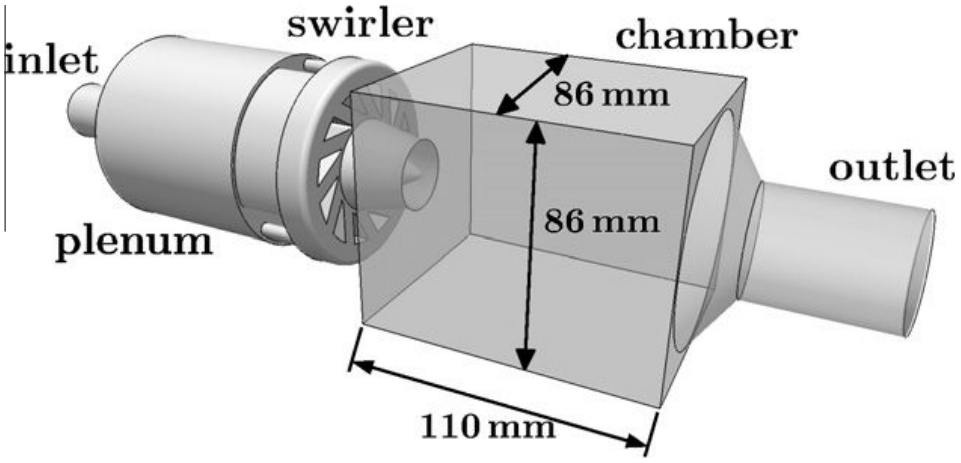


**Figure 5.3:** *PRECCINSTA swirled burner geometry.*

the sub-filter scale fluctuations. Two different FDF shapes were tested on both stable and unstable cases. Finally, the F-TACLES model (Fiorina et al., 2010) was also validated on the stable case, also selected for the present study.

### 5.2.3 A first alternative: increasing the flow filter size to $\overline{\Delta} = \overline{\overline{\Delta}}$

A solution is to filter the entire flow field at the filter size $\overline{\overline{\Delta}}$. A similar filter size for both flame and flow equation is retrieved, ensuring the mathematical consistency of the resolved LES equations and of the corresponding model closures. For that purpose, two different approaches are possible. The first one consist in adjusting the LES turbulence model to increase the dissipation of the small eddies and therefore to increase the flow filter size $\overline{\Delta}$. This approach will be called "Implicit filtering of the flow field" in the following. The second approach consists in conserving the resolved flow field filtered at the optimal size $\overline{\Delta}$ and to apply an explicit filtering operation to access the flow filed filtered at $\overline{\overline{\Delta}}$. This approach will be called "Explicit filtering of the flow field" in the following. Both approaches are briefly tested and discussed in this section.

#### 5.2.3.1 Implicit filtering the flow field

Filtering both flow and flame balance equations at size $\overline{\overline{\Delta}}$ leads to the following system:

$$\frac{\partial \overline{\overline{\rho}}}{\partial t} + \nabla \cdot \left( \overline{\overline{\rho}} \widetilde{\widetilde{\mathbf{u}}} \right) = 0 \tag{5.10}$$

$$\frac{\partial \overline{\overline{\rho}} \widetilde{\widetilde{\mathbf{u}}}}{\partial t} + \nabla \cdot \left( \overline{\overline{\rho}} \widetilde{\widetilde{\mathbf{u}}} \widetilde{\widetilde{\mathbf{u}}} \right) = -\nabla \overline{\overline{p_2}} + \nabla \cdot \left( \overline{\overline{\tau}} + \overline{\overline{\tau}}^t \right) \tag{5.11}$$

$$\frac{\partial \overline{\overline{\rho}} \widetilde{\widetilde{Y_k}}}{\partial t} + \nabla \cdot \left( \overline{\overline{\rho}} \widetilde{\widetilde{\mathbf{u}}} \widetilde{\widetilde{Y_k}} \right) = -\nabla \cdot \left( \overline{\overline{\rho Y_k V_k}} \right) - \nabla \cdot \left( \overline{\overline{\rho}} \widetilde{\widetilde{\mathbf{u}} Y_k} - \overline{\overline{\rho}} \widetilde{\widetilde{\mathbf{u}}} \widetilde{\widetilde{Y_k}} \right) + \overline{\overline{\rho \dot{\omega}_{Y_k}}} \tag{5.12}$$

$$p_0 = \overline{\overline{\rho}} \widetilde{\widetilde{r}} \widetilde{\widetilde{T}} \tag{5.13}$$

In this formalism, both the flow and the flame are filtered at a size $\overline{\overline{\Delta}}$ sufficiently large to resolve correctly the filtered flame front. Moreover, equations are correctly coupled, through $\overline{\overline{\rho}}$ and $\widetilde{\widetilde{\mathbf{u}}}$, and fully consistent in term of filter size. In practice the filtering at size $\overline{\overline{\Delta}}$ of the velocity field is achieved by the closure of the SGS momentum fluxes $\overline{\overline{\tau_{ij}}}^t$ :

$$\overline{\overline{\tau_{ij}}}^t = 2 \overline{\overline{\rho}} \nu_t^{\overline{\overline{\Delta}}} \left( \widetilde{\widetilde{S}}_{ij} - \frac{1}{3} \delta_{ij} \widetilde{\widetilde{S}}_{kk} \right) \tag{5.14}$$

where $\widetilde{\widetilde{S}}_{ij} = \frac{1}{2} \left( \frac{\partial \widetilde{\widetilde{u_i}}}{\partial x_j} + \frac{\partial \widetilde{\widetilde{u_j}}}{\partial x_i} \right)$ quantifies the rate of strain of the flow field resolved at size $\overline{\overline{\Delta}}$ and $\nu_t^{\overline{\overline{\Delta}}}$ is the sub-filter scale eddy viscosity associated to $\overline{\overline{\Delta}}$.

For a given grid of size $\Delta_x$, $\overline{\overline{\Delta}} > \overline{\Delta}$. Therefore, in comparison with the initial formalism developed in Sec. 5.2.2, this modeling approach will impact the flow field by increasing the LES cut-off scale. The size of the smallest resolved turbulent scale is increased. Consequently, the LES turbulence model will have a greater impact. A tetrahedral mesh, composed of 3 million nodes is used for two computations which only differ by the filter size parameter $\Delta$ in the turbulent eddy viscosity $\nu_t$ model (Smagorinsky, 1963):

$$\nu_t^{\Delta} = C_S^2 \Delta^2 \sqrt{2 \widetilde{S}_{ij} \widetilde{S}_{ij}} \tag{5.15}$$

In the first simulation $\Delta = \overline{\Delta}$ is used (classical approach) while $\Delta = \overline{\overline{\Delta}}$ is used in the second simulation (present approach). Figure 5.4 shows 2-D views of the instantaneous filtered progress variable $\widetilde{\widetilde{Y}}_c$ for the two different LES of the PRECCINSTA burner. Even if the same mesh is used in both computations, very few resolved wrinkling is noted in the second case compare to the first simulation. This figure actually illustrates the fact that increasing the turbulent eddy viscosity, from $\nu_t = \nu_t^{\overline{\Delta}}$ to $\nu_t = \nu_t^{\overline{\overline{\Delta}}}$, do not take full benefit of the mesh grid resolution since turbulent structures of size $\overline{\Delta} < \delta < \overline{\overline{\Delta}}$ are at the sub-filter scale while they could be resolved.

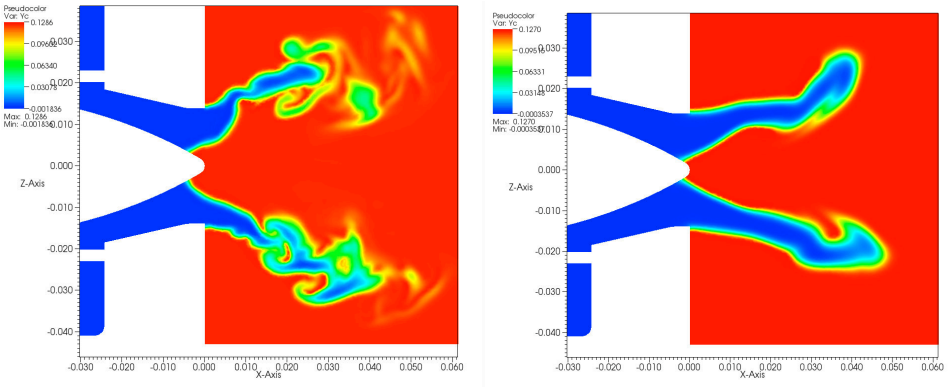


(a) Original F-TACLES model with the flow field implicitly filtered at $\overline{\Delta}$ ($\nu_t = \nu_t^{\overline{\Delta}}$)

(b) F-TACLES model with the flow field implicitly filtered at $\overline{\overline{\Delta}}$ ($\nu_t = \nu_t^{\overline{\overline{\Delta}}}$)

**Figure 5.4:** *LES of the PRECCINSTA burner using both formulations of the F-TACLES model. 2-D views of the instantaneous filtered progress variable* $\widetilde{\overline{Y}}_c$.

#### 5.2.3.2 Explicit filtering the flow field

To maintain the resolution of the turbulent structures at scale $\overline{\Delta}$, it is possible to use explicit filtering of the flow field to ensure the consistent transport of chemical species (or also progress variable). This alternative, discussed in the present section, involves an intermediate filter $\overbrace{\cdot}$ defined such as: $\overbrace{(\overline{\Phi})} = \overline{\overline{\Phi}}$. Assuming Gaussian filtering for $\overline{\cdot}$ and $\overline{\overline{\cdot}}$, the filter $\overbrace{\cdot}$ corresponds to a Gaussian filter of size $\overbrace{\Delta} = \sqrt{\left(\overline{\overline{\Delta}}\right)^2 - \left(\overline{\Delta}\right)^2}$.

The proposed methodology consists in first solving mass and momentum equations filtered at size $\overline{\Delta}$:

$$\frac{\partial \overline{\rho}}{\partial t} + \nabla \cdot (\overline{\rho}\widetilde{\mathbf{u}}) = 0 \tag{5.16}$$

$$\frac{\partial \overline{\rho}\widetilde{\mathbf{u}}}{\partial t} + \nabla \cdot (\overline{\rho}\widetilde{\mathbf{u}}\widetilde{\mathbf{u}}) = -\nabla \overline{p_2} + \nabla \cdot \left(\overline{\tau} + \overline{\tau}^t\right) \tag{5.17}$$

$$p_0 = \overline{\rho}\widetilde{rT} \tag{5.18}$$

Then, the transported momentum $\overline{\rho}\widetilde{\mathbf{u}} = \overline{\rho\mathbf{u}}$ is explicitly filtered using the intermediate Gaussian filter of size $\overbrace{\Delta}$ :

$$\overbrace{(\overline{\rho\mathbf{u}})} = \overline{\overline{\rho\mathbf{u}}} = \overline{\overline{\rho}}\widetilde{\overline{\mathbf{u}}} \tag{5.19}$$

The same procedure is applied to obtain the density filtered at size $\overline{\overline{\Delta}}$ as $\overline{\overline{\rho}} =$

$\widetilde{(\overline{\rho})}$. The knowledge of both $\overline{\overline{\rho}}$ and $\overline{\overline{\rho}}\widetilde{\widetilde{\mathbf{u}}}$ enable to close the filtered species mass fractions (or progress variable) balance equation:

$$\frac{\partial \overline{\overline{\rho}}\widetilde{\widetilde{Y_k}}}{\partial t} + \nabla \cdot \left( \overline{\overline{\rho}}\widetilde{\widetilde{\mathbf{u}}}\widetilde{\widetilde{Y_k}} \right) = -\nabla \cdot \left( \overline{\overline{\rho Y_k V_k}} \right) - \nabla \cdot \left( \overline{\overline{\rho}}\widetilde{\widetilde{\mathbf{u}Y_k}} - \overline{\overline{\rho}}\widetilde{\widetilde{\mathbf{u}}}\widetilde{\widetilde{Y_k}} \right) + \overline{\overline{\rho \dot{\omega}_{Y_k}}} \quad (5.20)$$

This methodology should decrease the impact of the LES turbulence model on the transport of the filtered species when it is compared to the implicit filtering approach (See Sec. 5.2.3.1). In other words, the flow scales of sizes $\overline{\Delta} < \delta < \overline{\overline{\Delta}}$ are resolved and filtered instead of being directly modeled by the SGS turbulence model. Nevertheless, the filtered mass fractions (or progress variable) are still transported using the velocity filtered at size $\overline{\overline{\Delta}}$ which means that the transport of the flame variables by the small structures of size $\delta < \overline{\overline{\Delta}}$ is not resolved. As in the previous section, a lower flame wrinkling is therefore expected compared to the classical approach where the flame scalars are transported using the turbulent flow field resolved at size $\overline{\Delta}$.

This approach has been implemented in the low-Mach number LES solver YALES2. The F-TACLES model has been used to close the filtered progress variable equation. The explicit filtering by a Gaussian filter is performed at each time step. The approach was also tested on the PRECCINSTA burner. The same mesh and numerical set-up as in Sec. 5.2.3.1 have been selected. Figure 5.5(a) shows instantaneous view of the transported velocity amplitude $\|\widetilde{\mathbf{u}}\|$. This velocity field is then explicitly filtered to compute $\|\widetilde{\widetilde{\mathbf{u}}}\|$, shown in Fig. 5.5(b). This filtered velocity is then used to transport the filtered progress variable $\widetilde{\widetilde{Y}}_c$. Instantaneous views of $\|\widetilde{\mathbf{u}}\|$, $\|\widetilde{\widetilde{\mathbf{u}}}\|$, $\widetilde{\widetilde{Y}}_c$ and $\widetilde{T}$ are shown in Fig. 5.5(c). In this simulation, burnt gas pockets penetrates the incoming flux of fresh gases. This behavior which differs from the other LES performed on finer grids (Roux et al., 2005; Fiorina et al., 2010; Franzelli et al., 2012) but also from quasi-DNS computation (Moureau et al., 2011b) seems unphysical. Indeed, these patterns probably result from numerical issues caused by the explicit Gaussian filtering near the injector walls. Figure 5.5(a) also shows very localized velocity overshoots induced by these burnt gases pockets.

Both implicit and explicit filtering of the flow field can therefore not be retained to ensure the consistency between flame and flow filter scales. The application of implicit filtering is straightforward and does not modify the CPU cost but this strategy do not take full benefits of the grid. The implementation of the procedure based on explicit filtering is complex. In the context of low-Mach number flows, since the conservation of mass and momentum have to be ensured at both $\overline{\Delta}$ and $\overline{\overline{\Delta}}$ scales, the algorithm of the solver has been modified leading to the resolution of two Poisson-like equations at each time step. The addition

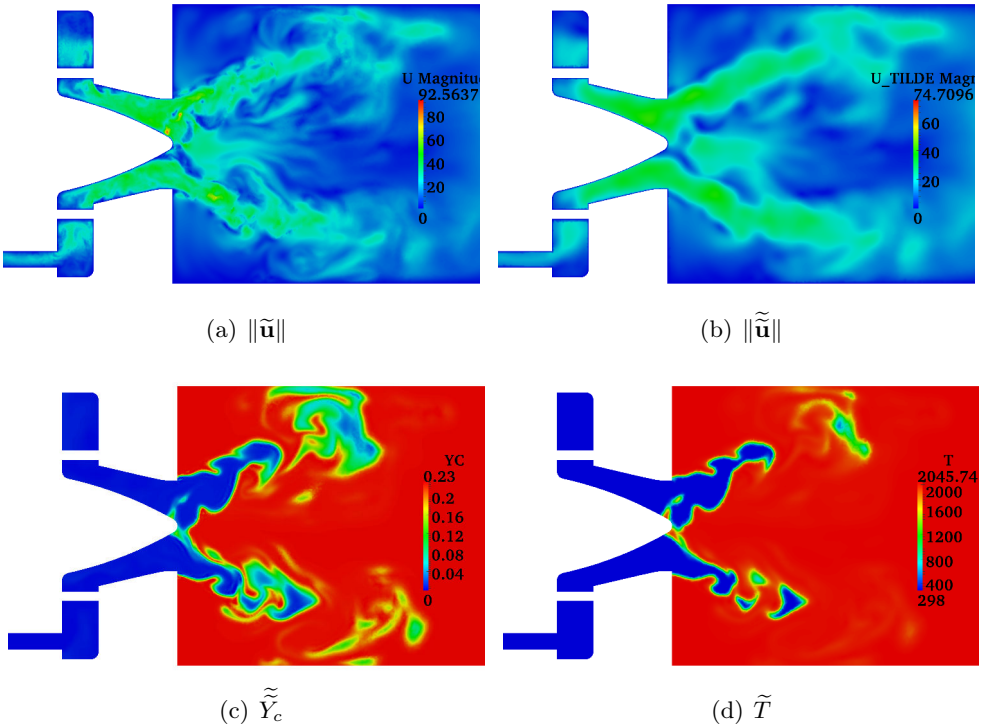


(a) $\|\widetilde{\mathbf{u}}\|$ (b) $\|\widetilde{\widetilde{\mathbf{u}}}\|$

(c) $\widetilde{\widetilde{Y}}_c$ (d) $\widetilde{T}$

**Figure 5.5:** *LES of the PRECCINSTA burner using F-TACLES CMS2 model with explicit filtering of velocity field. 2-D views of the instantaneous variables.*

of a second call of the Poisson solver as well as the explicit filtering of the three coordinates of the velocity makes the explicit filtering approach very expensive. This explicit filtering operation also generates numerical problems near the walls and lead to unphysical behaviors. The details of this implementation are not provided here since the approach is not retained in the following. An alternative to ensure the consistency between the two filter scales is proposed in the following.

### 5.2.4 New approach: a consistent and efficient coupling of flame and flow filtered equations

Whereas the transport of $\widetilde{\widetilde{Y_k}}$ by $\overline{\overline{\rho}}\widetilde{\widetilde{\mathbf{u}}}$ is not an efficient approach, an alternative is to transport $\widetilde{\widetilde{Y_k}}$ directly with the resolved turbulent flow field, filtered at $\overline{\Delta}$. For that purpose, the transport equation of $\widetilde{\widetilde{Y_k}}$ by $\overline{\rho}\widetilde{\mathbf{u}}$ is first derived in a non-conservative form. Using the total mass conservation at scale $\overline{\Delta}$ (Eq. (5.3)),

the following relation is first obtained:

$$\frac{\partial \overline{\rho}\widetilde{\widetilde{Y_k}}}{\partial t} + \nabla \cdot \left( \overline{\rho}\widetilde{\mathbf{u}}\widetilde{\widetilde{Y_k}} \right) = \overline{\rho}\frac{\partial \widetilde{\widetilde{Y_k}}}{\partial t} + \overline{\rho}\widetilde{\mathbf{u}} \cdot \nabla \widetilde{\widetilde{Y_k}} \tag{5.21}$$

$\partial \widetilde{\widetilde{Y_k}}/\partial t$ is substituted by the non-conservative form of Eq. (5.5) leading to:

$$\begin{aligned} \frac{\partial \overline{\rho}\widetilde{\widetilde{Y_k}}}{\partial t} + \nabla \cdot \left( \overline{\rho}\widetilde{\mathbf{u}}\widetilde{\widetilde{Y_k}} \right) &= -\frac{\overline{\rho}}{\overline{\overline{\rho}}} \nabla \cdot \left( \overline{\overline{\rho Y_k V_k}} \right) - \frac{\overline{\rho}}{\overline{\overline{\rho}}} \nabla \cdot \left( \overline{\overline{\rho}}\widetilde{\widetilde{\mathbf{u}Y_k}} - \overline{\overline{\rho}}\widetilde{\widetilde{\mathbf{u}}}\widetilde{\widetilde{Y_k}} \right) \\ &\quad -\overline{\rho}\left( \widetilde{\widetilde{\mathbf{u}}} - \widetilde{\mathbf{u}} \right) \cdot \nabla \widetilde{\widetilde{Y_k}} + \overline{\rho}\widetilde{\widetilde{\dot{\omega}_{Y_k}}} \end{aligned} \tag{5.22}$$

Equation (5.22) RHS exhibits four terms: $\nabla \cdot \left( \overline{\overline{\rho Y_k V_k}} \right)$ and $\nabla \cdot \left( \overline{\overline{\rho}}\widetilde{\widetilde{\mathbf{u}Y_k}} - \overline{\overline{\rho}}\widetilde{\widetilde{\mathbf{u}}}\widetilde{\widetilde{Y_k}} \right)$ are the laminar diffusion and convective fluxes occurring at subscale $\overline{\overline{\Delta}}$, both being weighted by the ratio $\overline{\rho}/\overline{\overline{\rho}}$. $\overline{\rho}\widetilde{\widetilde{\dot{\omega}_{Y_k}}}$ is the chemical reaction rate associated to the $k$-th species filtered at size $\overline{\overline{\Delta}}$. Finally, $\overline{\rho}\left( \widetilde{\widetilde{\mathbf{u}}} - \widetilde{\mathbf{u}} \right) \cdot \nabla \widetilde{\widetilde{Y_k}}$ is the inter-scale convection term associated to the scales between $\overline{\overline{\Delta}}$ and $\overline{\Delta}$. This term, which vanishes when flame and flow fields are filtered at the same size $\overline{\overline{\Delta}}$, can be either computed directly from the explicit filtering of resolved quantities or modeled as further suggested in Sec. 5.3.

The reactive flow is then described by the chemical species balance equation (Eq. (5.22)), completed with the flow governing equations given by Eqs. (5.3) and (5.4) and with the ideal gas law filtered at size $\overline{\Delta}$:

$$\frac{\partial \overline{\rho}}{\partial t} + \nabla \cdot \left( \overline{\rho}\widetilde{\mathbf{u}} \right) = 0 \tag{5.23}$$

$$\frac{\partial \overline{\rho}\widetilde{\mathbf{u}}}{\partial t} + \nabla \cdot \left( \overline{\rho}\widetilde{\mathbf{u}}\widetilde{\mathbf{u}} \right) = -\nabla \overline{p_2} + \nabla \cdot \left( \overline{\tau} + \overline{\tau}^t \right) \tag{5.24}$$

$$\begin{aligned} \frac{\partial \overline{\rho}\widetilde{\widetilde{Y_k}}}{\partial t} + \nabla \cdot \left( \overline{\rho}\widetilde{\mathbf{u}}\widetilde{\widetilde{Y_k}} \right) &= -\frac{\overline{\rho}}{\overline{\overline{\rho}}} \nabla \cdot \left( \overline{\overline{\rho Y_k V_k}} \right) - \frac{\overline{\rho}}{\overline{\overline{\rho}}} \nabla \cdot \left( \overline{\overline{\rho}}\widetilde{\widetilde{\mathbf{u}Y_k}} - \overline{\overline{\rho}}\widetilde{\widetilde{\mathbf{u}}}\widetilde{\widetilde{Y_k}} \right) \\ &\quad -\overline{\rho}\left( \widetilde{\widetilde{\mathbf{u}}} - \widetilde{\mathbf{u}} \right) \cdot \nabla \widetilde{\widetilde{Y_k}} + \overline{\rho}\widetilde{\widetilde{\dot{\omega}_{Y_k}}} \end{aligned} \tag{5.25}$$

$$p_0 = \overline{\rho} r \widetilde{T} \tag{5.26}$$

Both the density $\overline{\rho}$ and the term $r\widetilde{T}$ are filtered at a size $\overline{\Delta}$. The closure of this system of equations is now discussed.

## 5.3 Closure of the two-scale filtered progress variable balance equation: F2-TACLES model

In this section, a closure strategy based on the F-TACLES model, derived in the framework of FPI tabulated chemistry (see Sec. 1.4.2.2), is proposed. Note that a similar procedure is proposed for the thickened flame model TFLES-FPI in Appendix C. The transport of filtered species mass fractions $\widetilde{\widetilde{Y_k}}$ is replaced by the filtered progress variable $\widetilde{\widetilde{Y}}_c = \sum_{k=1}^{N_{sp}} n_k \widetilde{\widetilde{Y_k}}$ where $n_k$ is the coefficient associated to the $k$-th species and $N_{sp}$ the number of species in the chemical scheme leading to:

$$\begin{aligned}\frac{\partial \overline{\rho}\widetilde{\widetilde{Y}}_c}{\partial t} + \nabla\cdot\left(\overline{\rho}\widetilde{\mathbf{u}}\widetilde{\widetilde{Y}}_c\right) &= -\frac{\overline{\rho}}{\overline{\overline{\rho}}}\nabla\cdot\left(\overline{\sum_{k=1}^{N_{sp}} n_k \rho Y_k V_k}\right) - \frac{\overline{\rho}}{\overline{\overline{\rho}}}\nabla\cdot\left(\overline{\overline{\rho}}\widetilde{\widetilde{\mathbf{u}Y_c}} - \overline{\overline{\rho}}\widetilde{\widetilde{\mathbf{u}}}\widetilde{\widetilde{Y}}_c\right) \\ &\quad -\overline{\rho}\left(\widetilde{\widetilde{\mathbf{u}}} - \widetilde{\mathbf{u}}\right)\cdot\nabla\widetilde{\widetilde{Y}}_c + \overline{\rho}\widetilde{\widetilde{\dot{\omega}_{Y_c}}} \end{aligned} \tag{5.27}$$

As a first approach, closures for RHD terms are derived assuming adiabatic and fully-premixed combustion to enhance the clarity of the section. Note that the following developments can be extended to non-adiabatic and stratified flames.

Applying the F-TACLES formalism to Eqs. (5.23) to (5.26) leads to:

$$\frac{\partial \overline{\rho}}{\partial t} + \nabla\cdot\left(\overline{\rho}\widetilde{\mathbf{u}}\right) = 0 \tag{5.28}$$

$$\frac{\partial \overline{\rho}\widetilde{\mathbf{u}}}{\partial t} + \nabla\cdot\left(\overline{\rho}\widetilde{\mathbf{u}}\widetilde{\mathbf{u}}\right) = -\nabla\overline{p_2} + \nabla\cdot\left(\overline{\tau} + \overline{\tau}^t\right) \tag{5.29}$$

$$\frac{\partial \overline{\rho}\widetilde{\widetilde{Y}}_c}{\partial t} + \nabla\cdot\left(\overline{\rho}\widetilde{\mathbf{u}}\widetilde{\widetilde{Y}}_c\right) = \Xi_{\overline{\overline{\Delta}}}\nabla\cdot\left(\rho_0 D_0 \nabla\widetilde{\widetilde{Y}}_c\right) + \Xi_{\overline{\overline{\Delta}}}\Sigma_{Y_c}^{\mathrm{F2T}}\left[\widetilde{\widetilde{Y}}_c\right] \tag{5.30}$$

$$P_0 = \overline{\rho}\widetilde{r T^*}\left[\widetilde{\widetilde{Y}}_c\right] \tag{5.31}$$

where the notation $\Phi\left[\widetilde{\widetilde{Y}}_c\right]$ denotes that $\Phi$ is tabulated as a function of $\widetilde{\widetilde{Y}}_c$. $\rho_0$ and $D_0$ are reference values for the density and the molecular diffusion coefficient, respectively. $\Xi_{\overline{\overline{\Delta}}}$ is the subgrid scale wrinkling model associated to the resolved filtered flame front at scale $\overline{\overline{\Delta}}$. The term $\Sigma_{Y_c}^{\mathrm{F2T}}\left[\widetilde{\widetilde{Y}}_c\right]$ is tabulated as a function of the resolved filtered progress variable $\widetilde{\widetilde{Y}}_c$ for a given pair $\left(\overline{\overline{\Delta}}, \overline{\Delta}\right)$ and may be decomposed as follows:

$$\Sigma_{Y_c}^{\mathrm{F2T}}\left[\widetilde{\widetilde{Y}}_c\right] = \mathcal{D}_{Y_c}^{\mathrm{F2T}} + \mathcal{T}_{Y_c}^{\mathrm{F2T}} + \mathcal{I}_{Y_c}^{\mathrm{F2T}} + \mathcal{R}_{Y_c}^{\mathrm{F2T}} \tag{5.32}$$

The laminar diffusion correction term $\mathcal{D}_{Y_c}^{\mathrm{F2T}}$, which accounts for differential diffusion in the direction normal to the flame front, reads:

$$\mathcal{D}_{Y_c}^{\mathrm{F2T}} = -\left( \frac{\overline{\rho^*}}{\overline{\overline{\rho^*}}} \frac{\partial}{\partial x^*} \left( \overline{\overline{\sum_{k=1}^{N_{sp}} n_k \rho^* Y_k^* V_k^*}} \right) + \frac{\partial}{\partial x^*} \left( \rho_0 D_0 \frac{\partial \widetilde{\widetilde{Y_c^*}}}{\partial x^*} \right) \right)$$

where the superscript * stands for variables extracted from a 1-D laminar premixed flame. The laminar SGS convective fluxes, modeled by $\mathcal{T}_{Y_c}$, are also estimated from the chemical structure of a 1-D filtered laminar premixed flame:

$$\mathcal{T}_{Y_c}^{\mathrm{F2T}} = -\rho_f S_l \frac{\overline{\rho^*}}{\overline{\overline{\rho^*}}} \left( \frac{\partial \overline{\overline{Y_c^*}}}{\partial x^*} - \frac{\partial \widetilde{\widetilde{Y_c^*}}}{\partial x^*} \right) \tag{5.33}$$

where $\rho_f$ denotes the density in the fresh gases. This method is also applied to model the intercale convection term:

$$\mathcal{I}_{Y_c}^{\mathrm{F2T}} = \rho_f S_l \left( 1 - \frac{\overline{\rho^*}}{\overline{\overline{\rho^*}}} \right) \frac{\partial \widetilde{\widetilde{Y_c^*}}}{\partial x^*} \tag{5.34}$$

Finally, the filtered progress variable reaction rate is estimated as $\mathcal{R}_{Y_c}^{\mathrm{F2T}} = \overline{\rho^* \widetilde{\widetilde{\dot{\omega}_{Y_c}^*}}}$. In practice, the term $\Sigma_{Y_c}^{\mathrm{F2T}}$ is pre-computed and stored in a look-up table as a function of $\widetilde{\widetilde{Y_c}}$. This model, which combines tabulated variables filtered at two filter length scales $\overline{\Delta}$ and $\overline{\overline{\Delta}}$ is called F2-TACLES. These terms have been computed across a 1-D premixed laminar $CH_4$-air flame of equivalence ratio 0.83. They are plotted in Fig. 5.6 as a function of space coordinate $x$ for $\overline{\Delta} = 1.75$ mm and $\overline{\overline{\Delta}} = 7$ mm. In particular, it is shown that $\Sigma_{Y_c}^{\mathrm{F2T}}$ is well resolved on a grid of size $\Delta_x = 0.5$ mm($\approx \delta_{Y_c} = 0.46$ mm). Other thermochemical variables, such as chemical species mass fractions $Y_k$ can also be filtered at $\overline{\Delta}$ and tabulated as a function of the resolved progress variable $\widetilde{\widetilde{Y_c}}$ as $\widetilde{Y_k} = \widetilde{Y_k^*}\left[\widetilde{\widetilde{Y_c}}\right]$. The choice of the pair $\left(\overline{\overline{\Delta}}, \overline{\Delta}\right)$ used to generate the filtered chemical database is now discussed in section 5.4.1.

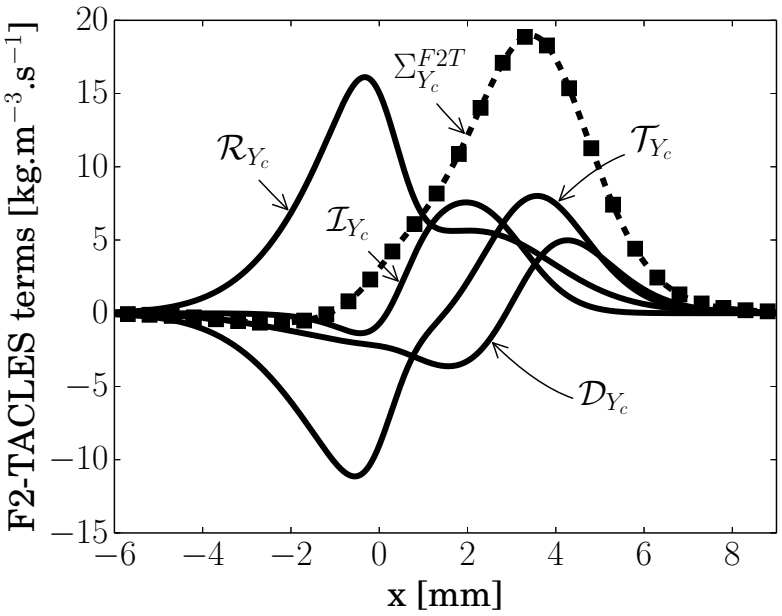


**Figure 5.6:** *F2-TACLES model terms computed from a $CH_4$-air 1-D premixed flame computed with detailed chemistry (Lindstedt, 1997) and for $\overline{\Delta} = 1.75$ mm and $\overline{\overline{\Delta}} = 7$ mm. A virtual LES mesh (squares) of size $\Delta_x = 0.5$ mm is added to the global source term $\Sigma_{Y_c}^{F2T}$ profile.*

## 5.4 Numerical applications

### 5.4.1 1-D filtered flame simulations

During the pre-processing step, F2-TACLES terms are computed explicitly prior to the LES. At this stage, both flow $\overline{\Delta}$ and flame $\overline{\overline{\Delta}}$ filter sizes has to be carefully prescribed. $\overline{\Delta}$ is the filter size associated to the thermochemical variables $\widetilde{T}$ and $\overline{\rho}$. A too small value of $\overline{\Delta}$ would cause numerical problems for strong gradients of density. The filter associated to the flame front, $\overline{\overline{\Delta}}$, is set to ensure a sufficient resolution of the filtered progress variable $\widetilde{\widetilde{Y}}_c$. As discussed previously, the value retained for $\overline{\overline{\Delta}}$ also depends on the numerical schemes.

1-D premixed flames computations are performed to assess the model properties and determine both minimum flow $\overline{\Delta}$ and flame $\overline{\overline{\Delta}}$ filter sizes for a given mesh. The YALES2 low-Mach number LES solver (Moureau et al., 2011a), retained here, uses a centered fourth-order scheme for spatial discretization while time integration of convective terms is performed with a fourth-order temporal scheme. Chemistry is tabulated from a 0.83 equivalence ratio 1-D laminar premixed $CH_4$-air flame computed with the Lindstedt (1997) chemical scheme, involving 29 species and 141 reactions. A parametric study on the ratio $\overline{\Delta}/\Delta_x$

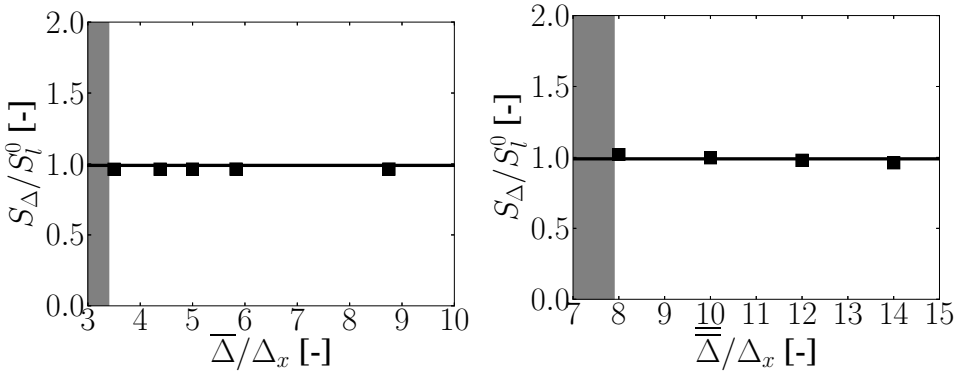


**Figure 5.7:** *Left:* $S_\Delta/S_l^0$ *in terms of* $\overline{\Delta}/\Delta_x$ *with* $\overline{\Delta} = 1.75$ *mm and* $\overline{\overline{\Delta}} = 7$ *mm. Right:* $S_\Delta/S_l^0$ *in terms of* $\overline{\overline{\Delta}}/\Delta_x$ *with* $\overline{\Delta} = 1.75$ *mm and* $\Delta_x = 0.5$ *mm. Inside the grey surface, simulation where unstable and the predicted flame speed value was meaningless.*

is first conducted varying the mesh size $\Delta_x$ for a constant filter size $\overline{\Delta} = 1.75$ mm. The width $\overline{\overline{\Delta}} = 7$ mm is also set constant and sufficiently large so that $\overline{\overline{\Phi}}$ quantities are always well resolved ($\delta_{\widetilde{\widetilde{Y_c}}} = 4.3$ mm). For each computation, the ratio of the effective flame propagation speed $S_\Delta$ and the laminar flame speed $S_l^0$ is plotted as a function of $\overline{\Delta}/\Delta_x$ in Fig. 5.7 and shows that the limiting criteria associated to the YALES2 code is $\overline{\Delta}/\Delta_x \geq 3.5$. Below this limit, the numerical scheme diverges and solutions are meaningless. A second parametric study on the ratio $\overline{\overline{\Delta}}/\Delta_x$, varying the flame filter size $\overline{\overline{\Delta}}$ for constant flow filter $\overline{\Delta} = 1.75$ mm and mesh $\Delta_x = 0.5$ mm sizes (respecting the criteria $\overline{\Delta}/\Delta_x \geq 3.5$), shows that the flame filter size should verify $\overline{\overline{\Delta}}/\Delta_x \geq 8.0$ for the YALES2 code. This criterion may be recast as $\delta_{\widetilde{c}}/\Delta_x \geq 5.0$ matching the limiting criterion of the original F-TACLES model (Fiorina et al., 2010).

### 5.4.2 LES of a turbulent swirl combustor

The F2-TACLES model (Sec. 5.3) is now compared to the original F-TACLES model (Fiorina et al., 2010) by performing LES of the PRECCINSTA swirl burner.

#### 5.4.2.1 Numerical set-up

The YALES2 low-Mach number LES solver (Moureau et al., 2011a) is chosen here. The computational domain is defined as in Fig. 5.3. A coarse and a fine unstructured tetrahedral meshes of 2.5 and 22 million nodes, respectively, are used for both F-TACLES and F2-TACLES simulations. The characteristic mesh size in the flame zone is $\Delta_x \approx 0.5$ mm and $\Delta_x \approx 0.25$ mm for the coarse and fine grids, respectively. The coarser mesh, shown in Fig. 5.8, is

representative of an industrial LES grid and is able to capture correctly the mean flow features. For the F2-TACLES model on the coarse mesh, the flow and flame filter sizes are $\overline{\Delta} = 2$ mm and $\overline{\overline{\Delta}} = 5$ mm, respectively, leading to $\delta_{\widetilde{\widetilde{Y_c}}}/\Delta_x = 7$. For the original F-TACLES model on the coarse mesh, the flame filter size is set to $\overline{\overline{\Delta}} = 5$ mm as for F2-TACLES. A summary of the simulated cases including the filter sizes used for the finer mesh is shown in Tab. 5.2.

**Table 5.2:** *Details of the simulations performed on the PRECCINSTA burner*

| LES # | Mesh size $\Delta_x$ | Model | Flame filter $\overline{\overline{\Delta}}$ | Flow filter $\overline{\Delta}$ | Plot legend |
|---|---|---|---|---|---|
| 1 | 0.5 mm | F-TACLES | 5.0 mm | - | - - - |
| 2 | 0.5 mm | F2-TACLES | 5.0 mm | 2.0 mm | — |
| 3 | 0.25 mm | F-TACLES | 2.5 mm | - | - - - |
| 4 | 0.25 mm | F2-TACLES | 2.5 mm | 1.0 mm | — |

Since the burner is fed by a $\phi = 0.83$ equivalence ratio $CH_4$-air mixture, both F-TACLES and F2-TACLES filtered databases have been built from the same 1-D laminar premixed flame introduced in Sec. 5.4.1. The total injected mass flow rate is $\dot{m} = 12.9$ g.s$^{-1}$. The burner is supposed fully adiabatic and mixture heterogeneities are neglected.

#### 5.4.2.2 Results analysis

Figure 5.9 shows 2-D views of the instantaneous resolved progress variable, temperature and density for both F-TACLES and F2-TACLES computations. The $\widetilde{\widetilde{Y_c}}$ fields (Fig 5.9(a)) does not exhibit notable differences as both are solved at the filter size $\overline{\overline{\Delta}}$. However, significant differences are observed in Figs. 5.9(b) and 5.9(c) since the filter sizes associated to both $T$ and $\rho$ differ between computations. In the original F-TACLES model, all the thermochemical values are filtered at $\overline{\overline{\Delta}}$ while only the resolved progress variable $\widetilde{\widetilde{Y_c}}$ is filtered at this size in the F2-TACLES model. Other thermochemical variables as $\overline{\rho}$, $\widetilde{T}$ and the chemical species $\widetilde{Y_k}$ are filtered at $\overline{\Delta}$, leading to a finer description of the flame front on a given mesh. Figure 5.10 shows the comparison of two instantaneous iso-surfaces of temperatures (T = 1000 K) extracted from both F-TACLES and F2-TACLES computations using the coarse grid. More resolved wrinkling is observed with F2-TACLES, in particular at the downstream location of the flame brush. These conclusions are actually confirmed when 1-D profiles are quantitatively analyzed.

Mean and RMS temperature radial profiles are plotted in Figs. 5.11(a) and 5.11(b), respectively. The black lines correspond to the coarser mesh ($\Delta_x \approx 0.5$ mm). Mean predictions are very close for all computations near the burner exit

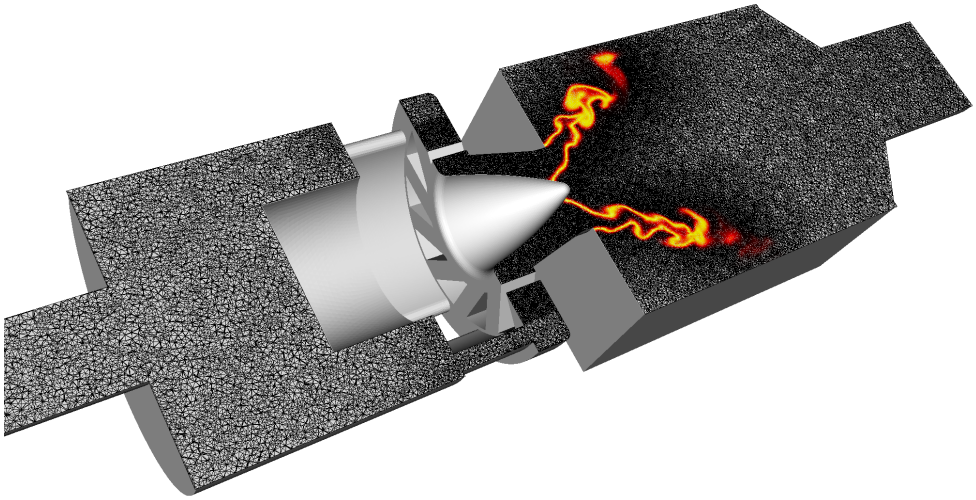

(a) Whole computational domain

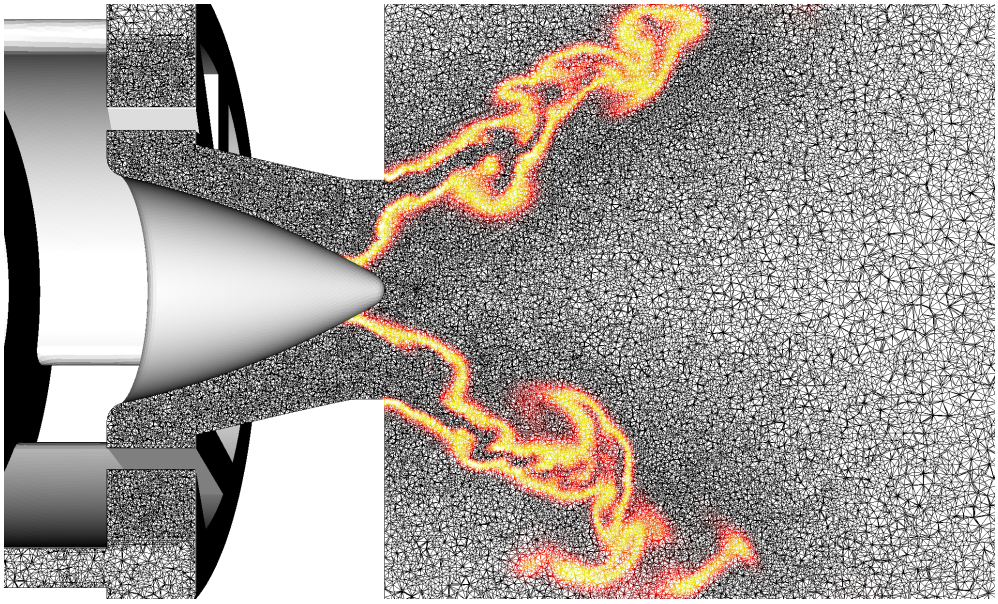

(b) Near flame region

**Figure 5.8:** *Half portion of the PRECCINSTA burner computational domain. A longitudinal cut of the coarse mesh is shown and colored by the filtered progress variable reaction rate* $\widetilde{\dot{\omega}}_{Y_c}$*. The mesh is refined within the injector and the flame region with a characteristic size of* $\Delta_x \approx 0.5$ *mm for the coarse mesh shown here.*

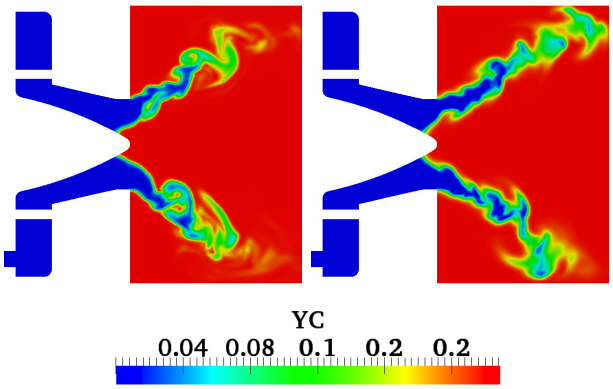


(a) Left: $\widetilde{\widetilde{Y}}_c$ (F-TACLES); Right: $\widetilde{\widetilde{Y}}_c$ (F2-TACLES).

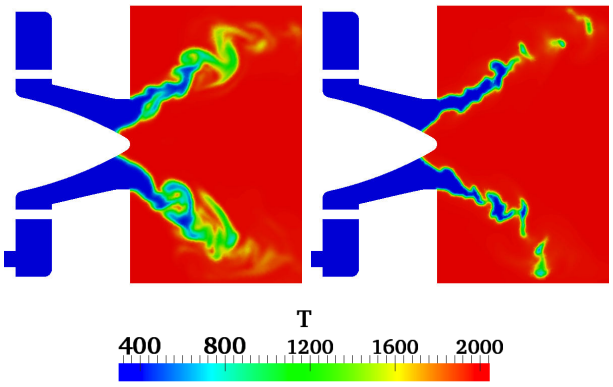


(b) Left: $\widetilde{\widetilde{T}}$ (F-TACLES); Right: $\widetilde{T}$ (F2-TACLES)

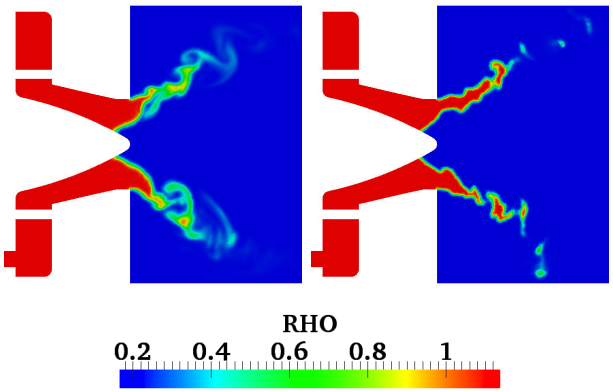


(c) Left: $\overline{\overline{\rho}}$ (F-TACLES); Right: $\overline{\rho}$ (F2-TACLES)

**Figure 5.9:** *2-D color mapping of instantaneous thermochemical variables extracted from LES of the PRECCINSTA burner using F-TACLES (left) and F2-TACLES (right) models.*

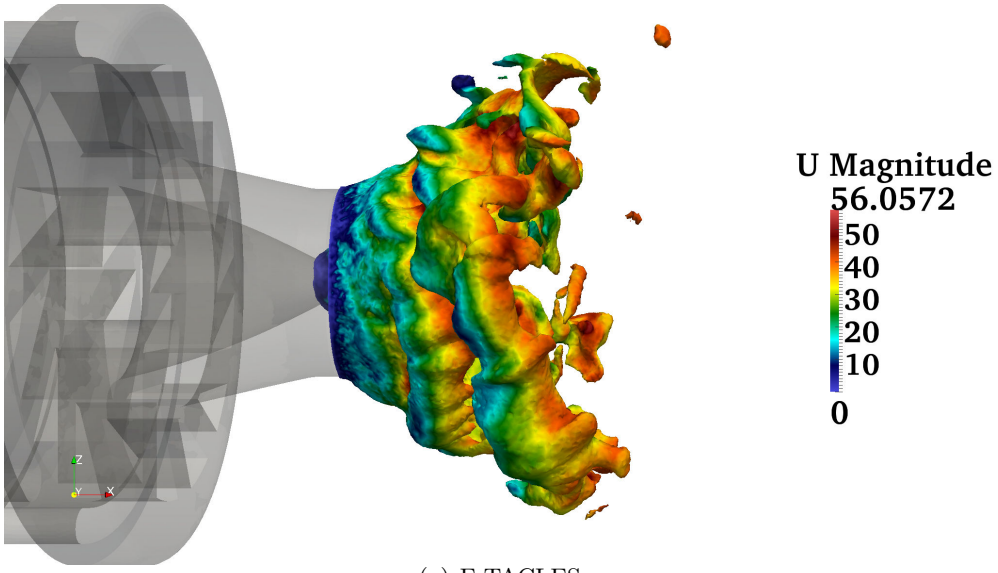


(a) F-TACLES

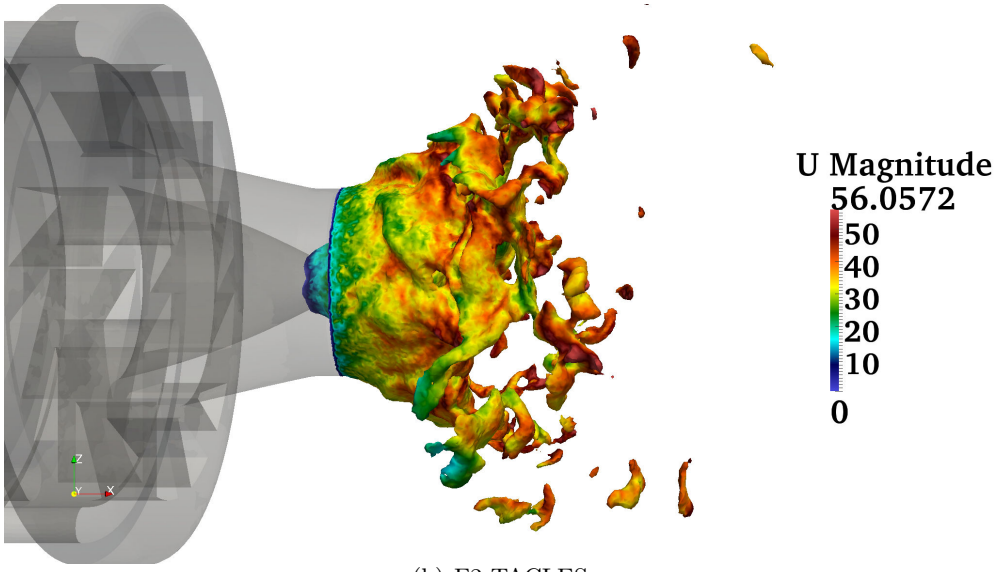


(b) F2-TACLES

**Figure 5.10:** *Instantaneous iso-surface of temperature (T = 1000 K) for two LES of the PRECCINSTA burner computed using F-TACLES and F2-TACLES models. 3-D surfaces are colored by the magnitude of the resolved velocity.*

(located at Z = 0 mm) while F2-TACLES provides a slightly better prediction of the mean flame brush thickness and temperature fluctuations further downstream. In particular, F2-TACLES predicts higher resolved RMS compared to F-TACLES. Indeed, as the thermal thickness of the resolved flame front is thinner, more interactions occur with the resolved turbulent motions. Finer

mesh ($\Delta_x \approx 0.5$ mm) solutions are added in Fig. 5.11 (red lines). F2-TACLES and F-TACLES solutions are closer when $\Delta_x$ decreases since subfilter wrinkling models become less influent. The main differences remain located at the end of the flame ($Z \geq 20$ mm) where the interactions with the turbulence is more intense. As expected, the RMS levels increase for the fine grid as more turbulent fluctuations are resolved.

Statistics of species mass fraction are shown in Figs. 5.12 to 5.17. A very good agreement is also noted for both models near the burner exit while the predictions from F2-TACLES model better agrees with experiments further downstream. The conclusions of the mesh sensitivity analysis drawn for the temperature profiles are also valid for the species mass fractions.

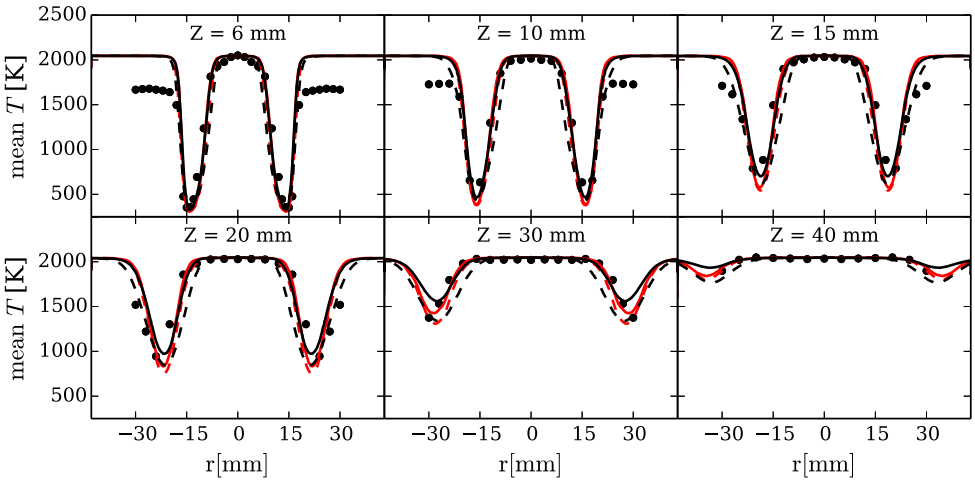


(a) Mean

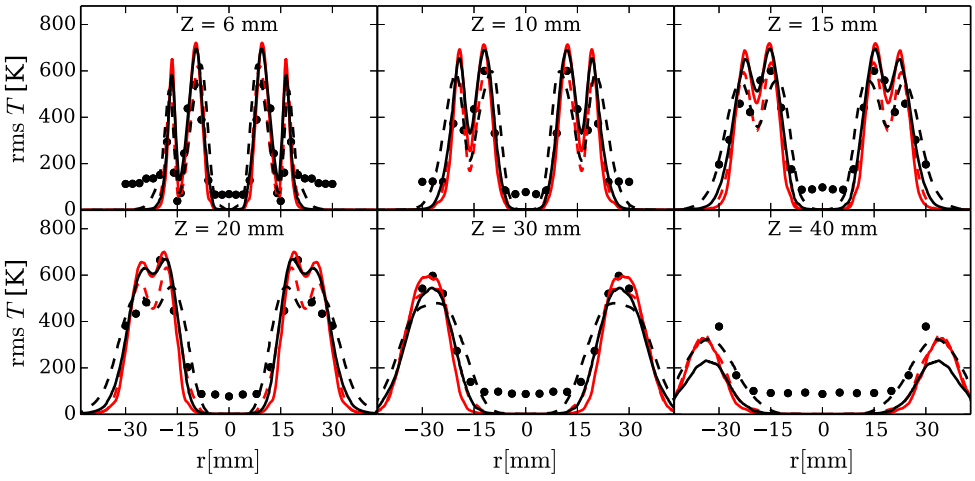


(b) RMS

**Figure 5.11:** *Radial profiles of temperature extracted from the LES of the PRECCINSTA burner using coarse (black lines) and fine (red lines) meshes. Legend: F-TACLES model ( $\widetilde{\widetilde{T}}$: - - -) ; F2-TACLES ( $\widetilde{T}$: —) ; Experiments ( • • ).*

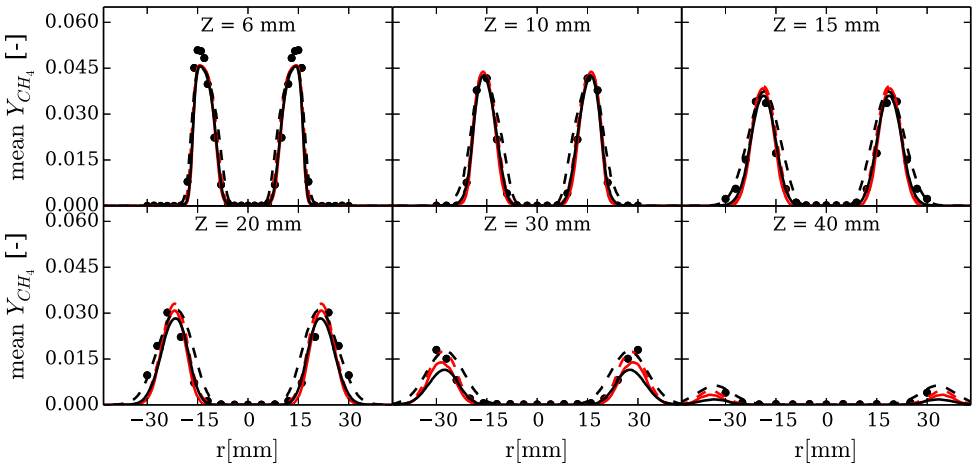


(a) Mean

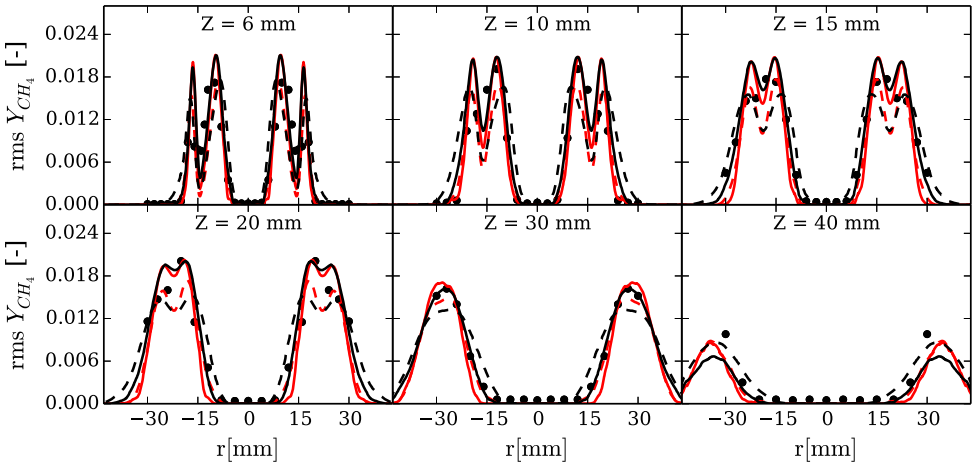


(b) RMS

**Figure 5.12:** *Radial profiles of* $CH_4$ *extracted from the LES of the PRECCINSTA burner using coarse (black lines) and fine (red lines) meshes. Legend: F-TACLES model (* $\widetilde{\widetilde{Y}}_{CH_4}$*: - - -) ; F2-TACLES (* $\widetilde{Y}_{CH_4}$*: —) ; Experiments ( • • ).*

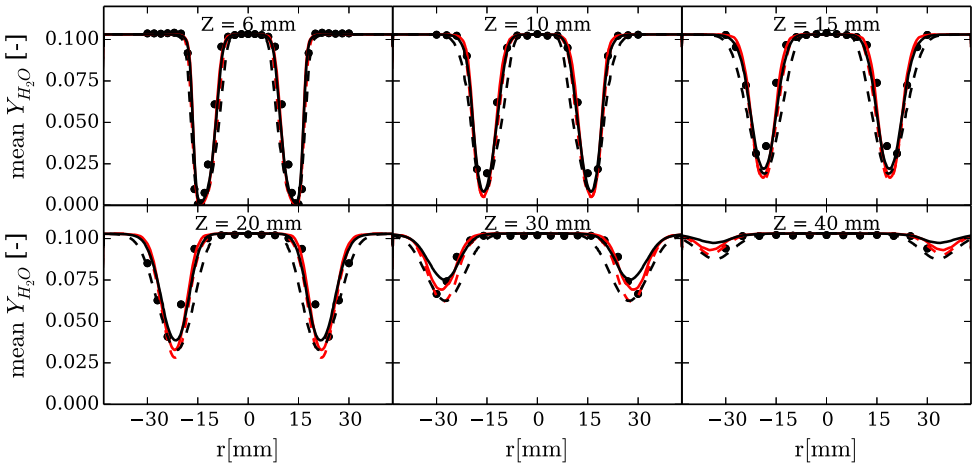


(a) Mean

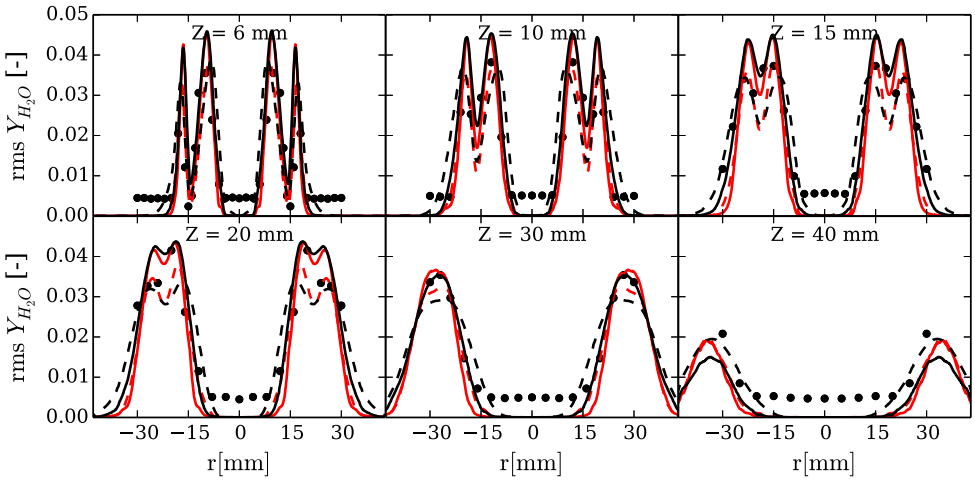


(b) RMS

**Figure 5.13:** *Radial profiles of* $H_2O$ *extracted from the LES of the PRECCINSTA burner using coarse (black lines) and fine (red lines) meshes. Legend: F-TACLES model (* $\widetilde{\widetilde{Y}}_{H_2O}$*: - - -) ; F2-TACLES (* $\widetilde{Y}_{H_2O}$*: —) ; Experiments ( • • ).*

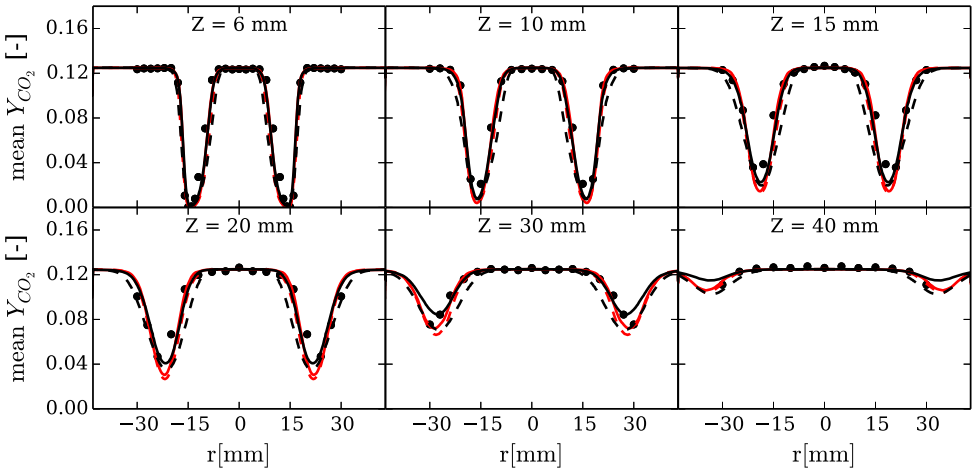


(a) Mean

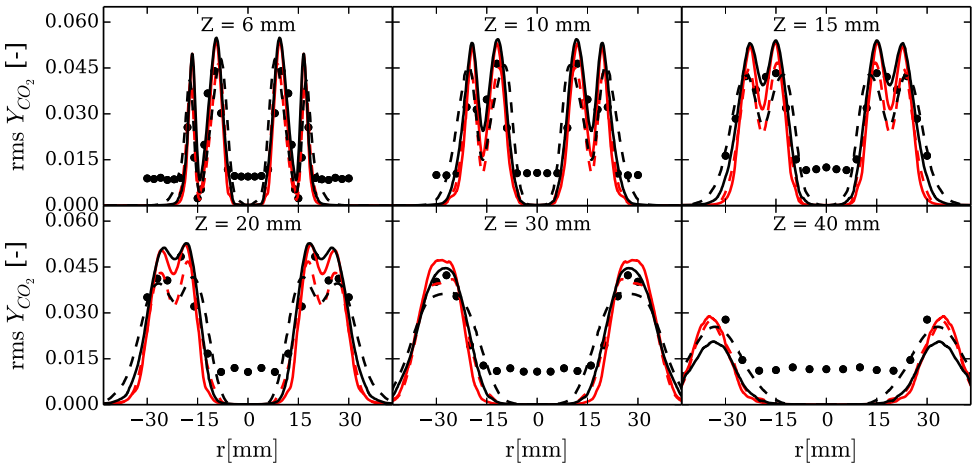


(b) RMS

**Figure 5.14:** *Radial profiles of* $CO_2$ *extracted from the LES of the PRECCINSTA burner using coarse (black lines) and fine (red lines) meshes. Legend: F-TACLES model (* $\widetilde{\widetilde{Y}}_{CO_2}$*: - - -) ; F2-TACLES (* $\widetilde{Y}_{CO_2}$*: —) ; Experiments ( • • ).*

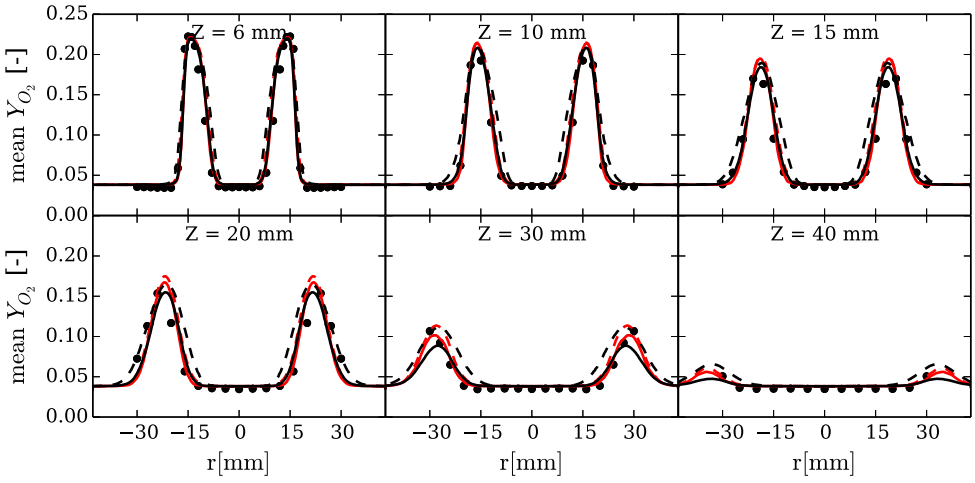


(a) Mean

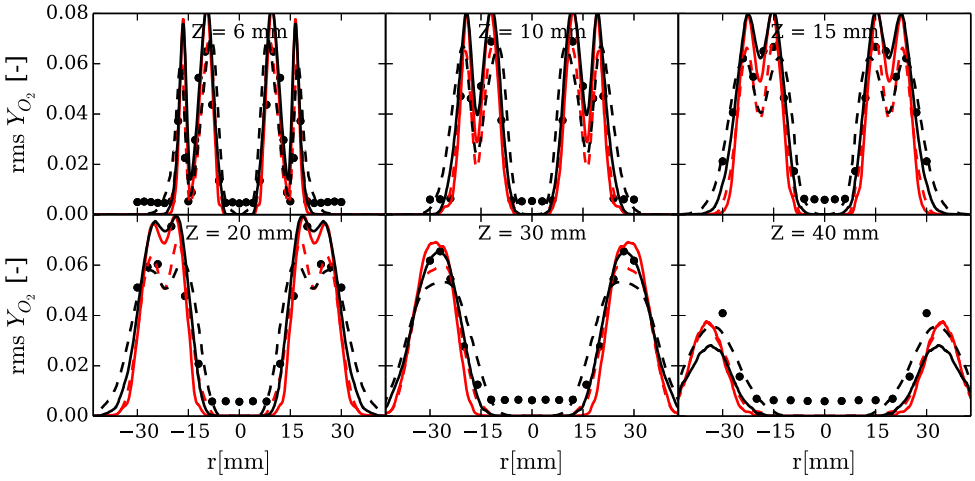


(b) RMS

**Figure 5.15:** *Radial profiles of* $O_2$ *extracted from the LES of the PRECCINSTA burner using coarse (black lines) and fine (red lines) meshes. Legend: F-TACLES model (* $\widetilde{\widetilde{Y}}_{O_2}$*: - - -) ; F2-TACLES (* $\widetilde{Y}_{O_2}$*: —) ; Experiments ( • • ).*

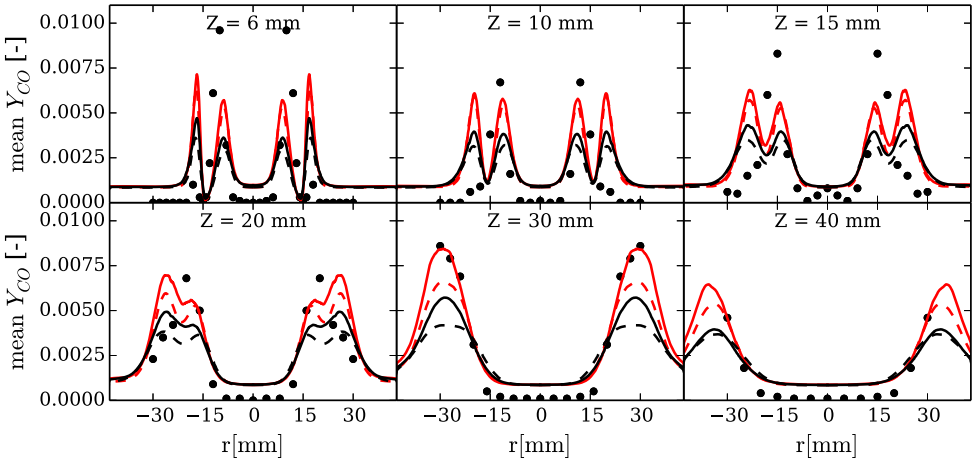


(a) Mean

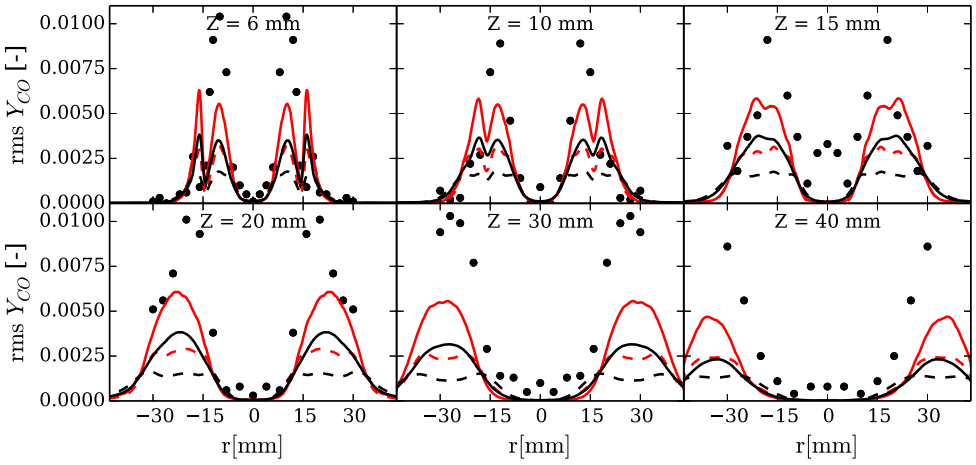


(b) RMS

**Figure 5.16:** *Radial profiles of* CO *extracted from the LES of the PRECCINSTA burner using coarse (black lines) and fine (red lines) meshes. Legend: F-TACLES model (* $\widetilde{\widetilde{Y}}_{CO}$*: - - -) ; F2-TACLES (* $\widetilde{Y}_{CO}$*: —) ; Experiments ( • • ).*

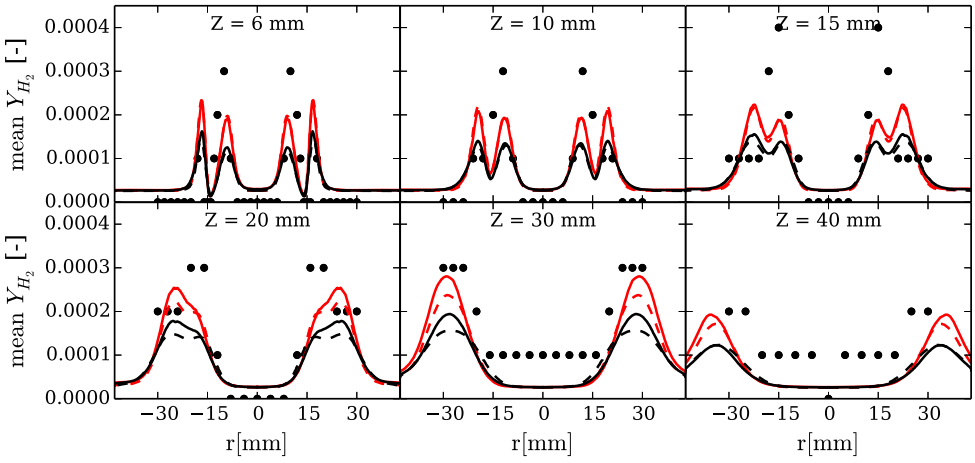


(a) Mean

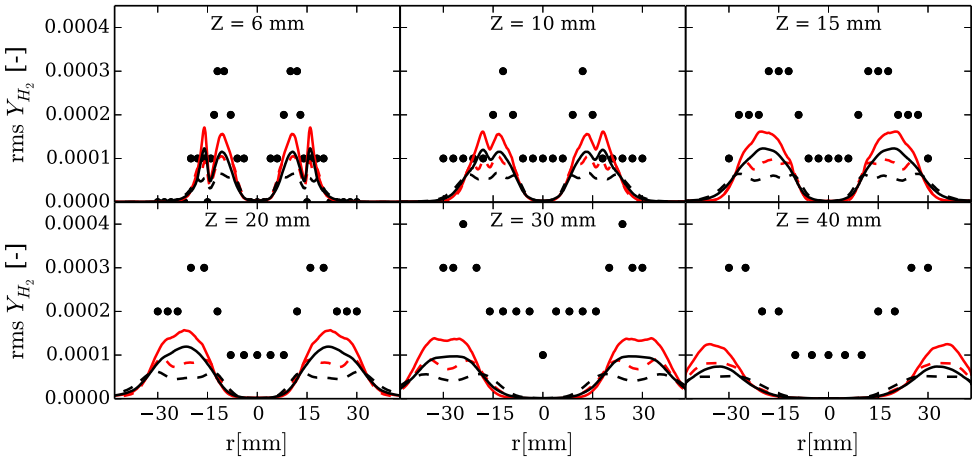


(b) RMS

**Figure 5.17:** *Radial profiles of* $H_2$ *extracted from the LES of the PRECCINSTA burner using coarse (black lines) and fine (red lines) meshes. Legend: F-TACLES model (* $\widetilde{\widetilde{Y}}_{H_2}$*: - - -) ; F2-TACLES (* $\widetilde{Y}_{H_2}$*: —) ; Experiments ( ● ● ).*

## 5.5 Generalization of the F2-TACLES model to non-adiabatic stratified combustion

F2-TACLES model has first been derived assuming adiabatic and fully-premixed combustion. In this section, the formalism proposed by Auzillon et al. (2012) is used to account for the effect of unresolved mixture fraction heterogeneities. Non-adiabaticity of the flow and its impact on the turbulent flame consumption speed is also accounted for by applying the strategy detailed in Chapter 2. The F2-TACLES governing equations for turbulent non-adiabatic stratified flames read :

$$\frac{\partial \overline{\rho}}{\partial t} + \nabla \cdot (\overline{\rho}\widetilde{\mathbf{u}}) = 0 \tag{5.35}$$

$$\frac{\partial \overline{\rho}\widetilde{\mathbf{u}}}{\partial t} + \nabla \cdot (\overline{\rho}\widetilde{\mathbf{u}}\widetilde{\mathbf{u}}) = -\nabla \overline{p_2} + \nabla \cdot \left(\overline{\tau} + \overline{\tau}^t\right) \tag{5.36}$$

$$\frac{\partial \overline{\rho}\widetilde{\widetilde{Y}}_c}{\partial t} + \nabla \cdot \left(\overline{\rho}\widetilde{\mathbf{u}}\widetilde{\widetilde{Y}}_c\right) = \gamma \Xi_{\overline{\overline{\Delta}}} \nabla \cdot \left(\rho_0 D_0 \nabla \widetilde{\widetilde{Y}}_c\right) + \gamma \Xi_{\overline{\overline{\Delta}}} \Sigma_{Y_c}^{\mathrm{F2T}} \tag{5.37}$$

$$\frac{\partial \overline{\rho}\widetilde{z}}{\partial t} + \nabla \cdot (\overline{\rho}\widetilde{\mathbf{u}}\widetilde{z}) = \nabla \cdot \left(\left(\overline{\rho} D_{th} + \frac{\mu_t}{S_{ct}}\right) \nabla \widetilde{z}\right) \tag{5.38}$$

$$\begin{aligned} \frac{\partial (\overline{\rho}\widetilde{z''^2})}{\partial t} + \nabla \cdot \left(\overline{\rho}\widetilde{\mathbf{u}}\widetilde{z''^2}\right) &= \nabla \cdot \left(\frac{\mu_t}{S_{ct}} \nabla \widetilde{z''^2}\right) + 2\frac{\mu_t}{S_{ct}} |\nabla \widetilde{z}|^2 \\ &\quad - 2C \frac{\mu_t}{S_{ct} \overline{\rho} \Delta_x^2} \widetilde{z''^2} \end{aligned} \tag{5.39}$$

$$\frac{\partial (\overline{\rho}\widetilde{h^{eq}})}{\partial t} + \nabla \cdot (\overline{\rho}\widetilde{\mathbf{u}}\widetilde{h^{eq}}) = \nabla \cdot \left(\left(\overline{\rho} D_{th} + \frac{\mu_t}{P_{rt}}\right) \nabla \widetilde{h^{eq}}\right) \tag{5.40}$$

$$P_0 = \overline{\rho} r \widetilde{T} \tag{5.41}$$

where the F2-TACLES global source term $\Sigma_{Y_c}^{\mathrm{F2T}}$ is now estimated from a series of adiabatic freely-propagating 1-D filtered flames as:

$$\Sigma_{Y_c}^{\mathrm{F2T}} \left[\widetilde{\widetilde{Y}}_c, \widetilde{z}, S_z, \overline{\overline{\Delta}}\right] = \mathcal{D}_{Y_c}^{\mathrm{F2T}} + \mathcal{T}_{Y_c}^{\mathrm{F2T}} + \mathcal{I}_{Y_c}^{\mathrm{F2T}} + \mathcal{R}_{Y_c}^{\mathrm{F2T}} \tag{5.42}$$

The computation of the four RHS terms is very similar to the fully-premixed version of the model except that the definition of the 1-D filtering operation is extended to include the impact of unresolved mixture fraction heterogeneities:

$$\overline{\overline{\Phi}}(\widetilde{\widetilde{Y}}_c, \widetilde{z}, S_z, \overline{\overline{\Delta}}) = \int_0^1 \left\langle \left\langle \Phi^* | z = z' \right\rangle \right\rangle P_\beta(z', \widetilde{z}, S_z) dz' \tag{5.43}$$

$$\overline{\Phi}(\widetilde{\widetilde{Y}}_c, \widetilde{z}, S_z, \overline{\overline{\Delta}}) = \int_0^1 \left\langle \Phi^* | z = z' \right\rangle P_\beta(z', \widetilde{z}, S_z) dz' \tag{5.44}$$

where $P_\beta$ is the mixture fraction filtered density function modeled here by a $\beta$-function. $\langle\langle\Phi^*|z=z'\rangle\rangle$ and $\langle\Phi^*|z=z'\rangle$ are the conditional value of the variable $\Phi^*$, extracted from an adiabatic freely-propagating 1-D flame computed at $z=z'$, filtered at size $\overline{\overline{\Delta}}$ and $\overline{\Delta}$ respectively. The four RHS term read:

$$\mathcal{D}_{Y_c}^{\mathrm{F2T}} = -\left(\frac{\overline{\rho^*}}{\overline{\overline{\rho^*}}}\frac{\partial}{\partial x^*}\left(\overline{\overline{\sum_{k=1}^{N_{sp}} n_k\rho^* Y_k^* V_k^*}}\right) + \frac{\partial}{\partial x^*}\left(\rho_0 D_0 \frac{\partial\widetilde{\widetilde{Y_c^*}}}{\partial x^*}\right)\right) \tag{5.45}$$

$$\mathcal{T}_{Y_c}^{\mathrm{F2T}} = -\frac{\overline{\rho^*}}{\overline{\overline{\rho^*}}}\left(\overline{\overline{\rho_f^*(z)S_l^*(z)\frac{\partial Y_c^*}{\partial x^*}}} - \overline{\overline{\rho_f^*(z)S_l^*(z)}}\frac{\partial\widetilde{\widetilde{Y_c^*}}}{\partial x^*}\right) \tag{5.46}$$

$$\mathcal{I}_{Y_c}^{\mathrm{F2T}} = \left(1-\frac{\overline{\rho^*}}{\overline{\overline{\rho^*}}}\right)\overline{\overline{\rho_f^*(z)S_l^*(z)}}\frac{\partial\widetilde{\widetilde{Y_c^*}}}{\partial x^*} \tag{5.47}$$

$$\mathcal{R}_{Y_c}^{\mathrm{F2T}} = \overline{\rho^*}\widetilde{\widetilde{\dot{\omega}_{Y_c}^*}} \tag{5.48}$$

where the superscript $^*$ again denotes that the variables are extracted from an adiabatic freely-propagating 1-D flame. The practical estimation of the terms $\mathcal{D}_{Y_c}^{\mathrm{F2T}}$, $\mathcal{T}_{Y_c}^{\mathrm{F2T}}$ and $\mathcal{I}_{Y_c}^{\mathrm{F2T}}$ implies to develop the derivation operators because the spatial derivation of a variable convoluted with a density-weighted FDF is not straightforward. The strategy proposed here consists in computing all the derivatives in space before applying the convolution with both the Gaussian filter and the mixture fraction FDF. For that purpose, the following terms are developed:

$$\frac{\partial\widetilde{\widetilde{Y_c^*}}}{\partial x^*} = \frac{1}{\overline{\overline{\rho^*}}}\left(\frac{\partial\overline{\overline{\rho^* Y_c^*}}}{\partial x^*} - \widetilde{\widetilde{Y_c^*}}\frac{\overline{\overline{\partial\rho^*}}}{\partial x^*}\right) \tag{5.49}$$

$$\frac{\partial}{\partial x^*}\left(\rho_0 D_0\frac{\partial\widetilde{\widetilde{Y_c^*}}}{\partial x^*}\right) = \rho_0 D_0\left[\frac{1}{\overline{\overline{\rho^*}}}\left(\overline{\overline{\frac{\partial^2\rho^* Y_c^*}{\partial x^{*2}}}} - \widetilde{\widetilde{Y_c^*}}\,\overline{\overline{\frac{\partial^2\rho^*}{\partial x^{*2}}}} - \overline{\overline{\frac{\partial\rho^*}{\partial x^*}}}\frac{\partial\widetilde{\widetilde{Y_c^*}}}{\partial x^*}\right)\right. \tag{5.50}$$

$$\left. -\frac{1}{\overline{\overline{\rho}}^{*2}}\overline{\overline{\frac{\partial\rho^*}{\partial x^*}}}\left(\overline{\overline{\frac{\partial\rho^* Y_c^*}{\partial x^*}}} - \widetilde{\widetilde{Y_c^*}}\overline{\overline{\frac{\partial\rho^*}{\partial x^*}}}\right)\right] \tag{5.51}$$

The temperature $\widetilde{T}$ and the ideal gas law term $\widetilde{rT}$ are estimated as proposed in Sec. 2.3.4.3. The impact of heat losses on the filtered flame consumption speed is accounted for by the correction factor $\gamma$ defined exactly as detailed in Sec. 2.3.3:

$$\gamma[\widetilde{z}, S_z, \Delta\widetilde{h}] = \frac{\widetilde{S}_l\left(\widetilde{z}, S_z, \Delta\widetilde{h}\right)}{\widetilde{S}_l\left(\widetilde{z}, S_z, \Delta\widetilde{h}=0\right)} \tag{5.52}$$

This formulation accounts for both heat losses and unresolved mixture fraction heterogeneities and is fully consistent in terms of filter scales.

## 5.6 Conclusion

Consistency issues between flame and flow filter sizes in LES of turbulent premixed flames have been discussed leading to a general mathematical formalism considering two different filter sizes. Filtered progress variable balance equation was recast accordingly. A new closure of the resulting LES balance equation system has been proposed in line with the F-TACLES formalism. This new model, called F2-TACLES, does not induce additional computational cost and its implementation within an LES code remains similar to F-TACLES. Only the tabulation process differs by the computation of the new closure terms. In particular, the inter-scale convection term $-\overline{\rho}\left(\widetilde{\widetilde{\mathbf{u}}}-\widetilde{\mathbf{u}}\right)\cdot\nabla\widetilde{\widetilde{Y_c}}$ has been modeled from 1-D filtered flames in this thesis. It is worth noting that this term could actually be computed directly from the resolved variables as it does not imply sub-filter scales quantities. The impact of the modeling strategy for this term is left for further studies. F2-TACLES has been first validated analyzing 1-D premixed filtered flames and through LES of the complex PRECCINSTA swirl burner. Comparisons of mean profiles show that the F2-TACLES model better predict the flame brush downstream of the burner exit where the flame-turbulence interactions are more developed. Mesh sensitivity analysis has shown that both F-TACLES and F2-TACLES models tend to the same solution when $\Delta_x$ decreases. However, the analysis of mean and RMS profiles on a stable turbulent flame is probably not sufficient to fully assess the impact of the new modeling approach on the resolved flame dynamics. This last point would necessitate further investigations on unstable or pulsed turbulent flames.

# Part IV

# Application of the non-adiabatic F-TACLES model to a confined swirled non-adiabatic combustor

# Chapter 6

# Application to the EM2C burner: non-reacting case

Contents

*The first chapter of this part presents the configuration used to assess the F-TACLES model. This burner has been designed and experimentally characterized during the Ph.D. thesis of Guiberti (2015). The experimental setup is first described as well as the operating conditions representative of practical combustion within steel preheating furnaces. A numerical strategy is described and the non-reacting case is then selected to validate its ability to capture the flow dynamics. Numerical results and experimental data are compared in the last section of this chapter.*

## 6.1 Introduction

Large amounts of gaseous by-products are generated during the steel production process. These gas mixtures may include combustible gases such as methane ($CH_4$), hydrogen ($H_2$) or carbon monoxide (CO). The Coke Oven Gas (COG) is one of the main gaseous by-products and is mainly composed of $CH_4$ and $H_2$. In practice, chemical species molar fractions vary with coal composition. In a context of energetic stress, valorization of this by-product is an efficient way to reduce the overall consumption of fuel in the steel production process. An advantageous method consists in recycling COG as a fuel in the preheating furnaces of the steel plant. Such industrial furnaces exhibit very large length scales (few meter to few tens of meters) and are often operated at atmospheric pressure. Because of very slow convective time scales, the heat exchange between the burnt gases and the combustor walls are important.

| | Coke Oven Gas (COG) | |
|---|---|---|
| LHV | 17 MJ.m$^{-3}$ | 40 MJ.kg$^{-1}$ |
| Composition | molar fractions $X_k$ | mass fractions $Y_k$ |
| $N_2$ | 0.04 | 0.125 |
| $CO_2$ | 0.02 | 0.098 |
| CO | 0.06 | 0.188 |
| $H_2$ | 0.63 | 0.141 |
| $CH_4$ | 0.25 | 0.448 |

**Table 6.1:** *Coke Oven Gas (COG) composition and lower heating value*

The design of these furnaces requires numerical tools able to predict the flame stabilization and dynamics. In particular, this strategy has to capture correctly the impact of the variations in fuel mixture composition as well as the impact of heat exchange between the combustion chamber walls and both the flame front and the burnt gases. The objective of this part IV of the manuscript is to assess the ability of the F-TACLES model to capture these different physical phenomena. For that purpose, a joint experimental and numerical analysis is conducted. A burner has been designed at EM2C laboratory (Guiberti, 2015)

to stabilize premixed turbulent flames using a swirling fresh gas injection. The geometry is representative of steel preheating furnaces burner. Advanced diagnostics have been used to characterize both the flow field and the flame front position (Guiberti et al., 2014b,a; Guiberti, 2015). For safety issues and as COG features a moderate amount of CO, $CO_2$ and $N_2$, a simplified $CH_4$-$H_2$-Air mixture is selected to represent the COG-Air combustion. The determination of the exact composition of the $CH_4$-$H_2$-Air mixture is described in the following sections as well as the design of the EM2C burner used for this study.

## 6.2 Description of the EM2C burner

The experimental setup presented in Fig. 6.2 features an axisymmetric burner similar to the one used by Palies et al. (2010, 2011) for the investigation of linear and nonlinear dynamics of swirling flames. The burner, fed by premixed methane, hydrogen and air, includes a cylindrical injection tube with an exit diameter of 14 mm. The flow is put in rotation by a radial swirling vane located upstream of the injection tube. A central rod of 6 mm diameter crossing the swirler is installed on the burner axis to help flame stabilization at the injection tube outlet located 2 mm above the injection plane. To ensure a nearly uniform velocity profile at the entrance of the swirler, the mixture enters the burner through a plenum and subsequently passes through a set of grid/honeycomb/grid arrangement before entering a water-cooled convergent nozzle. The flame is confined by a transparent square chamber featuring four 250 mm (height) $\times$ 92 mm (width) $\times$ 12 mm (thickness) quartz windows. Direct visualizations of the flame and laser diagnostics are then eased since cylindrical quartz confinements would have increased the complexity of laser based measurements due to beam deviation and reflection. Moreover, a square geometry for the combustion chamber is closer to those usually found in industrial furnaces. To prevent ambient air intrusion at the combustor outlet, a convergent exhaust is added on the top of the chamber to accelerate the outgoing flow. The outlet section contraction ratio of the nozzle is 0.45.

Figure 6.3 shows a 3D model of the radial swirling vane. The swirl number S was determined by Guiberti (2015) from the radial vane geometry using the expression from J. Beer (1983); Galley et al. (2011). The swirl number was also measured by particle imaging velocimetry (PIV) in vertical and horizontal planes at the injection tube outlet under non-reactive conditions and without confinement. The measured value S = 0.40, lower than the theoretical estimations S = 0.59 at the swirler outlet, is assumed constant when the combustion chamber is placed on the top of the burner. This is a reasonable approximation since the section expansion ratio at the burner outlet is quite large $S_1/S_0 = 62.9$ where $S_0$ and $S_1$ denote the sections of the injection tube and the combustion

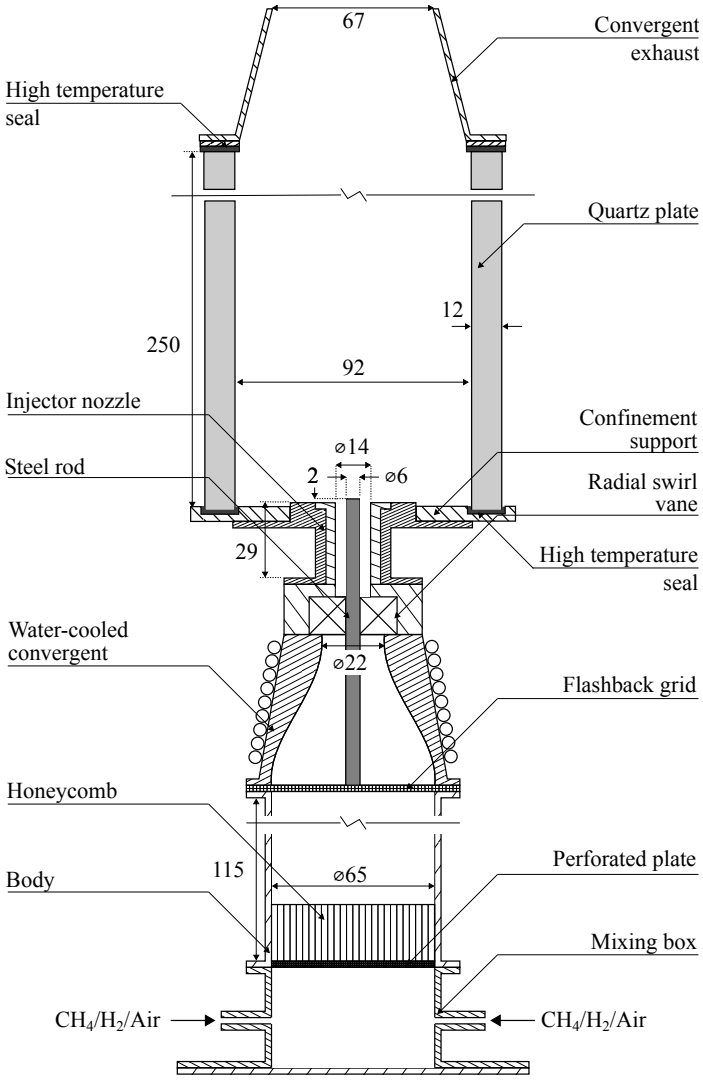


**Figure 6.1:** *Schematic of the EM2C burner*

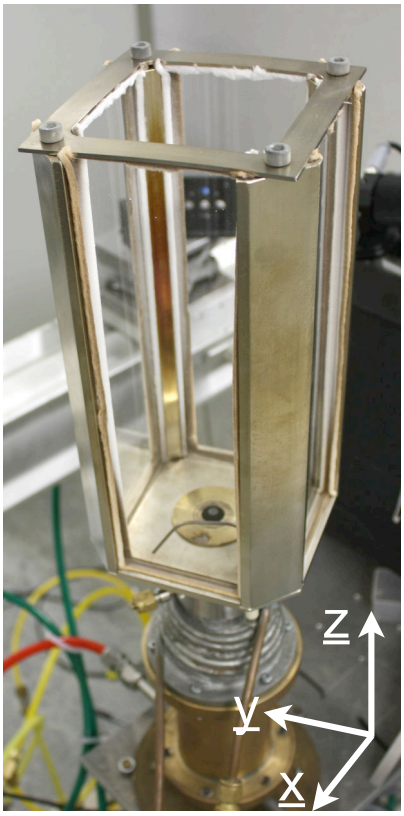


**Figure 6.2:** *Direct visualization of the EM2C burner. Convergent exhaust is not included in the displayed device but was added for experimental campaigns.*

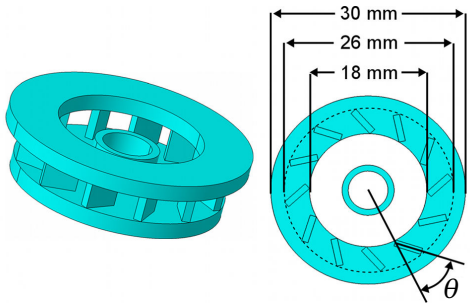


**Figure 6.3:** *3D model of the radial swirling vane. The transverse cut on the right shows the main dimensions and the swirl angle* $\theta = 35°$.

chamber, respectively. Note that $S_1/S_0$ is representative of an existing test furnace operated by Arcelor Mittal (private communication).

The flow rates of methane ($CH_4$), hydrogen ($H_2$) and air are regulated using thermal mass flow controllers and the mixture composition and bulk flow velocity at the injection tube outlet is known with a relative accuracy better than 5%.

## 6.3 Selection of the studied operating conditions

The objective of this section is to determine the $H_2$ and $CH_4$ molar fractions in a surrogate fuel allowing to mimic the properties of a COG-Air flame for a given equivalence ratio. The laminar burning velocity $S_L$ and adiabatic flame temperature $T_{ad}$ are calculated by computing 1D freely-propagating flames using the REGATH thermochemistry package (Pons et al., 2009; Candel et al., 2011) developed at the EM2C laboratory. For that purpose, the Lindstedt (1997) detailed chemical scheme is used without accounting for the NOx chemistry leading to 29 species and 141 reactions. Different fresh gas combustible compositions were explored by varying both the equivalence ratio $\phi$ and the fuel composition. The fuel, composed of $H_2$ and $CH_4$ is characterized by the pair ($X^{\text{fuel}}_{H_2}$ ; $X^{\text{fuel}}_{CH_4} = 1 - X^{\text{fuel}}_{H_2}$). Figures 6.4 and 6.5 respectively show the laminar burning velocity $S_L$ and the adiabatic flame temperature $T_{ad}$ of $CH_4$-$H_2$-Air mixtures as a function of $X^{\text{fuel}}_{H_2}$. This concentration goes from 0 (pure methane case) to 1.0 (pure hydrogen case). Calculations are performed for equivalence ratios $\phi$ ranging from $0.7 \leq \phi \leq 1$. Data obtained from COG-Air flame computations are superimposed in these graphs. The composition of COG selected for this study is provided in Fig.1.

Figure 6.4 indicates that a molar fraction of hydrogen $X^{\text{fuel}}_{H_2} \approx 0.70$ in the surrogate fuel is needed to reach the same laminar burning velocity as combustion of COG. This remains true for equivalence ratios ranging from $\Phi = 0.7$ to 1. Re-

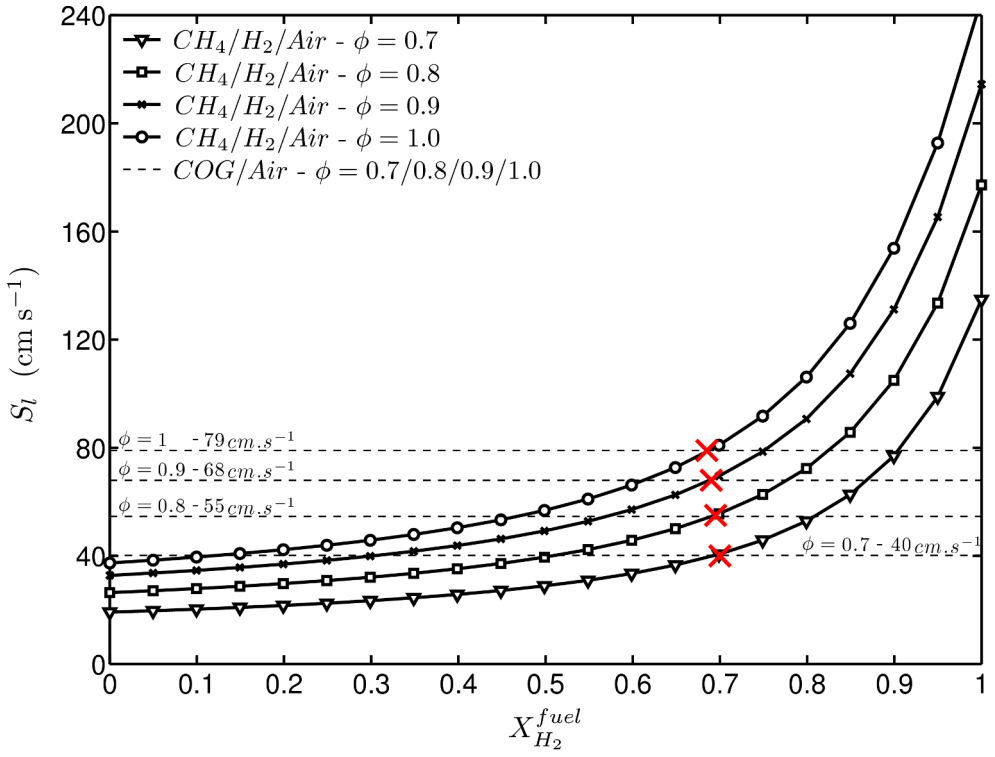


**Figure 6.4:** *Laminar burning velocity $S_L$ of $H_2/CH_4/Air$ mixtures in terms of $H_2$ molar fractions in the fuel $X_{H_2}^{fuel}$ for different equivalence ratios ($\Phi$ = 0.7, 0.8, 0.9, 1.0). Values are superimposed to the laminar burning velocity of $COG/Air$ mixtures for a given equivalence ratio. Red crosses show the $H_2$ molar fraction in the fuel of the $H_2/CH_4/Air$ mixtures having the same laminar burning velocities as the $COG/Air$ mixture. The detailed chemistry mechanism from Lindstedt (1997) is used for these computations. The pressure is set to 101325 Pa and the fresh gas temperature is $T_u = 298$ K.*

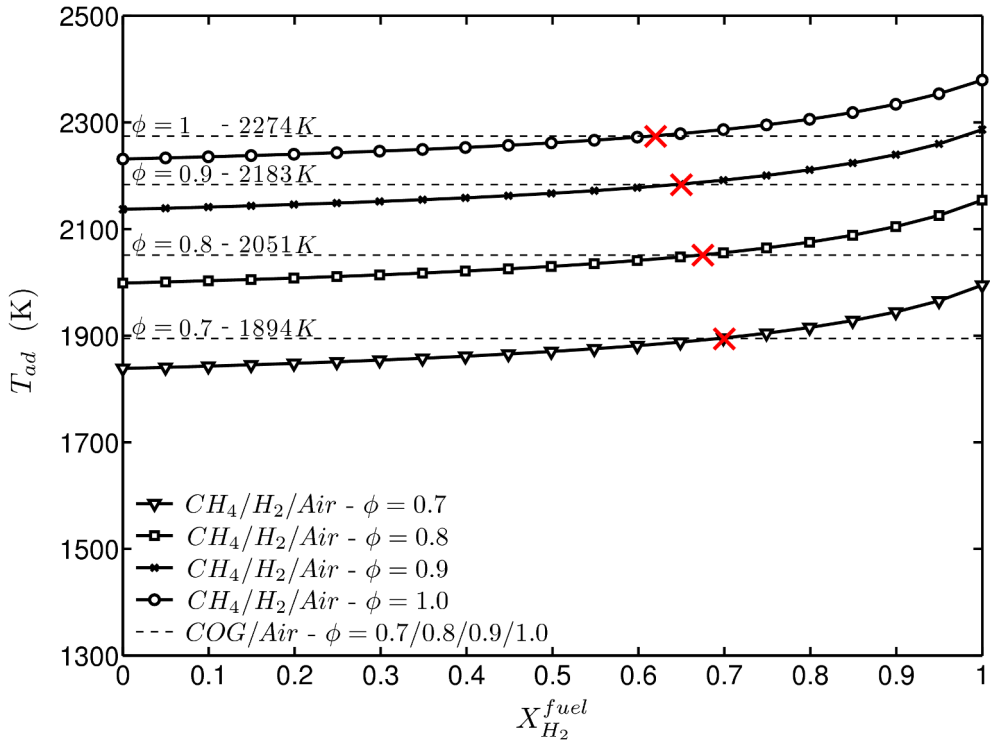


**Figure 6.5:** *Adiabatic flame temperature $T_{ad}$ of $H_2/CH_4/Air$ mixtures in terms of $H_2$ molar fractions in the fuel $X_{H_2}^{fuel}$ for different equivalence ratios ($\Phi$ = 0.7, 0.8, 0.9, 1.0). Values are superimposed to the adiabatic flame temperature of $COG/Air$ mixtures for a given equivalence ratio. Red crosses show the $H_2$ molar fraction in the fuel of the $H_2/CH_4/Air$ mixtures having the same adiabatic flame temperature as the $COG/Air$ mixture. The detailed chemistry mechanism from Lindstedt (1997) is used for these computations. The pressure is set to 101325 Pa and the fresh gas temperature is $T_u = 298$ K.*

**Table 6.2:** *Reference operating conditions*

| $X^{fuel}_{CH_4}$ | $X^{fuel}_{H_2}$ | $\phi$ | P (kW) | $S_L$( cm $s^{-1}$) | $T_{ad}(K)$ |
|---|---|---|---|---|---|
| 0.4 | 0.6 | 0.7 | 4 | 33.7 | 1882 |

sults slightly differ for the adiabatic flame temperatures presented in Fig. 6.5. The representative value for $X^{fuel}_{H_2}$ in the combustible mixture to reproduce the adiabatic temperature of COG/air flame changes with the equivalence ratio. An equivalence ratio of $\Phi = 0.7$ is retained for the $CH_4$-$H_2$-Air reference composition to mimic the combustion of COG/air flame at the same equivalence ratio. To comply with the optimal range of the experimental setup, the corresponding thermal power $P$ is fixed to $P = 4$ kW for an injected mass flow rate $\dot{m} = 1.86 \cdot 10^{-3}$ kg.s$^{-1}$.

The selected operating conditions $P = 4$ kW, $\phi = 0.7$ and $X^{fuel}_{H_2} = 0.70$ has been experimentally explored and showed an unstable behavior of the flame shape. To ensure a stable reference case, the operating conditions have been slightly modified to $P = 4$ kW, $\phi = 0.7$ and $X^{fuel}_{H_2} = 0.60$ with a minor impact on $T_{ad}$ and $S_L$ as shown in Figs. 6.4 and 6.5. Table 6.2 summarizes the final characteristics of the reference mixture.

## 6.4 Experimental and numerical characterization of the non-reacting flow

This section develops and validates against measurements the numerical strategy (computational domain, mesh, boundary conditions) retained to describe the non-reacting flow field.

### 6.4.1 Operating conditions

For safety reasons only air is injected for the non-reactive experiments. The inlet flow conditions are determined to conserve the same volume flow rate at the burner outlet than in the reacting case.

$$\begin{cases} Q^{R}_{CH_4} & = 81 \cdot 10^{-6} \text{ m}^3.\text{s}^{-1} = 4.8619 \text{ L.mn}^{-1} \\ Q^{R}_{H_2} & = 122 \cdot 10^{-6} \text{ m}^3.\text{s}^{-1} = 7.32 \text{ L.mn}^{-1} \\ Q^{R}_{air} & = 1522 \cdot 10^{-6} \text{ m}^3.\text{s}^{-1} = 91.32 \text{ L.mn}^{-1} \\ Q^{NR}_{air} & = 1725 \cdot 10^{-6} \text{ m}^3.\text{s}^{-1} = 103.5 \text{ L.mn}^{-1} \end{cases}$$

where $Q^{NR}_{air} = Q^{R}_{air} + Q^{R}_{CH_4} + Q^{R}_{H_2}$ is the air volume flow rate that is needed in the non-reacting (NR) case and $Q^{R}$ represents the volume flow rate of the reacting case.

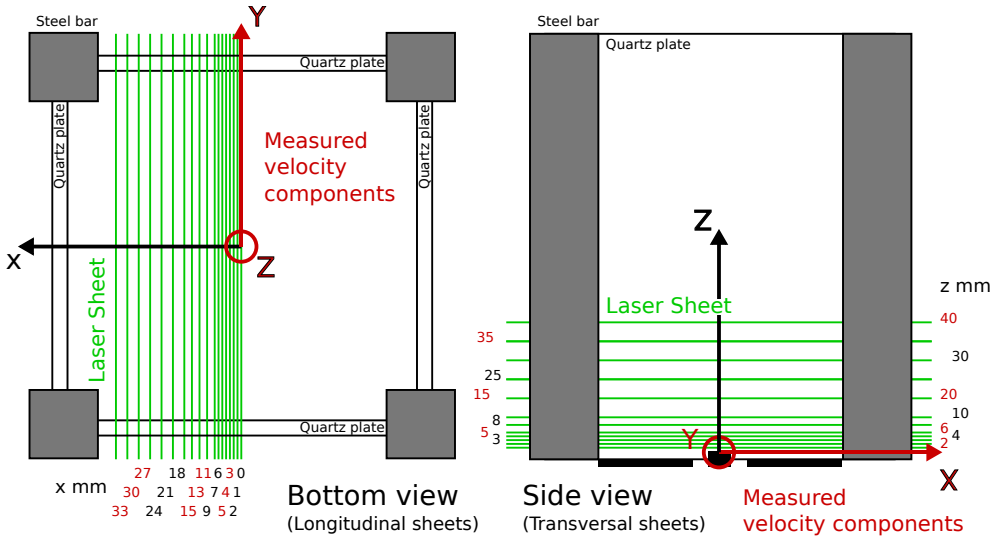


**Figure 6.6:** *Schematics of the selected measurement planes using PIV for the non reacting case.*

### 6.4.2 Velocity measurements

A 3D characterization of the flow has been carried out using Particle Imaging Velocimetry (PIV). Figure 6.6 shows the axial and transverse measured planes with the corresponding velocity components. A total of 31 planes (18 axial and 13 transverse) were examined using PIV. The spatial resolution used for planes selection is increased near the injector location, the main region of interest. Due to symmetry, only one half of the combustion chamber was explored with axial laser sheets. Due to the proximity of the planes in both directions, it is possible to evaluate the three velocity components in the measured region by linear interpolation of the data between measured points.

### 6.4.3 Numerical strategy

Considering the low Mach numbers encountered in the EM2C configuration ($M \approx 0.03$), the low-Mach LES solver YALES2 (Moureau et al., 2011a) is retained to perform the computations on an unstructured tetrahedral mesh. A centered fourth-order finite volume scheme is used for spatial discretization. A TRK temporal scheme, characterized in Kraushaar (2011), is used to perform time integration of convective terms. Closure of unresolved fluxes is performed using SIGMA model (Nicoud et al., 2011) for Reynolds stresses. Two complementary computational domains and meshes have been designed.

#### 6.4.3.1 Full domain - Refined mesh

The first domain, denoted as the full domain and shown in Fig.6.7(a), starts upstream the swirler and includes the swirler geometry. This domain has been discretized with a very fine mesh to ensure a sufficient resolution of the turbulent structures within both the swirler and the injection tube. The characteristic mesh size within the swirler is 0.1 mm ensuring a 40 nodes discretization between two consecutive swirler blades. The mesh size grows linearly within the tubes to reach 0.25 mm at the injection tube exit. In the reaction zone, the mesh size also evolutes linearly from 0.25 mm to 0.5 mm. The characteristic mesh sizes are summarized in the Fig.6.7(b). This mesh has been mainly refined within the injection system as the main objective is here to compute correctly the mean and RMS velocity profiles within the injection tube. The full mesh results in 50 million tetrahedral elements.

A first non-reacting computation is performed using this refined mesh. Considering the honeycomb placed upstream the swirler and not included in the computational domain, a constant and laminar velocity profile is injected upstream the swirler. The CPU cost of this computation is very high ($2.10^6$ hCPU for 10 flow characteristic time) because the high number of mesh cells within the swirler and the injection system. Moreover, the minimal mesh size ($\Delta_x \approx 0.1$ mm) imposed by the swirler geometry imposes very small time steps which increases the total CPU cost.

#### 6.4.3.2 Reduced domain - Final mesh

A reduced computational domain which excludes the injection system is shown in Fig.6.8. Z is the spatial coordinate along the burner axis and Z = 0 mm corresponds to the bluff-body wall surface position. The characteristic mesh size is kept similar to the one presented for the *Full domain - Refined mesh* but the full reduced mesh results in 33 million tetrahedral elements as the swirler device is not included and the minimum cell size is increased to $\Delta_x \approx 0.2$ mm.

Mean velocity profiles computed on the full domain are used to prescribe the reduced domain boundary conditions at Z = -20 mm. A Homogeneous and Isotropic Turbulence (HIT), generated from a Passot and Pouquet (1987) spectrum, is prescribed to be representative of the velocity fluctuations level extracted from the *Full domain - Refined mesh* simulation.

### 6.4.4 Results analysis

Figures 6.9 (a-f) and 6.10 (a-f) show 2-D experimental and numerical colormaps of mean velocities $U_x$ and $U_z$ in three different longitudinal planes (Y = 0 ; 4 ; 7 mm). The numerical results have been obtained on the reduced domain introduced previously. Figures 6.9 (a-b) show a correct prediction of the mean

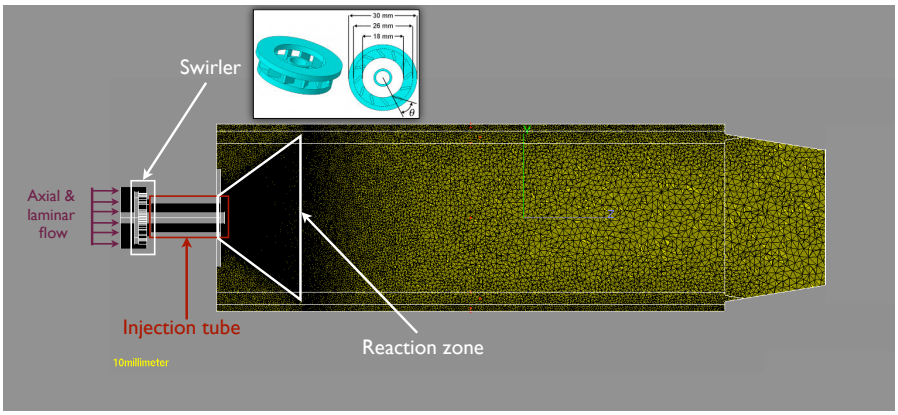


(a) Full domain

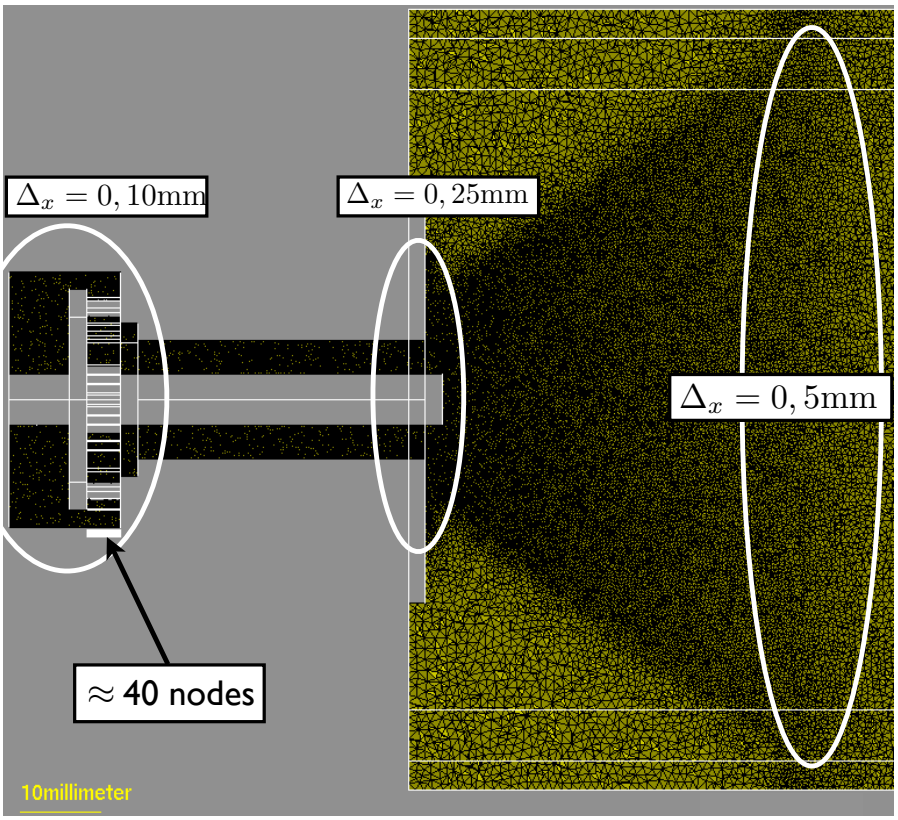


(b) Injection system

**Figure 6.7:** *Full domain - Refined mesh. 2-D longitudinal cut of the full computational domain and the refined mesh, including the swirler geometry.*

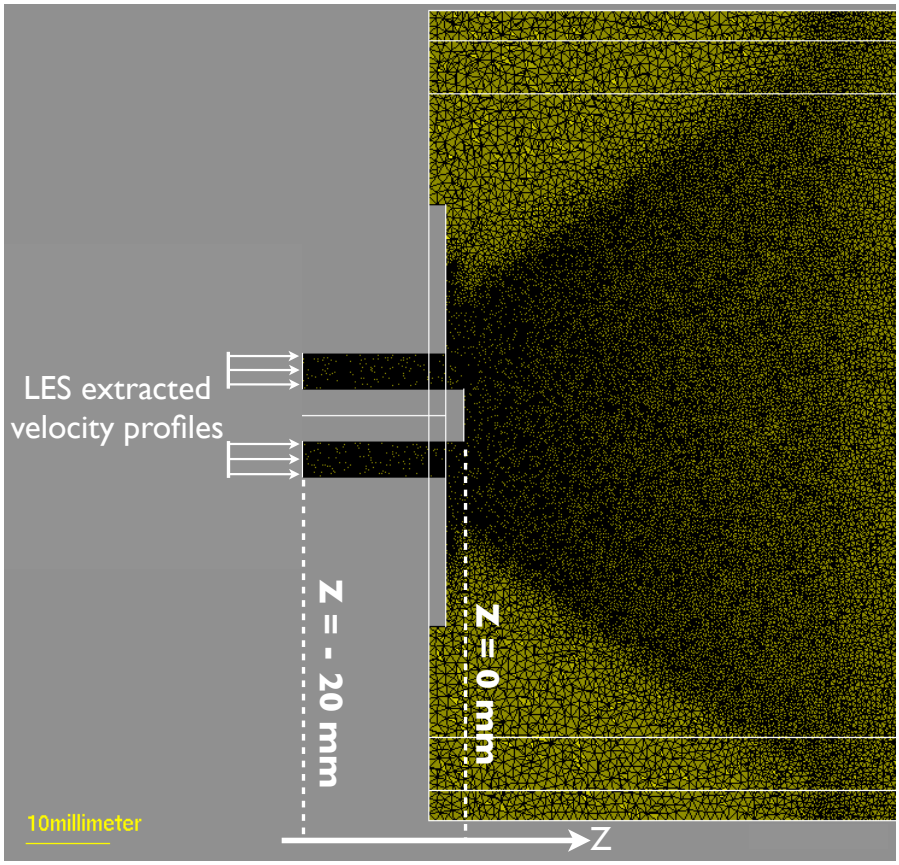


**Figure 6.8:** *Reduced domain - Final mesh. 2-D longitudinal cut of the reduced computational domain and the final mesh, starting downstream the swirler device.*

longitudinal component of the flow velocity in the central plane. Both the size of the inner recirculation zone (IRZ) (in the wake of the bluff-body) and the expansion of the flow due to swirl are captured in the simulations. The good agreement between the experimental and numerical results remains valid for off-axis longitudinal planes (see Fig. 6.9 (c-f)). Figure 6.10 presents similar results for the horizontal component of the flow velocity.

Figures 6.11 to 6.15 presents 1-D mean and RMS velocity profiles along X direction for the three velocity components $U_x$, $U_y$ and $U_z$. Figure 6.11 confirms that the LES well represents the size and intensity of the IRZ. However, the calculations underestimates the radial expansion of the flow for $Z > 20$ mm. A strong indicator for the quality of the calculations is that the RMS velocity along the Z axis (see Fig. 6.12) are very well represented in terms of position and amplitude. Maximums of RMS intensity are obtained in the shear layers between the jet and the IRZ (Inner Shear Layer - ISL) and between the jet and the ORZ (Outer Shear Layer - OSL). These similarities remain true for $Z < 35$

mm.

The swirl intensity is directly related to the horizontal component $U_y$ shown in Fig. 6.13. Experiments and computations agree for $Z < 15$ mm. Above that value, experiments feature lower value of rotational velocity.
Figures 6.14 and 6.15 presents mean and RMS of $U_x$ velocity component. In this case, calculations present a good agreement in terms of mean values for $Z < 6$ mm and of RMS values for all the measurement locations. Slight differences are observed for $Z > 15$ mm.

## 6.5 Conclusion

The EM2C burner presented in this chapter is representative of the geometry of industrial furnaces. Operating conditions representative of the combustion of COG/air mixtures have been determined using a simplified $CH_4$-$H_2$-Air premixing. A dedicated injection strategy (mean and RMS input velocity fields) has been developed and validated by exhaustive comparisons with velocity measurements (PIV) in longitudinal and transverse planes under non-reactive conditions. These comparisons validate the ability of the selected numerical strategy (computational domain, mesh grid, boundary conditions, LES solver) to capture the non-reacting flow properties.

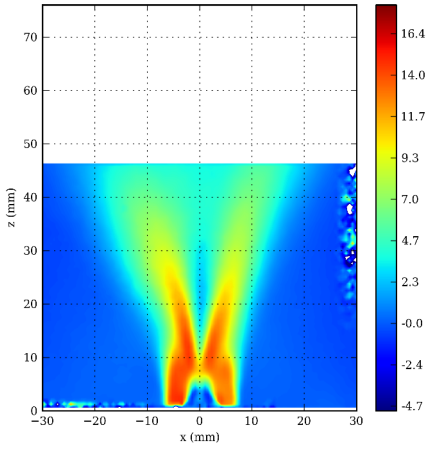


(a) PIV - Mean $U_z$ [m.s$^{-1}$] - Plane Y = 0 mm

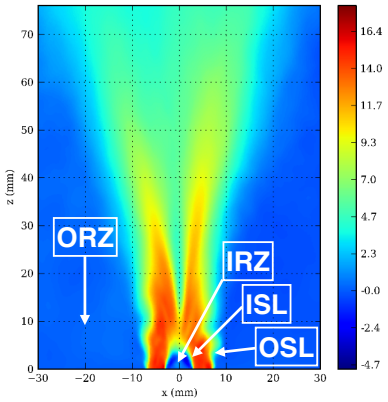


(b) LES - Mean $\widetilde{U_z}$ [m.s$^{-1}$] - Plane Y = 0 mm

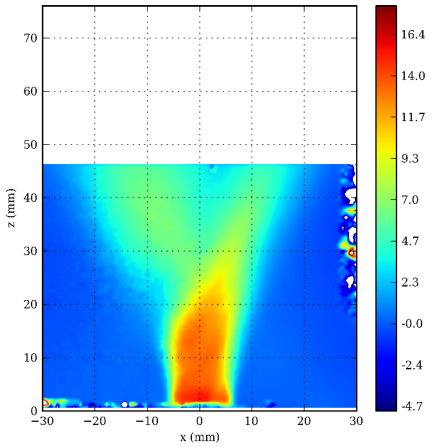


(c) PIV - Mean $U_z$ [m.s$^{-1}$] - Plane Y = 4 mm

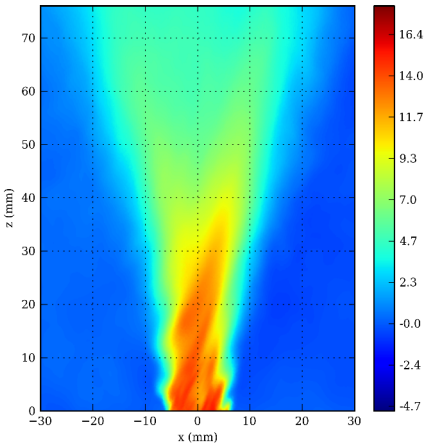


(d) LES - Mean $\widetilde{U_z}$ [m.s$^{-1}$] - Plane Y = 4 mm

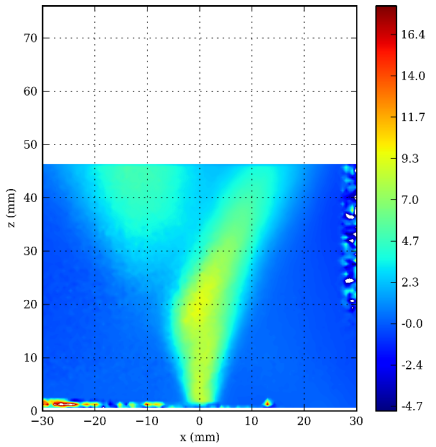


(e) PIV - Mean $U_z$ [m.s$^{-1}$] - Plane Y = 7 mm

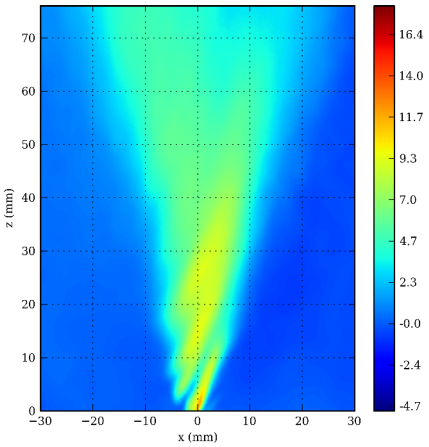


(f) LES - Mean $\widetilde{U_z}$ [m.s$^{-1}$] - Plane Y = 7 mm

**Figure 6.9:** *2-D cut of mean axial velocity $U_z$ in different longitudinal planes. Inner recirculation zone (IRZ), Inner shear layer (ISL) and Outer shear layer (OSL) are indicated in figure (b).*

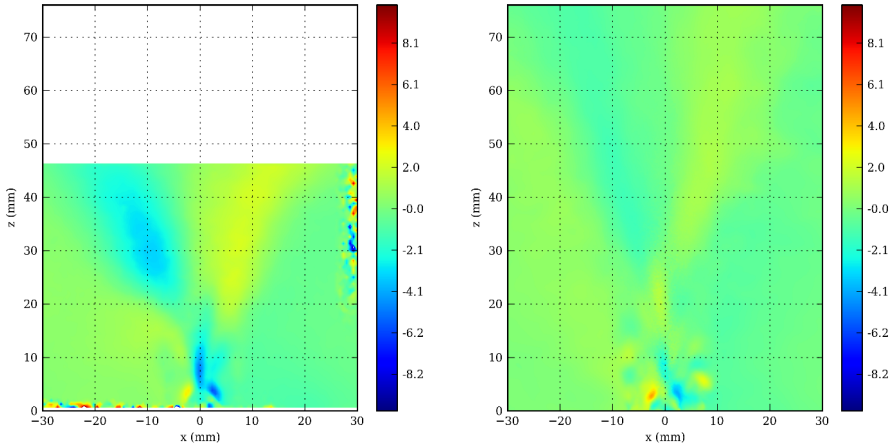


(a) PIV - Mean $U_x$ [m.s$^{-1}$] - Plane Y = 0 mm

(b) LES - Mean $\widetilde{U_x}$ [m.s$^{-1}$] - Plane Y = 0 mm

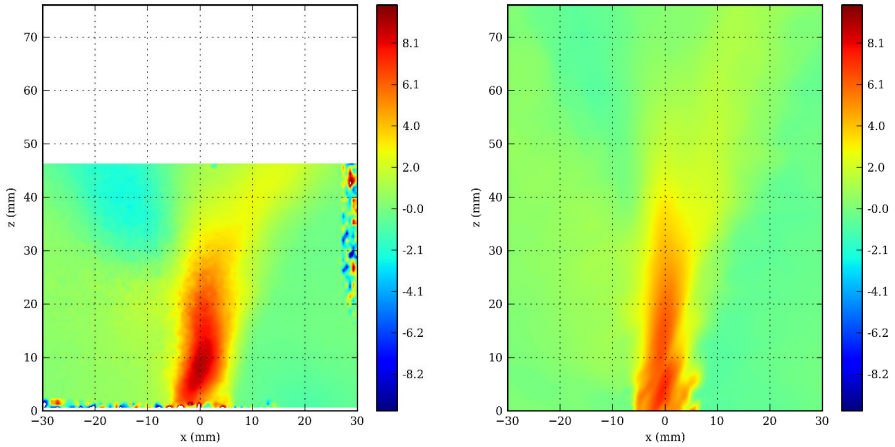


(c) PIV - Mean $U_x$ [m.s$^{-1}$] - Plane Y = 4 mm

(d) LES - Mean $\widetilde{U_x}$ [m.s$^{-1}$] - Plane Y = 4 mm

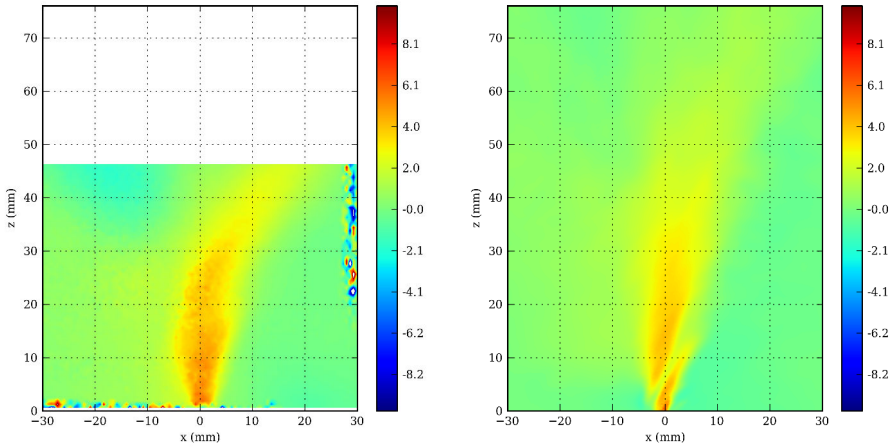


(e) PIV - Mean $U_x$ [m.s$^{-1}$] - Plane Y = 7 mm

(f) LES - Mean $\widetilde{U_x}$ [m.s$^{-1}$] - Plane Y = 7 mm

**Figure 6.10:** *2-D cut of mean velocity $U_x$ in different longitudinal planes*

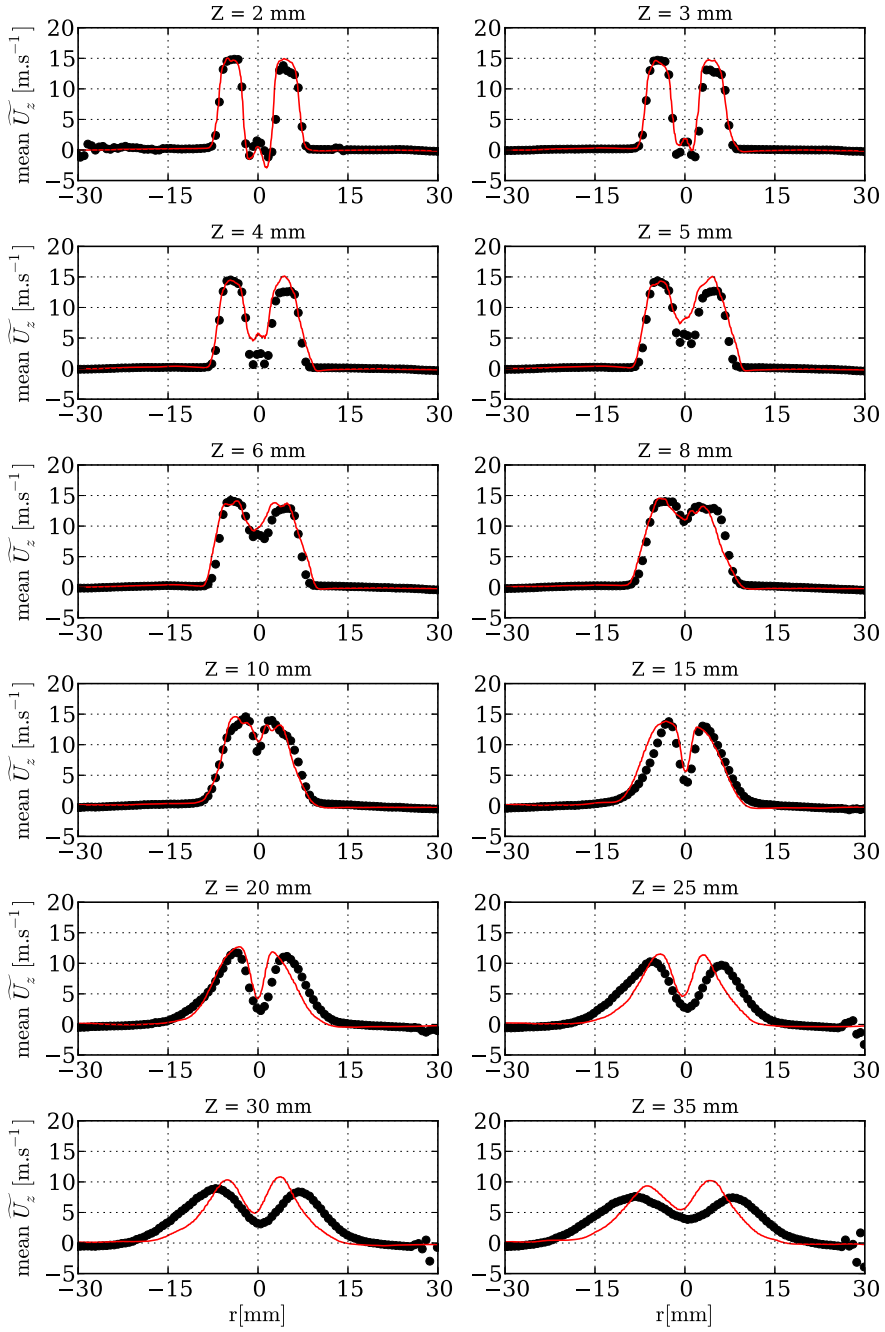


**Figure 6.11:** *1-D radial mean profiles of $U_z$ axial velocity component at different axial positions Z in the logitudinal plane Y = 0 mm. Red lines and black symbols correspond to LES calculations and PIV measurements, respectively.*

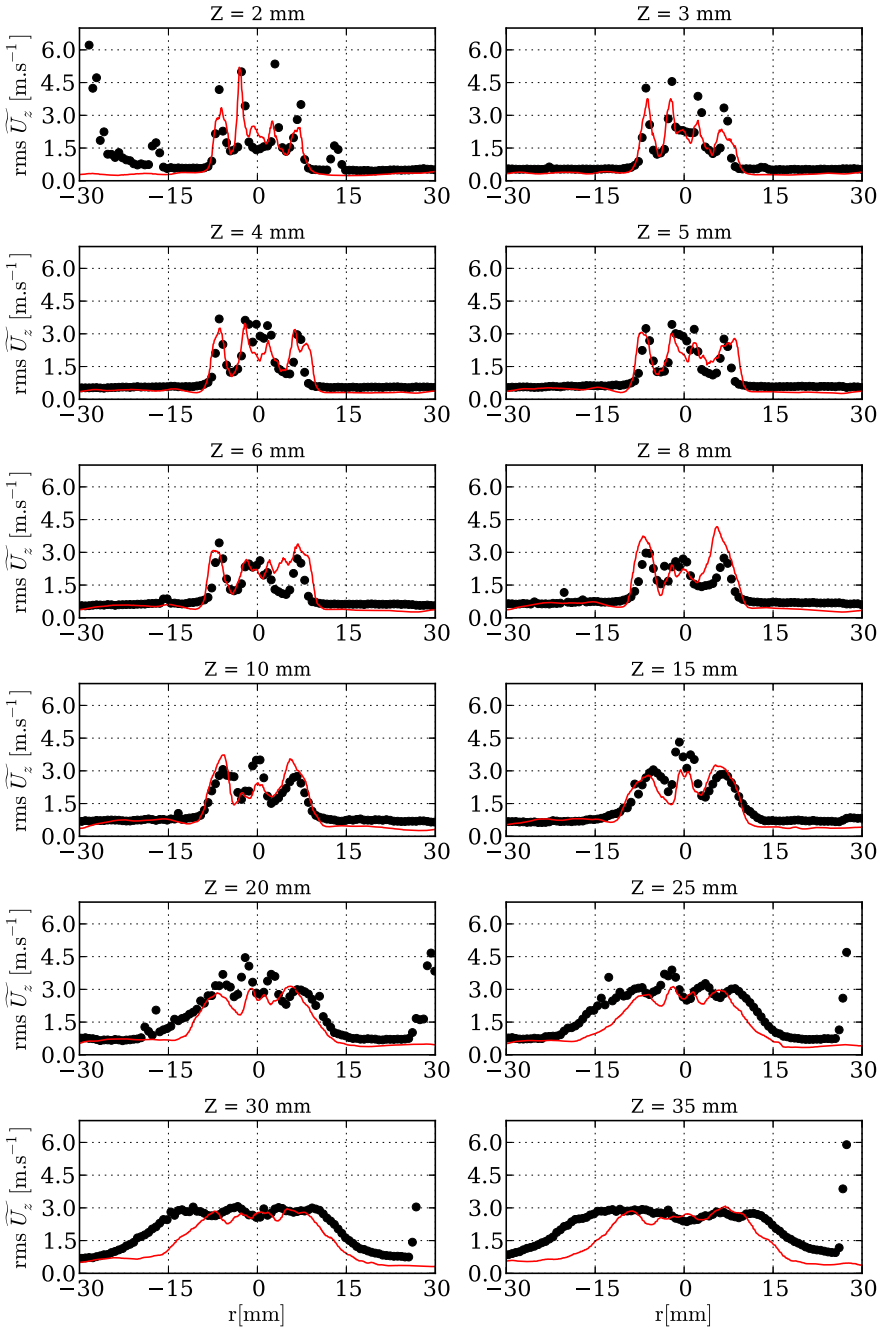


**Figure 6.12:** *1-D radial RMS profiles of $U_z$ axial velocity component at different axial positions Z in the logitudinal plane $Y = 0$ mm. Red lines and black symbols correspond to LES calculations and PIV measurements, respectively.*

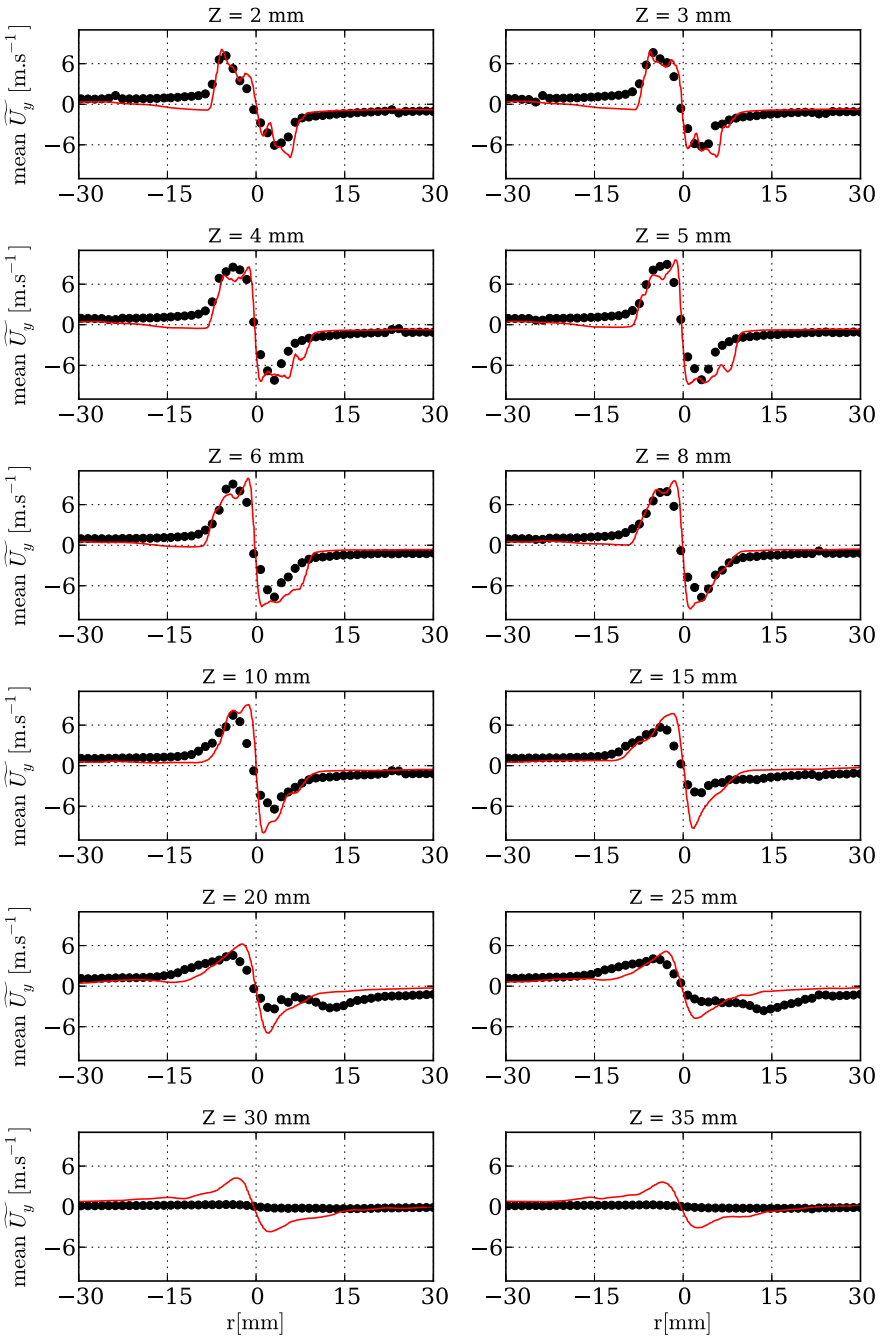


**Figure 6.13:** *1-D radial mean profiles of $U_y$ orthoradial velocity component at different axial positions Z in the logitudinal plane $Y = 0$ mm. Red lines and black symbols correspond to LES calculations and PIV measurements, respectively.*

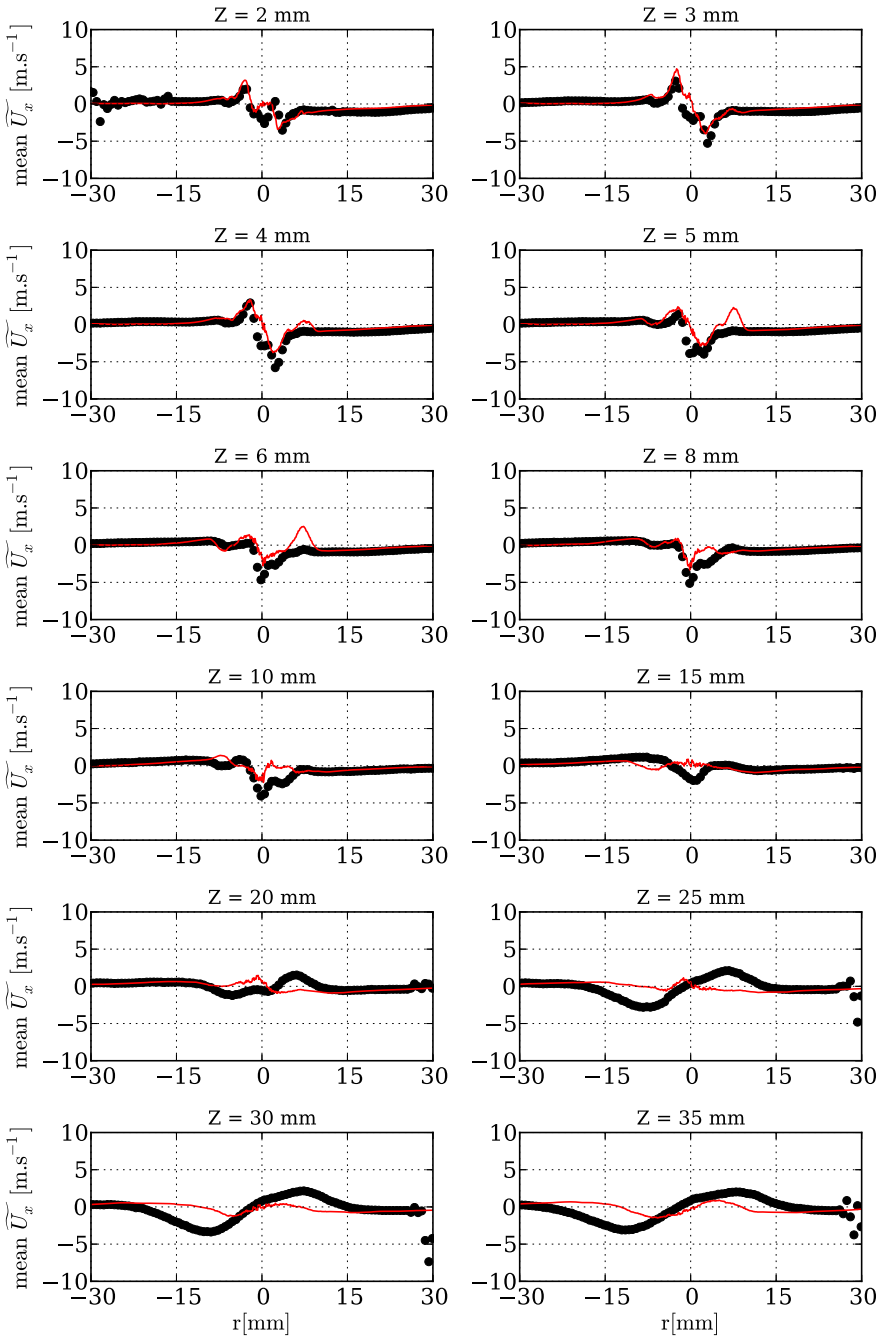


**Figure 6.14:** *1-D radial mean profiles of $U_x$ radial velocity component at different axial positions Z in the logitudinal plane Y = 0 mm. Red lines and black symbols correspond to LES calculations and PIV measurements, respectively.*

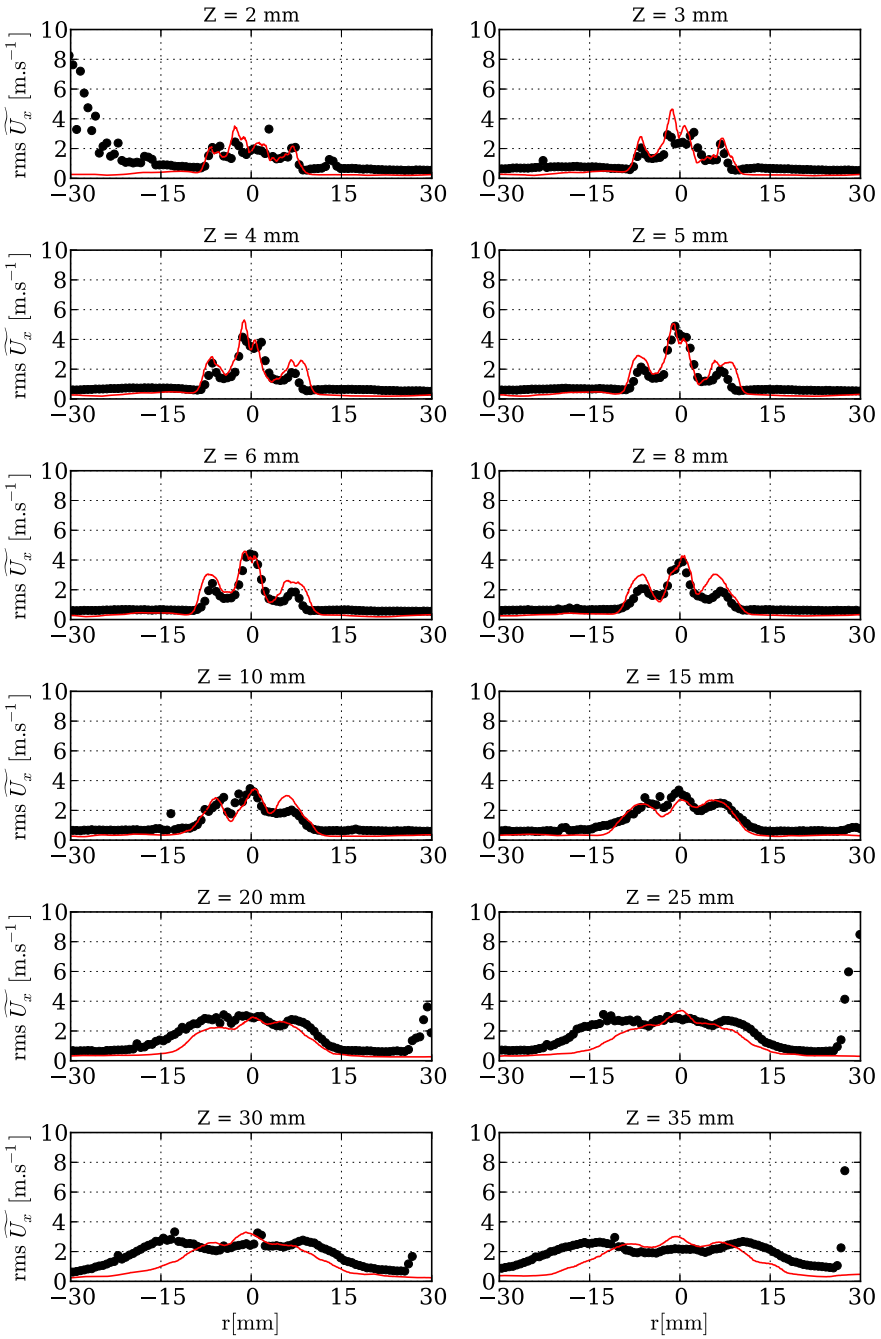


**Figure 6.15:** *1-D radial RMS profiles of $U_x$ radial velocity component at different axial positions Z in the logitudinal plane Y = 0 mm. Red lines and black symbols correspond to LES calculations and PIV measurements, respectively.*

# Chapter 7

# Application to the EM2C burner: prediction of flame topology

**Contents**

*The numerical strategy detailed previously is employed in this chapter to study the ability of the F-TACLES model to capture the different flame shapes observed experimentally by Guiberti (2015) when the fuel composition is varied. The results from the adiabatic and the non-adiabatic computations are compared to identify the impact of heat losses.*

## 7.1 Objectives of the study

The objectives of this chapter is to analyse the sensitivity of the flame topology to different physical parameters and to validate the ability of the F-TACLES model to capture these different governing phenomena. An experimental study conducted by Guiberti et al. (2014a) on the configuration presented in chapter 6 have shown that the turbulent flame shape was mainly governed by heat losses and fuel composition. Both factors are investigated numerically in this chapter.

First, the impact of heat losses on the flame shape will be analyzed on the case $X_{H_2}^{\text{fuel}} = 0.6$ detailed in Tab. 6.2 for which the flame stabilizes with a V shape. As the flame is confined, it is expected that heat exchange at the chamber walls will play an important role on turbulent combustion processes. As shown in Tab. 7.1, two different LES of this case will be performed using the F-TACLES model. The first one will assume an adiabatic burner while the second one will account for heat losses at the wall.

The second part of the study aims to understand the impact of a variation in COG chemical composition on the flame shape and stabilization process. In particular, the sensitivity analysis will focus on the impact of hydrogen enrichment on the flame shape. For that purpose, the fuel composition is increased from $X_{H_2}^{\text{fuel}} = 0.6$ to $X_{H_2}^{\text{fuel}} = 0.9$ while other operating conditions are kept constant. For this case, it is shown that flame shape bifurcates from V to an M shape. As shown in Tab. 7.1, a third LES will be performed on this new operating conditions to validate the ability of the numerical and modeling strategy to capture the effect of hydrogen enrichment on the flame topology.

**Table 7.1:** *Simulated cases*

| Fuel composition | Flame shape | Large Eddy Simulation | Simu. # |
|---|---|---|---|
| $X_{H_2}^{\text{fuel}} = 0.6$ | V | Adiabatic | 1 |
| | | Non-adiabatic | 2 |
| $X_{H_2}^{\text{fuel}} = 0.9$ | M | Non-adiabatic | 3 |

## 7.2 Available diagnostics

### 7.2.1 Velocity measurements

Particle Imaging Velocimetry is used under reacting conditions to measure mean and RMS axial ($U_z$) and radial ($U_x$) velocity profiles. This diagnostic has been applied to the case $X_{H_2}^{\text{fuel}} = 0.6$ in a longitudinal plane. Note that orthoradial component ($U_y$) of the velocity is not available here. Velocity measurements for the case $X_{H_2}^{\text{fuel}} = 0.9$ are not available.

### 7.2.2 Flame position measurments

Longitudinal planar Laser Induced Fluorescence of the hydroxyl radial (OH-PLIF) measurements are carried out to identify the flame front position As the intensity of the laser sheet may vary between each laser pulse, we have access only to qualitative OH molar fraction. To be able to compare experimental data with simulation, the "binarized" variable $X_{\text{OH}}^{\text{bin}}$ is introduced and computed for each OH-PLIF images as follows:

$$X_{\text{OH}}^{\text{bin}} = \begin{cases} 0 \text{ if } \frac{X_{\text{OH}}}{\max(X_{\text{OH}})} < 0.20 \\ 1 \text{ if } \frac{X_{\text{OH}}}{\max(X_{\text{OH}})} \geq 0.20 \end{cases} \tag{7.1}$$

The time averaging of $X_{\text{OH}}^{\text{bin}}$ gives the probability of being in the burnt gases. This methodology is used to post process both experimental and LES results. This diagnostic has been applied to both $X_{H_2}^{\text{fuel}} = 0.6$ and $X_{H_2}^{\text{fuel}} = 0.9$ cases.

OH* chemiluminescence has been performed to identify the heat release layer position. For that purpose, Abel transform has been applied to the OH* Chemiluminescence snapshots. Signals are normalized in both experiments and simulation assuming that OH* chemiluminescence intensity scales with the heat release (Katsuki et al., 1988):

$$\dot{\omega}_T^{\text{norm}} = \frac{\dot{\omega}_T}{\max(\dot{\omega}_T)} \approx \frac{I(\text{OH}^*)}{\max(I(\text{OH}^*))} \tag{7.2}$$

where $I(\text{OH}^*)$ represents the intensity of the OH* chemiluminescence signal. $\dot{\omega}_T$ represents the heat release and $\dot{\omega}_T^{\text{norm}}$ its normalized value.

### 7.2.3 Thermal boundary conditions

To prescribe the thermal boundary conditions in the non-adiabatic simulation, the burner walls temperature has been characterized experimentally. As indicated in Fig. 7.1, Laser Induced Phosphorescence (LIP) measurements have been performed to determine the temperature at one quartz wall (LIP2), at the

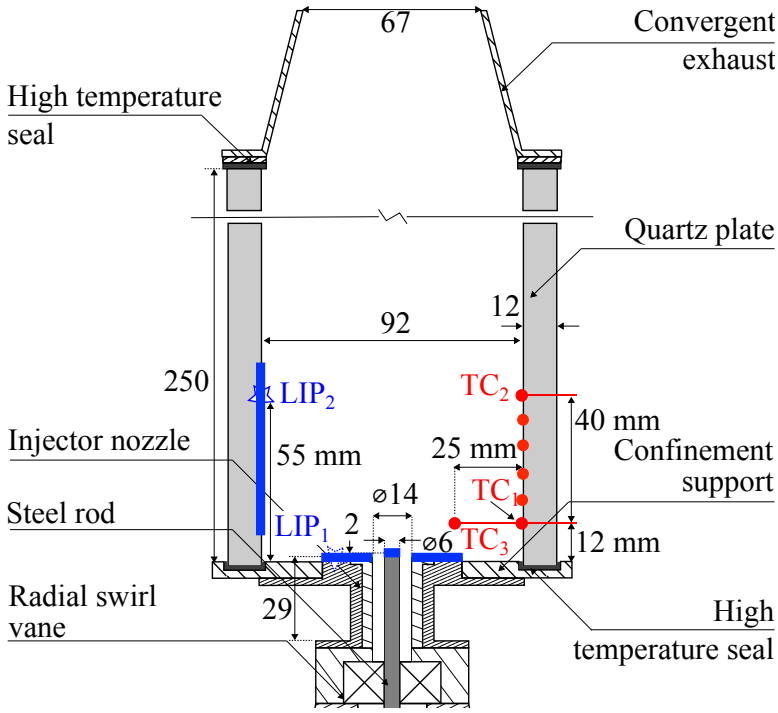


**Figure 7.1:** *Experimental set-up. Regions where LIP and thermocouple temperature measurements were performed are indicated using blue line (LIP) and red dots (thermocouple).*

dump plate and at bluff-body wall surfaces (LIP1). Thermocouple measurements have been also performed along one combustion chamber corner (vertical steel bars holding the quartz walls). Figure 7.2 displays the temperature measurements along a quartz window (LIP2). Figure 7.3 (left) plots thermocouple measurements performed at the surface of the vertical steel bars. The temperature slightly increases along with the distance from the dump plate. Fig. 7.3 (right) shows LIP measurements on area LIP1.In all the measured location, the temperature at the wall ($400\text{K} < T_{\text{wall}} < 800\text{K}$) is much lower than the adiabatic flame temperature ($T^{\text{ad}} \approx 1900\text{K}$) which demonstrates that intense heat exchange occurs between recirculated burnt gases and the burner walls.
As the wall temperature measurements only partially cover the combustor surface, a reconstruction using linear interpolations and extrapolations has been performed to provide complete temperature boundary conditions to the different LES computations.

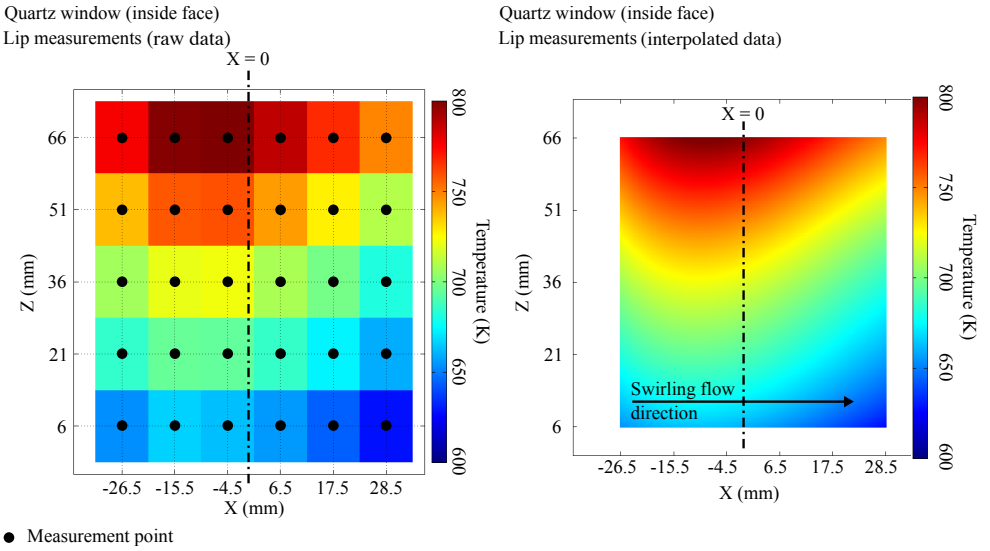


**Figure 7.2:** *LIP measurements on the quartz windows of the combustion chamber (LIP2 area). At the left, the raw data are display as well as the location of each measurements points. At the right, the temperature of the quartz windows is reconstructed using linear interpolations.*

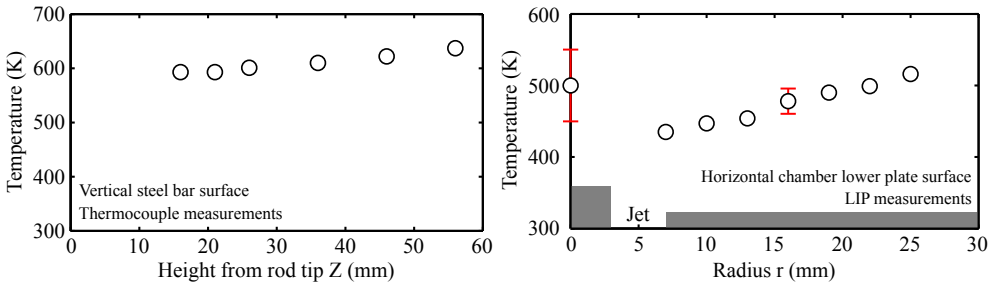


**Figure 7.3:** *Experimental set-up. Regions where LIP and thermocouple temperature measurements were performed are indicated using blue line (LIP) and red dots (thermocouple).*

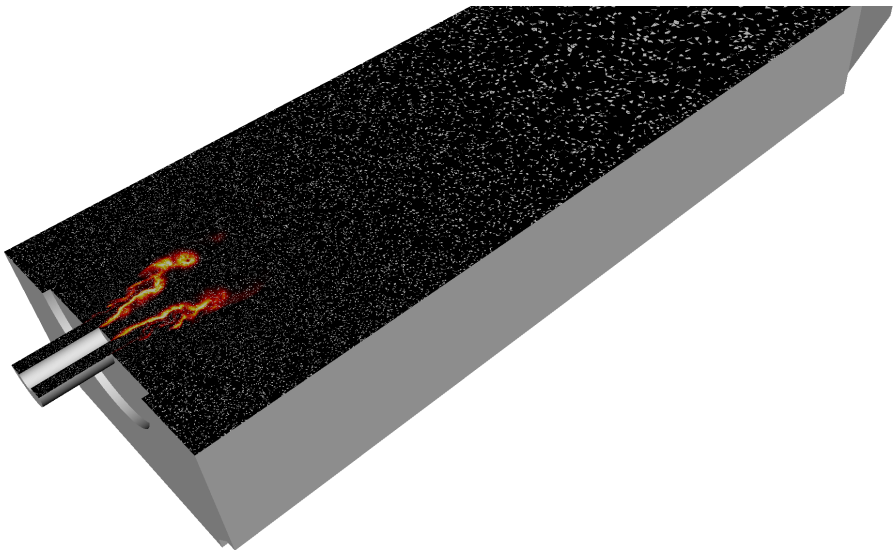

**Figure 7.4:** *Half portion of the VLG computational domain. A longitudinal cut of the mesh is shown and colored by the filtered volumic heat release* $\widetilde{\dot{\omega}}_T$.

## 7.3 Numerical strategy

### 7.3.1 Numerical set-up

The YALES2 code (Moureau et al., 2011a) is used with the same parametrization as for the non-reacting case computation. The mesh realized on the reduced computational domain is selected. The mean cell size at the flame location varies between 0.25 mm and 0.5 mm. It corresponds to 2 - 4 times the laminar flame reaction thickness and 0.5 - 1 times the thermal thickness, respectively. The F-TACLES database is computed with $\Delta/\delta_l^0 = 9$. Figure 7.4 shows the computational domain and mesh size repartition in a longitudinal plane.

A centered fourth-order finite volume scheme is used for spatial discretization. Time integration of convective terms is performed explicitly using the TRK4 fourth-order scheme characterized by Kraushaar (2011). Closure of Reynolds stresses is performed using the SIGMA model (Nicoud et al., 2011). In this chapter, the sub-filter scale winkling $\Xi_\Delta$ is estimated using the model proposed by Charlette et al. (2002a) discussed in Sec. 4.1 and described by Eq. 4.8. The parameter $\beta$ has been here set to $\beta = 0.5$ and the unresolved velocity fluctuations $u'_\Delta$ are modeled using the approach detailed in Sec. 4.2.2. Chemical look-up tables are computed with REGATH thermochemistry package developed at the EM2C laboratory (Pons et al., 2009; Candel et al., 2011) and using the Lindstedt (1997) detailed chemical scheme composed of 29 species and 141 reactions.

### 7.3.2 Estimation of the non-adiabatic thermochemical variables

Some additional post-processing variables, such as chemical mass and mole fractions, may be needed to analyze the results of the non-adiabatic computation. For instance, the molar fraction of OH, noted $X_{\mathrm{OH}}$, is used to compare numerical results with OH laser induced fluorescence measurements. As shown in Sec. 2.3.2, the non-adiabatic database does not give access to filtered variables. An alternative approach is proposed here to account for the impact of heat losses on post-processing quantities neglecting the impact of sub-grid scale fluctuations ($S_z = 0$) and the impact of subgrid scale flame wrinkling ($\Xi = 1$).

The unfiltered progress variable $Y_c$, also denoted $Y_c^{\mathrm{raw}}$ in this paragraph to ensure clarity, is first tabulated as a function of the filtered progress variable $\widetilde{Y_c}$ in the adiabatic database as:

$$Y_c^{\mathrm{raw}} = Y_c^{\mathrm{raw}}[\widetilde{Y_c}, \widetilde{z}, S_z = 0, \Delta] = Y_c^{\mathrm{raw}}[\widetilde{Y_c}, \widetilde{z}, \Delta] \tag{7.3}$$

where $Y_c^{\mathrm{raw}}$ is extracted from a 1-D adiabatic freely-propagating flame, computed at the mixture fraction $z = \widetilde{z}$, before being filtered at size $\Delta$.

The knowledge of the deconvolution relation $Y_c^{\mathrm{raw}} = f(\widetilde{Y_c})$ allows also the reconstruction of the unfiltered non-adiabatic variables using the following relation:

$$\Phi^{\Delta h} = \Phi^{\Delta h}\left(Y_c = Y_c^{\mathrm{raw}}, z = \widetilde{z}, \Delta h = \Delta\widetilde{h}\right) = \Phi^{\Delta h}\left[Y_c^{\mathrm{raw}}, \widetilde{z}, \Delta\widetilde{h}\right] \tag{7.4}$$

This strategy is used in this chapter to capture the impact of heat losses on the value of $X_{\mathrm{OH}}$ and enable a detailed comparison of LES results with measured OH fields.

### 7.3.3 Initialization of the non-adiabatic computation

Experimental and numerical results of the EM2C burner under non-reacting conditions presented in Sec. 6.4.4 have shown very slow velocities in the ORZ (see Figs. 6.9 and 6.11). The high residence times in the ORZ induce a very long time to reach steady-state thermal regime. Therefore, it is proposed to perform a first non-reacting RANS simulation using the same computational domain as for the LES. The Fluent commercial solver (ANSYS® Fluent, 2009) is selected for that purpose. Adiabatic burnt gases are injected at the tube inlet and measured wall temperatures are imposed at the wall surfaces of the combustion chamber.

Results obtained from this simulation give a first approximation of the temperature field within the combustion chamber. Figure 7.5 compares the temperature obtained by RANS simulation in the outer recirculation zone (ORZ) with

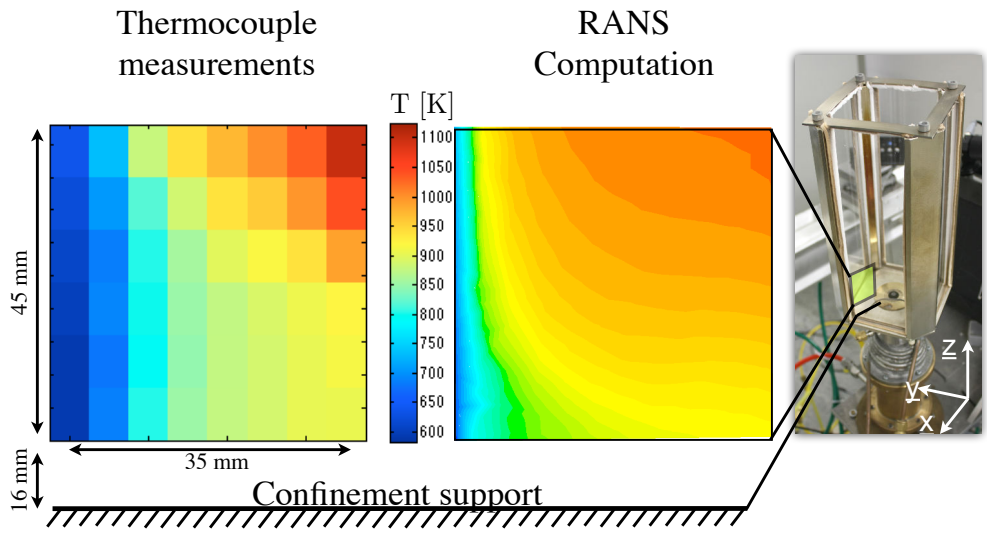


**Figure 7.5:** *Comparison of the mean temperature [K] obtained by both RANS simulation (right) and thermocouple measurements (raw data) (left).*

thermocouple measurements performed at the same plane location. A good agreement is found between the RANS simulation and the experiments.

The mean temperature field obtained by the steady RANS simulation is used to initialize the reacting LES computation under non-adiabatic conditions. This non-adiabatic simulation is compared to the adiabatic one in the following section.

## 7.4 Results analysis

### 7.4.1 Impact of heat losses on flame topology

Results obtained for the cases 1 and 2 ($X_{H_2}^{\text{fuel}} = 0.6$) are first analyzed. Figure 7.6 compares the mean flame position predicted by both simulations against the experimental measurements. The normalized mean heat release (left plots) and the binarized OH molar fraction (right plots) are presented. The adiabatic computation (Fig. 7.6(b)) predicts a M shape flame where both inner and outer flame fronts are observed. The inner flame front is located between the fresh stream and the inner recirculation zone (IRZ). The outer flame flame front delineates the fresh gas stream and the burnt gases in the outer recirculation zone (ORZ). This prediction is not in agreement with the measurements (Fig. 7.6(a)) where a V shape flame is identified. At the opposite, the non-adiabatic simulation (Fig. 7.6(c)) predicts a V flame shape and shows a good agreement with the measurements in terms of flame length and mean opening angle.

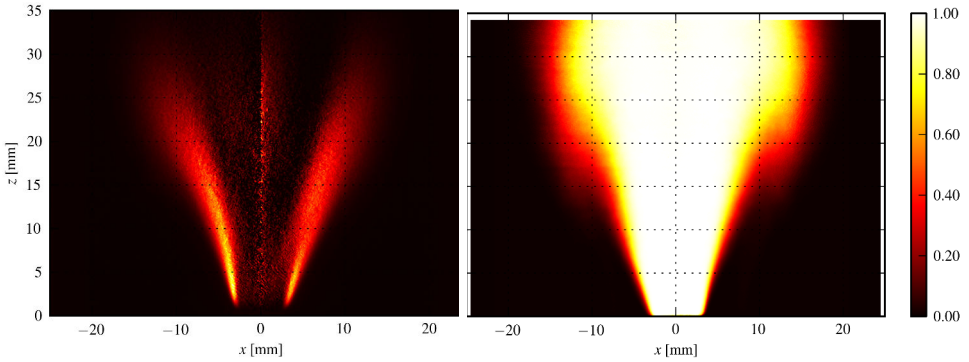


(a) Experimental measurments. (left) Normalized Abel deconvoluted OH* chemiluminescence. (right) Mean binarized OH-PLIF

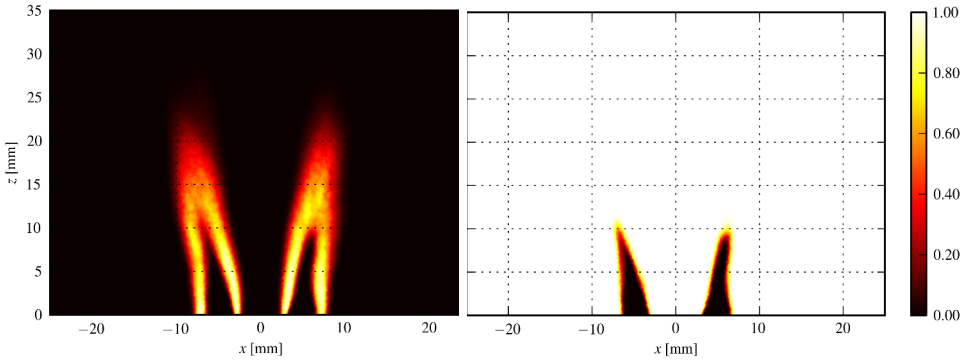


(b) Adiabatic simulation. (left) Normalized mean volumic heat release. (right) Mean binarized OH molar fraction $X_{\mathrm{OH}}$

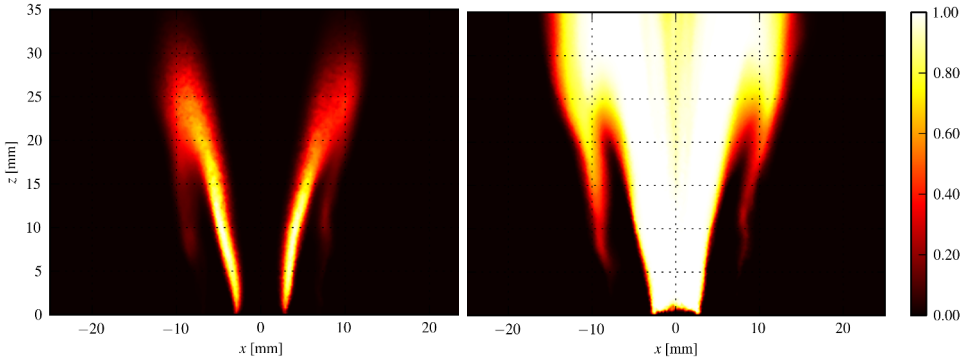


(c) Non-adiabatic simulation. (left) Normalized mean volumic heat release. (right) Mean binarized OH molar fraction $X_{\mathrm{OH}}$

**Figure 7.6:** *Comparisons of the mean flame position for the case* $X_{H_2}^{fuel} = 0.6$. *Experiments, adiabatic and non-adiabatic simulations results are shown.*

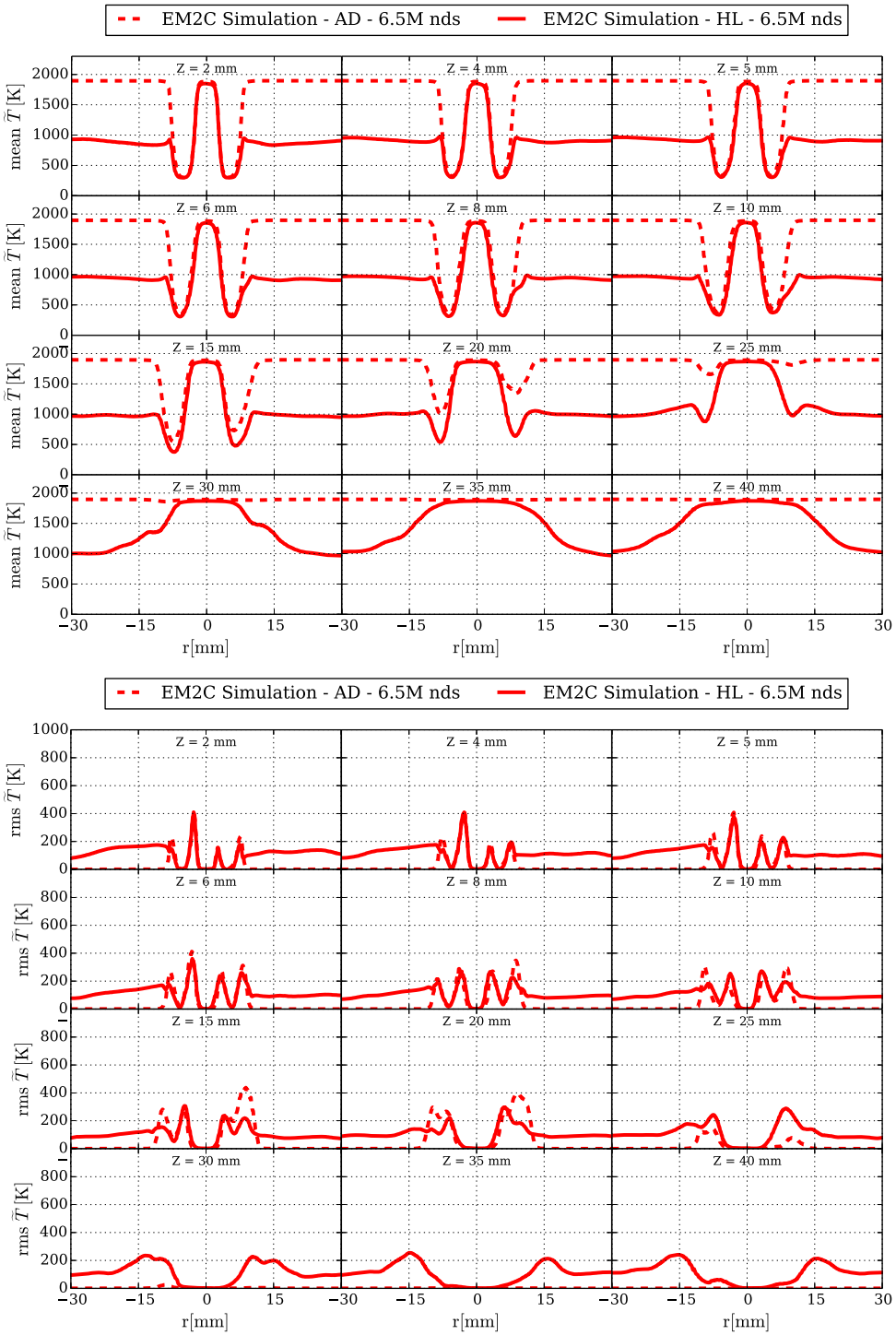


**Figure 7.7:** *1-D radial profiles of temperature at different distances Z from the bluff-body wall surface for the case* $X_{H_2}^{fuel} = 0.6$. *(top) Mean profiles. (bottom) RMS profiles.*

Figure 7.7 plots mean and RMS temperature profiles are shown at different distances from the bluff-body wall surface. Note that no azimuthal averaging has been applied to obtain these 1-D radial profiles since the combustion chamber has a square section. Important differences are observed between mean temperature profiles predicted by both adiabatic and non-adiabatic LES. In particular, a difference of approximately 1000K is observed in the very slow ORZ, for which an estimation of the characteristic time is $\tau_{ORZ} \approx 40$ ms (Guiberti et al., 2014a). During this recirculation time, hot gases exchange heat with cool walls ($T_{wall} \approx 800$ K). A very small reaction zone in the OSL regions predicted by the non-adiabatic simulation (Fig. 7.6(c)) is also identified in mean temperature profiles (Fig. 7.7) for $Z > 15$ mm : a slight temperature increase is observed in the layer between fresh gases temperature and cooled burnt gases for $r \approx 10$ mm. It can also be noted that for the non-adiabatic computation, turbulent structures are mixing cold and hot burnt gases in the ORZ which implies important RMS of temperature while no fluctuations of temperature are found in the adiabatic computation. In both computations, no fluctuations are found in the IRZ. This may be explained by the stability of the large recirculation zone and by the smaller gap between the temperature of burnt gases for both computations at the IRZ because of the limited surface area of the central rod. Flame fronts stabilized in the OSL are more subject to extinction due to heat losses in comparison to those lying in the ISL as shown in Guiberti et al. (2014a). This recirculation of cold burnt gases has a low enthalpy region which induces a heat loss correction factor $\gamma = 0$ and causes the flame extinction. The reaction process is then inhibited in the OSL leading to the extinction of the outer flame front. This conclusion is corroborated by the results obtained by Chong et al. (2009) on a similar configuration using a RANS simulation strategy. More recently, Nogenmyr et al. (2013) used a MILES (see Chapter 1) approach to capture the flame shape on a swirl burner with and without confinement. Heat losses were also identified as governing the flame shape.

The mean and RMS of the radial and axial velocity components are shown in Figs. 7.8 and 7.9, respectively. Radial velocity is a very good indicator of heat expansion. Therefore, the impact of the misprediction of the flame shape on the velocity field can be clearly identified in Fig. 7.8. The presence of the outer flame front in the adiabatic simulation induces an over prediction of the heat expansion from Z = 5 mm to Z = 20 mm while a better agreement with experiments is obtained with the non-adiabatic simulation. The difference can also be seen on RMS profiles because the misprediction of an outer flame fronts damps the flow dynamics (in fully burnt gases). At the opposite, more fluctuation is observed when heat expansion is inhibited in the non-adiabatic simulation. This flow dynamics is due to shear layer instabilities developing in the OSL between the injected stream and the slow ORZ. The very low and negative mean axial velocities in Fig. 7.9 at the highest radius confirms the

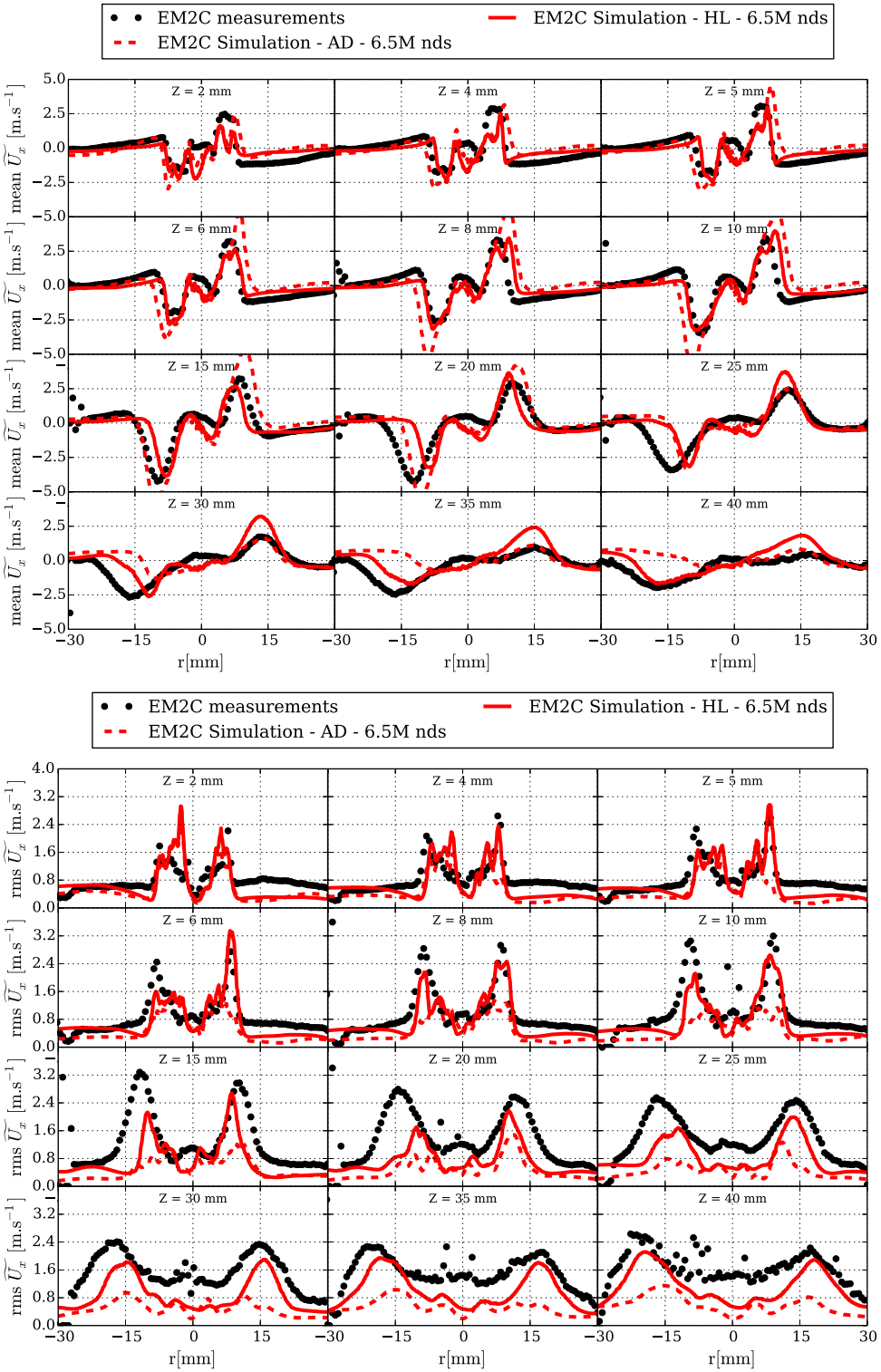


**Figure 7.8:** *1-D radial profiles of radial velocity at different distances Z from the bluff-body wall surface for the case* $X_{H_2}^{fuel} = 0.6$. *(top) Mean profiles. (bottom) RMS profiles.*

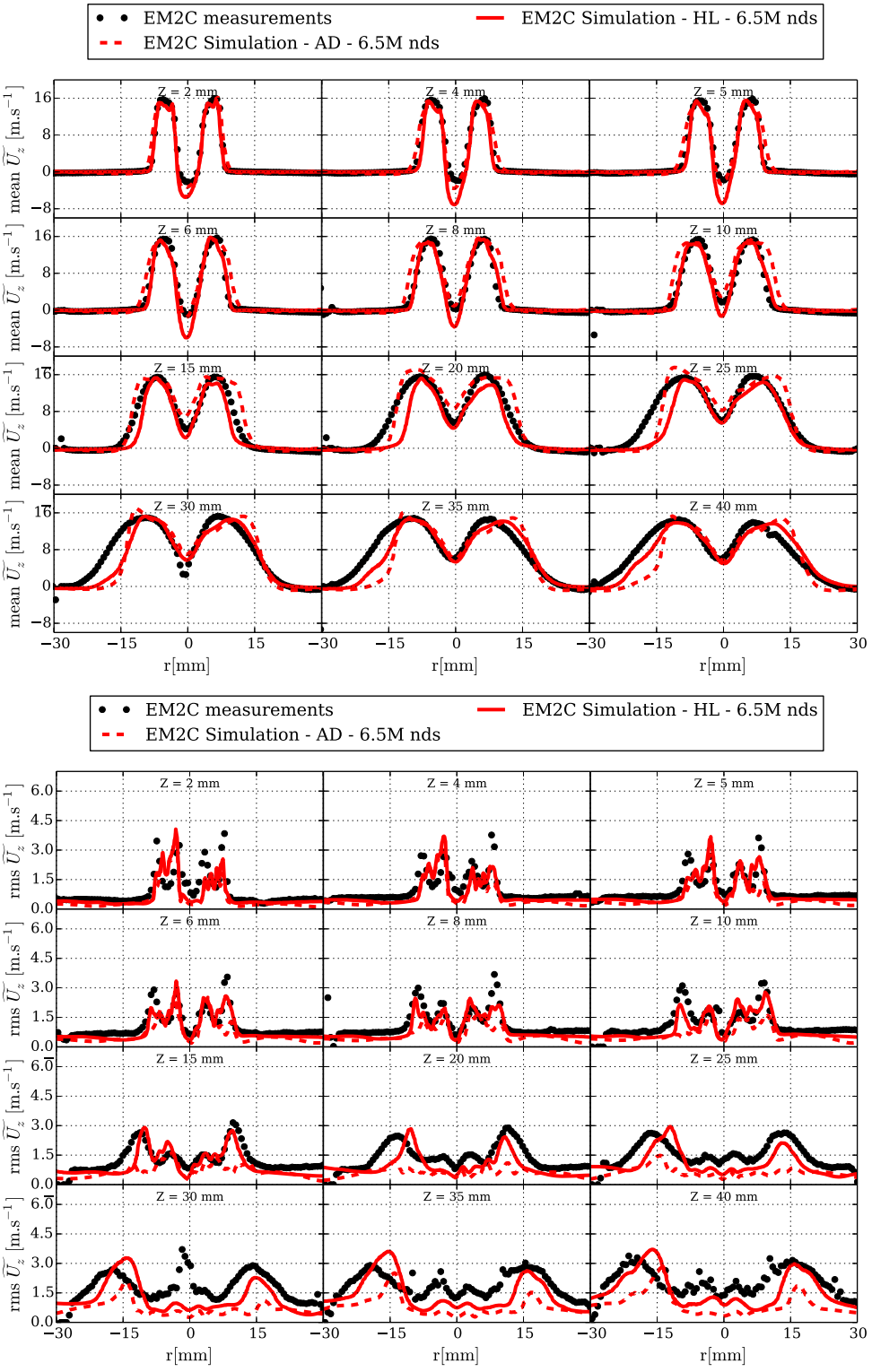


**Figure 7.9:** *1-D radial profiles of axial velocity at different distances Z from the bluff-body wall surface for the case* $X_{H_2}^{fuel} = 0.6$. *(top) Mean profiles. (bottom) RMS profiles.*

presence of the ORZ for all the distances Z where the measurements have been performed.

### 7.4.2 Impact of fuel composition on flame topology

The case $X_{H_2}^{\text{fuel}} = 0.6$ considered in simulations 1 and 2 exhibits a V shape flame only anchored on the central rod tip. The flame front lies in the inner shear layer (ISL) formed by the fresh combustible mixture jet and the IRZ filled with burnt gases. Guiberti et al. (2014a) have shown experimentally that increasing the molar fraction of $H_2$ in the fuel $X_{H_2}^{\text{fuel}}$ continuously increases the probability $p$ to find a flame front in the OSL. The range of $X_{H_2}^{\text{fuel}}$ explorers in the original publication goes from $p = 0.55$ to 0.78. The experimental probability to find a flame front is around 1 % for the case $X_{H_2}^{\text{fuel}} = 0.6$ and increases to 41 % for $X_{H_2}^{\text{fuel}} = 0.78$. The present study is performed with $X_{H_2}^{\text{fuel}} = 0.90$ leading to a very high probability to find a M shape flame ($p \approx 90\%$). Figure 7.10(a) shows mean flame position for $X_{H_2}^{\text{fuel}} = 0.90$ using two different diagnostics. The left plot shows mean Abel inverted OH* chemiluminescence while the right plot shows mean binarized OH-PLIF results. The outer flame front appears clearly leading to an M shape flame. As suggested by Kim et al. (2010), the increase in laminar burning velocity $S_l^0$ due to the increase of $X_{H_2}^{\text{fuel}}$ helps the reacting zone to propagate upstream through the OSL. Guiberti et al. (2014a,b) showed that this explanation was only partial and that the presence of the outer flame front was also depending on the stretch limit which is strongly extended when the Lewis number of the premixing decreases as it is the case when the fuel is enriched in hydrogen (Hawkes and Chen, 2004; Lipatnikov and Chomiak, 2005).

The main challenge is to capture correctly the M shape flame obtained when $X_{H_2}^{\text{fuel}} = 0.90$. Figure 7.10(b) show the mean flame position predicted by the simulation 3. Both mean $X_{\text{OH}}$ and $\dot{\omega}_T$ show a good agreement with the experiments. The non-adiabatic extension of the model correctly capture both the effect of heat losses and hydrogen enrichments on the mean flame position and topology.

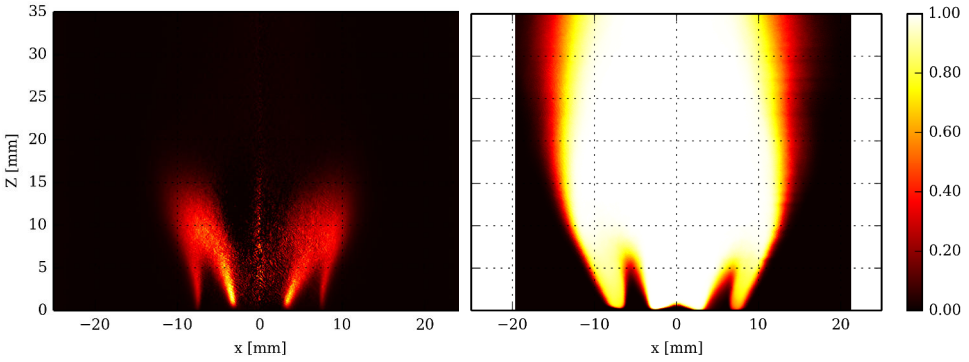


(a) Experimental measurments. (left) Normalized Abel deconvoluted OH* chemiluminescence. (right) Mean binarized OH-PLIF

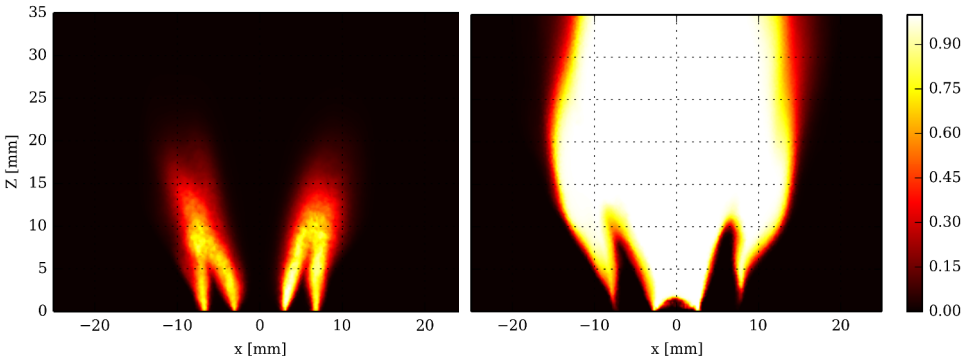


(b) Non-adiabatic simulation. (left) Normalized mean volumic heat release. (right) Mean binarized OH molar fraction $X_{\mathrm{OH}}$

**Figure 7.10:** *Comparisons of the mean flame position for the case* $X_{H_2}^{fuel} = 0.9$. *Experiments and non-adiabatic simulation results are shown.*

## 7.5 Capturing flame topology bifurcations : a challenge for LES turbulent combustion models

In the previous section, two different cases were considered. These cases exhibit different flame shapes (V shape for $X_{H_2}^{\text{fuel}} = 0.6$ and M shape for $X_{H_2}^{\text{fuel}} = 0.9$). The results of the numerical investigations indicate that heat losses and fuel composition both influence the mean flame shape. Two remarks are made:

- when intermediate cases such as $0.6 < X_{H_2}^{\text{fuel}} < 0.9$ are considered, the existence of the outer flame front is intermittent. For these more general cases, the physical processes leading to intermittent M to V and V to M shape bifurcations are not well understood and need to be further investigated.

- even if a very good agreement has been obtained between simulation and experiments for both cases $X_{H_2}^{\text{fuel}} = 0.6$ and $X_{H_2}^{\text{fuel}} = 0.9$, the non-adiabatic simulation of the case $X_{H_2}^{\text{fuel}} = 0.6$ still predicts a low probability of having a flame front in the OSL which is not the case in the experiments (see Fig. 7.6). This slight misprediction may indicate that other physical phenomena, not accounted for in the non-adiabatic F-TACLES model, may be part of the V or M shape stabilization process.

In order to propose an answer to these questions, Guiberti et al. (2014b) performed an experimental analysis to gain further insight in the physical phenomena governing the intermittent flame bifurcations. For that purpose, simultaneous OH-PLIF and PIV measurements have been used to estimate the strain rate in the OSL conditioned by presence of the flame front. In the other hand, a series of 1-D non-adiabatic counterflow premixed flames has been computed for different levels of heat losses and different strain rates. The measured level of heat losses and the global strain rate estimated from measured radial velocity are located very near the extinction limits found in the numerical simulations. It is shown that the maximum strain rate greatly decreases when the enthalpy defect of the counterflowing burnt gases increases. The flame front present in the OSL is therefore rapidly quenched due to the cross effects of heat losses (in the recirculating burnt gases) and the strain rate in the OSL (which fluctuates with turbulent motions). The impact of hydrogen enrichments on the extinction limit was also determined numerically. When the value of $X_{H_2}^{\text{fuel}}$ increases, the flame can support higher strain rates and higher enthalpy defects which explains that increasing experimentally $X_{H_2}^{\text{fuel}}$ leads to higher probability for the M shape topology. In other words, increasing $X_{H_2}^{\text{fuel}}$ seems to decrease the probability of having a M to V shape bifurcation.

The V to M shape bifurcation process has also been investigated in Guiberti et al. (2014b). Two different scenarios have been discussed to explain this transition. First, the auto-ignition of the injected fresh gases at the OSL thanks to the heating by the recalculating burnt gases located at the ORZ was investigated. For that purpose, a 0-D simulation series of homogeneous mixture auto-ignition has been performed. It is found that no auto-ignition of the mixture can occur in the OSL region for these conditions. Consequently, auto-ignition does not seem to be the appropriate candidate to explain the apparition of the outer flame front leading to the V to M shape transition. Turbulent flame front propagation through the OSL then remains a possible explanation for the considered transition mechanism. Further investigations are needed to better analyse the later V to M shape bifurcation process.

From the LES modeling point of view, Guiberti et al. (2014b) results suggest that the slight mean reaction zone predicted by the simulation 2 is due to the fact that the F-TACLES model does not explicitly account for the impact of local strain rate on turbulent consumption speed. Therefore, the modeling strategy should include the cross effects of strain rate and heat losses on the flame consumption speed. This drawback is a challenging issue for the chemistry tabulation techniques applied in an LES context. The main challenge would be to account for the impact of unresolved turbulence on the unresolved strain rate which will have a major impact on the estimation of the total (resolved + unresolved) strain rate.

# Conclusion

The general objective of this thesis was to improve the modeling of turbulent stratified flames in industrial combustion chambers. Two difficulties were identified. The first one consist in adopting a proper strategy to describe the inner thermochemical flame structure. Most of the combustion models are based on assumptions (for instance adiabatic flow or unity Lewis number) that make difficult their application to practical situations. The second difficulty is to capture the flame-turbulence interactions (wrinkling) at the resolved scale and to properly model it at the unresolved scale. This thesis addressed these two axis taking a particular care to the validation of each development using LES of academic or quasi-industrial combustors. The different points developed in this thesis led us to the following achievements.

## Major achievements

### Extension of the F-TACLES model for an applicability to practical combustion chambers

The F-TACLES model has been developed in the thesis of Vicquelin (2010) and Auzillon (2011) assuming adiabatic flows and unity Lewis number for the chemical species. This model was initially derived to correctly capture the turbulent flame speed as well as the inner thermochemical flame structure. During this thesis, F-TACLES has been extended to non-adiabatic combustion. This extension focuses on the proper prediction of the non-adiabatic turbulent flame speed as well as the thermochemical quantities at the equilibrium state. For that purpose, an additional non-adiabatic database is generated from a collection of 1-D burner-stabilized flames. The turbulent flame speed is corrected based non-adiabatic laminar flame speeds.

The F-TACLES formalism has also been generalized to use any model for the chemical species diffusion fluxes of the 1-D flame database. This accounts for the effects of differential diffusion in the laminar flame front in the direction of its propagation. The impact of differential diffusion on the laminar flame speed is now well captured.

These developments have been first validated on two academic turbulent partially-premixed flames. Then, the extended F-TACLES model has been used to analyse a semi-industrial combustion chamber designed at EM2C laboratory. Numerical studies have been conducted, jointly with the experimental analysis of Guiberti (2015), to better understand the impact of hydrogen enrichment, strain and heat losses on flame stabilization process and topology bifurcations. In this context, LES was used both for validation and physical analysis purposes.

### Modeling of flame-turbulence interactions in LES

The LES formalism separates the description of the reacting flow in a resolved and an unresolved parts. Flame-turbulence interactions generally appear at both levels.

The flame-turbulence interactions at the resolved scale is not properly described by the turbulent combustion models based on a broadening of the flame front. This misprediction is due to inconsistencies between flame and flow filter scales formulations. A general and consistent formalism has been proposed and applied to the F-TACLES model which is fully compatible with the filtering formalism. The corrected model, called F2-TACLES, has been validated on a lean turbulent combustion chamber showing promising results.

The estimation of the flame-turbulence interactions at the unresolved scale is also very challenging issue. Different subfilter scale wrinkling models have been assessed on an academic turbulent flame. Most of them fail when the intensity of unresolved flame-turbulence interactions varies along the flame front. In such situations, the tuning of model parameters seems to be necessary and difficult to perform a priori. A dynamic procedure for the estimation of the sub-filter scale wrinkling has been implemented and tested on a turbulent partially-premixed flame. A good agreement for both mean flame position and flow field has been obtained. At this stage, the non-adiabatic F-TACLES model combined with dynamic subfitler scale wrinkling model can be considered as a parameter-free combustion model for the LES of premixed and stratified flames.

## Future perspectives

The different points developed in this thesis open the way to further developments and analysis:

- The impact of the subfilter scale wrinkling model on unsteady flames should be further investigated. For that purpose, advanced experimental characterization of pulsed or naturally unstable flame should be encouraged in the coming years. The EM2C burner developed and studied

during this thesis is an ideal candidate for this investigations and the TNF workshop may also be a good opportunity to develop such measurements. The LES of highly unsteady configurations should allow a deeper assessment of the models for the unresolved flame wrinkling. Dynamic formulation of this model seems to be a very promising approaches which should be tested on a larger range of situations.

- Results from the F2-TACLES model applied to the PRECCINSTA premixed turbulent combustor have shown that this new formalism impact the flame dynamics. Further investigations are needed and should also be conducted on pulsed or naturally unstable configurations. The impact of this new model on phase averaged flame response or also turbulent Flame Transfer Function (FTF) should be further investigated. The inter-scale convection term, modeled from the 1-D flame structure in this thesis, should be estimated directly from the 3-D LES resolved scales.
- Impact of radiative heat exchange within combustion chambers has been neglected in this thesis. The estimation of the energy source term due to radiation at a reasonable CPU cost is a very challenging numerical issue. The coupling between radiation solvers and the LES simulations with the non-adiabatic F-TACLES model will be necessary to correctly capture the combustion process and the wall heat fluxes in industrial combustors such as steel preheating furnaces.
- The F-TACLES model should be extended to operate in pure diffusion regimes. Recent developments by Coussement et al. (2015) show promising results. A comparison between both models (based on premixed flames and on diffusion flames) on industrial burners having high levels of mixture fraction stratification would be very interesting.
- The present work focused on gaseous combustion. Practical combustion chambers are mainly operated with liquid fuels. The impact of two phase flow on mixing and combustion process remain very challenging issues. These challenges lie in both numerical methods to track atomization of the liquid and the spray characteristics and modeling of the impact of liquid droplets on the turbulent flame structures.

# Appendix A

# Estimation of turbulent combustion regime in industrial combustion chambers

*This appendix first proposes a short presentation of the different types of flame-turbulence interactions in the context of fully-premixed flames. Karlovitz number $K_a$ is introduced as a global indicator to determine the turbulent combustion regime and is therefore estimated for different practical applications.*

## A.1 Laminar flame regime

The most simple case is when the flame front propagates in a laminar flow. The whole flame structure then results from a reaction-diffusion equilibrium. In this case, the inner thermochemical flame structure is not impacted by any turbulent structure. Figure A.1 shows a stoichiometric $CH_4$-Air laminar premixed flame stabilized above an isothermal burner as well as a schematic of its inner thermochemical flame structure. Two main parts can be distinguished in such premixed flames:

- Preheating (or diffusion) layer where heat diffuses towards fresh gases increasing their temperature until chemical reactions start.
- Reaction layer where the major part of chemical reactions occurs to convert the reactants into products thanks to mostly exothermic reactions. The conversion of chemical energy into sensible energy is performed within this zone.

The laminar flame front propagates towards fresh gases at a speed $S_l$ which also represents, for planar flame fronts, the fresh gases consumption speed (Poinsot and Veynante, 2012): $S_l = 1/(\rho^u(Y_k^{eq} - Y_k^u)) \int_{-\infty}^{+\infty} \rho\dot{\omega}_{Y_k} dx_n$ where the superscripts $u$ and $eq$ denote the state in fresh and burnt gases, respectively. $Y_k$ is here the mass fraction of any chemical species present in fresh or burnt gases. The flame consumption speed is a key quantity that needs to be correctly cap-

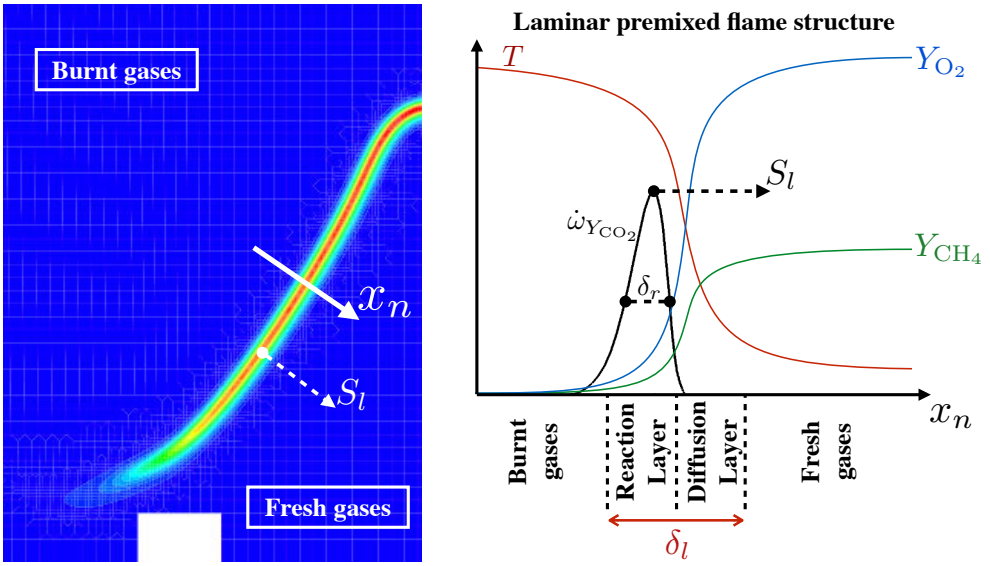


**Figure A.1:** *Schematic of the laminar flame structure. (Left) Direct Numerical Simulation (DNS) of a 2-D premixed laminar $CH_4$-Air flame stabilized above an isothermal burner performed by Fiorina et al. (2003). Fresh gases are injected at stoichiometry. (Right) Schematic of the thermochemical structure of a stoichiometric $CH_4$-Air laminar premixed flame. Source: Fiorina et al. (2003).*

tured by the combustion modeling strategies as it is directly or indirectly linked to several other important flame properties (position, response to heat losses, response to strain, quenching).

Another key quantity describing a flame front is the flame thickness $\delta$. $\delta$ can vary depending on the definition adopted. In order to ease the phenomenological description of a flame front, two definitions are selected in this thesis. The thermal flame thickness $\delta_l = (T^{eq} - T^u)/\max(|\partial T/\partial x_n|)$ is representative of the characteristic size of the temperature front. The thickness of the reactive layer $\delta_r$ is defined here as the half-heigh thickness of the reaction rate of major species such as $CO_2$, CO and $H_2O$.

## A.2 Thin flame (or flamelet) regime

The most energetic turbulent eddies are characterized by their size and velocity, also called integral length scale $l_t$ and integral characteristic speed $u'_{l_t}$, respectively. Assuming an homogeneous and isotropic turbulence (HIT) at a given turbulent Reynolds number $Re_t = u'_{l_t} l_t/\nu$, it is possible to compute the size of the smallest turbulent eddies, also called Kolmogorov scale $\eta_k \approx l_t/Re_t^{3/4}$. When the flame front thickness $\delta$ remains thiner than the Kolmogorov scale $\eta_k$, the inner flame structure is not altered by turbulence. Flame-turbulence

interactions then only result in a geometrical wrinkling of the flame front. In this regime, called flamelet regime, the thermochemical flame structure can be approximated by the laminar flame structure. In the literature, this regime is often identified using the Karlovitz number $K_a$ which compares the times scale associated to the flame propagation $\tau_c$ with the time scale of the Kolmogorov scale $\tau_k$. This number may also be seen as the comparison of the corresponding length scales:

$$K_a = \frac{\tau_c}{\tau_k} = \left(\frac{\delta}{\eta_k}\right)^2 \tag{A.1}$$

Therefore, the flamelet (or thin flame) regime is reached when $K_a < 1$. Note that the limit $K_a = 1$ is only qualitative since only order of magnitudes are compared here. This limit may also be different when the turbulent field differs from HIT as it is the case in most of the practical combustion chambers. Roberts et al. (1993); Driscoll (2008) showed that the criterion $K_a = 1$ was in fact too restrictive and that the deviations from flamelet structure were experimentally measured only with eddies larger and more energetic than Kolmogorov ones ($K_a \approx 10$).

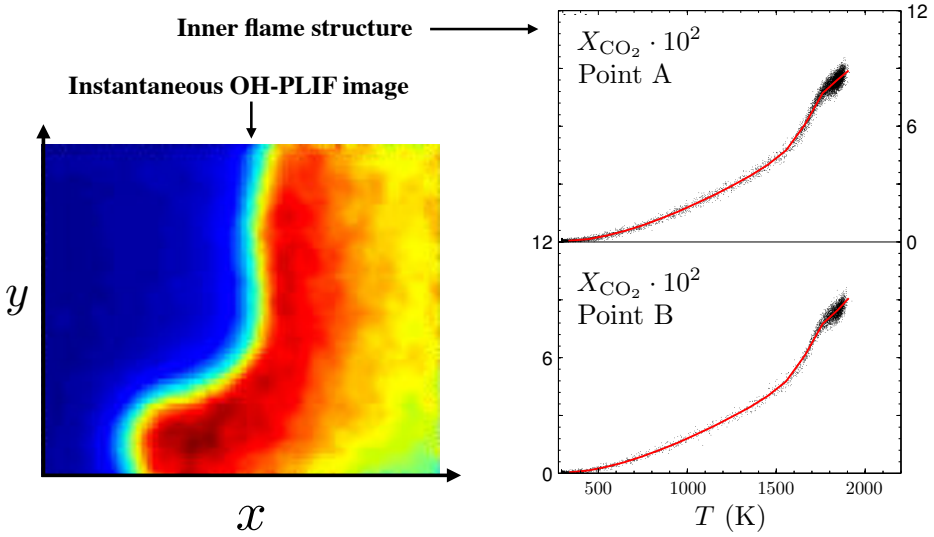


**Figure A.2:** *Scalar measurements performed on a premixed $CH_4$-Air turbulent flame at $K_a = 0.6$ by Sweeney et al. (2011a). (Left) Instantaneous OH-PLIF image of the turbulent flame front. (Right) Scatterplot of the measured $CO_2$ molar fraction conditioned to the local temperature at two different distances from the burner exit. The red line represents the structure of a unstretched laminar premixed flame computed using detailed chemical scheme. Source: Sweeney et al. (2011a).*

Figure A.2 illustrates the behavior of turbulent flame evolving in the flamelet

regime. It shows an instantaneous OH-PLIF (Planar Laser Iduces Fluorescence of OH) image of a $CH_4$-Air premixed flame front (and burnt gases) performed by Sweeney et al. (2011a) on the Cambridge stratified slot burner. First, the flame front thickness is not altered by turbulence and a large scale wrinkling is observed. Second, inner thermochemical structure remains very close to the laminar flame structure as shown by the scatterplot of the measured $CO_2$ molar fraction conditioned to the local temperature plotted in Fig A.2. Sweeney et al. (2011a) have measured the same laminar behavior for $O_2$, CO, $CH_4$, $H_2O$ and $H_2$.

## A.3 Thin reaction zone regime

When the smallest turbulent scales become smaller than the flame thickness $\delta$ (*i.e.* $K_a > 1$), some turbulent structures may be able to penetrate the preheating zone. In this situation, the flame thickness generally increases and its thermochemical structure progressively deviates from the laminar flame when $K_a$ increases (Aspden et al., 2011b). The thickness of the reactive layer $\delta_r$ is smaller than the overall flame thickness $\delta_l$. Thus, when the Karlovitz number $K_a$ is lower than a critical value $K_a < K_a^c$, the smallest turbulent eddies are not able to enter the reactive layer which remains unaffected (Poinsot et al., 1991; Roberts et al., 1993; Peters, 2000). This turbulent combustion regime is called thin reaction zone regime.

Figure A.3 displays 2-D cuts of the temperature field extracted from a 3-D Direct Numerical Simulation (DNS) of a turbulent premixed $H_2$-Air turbulent flame at $\phi = 0.4$ performed by Aspden et al. (2011b). From this DNS are extracted conditional mean of $H_2$ molar fractions as a function of local temperature (seen here as a reaction progress variable). The geometrical wrinkling is the dominating flame-turbulence interaction at $K_a = 10$ while the flame front is more thickened and less wrinkled when $K_a$ increases. The plots also confirm that for $K_a = 10$ the chemical flame structure slightly deviates from the unstretched laminar flame even if the fuel molar fraction stays very close to the laminar trajectory. This is not the case for high $K_a$ where chemical trajectories of the fuel mole fraction is completely different from the laminar one. Hawkes et al. (2012) have shown recently that the local fuel consumption speed of a turbulent flame lying in the thin reaction zone regime ($K_a \approx 20$ and $K_a \approx 90$) notably differs from the laminar burning rate because of the impact of turbulent scales on the inner flame structure.

## A.4 Distributed reaction zone regime

For very high Karlovitz numbers, the small turbulent eddies become able to penetrate both the preheating and reactive layers. In this situation, the whole

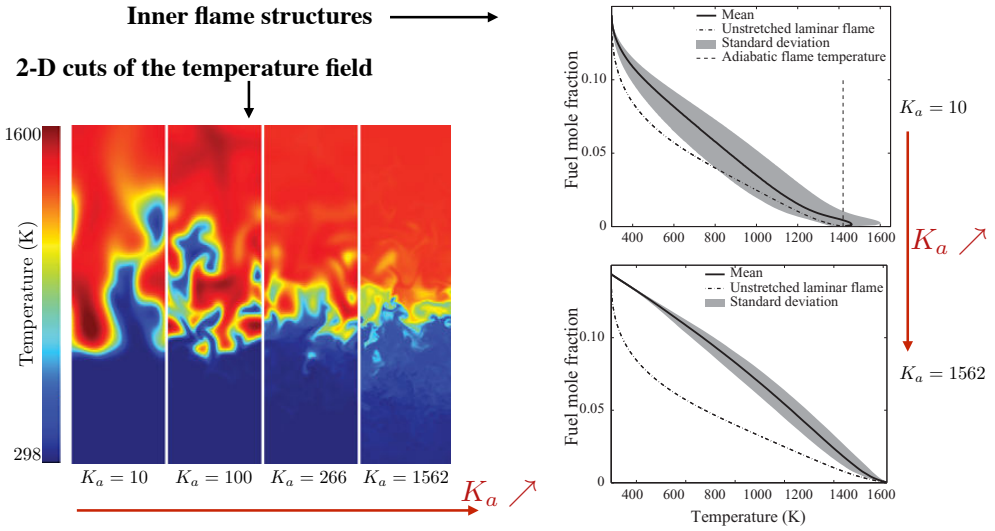


**Figure A.3:** *3-D DNS of a premixed $H_2$-Air turbulent flame at $\phi = 0.4$ interacting with a HIT performed by Aspden et al. (2011b). Karlovitz number $K_a$ is varied from 10 to 1562. (Left) 2-D cuts of instantaneous temperature field. (Right) Conditional mean of hydrogen molar fraction as a function of local temperature. Source: Aspden et al. (2011b).*

flame structure is disrupted and can not be assumed similar to laminar flame structure as turbulent mixing dominates laminar diffusion. The characterization of this combustion regime is very difficult as it is mainly governed by unsteady and local phenomena such as flame stretch and turbulent mixing. Asymptotic analysis are therefore more difficult to derive and DNS become very costly because they require to reach high turbulence intensities levels and account for 3-D effects as well as complex chemistry. Thus, only few and recent numerical studies have been conducted to gain further insight in the transition mechanism between thin reaction zone and distributed reaction zone regimes.

The definition of flame and flow conditions to obtain the distributed reaction zone regime is also difficult. The critical Karlovitz number $K_a^c$ defining the transition between regimes is not clearly identified. Peters (1999) estimated that $K_a^c = 100$ using theoretical considerations. Recent numerical investigations proposed by Poludnenko and Oran (2010) using one step chemical scheme to describe $H_2$-Air combustion have shown that the reactive layer thickness were not affected for $K_a \approx 100$. Savre et al. (2013) studied $CH_4$-Air premixed flames submitted to very high Karlovitz numbers $K_a = \{600; 2000; 9500\}$ using 2-D DNS with detailed chemistry. Figure A.4 shows the results obtained for $K_a = 600$ and $K_a = 9500$. They noticed that the transition to distributed reaction zone regime takes place near $K_a^c \approx 2000$ and results in a stretched, curved and broadened reaction zone. Other DNS studies (Aspden et al., 2011a,b) con-

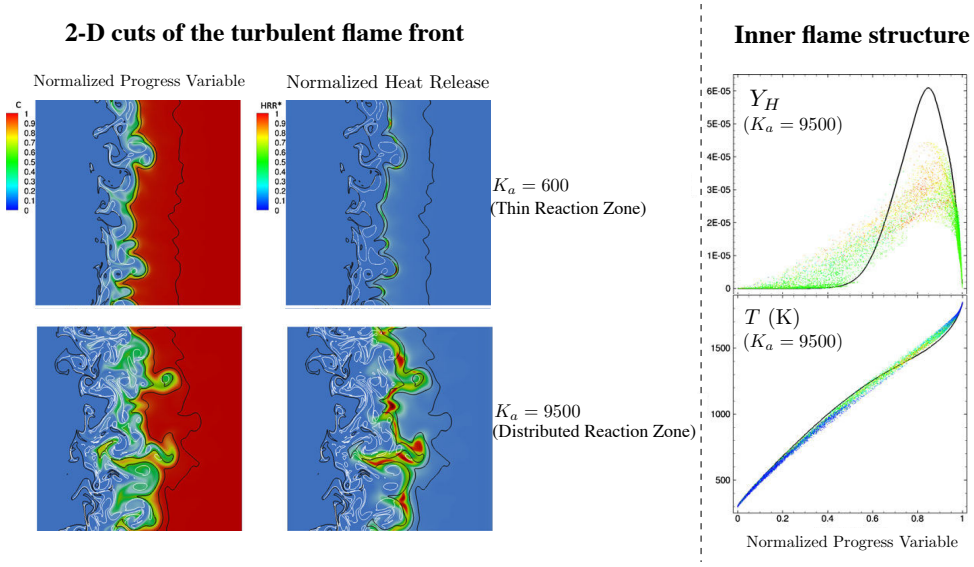


**Figure A.4:** *2-D DNS of a premixed $CH_4$-Air turbulent flame at $\phi = 0.7$ interaction with a HIT performed by Savre et al. (2013). Karlovitz numbers $K_a$ are 600 and 9500. (Left) Progress variable and heat release colormaps for both thin and distributed reaction zone regimes. (Right) Conditional mean of hydrogen mass fraction and temperature as a function of progress variable. Source: Savre et al. (2013).*

firmed that the effective critical Karlovitz number is globally higher than 100 and that it depends for instance on the Lewis number, the fuel composition and the isotropy of the turbulent field. Concluding, Karlovitz number remains a global criteria which does not account for all the phenomena likely to influence the transition to distributed reaction zone.

## A.5 Some estimations of the global Karlovitz number in industrial combustors

An *a priori* estimation of the turbulent combustion regime is obtained from orders of magnitude of the turbulent Reynolds number $Re_t$ and the Karlovitz number $K_a$. Three configurations of interest for this thesis are now considered and the corresponding $Re_t$ and $K_a$ are estimated. Note that only orders of magnitudes are given for the characteristic length scales and velocities.

### Case 1: Steel preheating furnace operated at atmospheric pressure with natural gas or coke oven gas

Considering a steel preheating furnace, of type "lateral long flame burner", operating at atmospheric pressure with natural gas, the size of the largest eddy $l_t = 1$ m is mainly controlled by the size of the device while its character-

istic speed $u'_{l_t} = 10$ m.s$^{-1}$ is controlled by the bulk velocity of injected fresh gases (Ferrand, 2003). The kinematic viscosity of the burnt gases is taken equal to $\nu = 37 \cdot 10^{-5}$ m$^2$.s$^{-1}$ leading to $Re_t = u'_{l_t} l_t / \nu \approx 27000$. An estimation of the Karlovitz number is deduced from Eq. A.1 by considering the combustion of natural gas or COG with a typical flame thickness of $\delta = 0.5$ mm:

$$K_a^{\text{furnace-COG}} = \left(\frac{\delta}{\eta_k}\right)^2 \approx 1$$

**Case 2: Steel preheating furnace operated at atmospheric pressure with blast furnace gas**

A furnace similar to the previous case is considered here. The only modification lies in the fuel composition which is mainly composed by low calorific value gases BFG extracted for blast furnaces. The combustion at atmospheric pressure of BFG-Air mixture is very difficult to stabilize and exhibits large flame thicknesses such as $\delta = 1.0$ mm. Assuming that the Reynolds number remains similar to the case 1, Karlovitz number now reads:

$$K_a^{\text{furnace-BFG}} = \left(\frac{\delta}{\eta_k}\right)^2 \approx 4$$

**Case 3: Aeronautical combustion chamber operated at 40 bars**

Considering an aeronautical combustion chamber, of type CFM56, operating at take-off conditions ($P \approx 40$ bars), the size of the largest eddy $l_t = 0.10$ m is also controlled by the geometry of the combustion chamber. In such combustion devices, characteristic speeds, estimated here at $u'_{l_t} = 100$ m.s$^{-1}$, are generally much higher than in furnaces. The same kinematic viscosity of the burnt gases is adopted $\nu = 37 \cdot 10^{-5}$ m$^2$.s$^{-1}$ leading to $Re_t = u'_{l_t} l_t / \nu \approx 27000$. In the present case, as the operating pressure is increased, the kerosene-Air flame thickness $\delta$ is lower than at atmospheric pressure and is taken equal to $\delta = 0.1$ mm. Karlovitz number then reads:

$$K_a^{\text{aero. ch.}} = \left(\frac{\delta}{\eta_k}\right)^2 \approx 4$$

These estimations, although qualitative, show that $K_a \sim 1$ despite the large range of considered geometries and operating conditions. The three different cases are located at the edge between flamelet and thin reaction zone regimes. Some authors actually locate these cases within the flamelet regime which seems to be valid for $K_a$ higher than unity (Roberts et al., 1993; Driscoll, 2008). This is actually the case for a large range of practical applications which justifies the experimental, numerical and modeling efforts of the turbulent combustion community to model the thin flame regime.

# Appendix B

# Governing equations for reacting flows

*This appendix presents the governing equations for reacting flows. Solving directly these equations is very costly but remains very useful to understand the physics controlling turbulent combustion processes. Simplification of these equations using the low-Mach number assumption is also introduced.*

Approximating a fluid as a continuum, it is possible to define everywhere a set of variables characterizing the thermodynamical and kinetic state of a given flow. The evolution of such variables can be locally described by a set of partial differential equations (PDE). The PDE associated to the conserved variable $\Phi$ then expresses the conservation law controlling the local evolution of $\Phi$. A brief description of the conservation laws considered in this manuscript is given in the following section. More details about the basic conservation equations for reacting flows and how they can be obtained can be found in Poinsot and Veynante (2012).

## B.1 Mass and chemical species conservation

The Reynolds' transport theorem (Reynolds, 1903) applied to a material element (where the variation of mass is null by definition) allows to write the mass conservation law:

$$\frac{\partial \rho}{\partial t} + \frac{\partial}{\partial x_i}(\rho u_i) = 0 \tag{B.1}$$

where $\rho$ stands for the fluid density while $\mathbf{u}(u_1, u_2, u_3)$ is the velocity vector associated to the material element. Following a similar strategy, it is also

possible to derive the species mass fraction conservation law:

$$\frac{\partial \rho Y_k}{\partial t} + \frac{\partial}{\partial x_i}\left(\rho Y_k u_i\right) = -\frac{\partial}{\partial x_i}\left(\rho Y_k V_{k,i}\right) + \rho\dot{\omega}_k \quad \forall k \in [1; N_{sp}] \tag{B.2}$$

where $Y_k$ is the $k$th species mass fraction, $N_{sp}$ is the total number of chemical species composing the fluid and $\mathbf{V_k}(V_{k,1}; V_{k,2}; V_{k,3})$ is the diffusion velocity of the $k$th species. The $k$th species reaction rate $\dot{\omega}_k$ has the dimension of $\mathrm{s}^{-1}$. By definition, the relations $\sum_{k=1}^{N_{sp}} Y_k V_{k,i} = 0$ and $\sum_{k=1}^{N_{sp}} \dot{\omega}_k = 0$ are verified (Poinsot and Veynante, 2012).

## B.2 Momentum conservation

Momentum balance equation is derived by applying both Reynolds' transport theorem and Newton's second law (Newton, 1687) to a material element:

$$\frac{\partial}{\partial t}(\rho u_j) + \frac{\partial}{\partial x_i}(\rho u_i u_j) = -\frac{\partial p}{\partial x_j} + \frac{\partial \tau_{ij}}{\partial x_i} + \rho f_j \quad \forall j \in \{1; 2; 3\} \tag{B.3}$$

where p is the thermodynamical pressure and $\mathbf{f}(f_1; f_2; f_3)$ is the volume force applied to the material element. In this thesis manuscript, fluids are supposed to be Newtonian and the $2^{nd}$ order shear stress tensor $\tau$ then expresses:

$$\tau_{ij} = \mu\left(\frac{\partial u_i}{\partial x_j} + \frac{\partial u_j}{\partial x_i}\right) - \frac{2}{3}\mu\frac{\partial u_k}{\partial x_k}\delta_{ij} \quad \forall i, j \in \{1; 2; 3\} \tag{B.4}$$

## B.3 Energy conservation

Energy transport equation is derived from both Reynolds' transport theorem and first law of thermodynamics (Clausius, 1851). Multiple forms of this equation are available depending on the energy definition (Poinsot and Veynante, 2012). In this thesis, mixture sensible plus chemical enthalpy $h = \sum_{k=1}^{N_{sp}} Y_k h_k$ is considered and species enthalpy $h_k$ reads:

$$h_k = \underbrace{\int_{T_0}^{T} Cp_k dT}_{\text{sensible}} + \underbrace{\Delta h^0_{f,k}}_{\text{chemical}} \quad \forall k \in [1; N_{sp}] \tag{B.5}$$

where $T$ is the mixture temperature and $T_0$ is the reference temperature. $\Delta h^0_{f,k}$ and $Cp_k$ are the $k$th species mass formation enthalpy at $T_0$ and heat capacity at constant pressure, respectively. Sensible plus chemical enthalpy is conserved across a isobaric laminar and adiabatic flame. The value of $h$ is then the same in both fresh and burnt gases which may be useful for the derivation of combustion

modeling strategies. The mixture enthalpy $h$ balance equation reads:

$$\frac{\partial}{\partial t}(\rho h) + \frac{\partial}{\partial x_i}(\rho u_i h) = \frac{\mathrm{d}p}{\mathrm{d}t} - \frac{\partial q_i}{\partial x_i} + \tau_{ij}\frac{\partial u_i}{\partial x_j} + \dot{Q} + \rho \sum_{k=1}^{N_{sp}} (Y_k f_{k,i} V_{k,i}) \quad \text{(B.6)}$$

where $\dot{Q}$ is the volume energy (for instance radiation) source term, $\mathbf{q}(q_1; q_2; q_3)$ is the energy diffusion flux modeled here as $q_i = -\lambda\frac{\partial T}{\partial x_i} + \rho\sum_{k=1}^{N_{sp}}(Y_k h_k V_{k,i})$ and $\lambda$ is the thermal conductivity. In the following, the radiation source term $\dot{Q}$ and the power produced by volume forces due to species diffusion $\rho\sum_{k=1}^{N_{sp}}(Y_k f_{k,i} V_{k,i})$ are neglected. In this context, Eq. B.6 is recast as follows:

$$\frac{\partial}{\partial t}(\rho h) + \frac{\partial}{\partial x_i}(\rho u_i h) = \frac{\mathrm{d}p}{\mathrm{d}t} + \tau_{ij}\frac{\partial u_i}{\partial x_j} + \frac{\partial}{\partial x_i}\left(\lambda\frac{\partial T}{\partial x_i} - \rho\sum_{k=1}^{N_{sp}}(Y_k h_k V_{k,i})\right) \quad \text{(B.7)}$$

The last Right Hand Side (RHS) term of Eq. B.7 represents the heat diffusion term modeled here by Fourrier's law (Fourier, 1822) and the heat transport associated to species diffusion.

## B.4 Gas state equation

In this thesis the gases are assumed ideal and are modeled using the ideal gas law:

$$P = \rho r T \quad \text{(B.8)}$$

where $r = \frac{R}{W}$. $R = 8.3143$ J.mol$^{-1}$.K$^{-1}$ is the universal gas constant and $W$ is the mixture molecular weight. Note also that $\frac{1}{W} = \sum_{k=1}^{N_{sp}}\frac{Y_k}{W_k}$ where $W_k$ is the $k$th species molecular weight.

## B.5 Low-Mach number flow assumption

The balance equation system describing the behavior of reacting flows is formed by Eqs (B.1), (B.2), (B.3), (B.7) and (B.8) and leads to the following system:

$$\frac{\partial \rho}{\partial t} + \frac{\partial}{\partial x_i}(\rho u_i) = 0 \tag{B.9}$$

$$\frac{\partial}{\partial t}(\rho u_j) + \frac{\partial}{\partial x_i}(\rho u_i u_j) = -\frac{\partial p}{\partial x_j} + \frac{\partial \tau_{ij}}{\partial x_i} + \rho f_j \tag{B.10}$$

$$\frac{\partial \rho Y_k}{\partial t} + \frac{\partial}{\partial x_i}(\rho Y_k u_i) = -\frac{\partial}{\partial x_i}(\rho Y_k V_{k,i}) + \rho \dot{\omega}_k \tag{B.11}$$

$$\frac{\partial}{\partial t}(\rho h) + \frac{\partial}{\partial x_i}(\rho u_i h) = \frac{\mathrm{d}p}{\mathrm{d}t} + \tau_{ij}\frac{\partial u_i}{\partial x_j} + \frac{\partial}{\partial x_i}\left(\lambda \frac{\partial T}{\partial x_i} - \rho \sum_{k=1}^{N_{sp}} (Y_k h_k V_{k,i})\right) \tag{B.12}$$

$$p = \rho r T \tag{B.13}$$

Explicit resolution in time of this equation system requires the capture of both flow convective scales propagating at the speed $v$ and acoustic (pressure) waves propagating at $v \pm c$ where $c$ is the speed of sound. In a general case, the maximum absolute propagation speed $u$ of an information is given by $u_{\text{compressible}} = |v| + |c|$. However, when the Mach number $M = v/c$ is lower than 0.3 (*i.e.* $v \ll c$), acoustic waves propagate much faster than the convective scales. In this particular situation, the impact of acoustics waves on the velocity field through density fluctuations can be neglected[1]. In other words, acoustic information propagates at a speed $c$ that can be assumed infinite compare to convective velocity:

$$\frac{1}{c^2} = \frac{\mathrm{d}\rho}{\mathrm{d}p} \to 0 \Longleftrightarrow c \to \infty \tag{B.14}$$

The low-Mach number assumption therefore implies an infinite speed of sound. As the propagation of acoustic waves does not need to be resolved anymore, the maximum absolute propagation speed $u$ of an information is given by $u_{\text{low-Mach}} = |v|$.

The Courant-Friedrichs-Lewy (CFL) number compares the mesh cell size $\Delta x$ and the distance crossed by any information propagating at $u$ during a simulated time step $\Delta t$:

$$\text{CFL} = \frac{u \Delta t}{\Delta x} \tag{B.15}$$

For a given spatial discretization and a given value of the CFL number (imposed by the numerical scheme) the simulation time step $\Delta t$ for both compressible

[1] Considering air flow at standard conditions of pressure and temperature, if $M < 0.3$ the density variation $\rho/\rho_0$ is lower that 5% where $\rho_0$ is the density at $M = 0$.

and low-Mach situations may be compared:

$$\frac{\Delta t_{\text{compressible}}}{\Delta t_{\text{low-Mach}}} = \frac{|v|}{|v| + |c|} \tag{B.16}$$

Equation B.16 shows that when the low-Mach number flow assumption is valid ($v \ll c$), the required time step for a fully compressible simulation $\Delta t_{\text{compressible}}$ is much smaller than the time step required by the low-Mach simulation $\Delta t_{\text{low-Mach}}$. Consequently, when compressibility effects can be neglected, the low-Mach assumption allows to simulate a given physical time using less iterations than in a fully compressible simulation. This assumption may be made for the simulation of large scales industrial furnaces operated at atmospheric pressure where convection velocities are small compare to $c$ and of the order of 10 $\text{m.s}^{-1}$ (Ferrand, 2003). However, compressible effects may not be negligible in aeronautical combustion chambers since the maximum flow velocities reach 100 $\text{m.s}^{-1}$ (Boileau et al., 2008; Janus et al., 2007). In practice, both the balance equation system and the numerical strategy greatly differ between low-Mach number and fully compressible solvers (Kraushaar, 2011).

## B.6 Governing equations for low-Mach number reacting flows

The balance equation system assuming a low-Mach number flow is briefly described in this section. The derivation procedure selected in this thesis has been proposed by Majda and Sethian (1985) and is also recalled in more recent studies (Day and Bell, 2000). First, Eqs (B.9) to (B.13) are recast in a dimensionless form. A Taylor series expansion of all dimensionless thermochemical variables $\Phi^*$ is then performed around the Mach number $M = 0$:

$$\Phi^* = \Phi_0^* + M\Phi_1^* + M^2\Phi_2^* + \mathcal{O}(M^3) \tag{B.17}$$

Expanded variables are then injected within dimensionless equations leading to polynomial equations functions of $M^{-2}$, $M^{-1}$, $M^0$, $M^1$ and $M^2$. Identifying the polynomial coefficients for each orders of $M$ leads to (only relations of interest are shown):

$$\frac{\partial \rho_0}{\partial t} + \frac{\partial}{\partial x_i}(\rho_0 u_{i0}) = 0 \tag{B.18}$$

$$\frac{\partial p_0}{\partial x_j} = 0 \tag{B.19}$$

$$\frac{\partial p_1}{\partial x_j} = 0 \tag{B.20}$$

$$\frac{\partial}{\partial t}(\rho_0 u_{j0}) + \frac{\partial}{\partial x_i}(\rho_0 u_{i0} u_{j0}) = -\frac{\partial p_2}{\partial x_j} + \frac{\partial \tau_{ij0}}{\partial x_i} + \rho_0 f_{j0} \tag{B.21}$$

$$\frac{\partial \rho_0 Y_{k0}}{\partial t} + \frac{\partial}{\partial x_i}(\rho_0 Y_{k0} u_{i0}) = -\frac{\partial}{\partial x_i}(\rho_0 Y_{k0} V_{k,i0}) + \rho_0 \dot{\omega}_{k0} \tag{B.22}$$

$$\frac{\partial}{\partial t}(\rho_0 h_0) + \frac{\partial}{\partial x_i}(\rho_0 u_{i0} h_0) = \frac{\partial}{\partial x_i}\left(\lambda \frac{\partial T_0}{\partial x_i} - \rho_0 \sum_{k=1}^{N_{sp}} (Y_{k0} h_{k0} V_{k,i0})\right) \tag{B.23}$$

$$p_0 = \rho_0 r T_0 \tag{B.24}$$

(B.25)

The full derivation procedure is presented in details by Benteboula (2006) who also highlights some differences between the low-Mach number equations (Eqs. (B.18) to (B.24)) and the fully compressible formulation (Eqs. (B.9) to (B.13)):

- Each variable $\Phi_0$ corresponds to the 0th-order Taylor expansion around Mach number $M = 0$ (See Eq. B.17). In the following, subscripts $_0$ will not be included in the notations except when ambiguity exists as it is the case for the pressure term.
- $p_0$ corresponds to the thermodynamic pressure and represents the absolute pressure which is constant in space.
- $p_1$ is also constant in space and steady acoustic waves are then neglected.
- $p_2$ is the hydrodynamic (or perturbational) pressure and now appears in the momentum equation. All thermodynamic quantities are assumed to be independent of $p_2$ which may vary in time and space.
- Both the pressure and viscous heating terms in the energy equation are neglected as the pressure is constant and the viscous heating is of high order in $M$.

As no assumptions are made on $\frac{\mathrm{d}\rho}{\mathrm{d}T}$, this approach captures density variations across a flame front (and then thermal expansion) as this density variation is associated to the temperature increase.

# Appendix C

# Closure of the two-scale filtered progress variable balance equation using the thickened flame approach: TFLES-FPI

*This appendix is complementary to chapter 5 and proposes a new formulation of the TFLES-FPI model considering both flame and flow filter sizes explicitly. Note that this is valid only in a tabulated chemistry context. Similar developments for reduced chemistry would be more complicated as the flame structure is not known* a priori.

As detailed in Sec. 1.5.2.3, the thickened flame model has been coupled with tabulated chemistry by Kuenne et al. (2011). Considering fully-premixed combustion, the progress variable equation filtered at the flame size $\overline{\overline{\Delta}}$ reads:

$$\frac{\partial \overline{\overline{\rho}}\widetilde{\widetilde{Y}}_c}{\partial t} + \nabla \cdot \left( \overline{\overline{\rho}}\widetilde{\widetilde{\mathbf{u}}}\widetilde{\widetilde{Y}}_c \right) = \nabla \cdot \left( \Xi_{\overline{\overline{\Delta}}} \mathcal{F}^{\overline{\overline{\Delta}}} \overline{\overline{\rho D}}^{*} \nabla \widetilde{\widetilde{Y}}_c \right) + \frac{\Xi_{\overline{\overline{\Delta}}}}{\mathcal{F}^{\overline{\overline{\Delta}}}} \overline{\overline{\rho \dot{\omega}_{Y_c}}}^{*} \tag{C.1}$$

where $\overline{\overline{\Phi}}^{*}$ denotes that the variable $\overline{\overline{\Phi}}$ is extracted from the laminar FPI database $\Phi^{*}\left(Y_c\right)$ as:

$$\overline{\overline{\Phi}}^{*} = \Phi^{*}\left(\widetilde{\widetilde{Y}}_c\right) = \Phi^{*}\left(Y_c\left(\frac{x^{*}}{\mathcal{F}^{\overline{\overline{\Delta}}}}\right)\right) \tag{C.2}$$

where $x^{*}$ denote the space coordinate normal to the flame front. Equation (C.2) actually corresponds to a dilatation of the spatial coordinate $x^{*}$ resulting in a thickening of $\Phi^{*}$ by a factor $\mathcal{F}^{\overline{\overline{\Delta}}}$ noted $\overline{\overline{\Phi}}^{*}$. Therefore, $\overline{\overline{\Phi}}^{*}$ is modeled by the laminar quantity $\Phi^{*}$ thickened by a factor $\mathcal{F}^{\overline{\overline{\Delta}}}$ in the direction normal to the flame front. In this context, the thickening factor $\mathcal{F}^{\overline{\overline{\Delta}}}$ is chosen to ensure a

proper resolution of the filtered progress variable $\widetilde{\widetilde{Y}}_c = Y_c\left(x^*/\mathcal{F}^{\overline{\overline{\Delta}}}\right)$ front and verifies:

$$\delta_{\widetilde{\widetilde{Y}}_c} = n\Delta_x = \mathcal{F}^{\overline{\overline{\Delta}}}\delta_{Y_c} \tag{C.3}$$

where $n$, which depends on the numerics of the LES code, is typically of the order of $n = 5$. A second thickening factor corresponding to the flow filter is introduced to close the two-scale progress variable equation (5.27):

$$\overline{\Delta} = m\Delta_x = \mathcal{F}^{\overline{\Delta}}\delta_{Y_c} \tag{C.4}$$

where $m$ also depends on numerics of the LES code and is typically of the order of $m = 3$ as previously discussed in Sec. 5.1. As a first approximation, one can use this additional thickening factor $\mathcal{F}^{\overline{\Delta}}$ to estimate the thermochemical variables filtered at size $\overline{\Delta}$ from the same laminar FPI database $\Phi^*(Y_c)$ as:

$$\overline{\Phi}^* = \Phi^*\left(\widetilde{Y}_c\right) = \Phi^*\left(Y_c\left(\frac{x^*}{\mathcal{F}^{\overline{\Delta}}}\right)\right) \tag{C.5}$$

Equation (C.1) can be recast following the procedure described in Sec. 5.2.4 so that the progress variable filtered at size $\overline{\overline{\Delta}}$ is transported by the momentum filtered at size $\overline{\Delta}$:

$$\frac{\partial\overline{\rho}\widetilde{\widetilde{Y}}_c}{\partial t} + \nabla\cdot\left(\overline{\rho}\widetilde{\mathbf{u}}\widetilde{\widetilde{Y}}_c\right) = \nabla\cdot\left(\Xi_{\overline{\overline{\Delta}}}\mathcal{F}^{\overline{\overline{\Delta}}}\overline{\overline{\rho D}}^*\nabla\widetilde{\widetilde{Y}}_c\right) + \Xi_{\overline{\overline{\Delta}}}\mathcal{F}^{\overline{\overline{\Delta}}}\mathcal{D}^{\mathrm{TF}}_{Y_c} + \Xi_{\overline{\overline{\Delta}}}\mathcal{I}^{\mathrm{TF}}_{Y_c} + \frac{\Xi_{\overline{\overline{\Delta}}}}{\mathcal{F}^{\overline{\overline{\Delta}}}}\mathcal{R}^{\mathrm{TF}}_{Y_c} \tag{C.6}$$

where the RHS terms $\mathcal{D}^{\mathrm{TF}}_{Y_c}$, $\mathcal{I}^{\mathrm{TF}}_{Y_c}$ and $\mathcal{R}^{\mathrm{TF}}_{Y_c}$ are computed prior to the computation and are tabulated as a function of the resolved progress variable $\widetilde{\widetilde{Y}}_c$. $\Xi_{\overline{\overline{\Delta}}}$ account for the unresolved wrinkling at the filter scales located under $\overline{\overline{\Delta}}$. In the following, the tabulation procedure is denoted by $[\,\cdot\,]$. The diffusion correction term $\mathcal{D}^{\mathrm{TF}}_{Y_c}$ reads:

$$\mathcal{D}^{\mathrm{TF}}_{Y_c}\left[\widetilde{\widetilde{Y}}_c\right] = \left(\frac{\overline{\rho}^*}{\overline{\overline{\rho}}^*} - 1\right)\nabla\cdot\left(\overline{\overline{\rho D}}^*\nabla\widetilde{\widetilde{Y}}_c^{\,*}\right) \tag{C.7}$$

The inter-scale convection term $\mathcal{I}^{\mathrm{TF}}_{Y_c}$ reads:

$$\mathcal{I}^{\mathrm{TF}}_{Y_c}\left[\widetilde{\widetilde{Y}}_c\right] = \rho_f S_l\left(1 - \frac{\overline{\rho}^*}{\overline{\overline{\rho}}^*}\right)\nabla\widetilde{\widetilde{Y}}_c^{\,*} \tag{C.8}$$

The chemical reaction term $\mathcal{R}^{\mathrm{TF}}_{Y_c}$ is slightly modified compared to its original

formulation:

$$\mathcal{R}_{Y_c}^{\mathrm{TF}}\left[\widetilde{\overline{Y}}_c\right] = \frac{\overline{\rho}^*}{\overline{\overline{\rho}}^*}\overline{\overline{\dot{\omega}_{Y_c}}}^* \tag{C.9}$$

Finally, the final equation system to solve is written as follows:

$$\frac{\partial\overline{\rho}}{\partial t} + \nabla\cdot\left(\overline{\rho}\widetilde{\mathbf{u}}\right) = 0 \tag{C.10}$$

$$\frac{\partial\overline{\rho}\widetilde{\mathbf{u}}}{\partial t} + \nabla\cdot\left(\overline{\rho}\widetilde{\mathbf{u}}\widetilde{\mathbf{u}}\right) = -\nabla\overline{p_2} + \nabla\cdot\left(\overline{\tau} + \overline{\tau}^t\right) \tag{C.11}$$

$$\begin{aligned}\frac{\partial\overline{\rho}\widetilde{\overline{Y}}_c}{\partial t} + \nabla\cdot\left(\overline{\rho}\widetilde{\mathbf{u}}\widetilde{\overline{Y}}_c\right) &= \nabla\cdot\left(\Xi_{\overline{\overline{\Delta}}}\mathcal{F}^{\overline{\overline{\Delta}}}\overline{\overline{\rho D}}^*\nabla\widetilde{\overline{Y}}_c\right) + \Xi_{\overline{\overline{\Delta}}}\mathcal{F}^{\overline{\overline{\Delta}}}\mathcal{D}_{Y_c}^{\mathrm{TF}}\left[\widetilde{\overline{Y}}_c\right] \\ &\quad + \Xi_{\overline{\overline{\Delta}}}\mathcal{I}_{Y_c}^{\mathrm{TF}}\left[\widetilde{\overline{Y}}_c\right] + \frac{\Xi_{\overline{\overline{\Delta}}}}{\mathcal{F}^{\overline{\overline{\Delta}}}}\mathcal{R}_{Y_c}^{\mathrm{TF}}\left[\widetilde{\overline{Y}}_c\right]\end{aligned} \tag{C.12}$$

$$p_0 = \overline{\rho}\widetilde{rT}^*\left[\widetilde{\overline{Y}}_c\right] \tag{C.13}$$

This model has neither been implemented nor tested during this thesis since the focus has been made on the filtered flame model F-TACLES, more suitable to handle spatial filtering formalism.

# Bibliography


Abani, N. and Ghoniem, A. F. (2013). Large eddy simulations of coal gasification in an entrained flow gasifier. *Fuel*, 104(0):664–680. *(p. 21)*

ACARE (2015). Advisory council for aviation research and innovation in europe. http://www.acare4europe.com/ documents/ acare-addressing-new-horizons-aviation. *(p. 2)*

Albouze, G., Poinsot, T., and Gicquel, L. (2009). Chemical kinetics modeling and les combustion model effects on a perfectly premixed burner. *Comptes Rendus Mécanique*, 337(6-7):319–328. *(p. 21)*

ANSYS® Fluent (2009). *Theory Guide*. Release 12.0. *(p. 74, 195)*

Aspden, A. J., Day, M. S., and Bell, J. B. (2011a). Lewis number effects in distributed flames. *Proceedings of the Combustion Institute*, 33(1):1473 – 1480. *(p. 46, 215)*

Aspden, A. J., Day, M. S., and Bell, J. B. (2011b). Turbulence-flame interactions in lean premixed hydrogen: transition to the distributed burning regime. *Journal of Fluid Mechanics*, 680:287–320. *(p. 46, 214, 215)*

Auzillon, P. (2011). *Modélisation de la structure et de la dynamique des flammes pour la simulation aux grandes échelles*. PhD thesis, Ecole Centrale Paris. *(p. 5, 207)*

Auzillon, P., Fiorina, B., Vicquelin, R., Darabiha, N., Gicquel, O., and Veynante, D. (2011). Modeling chemical flame structure and combustion dynamics in les. *Proceedings of the Combustion Institute*, 33(1):1331 – 1338. *(p. 33, 36, 39, 46)*

Auzillon, P., Gicquel, O., Darabiha, N., Veynante, D., and Fiorina, B. (2012). A filtered tabulated chemistry model for LES of stratified flames. *Combustion and Flame*, 159(8):2704 – 2717. *(p. 5, 33, 34, 36, 46, 49, 60, 112, 114, 161)*

Auzillon, P., Riber, E., Gicquel, L. Y., Gicquel, O., Darabiha, N., Veynante, D., and Fiorina, B. (2013). Numerical investigation of a helicopter combustion chamber using LES and tabulated chemistry. *Comptes Rendus Mécanique*,

341(1–2):257 – 265. Combustion, spray and flow dynamics for aerospace propulsion Combustion, spray and flow dynamics for aerospace propulsion. *(p. 37, 114)*

Bardina, J., Ferziger, J., and Reynolds, W. (1980). Improved subgrid scale models for large eddy simulation. *AIAA paper*, (80-1357). *(p. 13)*

Barlow, R. S., Dunn, M. J., Sweeney, M. S., and Hochgreb, S. (2012). Effects of preferential transport in turbulent bluff-body-stabilized lean premixed CH4/air flames. *Combustion and Flame*, 159(8):2563 – 2575. *(p. 46, 48, 69, 103)*

Barlow, R. S. and Frank, J. H. (1998). Effects of turbulence on species mass fractions in methane/air jet flames. *Proc. Combust. Inst.*, 27:1087–1095. *(p. 24)*

Benteboula, S. (2006). *Résolution des équations de Navier-Stokes à faible nombre de Mach : Application à l'étude de l'anneau de vorticité à masse volumique variable*. PhD thesis, Université de Marne-la-Vallée. *(p. 224)*

Biferale, L. and Vergassola, M. (2001). Isotropy vs anisotropy in small-scale turbulence. *Physics of Fluids*, 13(8):2139–2141. *(p. 13)*

Bilger, R. W. (1976). The structure of diffusion flames. *Combust. Sci. and technology*, 13:155–170. *(p. 24)*

Boger, M. and Veynante, D. (2000). Large eddy simulation of a turbulent premixed V-shaped flame. In Dopazo, C., editor, *Advances in Turbulence*, pages 449 – 452. Cimne, Barcelona. *(p. 31, 138)*

Boger, M., Veynante, D., Boughanem, H., and Trouvé, A. (1998). Direct numerical simulation analysis of flame surface density concept for large eddy simulation of turbulent premixed combustion. *Proceedings of the Combustion Institute*, 27(1):917 – 925. *(p. 26, 31, 118, 133)*

Böhm, B., Frank, J. H., and Dreizler, A. (2011). Temperature and mixing field measurements in stratified lean premixed turbulent flames. *Proceedings of the Combustion Institute*, 33(1):1583–1590. *(p. 68, 70)*

Boileau, M., Staffelbach, G., Cuenot, B., Poinsot, T., and Bérat, C. (2008). LES of an ignition sequence in a gas turbine engine. *Combustion and Flame*, 154(1 - 2):2 – 22. *(p. 33, 71, 223)*

Bradley, D., Kwa, L. K., Lau, A. K. C., and Missaghi, M. (1988). Laminar flamelet modelling of recirculating premixed methane and propane-air combustion. *Combust. Flame*, 71:109–122. *(p. 23)*

Bray, K., Domingo, P., and Vervisch, L. (2005). Role of the progress variable in models for partially premixed turbulent combustion. *Combustion and Flame*, 141(4):431 – 437. *(p. 31)*

Broeckhoven, T., Freitag, M., Lacor, C., Sadiki, A., and Janicka, J. (2007). *Investigation of Subgrid Scale Wrinkling Models and Their Impact on the Artificially Thickened Flame Model in Large Eddy Simulations*, volume 56, pages 353–369. Springer Berlin Heidelberg. *(p. 33)*

Butler, T. D. and O'Rourke, P. J. (1977). A numerical method for two-dimensional unsteady reacting flows. *Proceedings of the Combustion Institute*, 16:1503–1515. *(p. 32)*

Bykov, V. and Maas, U. (2007). The extension of the ILDM concept to reaction-diffusion manifolds. *Combustion Theory and Modelling*, 11(6):839–862. *(p. 23)*

Bykov, V. and Maas, U. (2009). Problem adapted reduced models based on reaction–diffusion manifolds (redims). *Proceedings of the Combustion Institute*, 32(1):561–568. *(p. 23)*

Candel, S., Schmitt, T., and Darabiha, N. (2011). Progress in transcritical combustion : experimentation, modeling and simulation. In *23rd ICDERS, Irvine*. *(p. 73, 172, 194)*

Chakraborty, N. and Cant, R. (2009). Direct numerical simulation analysis of the flame surface density transport equation in the context of large eddy simulation. *Proceedings of the Combustion Institute*, 32(1):1445 – 1453. *(p. 114)*

Chakraborty, N. and Klein, M. (2008). A priori direct numerical simulation assessment of algebraic flame surface density models for turbulent premixed flames in the context of large eddy simulation. *Physics of Fluids*, 20(8). *(p. 114)*

Charlette, F., Meneveau, C., and Veynante, D. (2002a). A power-law flame wrinkling model for les of premixed turbulent combustion, part I: non-dynamic formulation. *Combustion and Flame*, 131(1/2):159–180. *(p. 5, 7, 32, 36, 71, 114, 117, 118, 119, 120, 126, 194)*

Charlette, F., Meneveau, C., and Veynante, D. (2002b). A power-law flame wrinkling model for les of premixed turbulent combustion, part II: dynamic formulation. *Combustion and Flame*, 131(1/2):181–197. *(p. 13, 32, 36, 114, 117, 118)*

Choi, C. and Huh, K. (1998). Development of a coherent flamelet model for a spark ignited turbulent premixed flame in a closed vessel. *Combust. Flame*, 114(3/4):336–348. *(p. 31)*

Chong, L. T. W., Komarek, T., Zellhuber, M., Lenz, J., Hirsch, C., and Polifke, W. (2009). Influence of strain and heat loss on flame stabilization in a non-adiabatic combustor. In *Proceedings of the European Combustion Meeting*. *(p. 199)*

Clausius, R. (1851). On the moving force of heat, and the laws regarding the nature of heat itself which are deducible therefrom. *Philosophical Magazine Series 4*, 2(8):1–21. *(p. 220)*

Colin, O., Ducros, F., Veynante, D., and Poinsot, T. (2000). A thickened flame model for large eddy simulations of turbulent premixed combustion. *Physics of Fluids*, 12(7):1843–1863. *(p. 26, 32, 35, 36, 111, 116, 119, 138)*

Colin, O. and Rudgyard, M. (2000). Development of high-order taylor-galerkin schemes for unsteady calculations. *J. Comput. Phys.*, 162(2):338–371. *(p. 133)*

Cook, A. W. and Riley, J. J. (1994). A subgrid model for equilibrium chemistry in turbulent flows. *Phys. Fluids*, 8(6):2868–2870. *(p. 26)*

Coussement, A., Schmitt, T., and Fiorina, B. (2015). Filtered tabulated chemistry for non-premixed flames. *Proceedings of the Combustion Institute*, 35(2):1183 – 1190. *(p. 209)*

Dagaut, P., Reuillon, M., Boettner, J.-C., and Cathonnet, M. (1994). Kerosene combustion at pressures up to 40 atm: Experimental study and detailed chemical kinetic modeling. *Proceedings of the Combustion Institute*, 25(1):919 – 926. *(p. 20)*

Day, M. S. and Bell, J. B. (2000). Numerical simulation of laminar reacting flows with complex chemistry. *Combustion Theory and Modelling*, 4(4):535–556. *(p. 223)*

De, A. and Acharya, S. (2009). Large eddy simulation of a premixed bunsen flame using a modified thickened-flame model at two Reynolds number. *Combustion Science and Technology*, 181(10):1231–1272. *(p. 33)*

Deardorff, J. W. (1970). A numerical study of three-dimensional turbulent channel flow at large reynolds numbers. *Journal of Fluid Mechanics*, 41(02):453–480. *(p. 116)*

di Mare, F., Jones, W. P., and Menzies, K. R. (2004). Large eddy simulation of a model gas turbine combustor. *Combustion and Flame*, 137(3):278–294. *(p. 21)*

Di Sarli, V., Di Benedetto, A., Russo, G., Jarvis, S., Long, E. J., and Hargrave, G. K. (2009). Large eddy simulation and PIV measurements of unsteady premixed flames accelerated by obstacles. *Flow, Turbulence and Combustion*, 83(2):227–250. *(p. 114)*

Domingo, P., Vervisch, L., and Bray, K. N. C. (2002). Partially premixed flamelets in LES of nonpremixed turbulent combustion. *Combustion Theory and Modelling*, 6(4):529–551. *(p. 31)*

Domingo, P., Vervisch, L., and Veynante, D. (2008). Large-eddy simulation of a lifted methane jet flame in a vitiated coflow. *Combustion and Flame*, 152(3):415 – 432. *(p. 22)*

Driscoll, J. F. (2008). Turbulent premixed combustion: Flamelet structure and its effect on turbulent burning velocities. *Progress in Energy and Combustion Science*, 34(1):91 – 134. *(p. 4, 213, 217)*

Duclos, J., Veynante, D., and Poinsot, T. (1993). A comparison of flamelet models for premixed turbulent combustion. *Combust. Flame*, 95(1/2):101–118. *(p. 31)*

Ducros, F., Nicoud, F., and Poinsot, T. (1998). Wall-adapting local eddy-viscosity models for simulations in complex geometries. In J., B. M., editor, *ICFD*, pages 293–300. *(p. 15)*

Dunn, M. J. and Barlow, R. S. (2013). Effects of preferential transport and strain in bluff body stabilized lean and rich premixed CH4/air flames. *Proceedings of the Combustion Institute*, 34(1):1411 – 1419. *(p. 46, 48, 103)*

Duwig, C. (2007). Study of a filtered flamelet formulation for large eddy simulation of premixed turbulent flames. *Flow Turbulence and Combustion*, 79(4):433–454. *(p. 26, 32, 133, 138)*

Duwig, C. (2009). A filtered flame approach for simulation of unsteady laminar flames. *Combustion Theory and Modelling*, 13(2):251–268. *(p. 46, 133, 138)*

Duwig, C. and Fuchs, L. (2008). Large eddy simulation of a H2/N2 lifted flame in a vitiated co-flow. *Combustion Science and Technology*, 180(3):453–480. *(p. 27)*

Duwig, C. and Fureby, C. (2007). Large eddy simulation of unsteady lean stratified premixed combustion. *Combustion and Flame*, 151(1–2):85 – 103. *(p. 31)*

Duwig, C., Nogenmyr, K.-J., Chan, C.-k., and Dunn, M. J. (2011). Large eddy simulations of a piloted lean premix jet flame using finite-rate chemistry. *Combustion Theory and Modelling*, 15(4):537–568. *(p. 27, 28)*

Echekki, T., Kerstein, A. R., and Sutherland, J. C. (2011). *Turbulent Combustion Modeling*, volume 95, chapter The One-Dimensional-Turbulence Model, pages 249–276. Fluid Mechanics and Its Applications, springer edition. *(p. 26)*

Enjalbert, N., Domingo, P., and Vervisch, L. (2012). Mixing time-history effects in large eddy simulation of non-premixed turbulent flames: Flow-controlled chemistry tabulation. *Combustion and Flame*, 159(1):336 – 352. *(p. 22)*

Euler, M., Zhou, R., Hochgreb, S., and Dreizler, A. (2013). Temperature measurements of the bluff body surface of cambridge-sandia stratified swirl burner using phosphor thermometry. In *Proceedings of the European Combustion Meeting*. *(p. 95, 97)*

Euler, M., Zhou, R., Hochgreb, S., and Dreizler, A. (2014). Temperature measurements of the bluff body surface of a swirl burner using phosphor thermometry. *Combustion and Flame*, 161(11):2842 – 2848. *(p. 69, 95)*

Ferrand, L. (2003). *Modélisation et expérimentation des fours de réchauffage sidérurgiques équipés de brûleurs régénératifs à Oxydation sans Flamme*. PhD thesis, Ecole des Mines de Paris. *(p. 217, 223)*

Fichet, V., Kanniche, M., Plion, P., and Gicquel, O. (2010). A reactor network model for predicting NOx emissions in gas turbines. *Fuel*, 89(9):2202–2210. *(p. 22)*

Fiorina, B., Baron, R., Gicquel, O., Thévenin, D., Carpentier, S., and Darabiha, N. (2003). Modelling non-adiabatic partially-premixed flames using Flame Prolongation of ILDM. *Combustion Theory and Modelling*, 7(3):449–470. *(p. 22, 24, 25, 33, 47, 56, 59, 212)*

Fiorina, B., Gicquel, O., Vervisch, L., Carpentier, S., and Darabiha, N. (2005a). Approximating the chemical structure of partially-premixed and diffusion counterflow flames using FPI flamelet tabulation. *Combustion and Flame*, 140(3):147–160. *(p. 22)*

Fiorina, B., Gicquel, O., Vervisch, L., Carpentier, S., and Darabiha, N. (2005b). Premixed turbulent combustion modelling using tabulated chemistry and PDF. In *Proc. Combust. Inst.*, volume 30, pages 867–874. The Combustion Institute, Pittsburgh. *(p. 29)*

Fiorina, B., Mercier, R., Kuenne, G., Advić, A., Janicka, J., Dreizler, A., Alenius, E., Duwig, C., Trisjono, P., Kleinheinz, K., Kang, S., Pitsch, H., Proch, F., Marincola, F. C., and Kempf, A. M. (2015a). Challenging modeling strategies for LES of non-adiabatic turbulent stratified combustion. *Combustion and Flame*, Accepted for publication. *(p. 68)*

Fiorina, B., Veynante, D., and Candel, S. (2015b). Modeling combustion chemistry in large eddy simulation of turbulent flames. *Submitted*. *(p. 12, 21, 26, 133)*

Fiorina, B., Vicquelin, R., Auzillon, P., Darabiha, N., Gicquel, O., and Veynante, D. (2010). A filtered tabulated chemistry model for les of premixed

combustion. *Combustion and Flame*, 157(3):465 – 475. *(p. 5, 26, 29, 33, 36, 46, 133, 138, 139, 142, 148)*

Fourier, J. B. J. (1822). *Théorie analytique de la chaleur*. Firmin Didot. *(p. 221)*

Franzelli, B., Fiorina, B., and Darabiha, N. (2013). A tabulated chemistry method for spray combustion. *Proceedings of the Combustion Institute*, 34(1):1659 – 1666. *(p. 23)*

Franzelli, B., Riber, E., Gicquel, L. Y., and Poinsot, T. (2012). Large eddy simulation of combustion instabilities in a lean partially premixed swirled flame. *Combustion and Flame*, 159(2):621 – 637. *(p. 21, 33, 138, 142)*

Franzelli, B., Riber, E., Sanjosé, M., and Poinsot, T. (2010). A two-step chemical scheme for kerosene–air premixed flames. *Combustion and Flame*, 157(7):1364–1373. *(p. 21, 46)*

Fureby, C. (2005). A fractal flame-wrinkling large eddy simulation model for premixed turbulent combustion. *Proceedings of the Combustion Institute*, 30(1):593 – 601. *(p. 32)*

Fureby, C. (2007). Comparison of flamelet and finite rate chemistry les for premixed turbulent combustion. In of Aeronautics, A. I. and Astronautics, editors, *45th AIAA Aerospace Sciences Meeting and Exhibit*. *(p. 27)*

Galley, D., Ducruix, S., Lacas, F., and Veynante, D. (2011). Mixing and stabilization study of a partially premixed swirling flame using laser induced fluorescence. *Combustion and Flame*, 158(1):155 – 171. *(p. 169)*

Galpin, J., Naudin, A., Vervisch, L., Angelberger, C., Colin, O., and Domingo, P. (2008). Large-eddy simulation of a fuel-lean premixed turbulent swirl-burner. *Combust. Flame*, 155:247–266. *(p. 29, 138)*

Gao, F. and O'Brien, E. E. (1993). A large eddy simulation scheme for turbulent reacting flows. *Physics of Fluids*, 5(6):1282–1284. *(p. 26, 27)*

Garby, R., Selle, L., and Poinsot, T. (2013). Large-eddy simulation of combustion instabilities in a variable-length combustor. *Comptes Rendus Mécanique*, 341(1–2):220 – 229. Combustion, spray and flow dynamics for aerospace propulsion Combustion, spray and flow dynamics for aerospace propulsion. *(p. 114)*

Germano, M., Piomelli, U., Moin, P., and Cabot, W. H. (1991). A dynamic subgrid-scale eddy viscosity model. *Physics of Fluids*, 3(7):1760–1765. *(p. 13, 15, 71, 78, 117)*

Gicquel, O., Darabiha, N., and Thévenin, D. (2000). Laminar premixed hydrogen / air counterflow flame simulations using flame prolongation of ILDM with differential diffusion. *Proceedings of the Combustion Institute*, 28(2):1901–1908. *(p. 22, 23, 47)*

Gicquel, O., Thévenin, D., Hilka, M., and Darabiha, N. (1999). Direct numerical simulation of turbulent premixed flames using intrinsic low-dimensional manifolds. *Combustion Theory and Modelling*, 3(3):479–502. *(p. 22)*

Goldin, G. (2005). Evaluation of les subgrid reaction models in a lifted flame. In of Aeronautics, A. I. and Astronautics, editors, *43rd AIAA Aerospace Sciences Meeting and Exhibit*. *(p. 27)*

Gouldin, F. (1987). An application of fractals to modeling premixed turbulent flames. *Combustion and Flame*, 68(3):249–266. *(p. 113, 117)*

Gouldin, F., Hilton, S., and Lamb, T. (1989). Experimental evaluation of the fractal geometry of flamelets. *Proceedings of the Combustion Institute*, 22(1):541 – 550. *(p. 113)*

Grinstein, F. and Kailasanath, K. (1995). Three-dimensional numerical simulations of unsteady reactive square jets. *Combustion and Flame*, 100(1–2):2 – 10. *(p. 27)*

Guiberti, T., Durox, D., Scouflaire, P., and Schuller, T. (2014a). Impact of heat loss and hydrogen enrichment on the shape of confined swirling flames. *Proceedings of the Combustion Institute*, 35:1385 – 1392. *(p. 169, 190, 199, 202)*

Guiberti, T. F. (2015). *Analysis of the topology of confined swirling premixed flames*. PhD thesis, Ecole Centrale Paris. *(p. 6, 168, 169, 190, 208)*

Guiberti, T. F., Mercier, R., Fiorina, B., Zimmer, L., Durox, D., and Schuller, T. (2014b). Flame shape bifurcations in a confined swirled burner: analysis of the combined effects of strain rate and heat losses. *Submitted*. *(p. 169, 202, 204, 205)*

Hawkes, E. R. and Cant, R. S. (2000). A flame surface density approach to large-eddy simulation of premixed turbulent combustion. *Proc. Combust. Inst*, 28:51–58. *(p. 31)*

Hawkes, E. R., Chatakonda, O., Kolla, H., Kerstein, A. R., and Chen, J. H. (2012). A petascale direct numerical simulation study of the modelling of flame wrinkling for large-eddy simulations in intense turbulence. *Combustion and Flame*, 159(8):2690 – 2703. *(p. 32, 214)*

Hawkes, E. R. and Chen, J. H. (2004). Direct numerical simulation of hydrogen-enriched lean premixed methane–air flames. *Combustion and Flame*, 138(3):242–258. *(p. 202)*

Haworth, D. (2010). Progress in probability density function methods for turbulent reacting flows. *Progress in Energy and Combustion Science*, 36(2):168 – 259. *(p. 26, 27)*

Hernández-Pérez, F. E., Yuen, F. T. C., Groth, C. P. T., and Gülder, Ö. L. (2011). LES of a laboratory-scale turbulent premixed bunsen flame using FSD, PCM-FPI and thickened flame models. *Proceedings of the Combustion Institute*, 33(1):1365–1371. *(p. 114)*

Hirschfelder, J. O., Curtiss, C. F., and Bird, R. B. (1969). *Molecular theory of gases and liquids*. John Wiley & Sons, New York. *(p. 50, 77, 81, 96)*

Ihme, M., Shunn, L., and Zhang, J. (2012). Regularization of reaction progress variable for application to flamelet-based combustion models. *Journal of Computational Physics*, 231(23):7715 – 7721. *(p. 25)*

International Energy Agency (2015). Total primary energy supply in the world for 2012. http://www.iea.org/ statistics/ statisticssearch/ report/ ?country=WORLD &product=balances &year=2012. *(p. 1)*

IPPC (2015). Integrated Pollution Prevention and Control. https://en.wikipedia.org/ wiki/ Integrated _Pollution _Prevention _and _Control. *(p. 2)*

J. Beer, N. C. (1983). *Combustion Aerodynamics*. Robert E. Krieger Publishing, Melbourne, FL. *(p. 169)*

Janus, B., Dreizler, A., and Janicka, J. (2004). Flow field and structure of swirl stabilized non-premixed natural gas flames at elevated pressure. *ASME Conference Proceedings*, 1:189–198. *(p. 46)*

Janus, B., Dreizler, A., and Janicka, J. (2005). Experimental study on stabilization of lifted swirl flames in a model GT combustor. *Flow, Turbulence and Combustion*, 75:293–315. *(p. 46)*

Janus, B., Dreizler, A., and Janicka, J. (2007). Experiments on swirl stabilized non-premixed natural gas flames in a model gas turbine combustor. *Proceedings of the Combustion Institute*, 31(2):3091 – 3098. *(p. 46, 223)*

Jones, W. P. and Lindstedt, R. P. (1988). Global reaction schemes for hydrocarbon combustion. *Combust. Flame*, 73:233–249. *(p. 21)*

Katsuki, M., Mizutani, Y., Chikami, M., and Kittaka, T. (1988). Sound emission from a turbulent flame. *Proceedings of the Combustion Institute*, 21(1):1543 – 1550. *(p. 191)*

Katta, V. and Roquemore, W. M. (2013). C/H atom ratio in recirculation-zone-supported premixed and nonpremixed flames. *Proceedings of the Combustion Institute*, 34(1):1101 – 1108. *(p. 48, 69, 103)*

Kee, R. J., Grcar, J. F., Smooke, M. D., and Miller, J. A. (1992). A fortran program for modelling steady laminar one-dimensional premixed flames. Technical report, Sandia National Laboratories. *(p. 56, 57)*

Kerstein, A. (1988a). Fractal dimension of turbulent premixed flames. *Combustion Science and Technology*, 60(4-6):441–445. *(p. 117)*

Kerstein, A. R. (1988b). A linear-eddy model for turbulent scalar transport and mixing. *Combust. Sci Tech.*, 60:391–421. *(p. 26, 30)*

Ketelheun, A., Kuenne, G., and Janicka, J. (2013). Heat transfer modeling in the context of large eddy simulation of premixed combustion with tabulated chemistry. *Flow, Turbulence and Combustion*, 91(4):867–893. *(p. 33, 40, 42, 47, 68, 87, 114)*

Kim, K. T., Lee, J. G., Lee, H. J., Quay, B. D., and Santavicca, D. A. (2010). Characterization of forced flame response of swirl-stabilized turbulent lean-premixed flames in a gas turbine combustor. *Journal of Engineering for Gas Turbines and Power*, 132(4):041502–041502. *(p. 202)*

Knikker, R., Veynante, D., and Meneveau, C. (2002). A priori testing of a similarity model for large eddy simulations of turbulent premixed combustion. *Proceedings of the Combustion Institute*, 29(2):2105–2111. *(p. 13)*

Knudsen, E., Kim, S. H., and Pitsch, H. (2010). An analysis of premixed flamelet models for large eddy simulation of turbulent combustion. *Physics of Fluids*, 22(11):115109–1 — 115109–24. *(p. 30)*

Knudsen, E., Kolla, H., Hawkes, E. R., and Pitsch, H. (2013). LES of a premixed jet flame DNS using a strained flamelet model. *Combustion and Flame*, 160(12):2911–2927. *(p. 30)*

Knudsen, E. and Pitsch, H. (2008). A dynamic model for the turbulent burning velocity for large eddy simulation of premixed combustion. *Combust. Flame*, 154(4):740 – 760. *(p. 32)*

Knudsen, E. and Pitsch, H. (2012). Capabilities and limitations of multi-regime flamelet combustion models. *Combustion and Flame*, 159(1):242 – 264. *(p. 22)*

Kolmogorov, A. N. (1942). Equations of turbulent motion of an incompressible fluid. *Izv. Akad. Nauk, USSR, Seria fizicheska VI*, (1-2):56–58. *(p. 115)*

Kraushaar, M. (2011). *Application of the compressible and low-Mach number approaches to Large Eddy Simulation of turbulent flows in aero-engines*. PhD thesis, Université de Toulouse. *(p. 71, 133, 176, 194, 223)*

Kuenne, G., Ketelheun, A., and Janicka, J. (2011). LES modeling of premixed combustion using a thickened flame approach coupled with FGM tabulated chemistry. *Combustion and Flame*, 158(9):1750–1767. *(p. 33, 46, 114, 225)*

Kuenne, G., Seffrin, F., Fuest, F., Stahler, T., Ketelheun, A., Geyer, D., Janicka, J., and Dreizler, A. (2012). Experimental and numerical analysis of a lean premixed stratified burner using 1D Raman/Rayleigh scattering and large eddy simulation. *Combustion and Flame*, 159(8):2669 – 2689. *(p. 33, 68, 74, 79, 85, 114)*

Launder, B. and Spalding, D. (1974). The numerical computation of turbulent flows. *Computer Methods in Applied Mechanics and Engineering*, 3(2):269 – 289. *(p. 12)*

Légier, J.-P., Poinsot, T., and Veynante, D. (2000). Dynamically thickened flame LES model for premixed and non-premixed turbulent combustion. In Center for Turbulence Research, N., editor, *Proceedings of the Summer Program*, pages 157–168. *(p. 33)*

Li, J., Zhao, Z., Kazakov, A., and Dryer, F. (2003). An updated comprehensive kinetic model for H2 combustion. Fall technical meeting of the eastern states section of the combustion institute, Penn State University, University Park, PA. *(p. 20)*

Lilly, D. K. (1992). A proposed modification of the germano subgrid scale closure method. *Physics of Fluids*, 4(3):633–635. *(p. 15, 71, 78)*

Lindstedt, P. (1997). 12 month progress report 1. Technical Report TR-96 009, Brite Euram Program Project BRPR950056. *(p. 50, 73, 96, 135, 147, 172, 173, 174, 194)*

Lipatnikov, A. and Chomiak, J. (2005). Molecular transport effects on turbulent flame propagation and structure. *Progress in Energy and Combustion Science*, 31(1):1–73. *(p. 202)*

Luche, J. (2003). Obtention de modèles cinétiques réduits de combustion. application à un mécanisme du kérosène. Technical report, Université d'Orléans. *(p. 20, 21)*

Ma, T., Stein, O., Chakraborty, N., and Kempf, A. (2014). A posteriori testing of the flame surface density transport equation for LES. *Combustion Theory and Modelling*, 18(1):32–64. *(p. 31, 32)*

Ma, T., Stein, O. T., Chakraborty, N., and Kempf, A. M. (2013). A posteriori testing of algebraic flame surface density models for LES. *Combustion Theory and Modelling*, 17(3):431–482. *(p. 31, 32)*

Maas, U. and Pope, S. B. (1992a). Implementation of simplified chemicical kinetics based on intrinsic low-dimensional manifold. *Proceedings of the Combustion Institute*, 24:103–112. *(p. 22)*

Maas, U. and Pope, S. B. (1992b). Simplifying chemical kinetics: Intrinsic low-dimensional manifolds in composition space. *Combustion and Flame*, 88(3-4):239 – 264. *(p. 22)*

Majda, A. and Sethian, J. (1985). The derivation and numerical solution of the equations for zero mach number combustion. *Combustion Science and Technology*, 42(3-4):185–205. *(p. 223)*

Mantel, T. and Borghi, R. (1994). A new model of premixed wrinkled flame propagation based on a scalar dissipation equation. *Combust. Flame*, 96(4):443–457. *(p. 31)*

Maragkos, G., Rauwoens, P., and Merci, B. (2013). A new methodology to incorporate differential diffusion in CFD simulations of reactive flows. *Combustion and Flame*, 160(9):1903 – 1905. *(p. 47)*

Marincola, F. C., Ma, T., and Kempf, A. M. (2013). Large eddy simulations of the darmstadt turbulent stratified flame series. *Proceedings of the Combustion Institute*, 34(1):1307 – 1315. *(p. 46, 68, 79, 85)*

Meier, W., Weigand, P., Duan, X., and Giezendanner-Thoben, R. (2007). Detailed characterization of the dynamics of thermoacoustic pulsations in a lean premixed swirl flame. *Combustion and Flame*, 150(1-2):2 – 26. *(p. 138)*

Menon, S. and Jou, W. (1991). Large eddy simulations of combustion instability in an axisymetric ramjet combustor. *Combust. Sci. and Tech.*, 75:53–72. *(p. 13)*

Menon, S. and Kerstein, A. R. (2011). *Turbulent Combustion Modeling*, volume 95, chapter The Linear-Eddy Model, pages 220–248. Fluid Mechanics and Its Applications, springer edition. *(p. 26)*

Mercier, R., Auzillon, P., Moureau, V., Darabiha, N., Gicquel, O., Veynante, D., and Fiorina, B. (2013a). Modeling flame stabilization by heat losses using filtered tabulated chemistry for large eddy simulation. In *Eighth International Symposium On Turbulence and Shear Flow Phenomena*. *(p. 68)*

Mercier, R., Auzillon, P., Moureau, V., Darabiha, N., Gicquel, O., Veynante, D., and Fiorina, B. (2014). LES modeling of the impact of heat losses and differential diffusion on turbulent stratified flame propagation: Application to the TU Darmstadt stratified flame. *Flow, Turbulence and Combustion*, 93(2):349–381. *(p. 55, 68, 114)*

Mercier, R., Moureau, V., Veynante, D., and Fiorina, B. (2015a). LES of turbulent combustion: on the consistency between flame and flow filter scales. *Proceedings of the Combustion Institute*, 35. *(p. 114)*

Mercier, R., Proch, F., Kempf, A. M., and Fiorina, B. (2013b). Numerical and modeling strategies for the simulation of the Cambridge stratified flame series. In *Eighth International Symposium On Turbulence and Shear Flow Phenomena*. *(p. 69, 98)*

Mercier, R., Schmitt, T., Veynante, D., and Fiorina, B. (2015b). The influence of combustion SGS sub-models on the resolved flame propagation. application to the LES of the Cambridge stratified flames. *Proceedings of the Combustion Institute*, 35. *(p. 69, 114)*

Moureau, V. (2004). *Simulation aux grandes échelles de l'aérodynamique interne des moteurs à piston*. PhD thesis, Ecole Centrale Paris. *(p. 116)*

Moureau, V., Domingo, P., and Vervisch, L. (2011a). Design of a massively parallel CFD code for complex geometries. *Comptes Rendus Mécanique*, 339(2-3):141 – 148. *(p. 6, 66, 71, 96, 147, 148, 176, 194)*

Moureau, V., Domingo, P., and Vervisch, L. (2011b). From large-eddy simulation to direct numerical simulation of a lean premixed swirl flame: Filtered laminar flame-PDF modeling. *Combustion and Flame*, 158(7):1340 – 1357. *(p. 29, 37, 117, 142)*

Moureau, V., Fiorina, B., and Pitsch, H. (2009). A level set formulation for premixed combustion les considering the turbulent flame structure. *combust. and Flame*, 156(4):801–812. *(p. 30)*

Moureau, V., Minot, P., Pitsch, H., and Berat, C. (2007). A ghost-fluid method for large-eddy simulations of premixed combustion in complex geometries. *Journal of Computational Physics*, 221(2):600 – 614. *(p. 138)*

Nambully, S., Domingo, P., Moureau, V., and Vervisch, L. (2014a). A filtered-laminar-flame PDF sub-grid scale closure for LES of premixed turbulent flames. part I: Formalism and application to a bluff-body burner with differential diffusion. *Combustion and Flame*, 161(7):1756–1774. *(p. 25, 37, 47, 48, 55, 69, 103, 121)*

Nambully, S., Domingo, P., Moureau, V., and Vervisch, L. (2014b). A filtered-laminar-flame PDF sub-grid-scale closure for LES of premixed turbulent flames. part II: Application to a stratified bluff-body burner. *Combustion and Flame*, 161(7):1775–1791. *(p. 37, 47, 48, 55, 69, 104, 121)*

Nambully, S. K. (2013). *A Filtered-Laminar-Flame PDF Subgrid Scale Closure for LES of Premixed Turbulent Flames. Application to a Stratified Bluff-body Burner with Differential Diffusion*. PhD thesis, INSA Rouen. *(p. 37)*

Newton, I. (1687). *Philosophiæ Naturalis Principia Mathematica.* *(p. 220)*

Nguyen, P., Vervisch, L., Subramanian, V., and Domingo, P. (2010). Multidimensional flamelet-generated manifolds for partially premixed combustion. *Combustion and Flame*, 157(1):43–61. *(p. 22)*

Nicoud, F. and Ducros, F. (1999). Subgrid-scale stress modelling based on the square of the velocity gradient tensor. *Flow, Turbulence and Combustion*, 62(3):183–200. *(p. 71, 78)*

Nicoud, F., Toda, H. B., Cabrit, O., Bose, S., and Lee, J. (2011). Using singular values to build a subgrid-scale model for large eddy simulations. *Physics of Fluids*, 23(8):085106. *(p. 15, 96, 176, 194)*

Nogenmyr, K.-J., Cao, H. J., Chan, C. K., and Cheng, R. K. (2013). Effects of confinement on premixed turbulent swirling flame using large eddy simulation. *Combustion Theory and Modelling*, 17(6):1003–1019. *(p. 199)*

Olbricht, C., Stein, O., Janicka, J., van Oijen, J., Wysocki, S., and Kempf, A. (2012). LES of lifted flames in a gas turbine model combustor using top-hat filtered PFGM chemistry. *Fuel*, 96(0):100 – 107. *(p. 29)*

O'Rourke, P. J. and Bracco, F. V. (1979). Two scaling transformations for the numerical computation of multidimensional unsteady laminar flames. *Journal of Computational Physics*, 33(2):185–203. *(p. 32)*

Palies, P., Durox, D., Schuller, T., and Candel, S. (2010). The combined dynamics of swirler and turbulent premixed swirling flames. *Combustion and Flame*, 157(9):1698–1717. *(p. 169)*

Palies, P., Durox, D., Schuller, T., and Candel, S. (2011). Experimental study on the effect of swirler geometry and swirl number on flame describing functions. *Combustion Science and Technology*, 183(7):704–717. *(p. 169)*

Passot, T. and Pouquet, A. (1987). Numerical simulation of compressible homogeneous flows in the turbulent regime. *Journal of Fluid Mechanics*, 181:441–466. *(p. 74, 97, 177)*

Peters, N. (1984). Laminar diffusion flamelet models in non-premixed turbulent combustion. *Prog. Energy Combustion. Sci.*, 10:319–339. *(p. 22)*

Peters, N. (1999). The turbulent burning velocity for large-scale and small-scale turbulence. *J. Fluid Mech.*, 384(107):107–132. *(p. 215)*

Peters, N. (2000). *Turbulent Combustion.* Cambridge University Press. *(p. 12, 17, 22, 138, 214)*

Philip, M., Boileau, M., Vicquelin, R., Schmitt, T., Durox, D., Bourgouin, J.-F., and Candel, S. (2014). Simulation of the ignition process in an annular multiple-injector combustor and comparison with experiments. In *ASME Turbo Expo*. *(p. 37)*

Piana, J., Veynante, D., Candel, S., and Poinsot, T. (1997). Direct numerical simulation analysis of the G-equation in premixed combustion. *ERCOFTAC Series. Direct and Large-Eddy Simulation II*, 5:321–330. *(p. 30)*

Pierce, C. D. and Moin, P. (2004). Progress-variable approach for large-eddy simulation of non-premixed turbulent combustion. *Journal of Fluid Mechanics*, 504:73–97. *(p. 22)*

Pitsch, H. (2005). A consistent level set formulation for large-eddy simulation of premixed turbulent combustion. *Combust. Flame*, 143(4):587–598. *(p. 138)*

Pitsch, H. (2006). Large-eddy simulation of turbulent combustion. *Ann. Rev. Fluid Mech.*, 38:453–482. *(p. 26)*

Poinsot, T. and Veynante, D. (2012). *Theoretical and numerical Combustion*. Third edition. *(p. 12, 14, 17, 19, 26, 36, 46, 48, 50, 211, 219, 220)*

Poinsot, T., Veynante, D., and Candel, S. (1991). Quenching processes and premixed turbulent combustion diagrams. *J. Fluid Mech.*, 228:561–605. *(p. 214)*

Poludnenko, A. and Oran, E. (2010). The interaction of high-speed turbulence with flames: Global properties and internal flame structure. *Combustion and Flame*, 157(5):995–1011. *(p. 215)*

Pons, L., Darabiha, N., Candel, S., Ribert, G., and Yang, V. (2009). Mass transfer and combustion in transcritical non-premixed counterflows. *Combustion Theory and Modelling*, 13(1):57–81. *(p. 73, 172, 194)*

Pope, S. B. (2000). *Turbulent flows*. Cambridge University Press. *(p. 132, 138)*

Pope, S. B. (2004). Ten questions concerning the large-eddy simulation of turbulent flows. *New Journal of Physics*, 6(1):35. *(p. 13)*

Prandtl, L. (1946). Uber ein neues formelsystem für die ausgebildete turbulenz. *Akad. Wiss. Göttingen, Math.-Phys*, (6-19). *(p. 115)*

Proch, F. and Kempf, A. M. (2014). Numerical analysis of the cambridge stratified flame series using artificial thickened flame LES with tabulated premixed flame chemistry. *Combustion and Flame*. *(p. 46, 69, 121)*

Proch, F., Pettit, M., Ma, T., Rieth, M., and Kempf, A. (2013). Investigations on the effect of different subgrid models on the quality of LES results. In *Workshop on Direct and Large-Eddy Simulation 9*. *(p. 96)*

Regele, J. D., Knudsen, E., Pitsch, H., and Blanquart, G. (2013). A two-equation model for non-unity lewis number differential diffusion in lean premixed laminar flames. *Combustion and Flame*, 160(2):240 – 250. *(p. 25, 47)*

Reynolds, O. (1903). Papers on mechanical and physical subjects. In *The Sub-Mechanics of the Universe*, volume 3. Cambridge University Press. *(p. 219)*

Roberts, W. L., Driscoll, J. F., Drake, M. C., and Goss, L. P. (1993). Images of the quenching of a flame by a vortex to quantify regimes of turbulent combustion. *Combustion and Flame*, 94(1–2):58–69. *(p. 4, 213, 214, 217)*

Roux, A. and Pitsch, H. (2010). Large-eddy simulation of stratified combustion. In for Turbulence Research, C., editor, *Annual Research Briefs*, pages 275–288. *(p. 30, 42, 47, 68)*

Roux, S., Lartigue, G., Poinsot, T., Meier, U., and Berat, C. (2005). Studies of mean and unsteady flow in a swirled combustor using experiments, acoustic analysis, and large eddy simulations. *Combustion and Flame*, 141(1-2):40 – 54. *(p. 138, 142)*

Sagaut, P. (2006). *Large Eddy Simulation for Incompressible Flows: An Introduction*. Scientific Computation. Springer, third edition. *(p. 13)*

Savre, J., Carlsson, H., and Bai, X. S. (2013). Turbulent methane/air premixed flame structure at high Karlovitz numbers. *Flow Turbulence and Combustion*, 90:325–341. *(p. 46, 215, 216)*

Schmitt, P., Poinsot, T., Schuermans, B., and Geigle, K. P. (2007). Large-eddy simulation and experimental study of heat transfer, nitric oxide emissions and combustion instability in a swirled turbulent high-pressure burner. *Journal of Fluid Mechanics*, 570:17–46. *(p. 33)*

Schmitt, T., Boileau, M., Veynante, D., and Moureau, V. (2013a). Flame wrinkling factor dynamic modeling for large eddy simulations of turbulent premixed combustion. In *Eighth International Symposium On Turbulence and Shear Flow Phenomena*. *(p. 32, 114, 117, 118, 120)*

Schmitt, T., Sadiki, A., Fiorina, B., and Veynante, D. (2013b). Impact of dynamic wrinkling model on the prediction accuracy using the F-TACLES combustion model in swirling premixed turbulent flames. *Proceedings of the Combustion Institute*, 34(1):1261 – 1268. *(p. 32, 36, 114, 117, 118)*

Seffrin, F., Fuest, F., Geyer, D., and Dreizler, A. (2010). Flow field studies of a new series of turbulent premixed stratified flames. *Combustion and Flame*, 157(2):384 – 396. *(p. 68, 70, 75)*

Selle, L., Lartigue, G., Poinsot, T., Koch, R., Schildmacher, K. U., Krebs, W., Prade, B., Kaufmann, P., and Veynante, D. (2004). Compressible large eddy simulation of turbulent combustion in complex geometry on unstructured meshes. *Combustion and Flame*, 137(4):489–505. *(p. 33)*

Smagorinsky, J. (1963). General circulation experiments with the primitives equations. *Monthly Weather Review*, 91(3):99–164. *(p. 13, 15, 71, 78, 140)*

Smith, G. P., Golden, D. M., Frenklach, M., Moriarty, N. W., Eiteneer, B., Goldenberg, M., Bowman, C. T., Hanson, R. K., Song, S., Jr., W. C. G., Lissianski, V. V., and Qin, Z. (1999). Gri-mech 3.0. *http://www.me.berkeley.edu/gri-mech/*. *(p. 19, 20)*

Sommerer, Y., Galley, D., Poinsot, T., Ducruix, S., Lacas, F., and Veynante, D. (2004). Large eddy simulation and experimental study of flashback and blow-off in a lean partially premixed swirled burner. *Journal of Turbulence*, 5. *(p. 33)*

Staffelbach, G., Gicquel, L. Y. M., Boudier, G., and Poinsot, T. (2009). Large eddy simulation of self excited azimuthal modes in annular combustors. *Proceedings of the Combustion Institute*, 32(2):2909–2916. *(p. 33)*

Sweeney, M. S., Hochgreb, S., and Barlow, R. S. (2011a). The structure of premixed and stratified low turbulence flames. *Combustion and Flame*, 158(5):935 – 948. *(p. 213, 214)*

Sweeney, M. S., Hochgreb, S., Dunn, M. J., and Barlow, R. S. (2011b). A comparative analysis of flame surface density metrics in premixed and stratified flames. *Proceedings of the Combustion Institute*, 33(1):1419–1427. *(p. 69, 95)*

Sweeney, M. S., Hochgreb, S., Dunn, M. J., and Barlow, R. S. (2012a). The structure of turbulent stratified and premixed methane/air flames I: Non-swirling flows. *Combustion and Flame*, 159(9):2896–2911. *(p. 69, 95)*

Sweeney, M. S., Hochgreb, S., Dunn, M. J., and Barlow, R. S. (2012b). The structure of turbulent stratified and premixed methane/air flames II: Swirling flows. *Combustion and Flame*, 159(9):2912 – 2929. *(p. 69, 95)*

Sweeney, M. S., Hochgreb, S., Dunn, M. J., and Barlow, R. S. (2013). Multiply conditioned analyses of stratification in highly swirling methane/air flames. *Combustion and Flame*, 160(2):322 – 334. *(p. 69, 95)*

TNF Workshop (2014). International workshop on measurement and computation of turbulent (non)premixed flames. url: http://www.ca.sandia.gov/TNF/abstract.html. *(p. 68)*

Trisjono, P., Kleinheinz, K., Pitsch, H., and Kang, S. (2014). Large eddy simulation of stratified and sheared flames of a premixed turbulent stratified flame burner using a flamelet model with heat loss. *Flow, Turbulence and Combustion*, 92(1-2):201–235. *(p. 30, 40, 47, 68, 87)*

van Oijen, J. A. and de Goey, L. P. H. (2000). Modelling of premixed laminar flames using flamelet-generated manifolds. *Combustion Science and Technology*, 161(1):113–137. *(p. 22, 24, 56)*

Vervisch, L., Bidaux, E., Bray, K. N. C., and Kollmann, W. (1995). Surface density function in premixed turbulent combustion modelling, similarities between probability density function and flame surface approaches. *Phys. Fluids*, 10(7):2496–2503. *(p. 31)*

Vervisch, L., Haugel, R., Domingo, P., and Rullaud, M. (2004). Three facets of turbulent combustion modelling: DNS of premixed flame, LES of lifted nonpremixed V-flame and rans of jet-flame. *Journal of Turbulence*, 5(4):1–36. *(p. 29)*

Vervisch, L. and Veynante, D. (2000). Interlinks between approaches for modelling turbulent flames. *Proc. Combust. Inst.*, 28:175–183. *(p. 26)*

Veynante, D. and Knikker, R. (2006). Comparison between LES results and experimental data in reacting flows. *Journal of Turbulence*, 7(35):1–20. *(p. 77, 87)*

Veynante, D., Schmitt, T., Boileau, M., and Moureau, V. (2013). Analysis of dynamic models for turbulent premixed combustion. In *Proceedings of the Summer Program 2012*. Center For Turbulence Research, Stanford University. *(p. 113, 117, 118, 119, 122)*

Veynante, D. and Vervisch, L. (2002). Turbulent combustion modeling. *Progress in Energy and Combustion Science*, 28(3):193 – 266. *(p. 12, 26)*

Vicquelin, R. (2010). *Tabulation de la cinetique chimique pour la modélisation et la simulation de la combustion turbulent*. PhD thesis, Ecole Centrale Paris. *(p. 207)*

Wang, G., Boileau, M., and Veynante, D. (2011). Implementation of a dynamic thickened flame model for large eddy simulations of turbulent premixed combustion. *Combustion and Flame*, 158(11):2199 – 2213. *(p. 32, 71, 96, 114, 115, 116, 117, 118)*

Wang, G., Boileau, M., Veynante, D., and Truffin, K. (2012). Large eddy simulation of a growing turbulent premixed flame kernel using a dynamic flame surface density model. *Combustion and Flame*, 159(8):2742 – 2754. *(p. 32, 114, 117)*

Wang, P., Platova, N. A., Fröhlich, J., and Maas, U. (2014). Large eddy simulation of the PRECCINSTA burner. *International Journal of Heat and Mass Transfer*, 70(0):486–495. *(p. 138)*

Williams, F. A. (1985a). *Combustion theory*. The Benjamin/Cummings Publishing Company, Inc. *(p. 24)*

Williams, F. A. (1985b). Turbulent combustion. In Buckmaster, J. D., editor, *The mathematics of combustion*, pages 116–151. SIAM. *(p. 30)*

Zhou, R., Balusamy, S., Sweeney, M. S., Barlow, R. S., and Hochgreb, S. (2013). Flow field measurements of a series of turbulent premixed and stratified methane/air flames. *Combustion and Flame*, 160(10):2017–2028. *(p. 69, 95, 98)*